DESIGN OF MULTIFUNCTIONAL METAL-ORGANIC FRAMEWORK (MOF) FOR THE NEXT GENERATION APPLICATIONS

Thesis Submitted for the Degree of Doctor of Philosophy (Science) of Jadavpur University
2024

By

SUSANTA DINDA

DEPARTMENT OF CHEMISTRY

JADAVPUR UNIVERSITY

JADAVPUR, KOLKATA 700032

INDIA

JADAVPUR UNIVERSITY

Department of Chemistry

Kolkata 700032, India

Prof. Debajyoti Ghoshal

Professor

Email: Debajyoti.ghoshal@jadavpuruniversity.in

CERTIFICATE FROM THE SUPERVISOR

This is to certify that the thesis entitled **"DESIGN OF MULTIFUNCTIONAL METAL-ORGANIC FRAMEWORK (MOF) FOR THE NEXT GENERATION APPLICATIONS"** submitted by Mr. **Susanta Dinda**, who got his name registered on 16th October, 2020 for the award of Ph.D. (Science) degree of Jadavpur University, is absolutely based upon his own work under the supervision of Prof. Debajyoti Ghoshal and that neither this thesis nor any part of it has been submitted for either any degree/diploma or any other academic award anywhere before.

15/02/24

(Prof. Debajyoti Ghoshal)

(Signature of the supervisor date with official seal)

Dr. Debajyoti Ghoshal
Professor
Department of Chemistry
Jadavpur University
Kolkata - 700032

Dedicated to

Baba, Maa, Mampi and Rini

Acknowledgements

Finally, the opportunity has come to dedicate my sincere thanks to the many people whom I have come across with during my PhD tenure, and also to some without whom this thesis could never have been written. Though I shall try my best to mention everybody and thank them for having, directly or indirectly, supported me throughout the journey, pardon me if I miss someone. The first name that comes to my mind is my supervisor Prof. Debajyoti Ghoshal, of Department of Chemistry, Jadavpur University for his continuous encouragement throughout the course of my research work. His friendly behaviour and capability to make me understand even a very tough topic in lucid way, no doubt helped me to increase the circumference of my knowledge, especially in X-Ray spectroscopy and adsorption related things. Above all, he has always provided a homely environment for students and the platform of healthy discussion to overcome the difficulties occurring during lab work, which happened almost every time! I am greatly indebted to Prof. Ghoshal for all academic and non-academic supports that I have received from him while working for this thesis. Next, I would like to thank all of my lab-mates Dr. Arijit Halder, Dr. Goutam Pahari, Dr. Fazle Haque, Dr. Saheli Ghosh, Mr. Anupam Maiti, Mr. Pintu Das, Mr. Bidhyadhar Mahato and Mr. Rakesh Kumar for their immense help in my research work by sharing the ideas and providing mental strength. I am blessed to have had such a friendly environment and valuable lab-mates which actually helped to continue my work even in various academic and personal difficulties that I faced during this tenure. I am thankful to my all lab seniors Dr. Rajdip Dey, Dr. Biswajit Bhattacharya, Dr. Dilip kumar Maity, Dr. Anamika Das and Dr. Sourav Biswas also, for their valuable suggestions whenever I had asked for. I would like to thank my collaborators Prof. Subrata Kundu, Prof. Sujoy Kumar Baitalik, Mr. Arun Karmakar and Mr. Sourav Dev. I would like to special mention my sincere regards to Dr. Anamika Das for her valuable supports and valuable words throughout my carrier. I would also like to mention my sincere regards to Prof. Samaresh Bhattattacharya, Prof. Chittaranjan Sinha, Prof. Kalyan Kumar Das, Prof. Arup Gayen, Prof. Sujoy Kumar Baitalik, Prof. Kajal Krishna Rajak, Dr. Saurabh Das, Dr. Partha mahata and Prof. Partha Roy for their constant encouragement and valuable suggestions. All other faculty members of the Department of Chemistry, Office of HOD and Dean are also acknowledged for their timely help.

Here I want to mention my beloved teachers who set my destiny to do research Prof. Ashutosh ghosh, Dr. Ramananda Maity and Mr. Sukumar Maity. I am grateful to the staff of Inorganic Section of Department of Chemistry, Jadavpur University, especially Mr.Samar Bhowmick, Mr. Soumendu Bhattacharya, Mr. Swapan Adhikary and Mrs. Ratna Roy Choudhury for their occasional help and mental support.

I deeply acknowledge my beloved friend Mr. Chhatan Das for his constant support and motivation, who always give me ideas. A caring, helpful and intelligent researcher in know.

Here I also want to mention my brother Arun Karmakar for his immense support and love, an inspiring researcher I know.

I deeply acknowledge Debu, Manas, Arunava da, Pintu da, Sudipta, Gopal da, Riti, Ayan, Progna Promita, Kiran and other friends.

I financial assistance received from the CSIR, India and SERB, INDIA is also gratefully acknowledged. I would like to gratefully acknowledge Jadavpur University for providing all the infrastructure of laboratory setup required for carrying out my thesis work.

I express my deepest gratitude from my deep heart to my beloved parents for their unflagging love, support, and constant encouragement being a very essential part of my life and for their emotional and inspirational support throughout my life-how far and how long the distance may be. I would like to special thanks to my elder brother, Khokan Jana who takes my special care for every time. A special mention and lot of thanks to my aunties Kishna Jana, Basanti jana, Kalpana Dinda, khuki pisi, Shibani pisi, Boro pisi along with them I also thanks my uncles Uttam kaku, Goutam kaku, Arun Jana, Durgapada Jana, Sudharshan Kaku.

I also want to mention my brothers and sisters for their love and caring, it gives me so much joy, Chiku, Piku, Rik, Risav, Abhi, Ashok, Swapan, Chotu, Akash, Mampi, Rinku, Bulti, Raina. Special mention for my little sister Pomi.

Department of Chemistry
Jadavpur University
Kolkata 700032

Susanta Dinda
15/02/24

(Susanta Dinda)

CONTENTS

Chapter 7

CHAPTER-1

General Introduction and Summary of Works

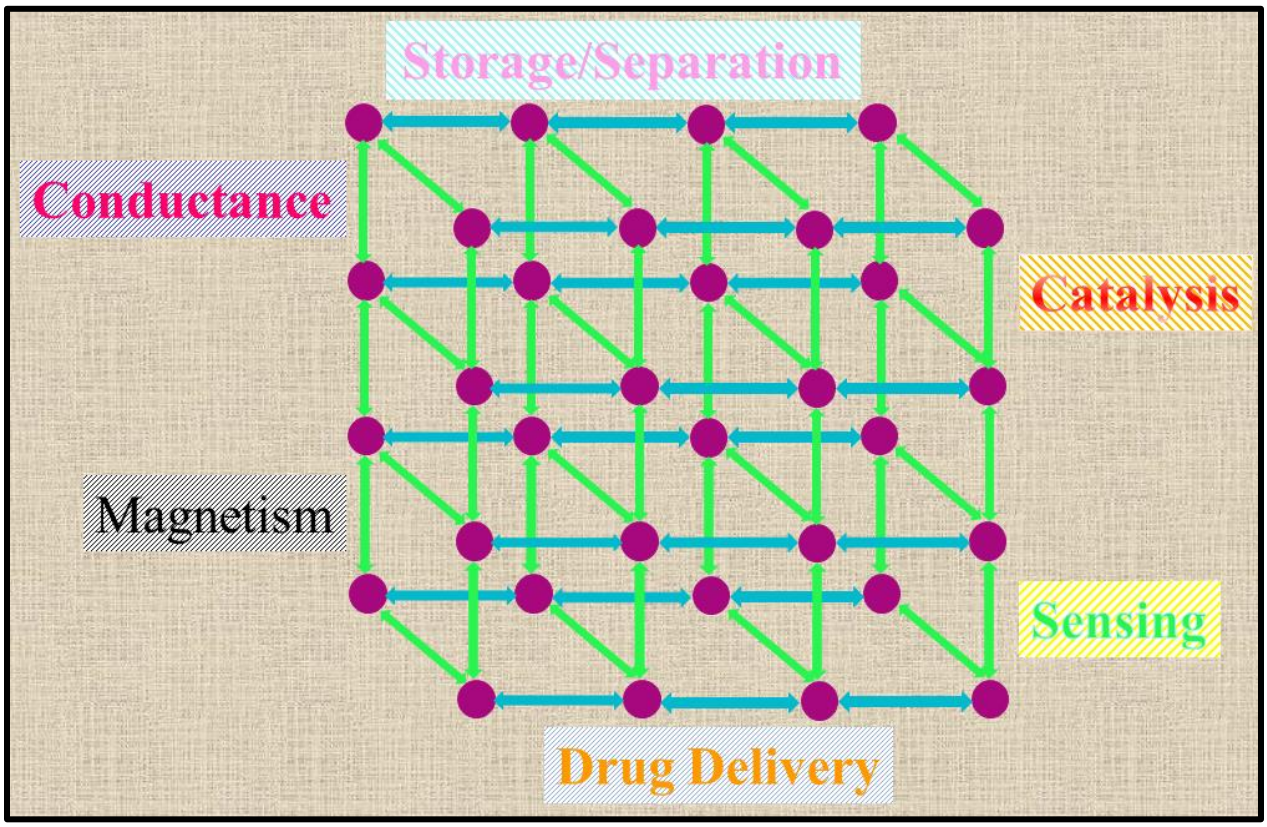

CHAPTER-1A

Section A: General Discussion on Metal Organic Frameworks (MOFs)

1A.1. INTRODUCTION

1A.1.1. Definition of Metal Organic Frameworks (MOFs)

Coordination polymers (CPs) represent an intriguing category of hybrid materials blending inorganic vertices (like metal ions or clusters) with organic ligands[1,2]. In this hybrid, the metal ion or cluster acts as a 'node,' while the organic ligand serves as a 'linker or rod.' Consequently, the organic linkers connect to the metal ions through coordination bonds, constructing diverse structures-ranging from one-, two-, or three-dimensional frameworks[3-5]. When higher-dimensional CPs feature solvent-accessible voids and retain structural integrity after solvent removal, they qualify as porous coordination polymers (PCPs). Owing to these inherent voids, they act as porous materials, sometimes termed as metal-organic frameworks (MOFs)[6,7].

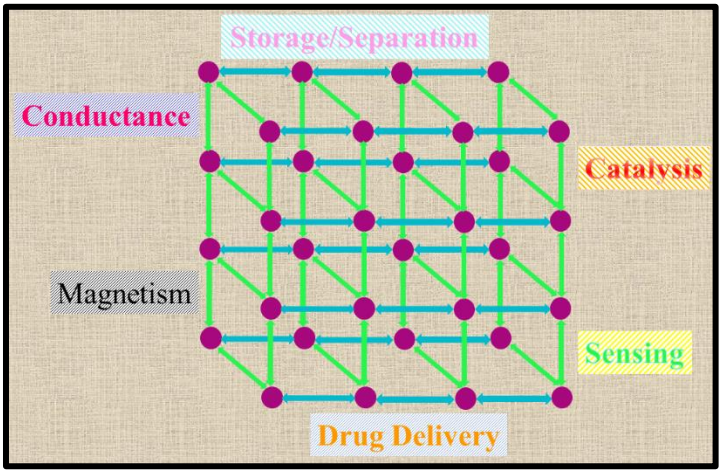

Scheme 1. Applications of MOFs

Despite other porous materials-like zeolites, activated carbon, and molecular sieves-displaying porous properties, they exhibit drawbacks in terms of structural organization and stability. In contrast, porous CPs emerge as highly effective materials for gas storage and separation due to their ordered, thermally stable structures with customizable pore size, volume, and functional pore surfaces[8,9]. Notably, MOFs crystalline nature enables the determination of their precise structure via single crystal X-ray analysis. Presently, designing MOFs synthetically holds significant importance. It not only facilitates the creation of versatile structural topologies but also extends to a wide array of applications, including gas storage and separation,[10] photoluminescence,[11-13] magnetism,[14,15] anion exchange,[16,17] catalysis,[18,19] electrical/proton conduction,[20,21] and more (refer

to Figure 1). These functionalities in CPs primarily rely on modulating their structure, achieved by varying organic ligands concerning their size, shape, and functional groups. Hence, contemporary researchers extensively synthesize a wide range of MOFs, leveraging a thoughtful selection of organic ligands and metal ions to obtain MOFs with desired functionalities.

1A.1.2. Historical Evolution and Terminology

The term "coordination polymers (CPs)"[22] garnered attention among researchers primarily from the 1960s, whereas the term "metal-organic frameworks (MOFs)"[23] emerged in the late 1990s, specifically referring to a distinct subset within coordination polymers. Statistical data also shows a remarkable surge in the usage of these two terminologies during the period of 2001 to 2010, coinciding with the advancement of this new frontier in research. Distinguishing between organic polymers and CPs, organic polymers comprise macromolecules formed from monomers or oligomers linked via covalent bonds, possessing defined molecular weights. Conversely, coordination polymers (CPs) constitute an infinite arrangement of metal-ligand coordination through various non-covalent interactions, resulting in the formation of at least one-dimensional frameworks[24]. In 1964, J. C. Bailar initially coined the term "coordination polymer" to draw a comparison between organic polymers and inorganic polymeric species[25]. He also outlined specific properties necessary for considering inorganic polymeric structures as CPs. Subsequently, in 1977, Buser et al. reported the first X-ray structure of a coordination polymer-Prussian blue. The structural analysis of Prussian blue unveiled a three-dimensional framework with mixed-valent Fe(II)/Fe(III) states[26]. Over time, the term "coordination polymers (CPs)" appeared somewhat ambiguous to researchers as it encompassed all extended structures of metal-ligand coordination without specifying a final structure or morphology. Conversely, "metal-organic frameworks (MOFs)" specifically denoted three-dimensional structures with porosity or possessing gas storage properties. Inorganic chemists tended to favour the term "CPs," while solid-state chemists leaned towards "MOFs." The field's use of multiple terminologies has indeed led to confusion among researchers. To address this ambiguity, a distinction has been proposed: "CPs" now encompasses all extended structures of metal-ligand coordination forming infinite 1D chains, 2D sheets, or 3D frameworks. In contrast, "MOF" is reserved for porous three-dimensional frameworks, excluding one or two-dimensional networks[27]. However, the attempt to differentiate between CPs and MOFs hasn't entirely resolved the issue. O.M. Yaghi, credited with introducing the term "MOF" for a copper bipyridine complex based on metal-ligand coordination, expressed

disappointment with this clarification[28]. He proposed that restricting "MOF" solely to three-dimensional structures with porosity or gas storage properties is limiting, especially considering the challenge of identifying porosity within crystals. Consequently, alternative terminologies have emerged in an effort to provide more precise descriptors within this field. These include terms such as "porous coordination polymers (PCPs),"[29] "metal-organic coordination networks,"[30] "metal-organic hybrid,"[31] and "metal-organic rotaxane frameworks (MORFs)."[32] These new terms aim to offer nuanced categorizations and clarify specific structural or functional aspects of these materials beyond the limitations of CPs or MOFs (Scheme 2). The ongoing evolution of terminologies reflects the complexity and diversity of these materials, as well as the endeavour to accurately categorize and describe their structural features and functionalities in research and application.

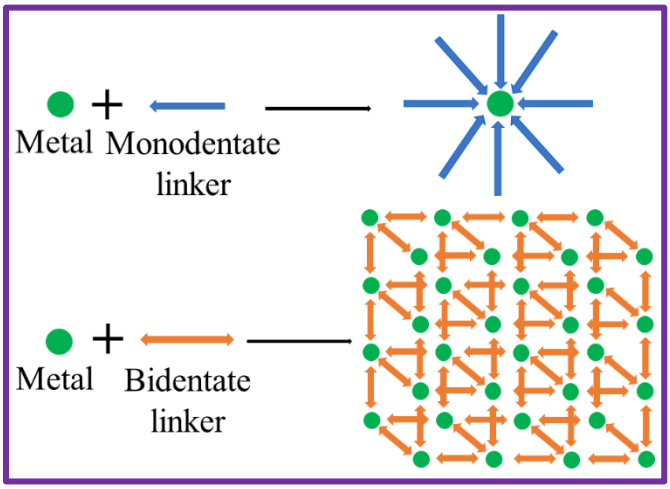

Figure 2. Schematic representation of the development of extended metal organic frameworks (MOFs) and mono-donor coordination complex.

1A.2. DESIGN STRATEGY OF DIFFERENT MULTI-FUNCTIONAL METAL ORGANIC FRAMEWORKS

Designing multifunctional (Scheme 3) metal-organic frameworks (MOFs) involves a thoughtful approach to integrate multiple desired properties into the structure. Here is a strategy outlining how these MOFs can be designed: Over the past two decades, the quest for diverse functional metal-organic frameworks (MOFs) has driven the advancement of a mixed ligand approach. This technique involves employing multiple types of ligands during MOF synthesis, as depicted in Scheme 4. The process of synthesizing MOFs with mixed ligands demands a meticulous selection of ligands based on their compatibility, coordination preferences, and desired functionalities.

Achieving the right balance between different ligands and their proportions, alongside controlling the reaction conditions during MOF formation, significantly shapes the final structure and properties of the material. Integrating more than one type of ligand amplifies structural diversity, enriching the potential for creating functional materials through this multifaceted ligand approach.

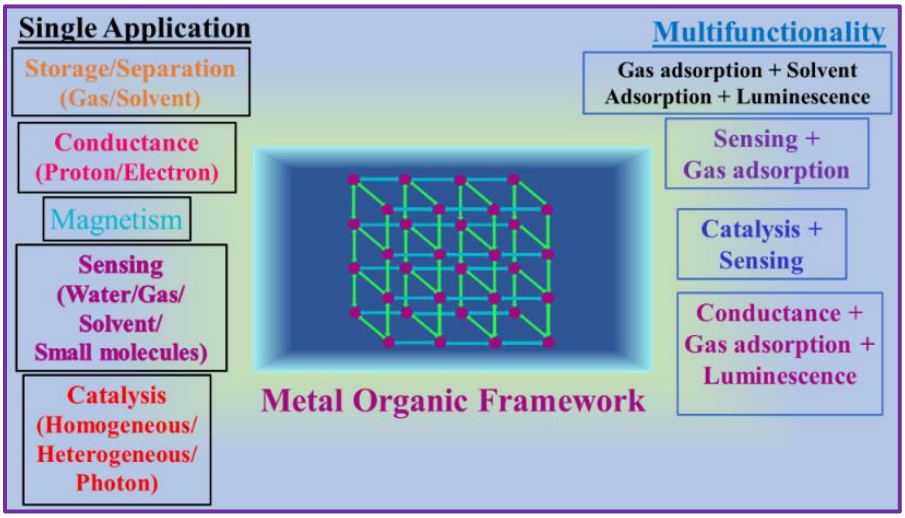

Scheme 3. Single and multifunctional applications of MOFs

1A.2.1. Mixed Ligand Methodology for Synthesis of MOFs

This approach facilitates property tuning tailored for specific applications like gas storage, catalysis, or drug delivery. Typically, three primary types of mixed ligand approaches are employed to explore and harness the diverse functionalities and structural variations within MOFs (Scheme 5).

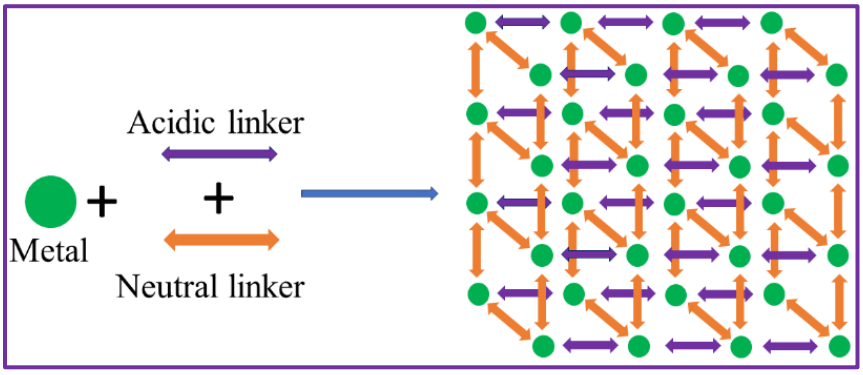

Scheme 4. Synthetic representation of mixed ligands of MOFs.

1A.2.1.1. Anionic-Anionic Mixed-Ligand MOFs

Anionic-anionic mixed-ligand MOFs are metal-organic frameworks incorporating multiple anionic ligands in their structure. These ligands, characterized by their acidic properties, play a

pivotal role in constructing the coordination framework. Their presence can significantly impact properties like acidity, catalytic activity, and interactions with other molecules or ions within the MOF structure. Few examples, A pillared-layered structure microporous MOF $[Co_2(ma)(ina)]_n \cdot 2nH_2O$ (ma = malate and ina = isonicotinate) was synthesized via a hydrothermal reaction involving fumaric acid, maleic acid, or maleic anhydride and isonicotinic acid. This reaction utilized $Co(NO_3)_2 \cdot 6H_2O$ and a base to generate the mentioned MOF[33]. The first structurally authenticated example of coordinated polymer featuring homometallic pillared-trilayer structure, $[Co_3(ina)_2(pico)_2(H_2O)_2]_n$ was built from mixed pyridyl-type monocarboxylates, isonicotinate (ina)and 3-hydroxypicolinate (pico), containing Kagome-type $[Co_3(pico)_2(H_2O)_2]_n^{2n+}$ trilayers.[34]

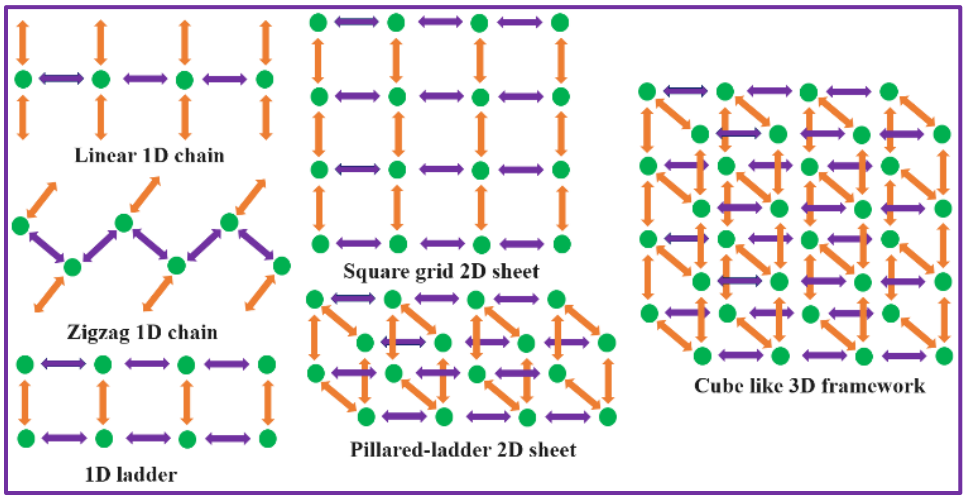

Scheme 5. Various geometry of MOFs in one-, two- and three-dimension.

1A.2.1.2. Neutral–Neutral Mixed-Ligand MOFs

Neutral–neutral mixed-ligand MOFs encompass coordination polymers that integrate multiple neutral ligand types within their structure. These ligands, lacking a net charge, actively participate in shaping the metal-organic framework. Their incorporation can impact diverse properties of the MOF, including structural diversity, pore attributes, and specific interactions occurring within the framework. A three-dimensional coordination polymer $[Co(bpy)(bimb)(SCN)_2]_n$ is created through a hydrothermal reaction involving the mixed ligands bpy and bimb in conjunction with $Co(SCN)_2$.[35]

1A.2.1.3. Anionic–Neutral Mixed-Ligand MOFs

Anionic–neutral mixed-ligand MOFs represent coordination polymers incorporating both anionic and neutral ligands within their structure. The incorporation of these ligands, possessing different charges, actively contributes to constructing the coordination framework. This combination influences various properties of the MOF, potentially impacting features like reactivity, selectivity, or structural attributes within the framework. Few examples When hydroxy-phenyl-acetic acid (H_2hypa) reacts with Co^{2+} and 4,4′-bipyridine (4,4′-bpy), the pillared-layered compound [Co_2(hypa)$_2$(4,4′-bpy)] was obtained.[36] In another report the 2D pillared-bilayer compound [Co(5-NH_2-bdc)(4,4′-bpy)$_{0.5}$(H_2O)]$_3$·2H_2O (5-NH_2-bdc = 5-aminoisophthalate) was reported.[37]

1A.2.2. Mixed Metal Methodology for Synthesis of MOFs

The method of incorporating multiple metal ions into the framework during metal-organic framework (MOF) synthesis, known as mixed-metal methodology, holds several advantages. These advantages encompass enhanced stability, customizable electronic properties, and improved catalytic activity. Moreover, the resulting structural diversity proves beneficial across multiple applications, such as gas storage or separation processes. Each variant of mixed-metal MOFs presents unique properties and functionalities, rendering them adaptable materials for applications in catalysis, gas storage, sensing, and separation processes. The choice of metals and their combinations plays a pivotal role in shaping the properties and overall performance of the resulting MOF. Variations in mixed-metal MOFs arise from diverse combinations of metals utilized during synthesis. These variations include:

1A.2.2.1. Heterometallic MOFs.

Heterometallic MOFs belong to a category of MOFs incorporating diverse metal ions within their structure. What sets these MOFs apart is their amalgamation of various metal species, forming a composite lattice framework. This integration of different metals results in distinctive properties and functionalities absent in MOFs composed of a single metal type. Heterometallic MOFs boast adaptability in structural design and chemical composition. Examples The alkaline-resistant MOF, denoted as [{Fe_3(μ_3-O)(BDC)$_3$}$_4${Co_2(NA)$_4$(LT)$_2$}$_3$], exhibits remarkable catalytic activity in the oxygen evolution reaction (OER)[38], showcasing an impressively low overpotential of 225 mV at a current density of 10.0 mA cm^{-2}. A recently reported heterometallic Ni–Co MOF ([CoNi(μ_3-BDC)$_2$(μ_2-PYZ)$_2$] (PYZ = pyrazine)) has been highlighted in supercapacitor development.[39]

1A.2.2.2. Bimetallic MOFs.

Bimetallic MOFs belong to a specialized category of MOFs integrating two diverse metal ions into their structure. These MOFs stand out by harmonizing two distinct metal species within one framework, resulting in elevated functionalities and properties when compared to single-metal MOFs. The synergy between these two metals fosters unique effects, facilitating customized structural attributes and enabling a wide array of applications in realms like catalysis, gas storage, and separation processes. An amalgamated Co/Ni metal-organic framework (MOF) serves as a sacrificial template, undergoing an alkaline hydrolysis and selective oxidation process to create a composite material featuring an accordion-like structure composed of ternary $NiCo_2O_4$/β-$NixCo1–x(OH)_2$/α-$NixCo1–x(OH)_2$[40]. Bimetallic MOF has been utilized to calculate OER, {$Fe_2Ni(\mu_3$-$O)(COO)_6(H_2O)_3$}[41].

1A.2.2.3. Trimetallic and Multimetallic MOFs.

Trimetallic and multimetallic MOFs represent distinct categories within the realm of MOFs, integrating three or more diverse metal ions into their structure. These MOFs are notable for their intricacy, amalgamating multiple metal species within a unified framework. By incorporating three or more metals, these MOFs form elaborate structures endowed with heightened functionalities and properties, surpassing those of traditional MOFs. Their versatile nature extends to tailored properties and diverse applications across fields like catalysis, sensing, gas storage, and separation processes, owing to their exceptional composition and structural complexity. Films of trimetallic MnxFeyNi-MOF-74, shaped like fusiform structures, are crafted using a one-step solvothermal process, enhancing the electrochemical catalytic performance for both oxygen evolution reaction (OER) and hydrogen evolution reaction (HER)[42].

1A.2.2.4. Isoreticular MOFs.

Isoreticular MOFs form a distinct category within the family of MOFs. They exhibit a consistent network topology despite changes in their metal ions or organic linkers. These MOFs excel in maintaining a uniform framework structure while incorporating diverse metal ions or organic constituents. The term "isoreticular" signifies their ability to retain fundamental structural aspects across different MOFs, facilitating modifications in composition without disrupting the overall framework architecture. This exceptional trait allows for crafting MOFs with varied properties while upholding a consistent lattice structure. MOF-5 stands as an archetypal example within the realm of MOFs, inspiring the synthesis of numerous isoreticular counterparts[43]. A novel series of

envisaged MOF-5 analogues has been proposed, crafted from readily available organic compounds, adding then to the expanding library of MOF structures[44].

1A.2.3. Incorporating Functionalities for Synthesis of MOFs

In MOF synthesis, adding functionalities means deliberately creating unique properties like customized surface chemistry, precise pore sizes, improved stability, or specific reactivity. Achieving these traits involves strategic choices of metal ions, organic linkers, and post-synthesis modifications. By enhancing functionalities, MOFs become well-suited for gas storage, catalysis, sensing, drug delivery, and other diverse applications. The introduction of N,N′-cycloalkylation to UiO-67-bpy (bpy = 2,2′-bipyridyl) results in the creation of a new ionic MOF named UiO-67-DQ, which is enriched with the electron-deficient diquat (DQ) chromophore[45].

1A.2.4. Tailoring the Pore Size for Synthesis of MOFs

Tailoring pore size in MOF synthesis means intentionally adjusting the empty spaces (pores) within the structure. This involves shaping and sizing the pores to fit specific guest molecules or ions. Changing the metal ions, organic linkers, or using templating methods allows precise control of MOFs' pore sizes. This customization is vital for optimizing gas storage, separations, catalysis, and molecular sensing, as it impacts how well MOFs can absorb and select certain molecules or ions. Tailoring the pore sizes of UiO-66 and UiO-67 MOF produce UiO-66-NH_2 UiO-67-NH_2 use as catalysts[46].

1A.2.5. Modular Design of MOFs

In MOFs, modular design[47,48] means parts can be swapped or combined, giving flexibility. This involves making components-like metal ions or linkers-easy to change. By mixing these parts, different MOFs with specific features can be made, such as specific functions or pore sizes. This makes it easier to create MOFs for particular uses, making the material adaptable for different needs.

1A.2.6. Enhancing the flexibility in synthesis of MOFs

Making MOFs more flexible[49,50] (Scheme 6) during their creation means finding ways to make them more adaptable and versatile. This involves methods that give more choices and control over the MOF's structure, properties, or functions. Flexibility can come from adjusting reaction conditions, changing the types or amounts of metals and linkers used, using different synthesis methods, or making alterations after the synthesis. The aim is to expand the options for MOF

designs and features, making it easier to customize MOFs for specific uses or improve their usefulness across different areas.

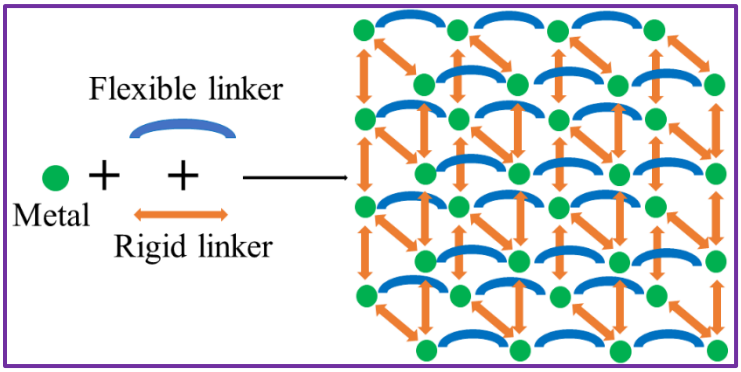

Scheme 6. Synthetic scheme for flexible MOFs

1A.2.7. Apply Post Synthesis Modification in Synthesis of MOFs

Post-synthetic modification[51-53] (PSM) enhances MOFs' multifunctionality by tweaking their structure or properties after creation. PSM involves adding new features or changing traits in MOFs that were already made. It allows the integration of various functions after the initial MOF synthesis. PSM provides flexibility to modify MOFs by adding functional groups, nanoparticles, or molecules to the existing framework. This modification broadens MOFs' capabilities, enabling the introduction of multiple functions within one material. By adding different functional groups or additives via PSM, MOFs gain diverse capabilities like catalysis, adjustable porosity, improved adsorption, or customized surface properties. This versatility enables MOFs to be used in various applications simultaneously or adapt to different conditions, making them multifunctional materials. Overall, PSM is a critical approach to customize MOFs, making them suitable for diverse fields and purposes.

1A.3. FACTORS INFLUENCING THE SYNTHESIS OF VERSATILE FRAMEWORKS

Designing Metal-Organic Frameworks (MOFs) is a detailed process that relies on important factors, each playing a part in creating specific abilities in these adaptable materials.

1A.3.1. The Function of Metal Ions

Metal centers, also termed nodes, form connections with linkers at specific angles, profoundly impacting the synthesis of MOFs. Their influence depends on attributes like size, hardness, coordination number, geometry, and ligand field stabilization energy. The coordination number and geometry of a metal centre result from the uneven distribution of electron density. Larger

cations generally lead to higher coordination numbers. This prompts the use of various metal ions[54] alkali and alkaline earth metals, transition metals, and lanthanides-each offering distinct outcomes based on their properties. Transition metal ions, possessing partially filled d-orbitals, are favoured for MOF synthesis due to their adaptable coordination numbers and effective bonding with organic ligands. Lanthanide metal ions[55], larger in size with coordination numbers between 7 and 10, pose challenges in determining their coordination environment, making them complex for use as nodes in MOFs. Common transition metal salts like nitrate, chloride, and phosphate are often used in MOF synthesis. Transition metal ions can also function as metal clusters or secondary building units (SBU)[56] within MOFs. These units, comprising multiple metal centers interconnected by bridging oxide moieties, exhibit diverse geometries. However, alkali or alkaline earth metal ions are less preferred due to drawbacks like undefined coordination numbers, geometry, and a lack of ligand field stabilization for coordinate bond formation. Their tendency to form solvated metal centers, especially in aqueous environments, results in the creation of organic-inorganic ionic layers. Consequently, exploration into MOFs based on alkali or alkaline earth metals has been relatively limited.

1A.3.2. The Function of Ligands

The conversation focuses on several factors that contribute to the creation of diverse dimensionalities and topologies in MOFs. Of these factors, organic ligands stand out as pivotal. These ligands serve as bridges with metal centers, facilitating the formation of infinite polymeric structures recognized as metal–organic frameworks (MOFs). For this purpose, the linkers must be bi-dentate or multi-dentate, showcasing a range of characteristics including varied charges (neutral or ionic), donor atoms (N-, O-, S- or a blend of N and O-donors), diverse shapes, sizes, and functional groups.

1A.3.2.1. The Function of N-donor Ligands

Since 1990, N-donor ligands have dominated the realm of organic ligands for MOF synthesis. Typically, these ligands act in their neutral form, utilizing the lone pair of N-atoms from amine groups or pyridyl, imidazole, triazole, and tetrazole rings to coordinate with metal centers, forming the infinite structure of MOFs. In general, pyridyl or imidazole/triazole N-atoms coordinate more readily with metal centers compared to amine groups. However, the metal-N coordinate bond is more labile than the stable metal-O bond, allowing for structural variation in MOFs through easy rearrangements during the self-assembly process, often leading to supramolecular isomerism.

Researchers have extensively employed various N-donor ligands for MOF synthesis[57-59], a few of which are illustrated in Figure 1. When N-donor ligands bind with cationic metal centers, the resulting metal-ligand complex becomes cationic. To neutralize this complex, counter anions might be present in the framework, preventing interpenetration of compounds. Additionally, the size of N-donor ligands can influence the structures of formed MOFs. Smaller N-donor ligands like pyrazine (pyz), diazabicyclooctane (dabco), or 4,4′-bipyridine (bpy) tend to form non-flexible, robust structures with smaller pores, less prone to interpenetration. Conversely, N-donor ligands containing longer, flexible chains such as 1,2-bispyridylethane (bpe), 1,3-bispyridylpropane (bpp), or bisimidazolepropane (bip) generally yield interpenetrated structures and exhibit structural dynamism. Furthermore, N-donor ligands with azo/azine groups like 4,4′-azobispyridine (azbpy), 1,4-bis-(4-pyridyl)-2,3-diaza-1,3-butadiene (4-bpdb), and 2,5-bis-(4-pyridyl)-3,4-diaza-2,4-hexadiene (4-bpdh) contain Lewis basic N-atoms effective for MOFs to exhibit enhanced CO_2 adsorption capacity. Therefore, N-donor ligands not only significantly influence the structural modulation of MOFs but also play a pivotal role in diversifying their functionalities.

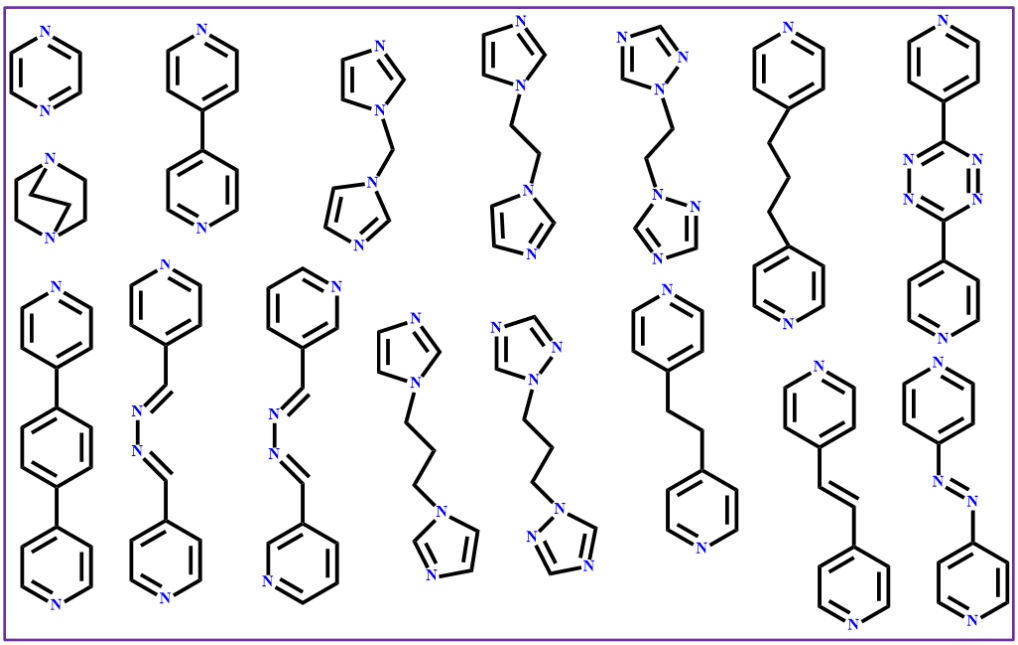

Figure 1. Some N, N′-donor ligands to prepare the MOFs

1A.3.2.2. The function of O-donor ligands

Another class of frequently utilized organic ligands in constructing coordination polymers are O-donor ligands, which predominantly function in their anionic form, such as alkoxides,

carboxylates, sulfonates, nitrates, and phosphates. While various types of O-donors are employed in MOF synthesis, carboxylate O-donors, especially bi-dentate or multi-dentate ones, have become extensively prevalent for yielding meaningful outcomes in MOFs[60-63].

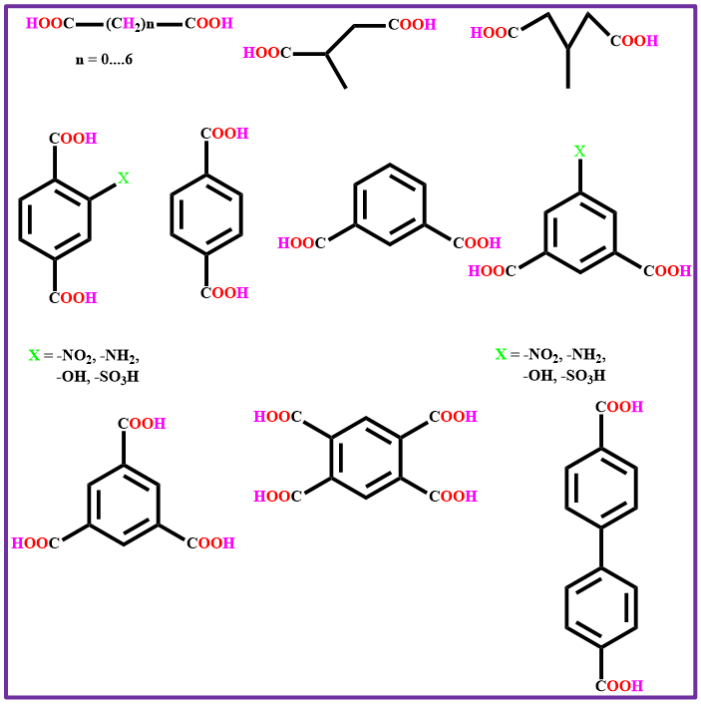

Figure 2. Some O-donor ligands to prepare the MOFs

Carboxylates, owing to their multi-dentate anionic donor sites, efficiently bridge with cationic metal centers, resulting in the formation of diverse dimensional MOFs. Consequently, numerous O-donor poly-carboxylates are employed in materials science, some of which are indicated in Figure 2. These poly-carboxylates exhibit differences in size, shape, rigidity/flexibility, and the presence of functional groups, among other characteristics. Like N-donor ligands, poly-carboxylates significantly influence the structural variations in MOFs. For instance, small-sized dicarboxylates like oxalate, malonate, or fumarate typically yields non-interpenetrated MOF[64-66] due to the formation of smaller cavities, while larger aliphatic dicarboxylates like glutarate or adipate often lead to interpenetrated frameworks because of larger cavities[67]. Aromatic dicarboxylates generally result in robust MOFs due to their structural rigidity, while both aliphatic and aromatic dicarboxylates, based on their functional groups, generate diverse functional MOFs suitable for various applications[68,69]. Carboxylates, recognized as hard ligands, form robust bonds with hard metal centers. Transition metals are the preferred choice due to their ability to form

various coordination geometries, leading to diverse network architectures. These polycarboxylate ligands[70,71] exhibit diverse bridging modes when coordinating with cationic metal centers, such as monodentate, bis-monodentate, mono-chelatate, bis-chelatate, mono-bidentate, bis-bidentate, chelating-monodentate, chelating-bidentate, and various oxo-bridging modes, as depicted in the example of terephthalic acid (Figure 3).

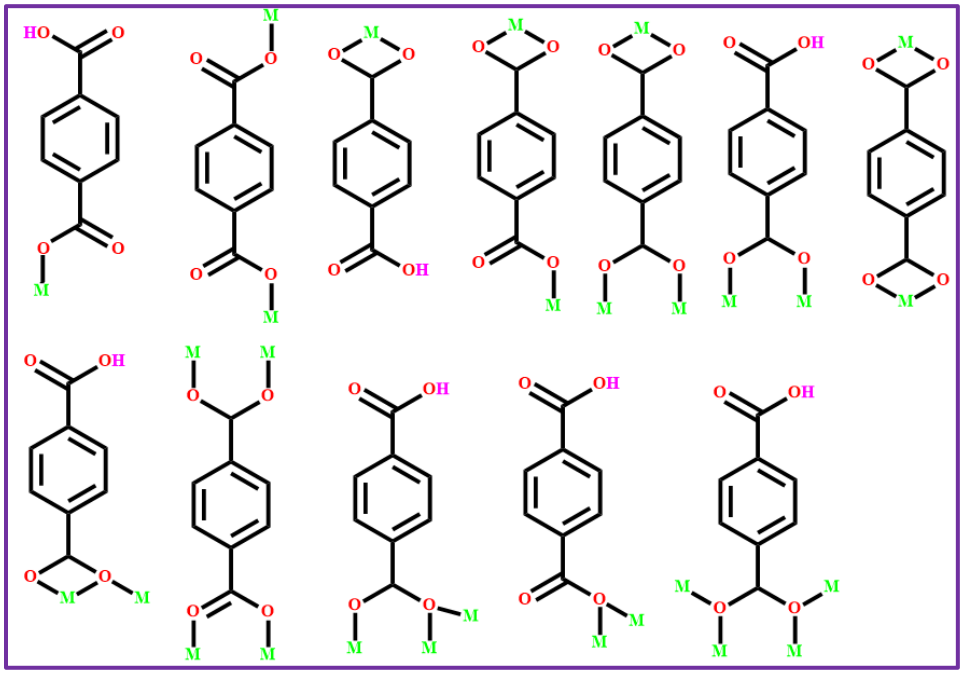

Figure 3. Various bridging fashion of terephthalic acid

1A.3.3. The Role of Solvents

Typically, MOFs are synthesized within solvent mediums, but once formed, they tend to be insoluble due to their polymeric structure. The solvent employed during synthesis is crucial, contributing to the crystalline structure of MOFs and ensuring the framework's stability via weak interactions like hydrogen bonding or C–H···π interactions within the ligand systems. Variations in solvents can result in entirely different structures[72,73], offering diverse potential applications. Additionally, dynamic mixed-ligand MOFs demonstrate solvent-induced effects such as breathing or swelling[74-76] (Scheme 4). These effects involve the expansion and contraction of pores within the coordination networks during hydration and dehydration processes. Therefore, the choice of solvent is vital for obtaining phase-pure crystalline materials and constructing a wide array of coordination networks with distinct properties.

1A.3.4. The Role of Weak Non-Covalent Interaction

Weak non-covalent interactions, such as hydrogen bonding (4–120 kJ/mol), π–π interactions (<50 kJ/mol), CH…π, cation–π interactions (5–80 kJ/mol), anion…π, van der Waals interactions (5–80 kJ/mol), electrostatic interactions (e.g., ion-ion, dipole-dipole ~20 kJ/mol), and hydrophobic interactions (<40 kJ/mol), play vital roles in shaping unique architectures. The spatial arrangement of individual atoms or groups significantly contributes to fostering these weak interactions within the structure. The stability MOFs heavily rely on the various short-range and weak interactions between their building blocks[77-79]. Manipulating these weak forces allows for the design of the final architecture of the crystal network. Although controlling these weak interactions presents a challenge, comprehending these non-covalent interactions is crucial for constructing diverse functional coordination polymers with distinct structures[80-82].

1A.3.5. The Role of pH

The pH level of a MOF system's medium can significantly influence the resulting crystalline product. It impacts the crystals by altering existing forms, changing the binding patterns of carboxyl ligands, forming hydroxy bridges[83], and initiating assembling reactions. For instance, the pH level of the reaction medium plays a crucial role in producing various products within mixed-ligand MOF systems[84]. This pH effect also holds considerable sway over coordination systems involving multicarboxylic acids as ligands[85].

1A.3.6. The Role of Temperature

Temperature significantly influences chemical reactions, playing a pivotal role in the formation of various MOFs[86-88]. By adjusting temperature while maintaining other conditions, different MOFs can be obtained. Temperature-sensitive MOFs can showcase diverse phases with distinct functionalities. Hence, researchers in this field must carefully consider the role of temperature when aiming to design a range of functional MOFs.

1A.3.7. The Function of Counter Anion

Various counter anions play a significant role in shaping the synthesis of specific MOFs[89-92]. Incorporating different counter anions can be part of the post-synthetic modification of MOFs, where these counter anions replace weakly coordinated or lattice anions, leading to the formation of distinct crystals. Occupying the framework void, these counter anions might weakly coordinate or remain uncoordinated to the metal centers. In MOFs containing lattice and coordinated anions, these anions determine the void area's polarity, suggesting that post-synthetic modification through

anion exchange could enhance the MOFs' properties. Additionally, this method offers a unique opportunity to create anion receptors based on an anion-exchange approach.

1A.4. SYNTHETIC PROCEDURE OF THE SYNTHESIS OF MOFS

Currently, numerous methods exist for crafting coordination polymers (CPs) and metal-organic frameworks (MOFs) within material science and synthetic chemistry. Let's delve into a few prominent techniques below.

1A.4.1. Stirring Method

Typically, researchers rely on this conventional method for preparing MOFs. Initially, a concentrated solution of the reactants is mixed thoroughly by stirring for several hours at room temperature, ensuring a uniform solution. Subsequently, this meticulously mixed concentrated solution is left to evaporate in a non-humid environment, facilitating the formation of high-quality single crystals ideal for X-ray diffraction analysis.

1A.4.2. Solvothermal Method

This stands as the most favoured method for MOFs synthesis, involving crystallization from high-temperature solutions of reactants in desired solvents under elevated vapor pressures. A range of solvents or their combinations water, dimethylformamide, dimethylacetamide, acetonitrile, methanol is employed. Alongside solvent variation, factors like reactant concentration, stoichiometry, pH, reaction duration, and temperature demand consideration in solvothermal synthesis planning. Samples are placed in robust, high-temperature Teflon cups suitable for enduring extreme pressure and temperature. These cups, non-corrosive under such conditions, are sealed within an autoclave. Temperatures typically range from 80-160 ºC within the tightly sealed space, maintaining autogenous pressure. Post-reaction, the mixture slowly cools with a regulated cooling rate. Generally, crystals form upon cooling. The crystallization process here is straightforward. Particles within a crystal vibrate in fixed positions, and increased temperature intensifies these vibrations. If the particles acquire enough kinetic energy to break free from their positions, the crystal breaks down (melts). A dynamic equilibrium between melting and freezing rates can occur if solid and liquid phases are in contact. Yet, crystal formation is more complex; while entropy decreases as molecular ordering intensifies within the system, thermal randomization in the surroundings offsets this, especially with the release of fusion heat. Therefore, crystal growth is kinetically controlled rather than thermodynamically.

1A.4.3. Slow Diffusion Method

This technique primarily involves the gradual mixing of reactants to enhance the likelihood of forming the desired crystal. The process entails keeping separate solutions of different reactants (metal and ligand) in a layered tube, divided by a buffer solution prepared by blending two solvents used for metals and ligands at specific ratios. Through the slow diffusion technique, the two distinct solutions gradually mix, and at their interface, crystals begin to form after a certain duration. Additionally, there exist several other well-known methods such as reflux and ultrasonic techniques that synthetic chemists commonly employ for the controlled and convenient synthesis of coordination polymers.

1A.4.4. Reflux Method

Synthetic chemists employ this method to obtain single crystals. Here, reactant solutions are mixed and refluxed at a specific temperature for a few hours. Subsequently, the mixture is poured into a beaker, and over a certain period, high-quality single crystals suitable for single-crystal analysis emerge.

1A.4.5. Microwave or Ultrasonic Reaction

This method isn't widely used for producing single crystals of MOFs due to its limitations in achieving high-speed synthesis. However, it serves as a valuable technique for precisely controlling the size and shape of the resulting products.

1A.5. STRUCTURAL CHARACTERIZATIONS OF MOFS

Understanding the complete structure of a synthesized metal organic framework (MOF) is fundamental. Numerous methods have been employed for structural characterization, but X-ray crystallography takes precedence. Both single crystal and powder forms of crystallography are essential to precisely determine MOFs. Single crystal X-ray diffraction (XRD) helps obtain crystallographic parameters, elucidating the complete structure, crystal packing, and weak forces within a particular structure. In contrast, powder X-ray diffraction verifies the phase purity by comparing patterns with simulated data from single crystal XRD. Many software packages aid in determining crystallographic parameters from PXRD patterns. Additionally, basic spectroscopic techniques like Fourier transform infrared (FT–IR), diffused reflectance UV–vis, and solid-state nuclear magnetic resonance (NMR) spectroscopy are used for primary characterization of ligands and synthesized frameworks. FT–IR identifies functional groups by matching theoretical frequencies. Solid-state UV–vis spectroscopy characterizes electronic transitions in the UV or

visible region. NMR spectroscopy examines nuclear spin state interactions with magnetic fields. Further methods like thermogravimetric analysis are employed to measure thermal stability and decomposed products at varying temperatures in solid samples, providing valuable insights into synthesized MOFs.

1A.5.1. Fourier Transform Infrared (FT–IR) Spectroscopy

Fourier transform infrared (FT–IR) spectroscopy stands as one of the primary and widely employed spectroscopic techniques across organic and inorganic chemistry. In this method, infrared radiation is directed through a sample made with KBr, forming a homogeneous mixture. The detector then measures the energy of the transmitted radiation. This process reveals the amount of energy absorbed at each wavelength. The resulting spectra offer insights into the specific wavelengths at which the sample absorbed energy, highlighting the structural characteristics of materials and identifying various functional groups based on their characteristic frequencies.

1A.5.2. Nuclear Magnetic Resonance (NMR) Spectroscopy

Nuclear magnetic resonance (NMR) spectroscopy is a highly effective absorption technique employed in chemistry. Samples are exposed to a strong magnetic field where the nuclei in the atoms absorb energy from radio waves. This technique is applicable in both liquid and solution states, relying on interactions between the nuclei and the magnetic field to facilitate transitions between nuclear spin states. Its significance lies in providing valuable chemical and structural insights into samples. NMR spectroscopy is versatile, enabling the prediction of structural information in various states, including solutions and solid forms.

1A.5.3. Electron Paramagnetic Resonance (EPR)

Electron paramagnetic resonance (EPR) spectroscopy serves as a technique for analyzing materials that contain unpaired electrons. It involves the excitation of electron spin. EPR spectroscopy is commonly employed in the study of metal complexes or organic radicals.

1A.5.4. Elemental Analysis

Elemental analysis involves determining the percentages of elements like C, H, and N. This analysis, focusing on these elements, helps validate the likely empirical formula of the structures under examination.

1A.5.5. Single Crystal X-ray Diffraction Analysis

Single crystal X-ray diffraction analysis stands as an authoritative technique, offering detailed insights into the crystal structure of a compound. It provides a wealth of information encompassing

crystal symmetry, unit cell parameters, space group, structural dimensions, site-ordering details, and atomic positions. The resulting unit cell parameters can confirm whether the structures are novel or already cataloged within databases like the Cambridge Structural Database (CSD). This method relies on utilizing graphite-monochromated X-rays of Mo-Kα radiation (λ= 0.71073Å) and a crystalline sample. These X-rays, generated by a sealed tube source and filtered to produce monochromatic radiation, are focused onto the sample. Interaction between the incident rays and the sample creates constructive interference and diffracted rays, adhering to Bragg's Law ($n\lambda = 2d \sin\theta$). This law correlates electromagnetic radiation wavelength, diffraction angle, and lattice spacing within a crystalline sample. The resultant diffracted X-rays are detected, processed, and counted. Manipulating the incident ray geometry, crystal orientation, and detector placement allows accessing all feasible diffraction directions of the lattice. Collected data is then processed, correcting for absorption via various software tools. Following data collection, integration, and solution using successive Fourier and difference Fourier synthesis techniques are employed. Full matrix least-squares refinements are applied to F2 values for all non-hydrogen atoms using diverse refinement software.

1A.5.6. X-ray Powder Diffraction

The X-ray powder diffraction pattern represents the scattered intensity from a sample, depicting incident and scattered angles, polarization, and wavelength or energy. This pattern is akin to a unique "fingerprint" for crystalline materials, allowing for their identification based on distinct characteristics. Additionally, it aids in justifying phase transformations within a solid sample by comparing unit cell parameters before and after studies. To conduct this study, the initially synthesized solid samples are uniformly ground into a bulk form. Subsequently, X-ray powder diffraction patterns of these samples are captured using Cu-Kα radiation (λ = 1.5406 Å) employing a suitable powder diffractometer set in Bragg–Brentano (reflection) mode.

1A.5.7. Thermogravimetric Analysis (TGA)

Thermogravimetric analysis (TGA) is an invaluable technique that tracks the weight variation of a solid material as temperature changes within a controlled atmosphere. It provides a quantitative assessment of weight loss attributed to material transitions and thermal degradation. This method serves to determine the thermal stability of a substance and identify its decomposition products.

1A.5.8. UV–Vis Spectroscopy

This type of absorption spectroscopy reveals the electronic transitions like π–π*/n–π* or d–d transition, illustrating intra-ligand (ILCT) or metal to ligand (MLCT) charge transfer within the UV or visible range for solid samples in experiments. Coordination polymers are typically insoluble in common organic solvents, prompting the need for structural characterization in their solid state. UV-VIS spectroscopy is conducted using diffuse reflectance spectra (DRS) on powdered samples, utilizing a diffuse reflectance accessory, hence termed diffused reflectance UV-VIS spectroscopy.

1A.5.9. Nitrogen Gas Adsorption

Determining the surface area and pore volume of synthesized structures holds fundamental importance in coordination chemistry. The successful combination of metals and ligands forms intricate coordination polymer structures, often acting as hosts for small molecules. These frameworks showcase their potential through high surface areas and porosities, pivotal for various applications. Surface area, a crucial aspect governing the practical utility of coordination polymers, demands careful manipulation to achieve desired or enhanced values for effective usage in diverse applications. Expanding the organic linker has often been a strategy employed to create microporous coordination polymers (MCPs), resulting in higher surface areas. However, issues like framework collapse, incomplete guest removal, or the presence of non-optimal linkers may lead to lower surface areas or nonporous behaviour in the final framework[93,94]. To address these challenges, theoretical calculations are also being used to ascertain whether the synthesized material can achieve its optimal surface area. The Grand Canonical Monte Carlo (GCMC) simulation stands as one of the most accurate methods for calculating theoretical surface areas of crystal structures[95]. This theoretical value is compared with experimental data obtained from BET surface area analysis, typically associated with nitrogen gas adsorption studies on coordination polymers. Various calculations, such as BET or Langmuir, can be employed to determine surface areas, with BET being considered more reliable[96]. Recent studies have also explored the separation of nitrogen from different gas mixtures using various adsorbents while controlling gas pressure, showcasing the diverse applications of these materials beyond surface area characterization.

1A.6. VARIOUS POTENTIAL APPLICATIONS OF MOFS

1A.6.1. Gas and Solvent Sorption

Among the numerous applications of coordination polymers, gas and solvent adsorption[97,98] stand out as extensively studied subjects due to their versatile industrial and practical utility. The presence of significant void-containing frameworks in these materials facilitates their multifunctional applications (Scheme 3). These frameworks cater to specific adsorbates based on their inherent properties such as kinetic diameter, polarity, and shape, making them suitable hosts for diverse molecules. Measuring the pore size of synthesized coordination polymers is crucial for understanding their adsorption capabilities. This is often be achieved by analyzing their various nitrogen adsorption isotherms.

1A.6.1.1. Carbon Dioxide Adsorption

The Earth's atmospheric CO_2 levels are progressively rising due to the combustion of fossil fuels, significantly contributing to dramatic climate changes like global warming. To address this concerning increase in CO_2, capturing the emitted CO_2 becomes pivotal, especially considering the crucial role of energy in sustaining civilization. Most flue gases contain substantial amounts of nitrogen (N_2). Therefore, achieving selectivity in the absorption process is crucial to ensure that the capturing material exclusively traps CO_2 from the nitrogen-carbon dioxide gas mixture. While carbon capture and sequestration (CCS) technologies[99] using methods like amine scrubbing[100] or membrane separation have been widely employed for CO_2 capture, they often face economic durability issues[101]. However, zeolites have gained prominence in CO_2 separation due to their well-defined structures and stability. Recently, researchers have turned their focus to metal-organic frameworks (MOFs) as porous solids for CO_2 separation. Numerous groups have reported thousands of porous CPs/MOFs due to their capacity for selective CO_2 adsorption. Ghoshal and colleagues (Scheme 8) provided a comprehensive explanation of how the functional group's presence and the framework's flexibility significantly influence the carbon dioxide adsorption within the synthesized structure. Furthermore, they highlighted the structure's capability for selectively adsorbing carbon dioxide over other gases[102]. Yan and colleagues demonstrated the effect of -O-Li, -NH_2, -SH, -F, -COOH, and -NO_2 functional groups on the adsorption and separation of pure CO_2 and a mixture of CO_2 and CH_4 by changing the functionality of Mg-MOF-74 at 298 K and 10–3000 kPa. The results showed that -O-Li, -NH_2, and -SH groups increased the

CO_2 adsorption followed the order Li-O-Mg-MOF-74 > NH2-Mg-MOF-74 > SH-Mg-MOF-74. conclusively demonstrating the selectivity between CO_2 and CH_4[103].

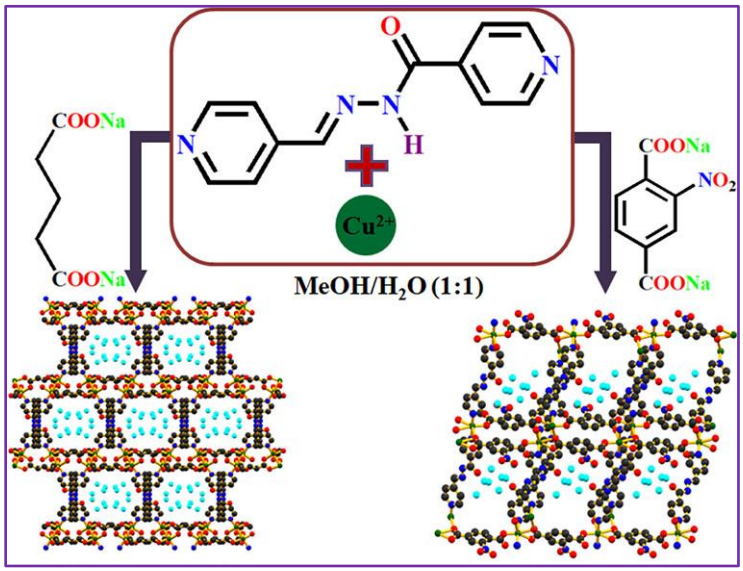

Scheme 8. Schematic Representation of the Role of amide and nitro groups in CO_2 Adsorption.

1A.6.1.2 Hydrogen Adsorption

Due to the petroleum fuel crisis and the substantial CO_2 emissions from combustion, alternative energy sources for automotive transportation are crucial. Battery and fuel-cell technologies emerge as robust candidates to replace gasoline and diesel engines. Hydrogen, in particular, stands out as an appealing energy carrier due to its carbon-free nature, abundant availability from water, and exceptional mass energy density[104]. However, effective hydrogen storage remains a significant challenge, posing a bottleneck to commercializing fuel-cell vehicles. This challenge stems from hydrogen's high fugacity and related safety concerns. CPs/MOFs possess several key features that make them promising for hydrogen storage. These materials exhibit open metal sites, catenation/interpenetration[105] (Scheme 9), high specific surface area, suitable pore sizes, and structural flexibility, all contributing to enhanced H_2 uptake capacity under optimal conditions. Catenation and interpenetration within CPs/MOFs can significantly enhance H_2 uptake while simultaneously improving thermal stability, thereby reducing the likelihood of framework collapse during desolvation. Ghoshal et. al. extended this experiments by creating 2D+2D inclined polycatenated structure changing the metal center Cu(II) to Co(II), which also shows selective capture of the hydrogen gas.[106] Farha et. al. reported air-stable Cu(I)-based MOFs that contain

open metal sites have the potential for storing hydrogen (H_2) at ambient temperatures. In particular, that demonstrate very high isosteric heats of adsorption for hydrogen relative to other reported MOFs with open metal sites.[107]

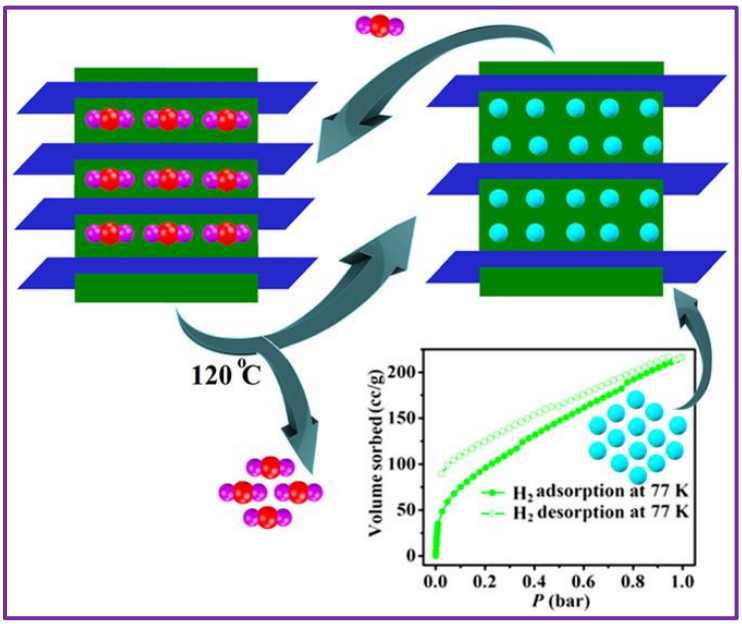

Scheme 9. Inclined polycatenated metal organic framework showing hydrogen adsorption by pore opening.

Silvestre-Albero et. al. incorporated graphite flakes in the HKUST-1 MOF, which gives different shapes crystals, octahedral-shape crystals, cauliflower-shape crystals and truncated pyramids. The incorporation of graphite in the composites improves the structural Furthermore, composites exhibit a significant improvement in thermal management, associated with the excellent thermal and electrical properties of the graphite microdomains incorporated. The improved stability of the composites is also reflected in the adsorption performance for hydrogen at atmospheric pressure and cryogenic temperatures. The best adsorption performance is achieved with HKUST-1@10GF, in monolithic form[108]. Additionally, Maity et al. highlighted the flexibility inherent in the inclined polycatenated 3D framework, which varied with temperature changes. This particular structural characteristic was attributed to the exceptional hydrogen uptake capability of this framework type[109].

1A.6.1.3. Solvent Adsorptions

Activated carbon is widely employed in solvent recovery due to its proficiency in adsorbing organic solvents from diluted gas streams. However, its high capacity for solvent adsorption leads to an increase in gas humidity during treatment. Metal-organic frameworks (MOFs) have emerged

as alternatives with the ability to adsorb solvent vapours, serving various purposes such as separation and solvent retrieval. The adsorption of solvents by MOFs encounters challenges from adsorbed water. Studies have shed light on how pre-adsorbed and co-adsorbed water affect adsorption equilibrium, especially in small fixed beds. Unlike many hybrid materials, MOFs often lack a distinct pressure threshold due to their high attraction to water, stemming from hydrophilic sites present within their network. Chuang et. al synthesized two solvent-dependent 3D supramolecular architectures, 2D + 2D polycatenated and triply-interpenetrating 3D MOF. The reversible solvent vapor ad-/desorption behaviors were investigated by cyclic de-/rehydration.[110] Tang et al. reported the in-situ polymerization of poly(N-isopropylacrylamide) (PNIPAM) chains within the one-dimensional (1D) pores of a zinc-based metal-organic framework. This pioneering method yielded new MOF-based composites exhibiting selective adsorption for water and methanol over ethanol, notably in equimolar mixtures of methanol-ethanol and water-ethanol[111]. Zheng et. al. purifies the ethylene (C_2H_4) by selective adsorption ethane (C_2H_6) from the mixture of these two molecules, which is a crucial industrial process. The construction of ethane-selective adsorbents for ethylene purification is a very challenging task. Three MOFs have been synthesized Co-1-ina**,** Co-5-ina and Co-9-ina. Among them, Co-9-ina has the highest C_2H_6 adsorption capacity and C_2H_6/C_2H_4 separation performance. The C_2H_6/C_2H_4 selectivity of Co-9-ina at 298 K and 1 bar is astoundingly 2.69, which is greater than most C_2H_6-selective MOFs. The C_2H_6/C_2H_4 separation performance for Co-9-ina was further validated by breakthrough studies under dynamic conditions.[112]

1A.6.2. Photo Luminescence

Fluorescence holds captivating potential in the realm of inorganic-organic hybrid materials, where both components contribute substantially to the remarkable photoluminescence observed. Its versatility spanning lighting, sensing, displays, and optical devices has captivated contemporary researchers' attention. A wealth of literature underscores the intricate connection between a material's luminescent characteristics and its composition, structure, and intermolecular arrangement, all directly influencing energy transfer within the material. Controlling the three-dimensional structure and intermolecular packing at the molecular level stands as a pivotal strategy in crafting highly photoluminescent metal-organic frameworks (MOFs). Luminescent MOFs attract significant interest owing to diverse elements, including their metal centers, metal-organic charge transfer, organic components, and guest molecules housed within porous MOFs,

collectively contributing to luminescence. Their multifunctional nature distinguishes them, rendering them particularly compelling compared to other inorganic and organic luminescent materials. By employing synthetic modifications, MOFs can systematically adjust emission wavelengths, a critical aspect for applications in lighting, displays, and optical devices. For the advancement of luminescent sensing materials, achieving enduring porosity and collaborative luminescent properties in the synthesized structures remains immensely crucial. Moreover, solid CPs frequently exhibit organic ligand-based emission properties at room temperature. The fluorescence observed in CPs arises from electron transfers via various mechanisms, including ligand-to-ligand (LLCT)[113], metal-to-ligand (MLCT)[114], ligand-to-metal (LMCT)[115], or metal-to-metal charge transfer (MMCT)[116] (Scheme 10). This property's significance has spurred substantial interest among researchers, driving a heightened focus on synthesizing photo-luminescent CPs tailored for diverse purposes. Numerous applications are actively under discussion and exploration, tapping into the potential of these materials

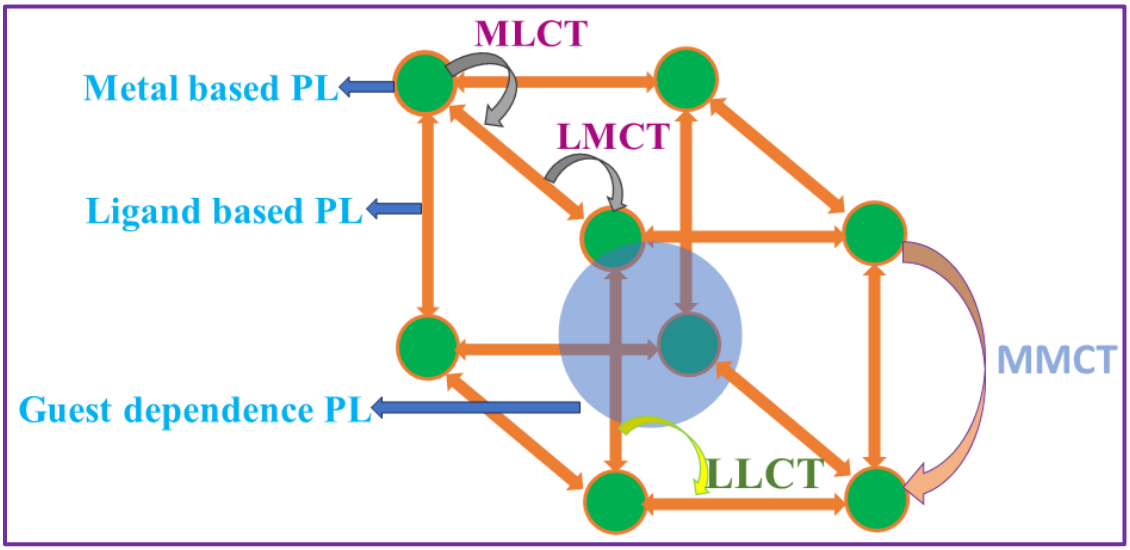

Scheme 10. Different types of photoluminescence in MOF.

Fluorescence quenching stands out as one of the most prominent and active areas of exploration in this domain. Countless esteemed researchers have dedicated their efforts to synthesizing luminescent CPs/MOFs, aiming to delve deeper into this phenomenon. Duan et. al. reported a three-dimensional (3D) acridone-based Co-MOF. This exhibits a promising approach to modulating the direction of PET in MOFs by fine modifications of the ligands, thus providing a new avenue to develop multipurpose and flexible catalytic systems.[117] Yang and colleagues have

detailed a collection of host-guest compounds, utilizing a magnesium metal-organic framework (Mg-MOF) as the host and various pyridine derivatives as guests. While these host-guest compounds do not incorporate photochromic modules, they are capable of generating long-lived charge-separated states with noticeable colour alterations upon exposure to UV light. The nature of substituents in the pyridines and the proton delocalization ability between the host and guests significantly impact the photoinduced electron transfer process, thereby enabling the fine-tuning of photoinduced charge-separated states in the MOF materials.[118] Li et. al. introduced an innovative dual-emissive platform, Tb@Zr-MOF, characterized by high water stability, achieved through the strategic incorporation of lanthanide Tb3+ ions into a Zr(IV)-bipyridine framework. This design enables Tb@Zr-MOF to demonstrate a distinct double-enhancement feature, attributed to the significantly enhanced photoinduced electron transfer (PET) effect, when compared to pristine Zr-MOF.[119]

Luminescence can be categorized into two primary types based on different spin state emission processes. Firstly, there's fluorescence, characterized by the emission of light between energy states with the same spin multiplicity, lasting for around 10 nanoseconds. Secondly, phosphorescence involves light emission between states of differing spin multiplicity, enduring from microseconds to seconds. Understanding this property often involves studying specific parameters of the samples: Luminescence spectra, which display fluorescence intensity concerning wavelength, quantum yield[120], representing the efficiency of the fluorescence process by indicating the ratio between emitted photons released during fluorescence and absorbed photons and lifetime[121], denoting the average duration a molecule remains in its excited state before emitting a photon. This duration is inversely proportional to the sum rate constants of both radiative and nonradiative processes.

The movement of protons within or between molecules is also a very fundamental and prominent aspect in the process of luminescence. Proton transfers can occur in both ground and excited states within specific molecular systems. Among these processes, excited-state intramolecular proton transfer (ESIPT)[122-125] stands out for its fascinating characteristics: it displays notably large Stokes' shifted fluorescence emission, ranging from 6000 to 12000 cm^{-1}, and lacks self-reabsorption. ESIPT follows a distinct four-level[126] photocycle scheme, initiated by enol (E)–keto (K) phototautomerization (E → E∗ → K∗ → K → ...). Notably, ESIPT occurs rapidly (kESIPT > 10^{12} s^{-1}), even in challenging conditions like rigid environments and low

temperatures. Typically, ESIPT molecules showcase intramolecular hydrogen bonds between a proton donor (–OH, $–NH_2$) and a proton acceptor (–C=O, –N=), positioned closely together. Maji et al[127,128] initially presented the H_4dhtp-based Mg-MOF [Mg(H_2dhtp$^{2–}$)(DMF)$_2$]n (DMF =N,N-dimethylformamide) and its ligand-driven multicolour emission through ESIPT. The Mg-MOF exhibited diverse fluorescent hues in solvents of varying polarities, such as EtOH, DMSO, H_2O, and DMF. Ghoshal et al.[129] synthesized a Zn-MOF {[Zn(4-bpdh)(H_2dhpt)]·(MeOH)(H_2O)}$_n$. The framework, once stripped of solvents, exhibited a fluorescent response to specific polar molecules. Notably, immersion in THF, MeOH, EtOH, and MeCN produced emission spectra displaying a single peak within the range of 450–525 nm. This phenomenon was interpreted as water and DMF molecules possessing a higher stabilization energy for the intramolecular charge transfer state, thereby promoting the ESIPT process. Such spectral distinctions could potentially be utilized for detecting traces of water in various organic solvents (Figure 4).

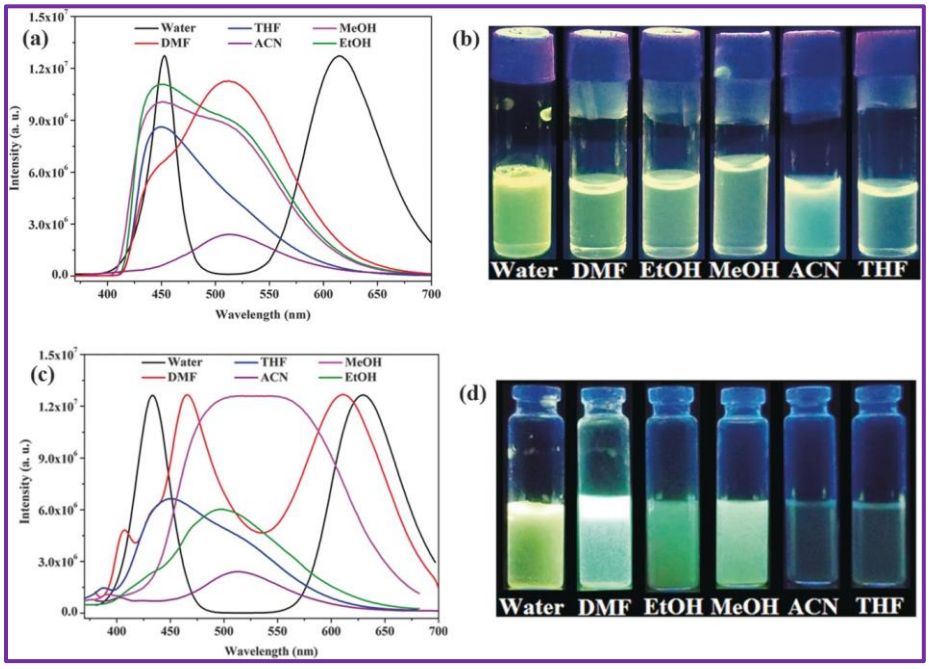

Figure 4. Fluorescence spectra (λ_{ex}=350 nm) of DHT (a) and dehydrated Zn-MOF (c) suspended in various solvents. Photographic images of the suspension of DHT (b) and (d) in different solvents after photoexcitation with a UV lamp[129].

With an extension to this study, they further reported two MOFs, [{Cd(bpe)1.5(dht)}·solvent] and [{Cd(bpe)1.5(dht)}], that detect the polar solvents among the non-polar solvent (Scheme 11).[130] Li et al.[131] presented a Mg-MOF synthesized from a [Mg_3(OH)(CO_2)$_6$] cluster. Notably, ESIPT ligands and corresponding Mg−MOFs displayed turn-

off-on fluorescence sensing behaviour upon the addition of Al^{3+} ions. Particularly, Mg−TPP−DHBDC (DHBDC = 2,5-dihydroxybenzene-1,4-dicarboxylic) exhibited exceptionally high sensitivity compared to reported Al^{3+} probes.

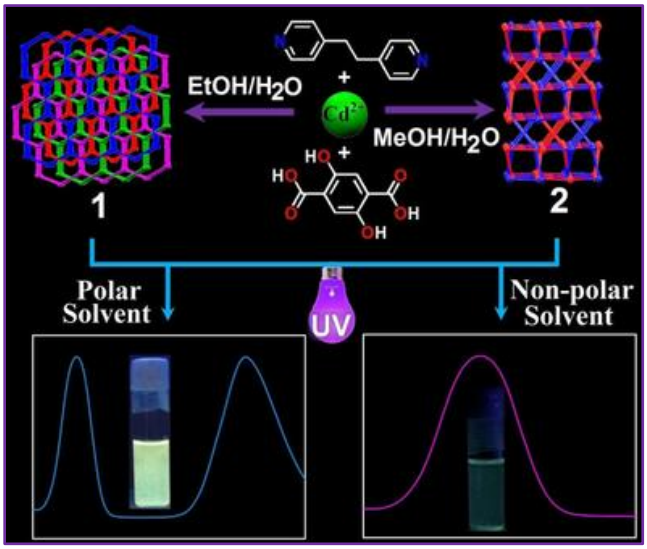

Scheme 11. Effect of polar and non-polar solvents to ESIPT.

The fluorescence of these Mg-MOFs exhibited a "continuously decreasing and then blue shift and continuously increasing" pattern upon the introduction of Al^{3+}. The binding of Al^{3+} to the –OH group in the ESIPT active site disrupted the intramolecular proton transfer process, resulting in a blue shift of the emission.

1A.6.3. Electrocatalysis

Metal-organic frameworks (MOFs), stand out as a pioneering class of catalyst materials. Their catalytic effect is extraordinary[132-134], owing to their remarkable porosity, dynamic structure, customizable design, ultrahigh surface area, and crystalline composition. MOFs serve as active catalysts for electrochemical hydrogen (H_2) production[135], boasting inherent traits that uphold their functionality and structural integrity even after undergoing synthetic modifications. This inherent property renders MOFs compelling catalysts for water-splitting processes. In the realm of water-splitting reactions, MOFs offer unparalleled versatility in physical, spatial, chemical, and electronic attributes.[136,137] They outshine conventional semiconductor catalysts and can serve as templates or precursors for crafting functionalized materials such as porous carbon, metal sulfides, metal oxides, and carbon-metal/metal oxide hybrids. Derivatives derived from MOFs typically retain the structural characteristics of their parent materials, often exhibiting enhanced catalytic

performance. Over the past few years, numerous studies have explored the application of MOFs as electrocatalysts for water splitting, indicating a growing interest in this field of research. Electrochemical water splitting involves an aqueous electrolyte, a cathode, and an anode. Applying a potential difference between the two electrodes triggers the generation of oxygen gas at the anode and hydrogen gas at the cathode. Oxygen evolution reaction (OER) in water electrolysis tends to be kinetically sluggish with high over-potential compared to the hydrogen evolution reaction due to its multistep nature and energy accumulation in each step. Moreover, OER's efficiency heavily depends on the pH of the electrolyte solution, exhibiting different mechanisms in acidic and basic environments.[138,139] In acidic and neutral media, hydrogen and oxygen are produced by oxidizing two water molecules with a potential of 0.404 V, while in alkaline media, hydroxyl groups transform into oxygen and water, consuming 1.230 V (vs RHE). Thus, the process operates more smoothly in alkaline conditions than in acidic environments. Recent advancements in MOF synthesis have led to innovative designs tailored for enhanced catalytic performance. For instance, Yang et al.[140] developed a novel MOF-5 with a distinctive flower-shaped morphology using a mild in situ electrochemical synthesis process, employing terephthalic acid as an organic ligand and zinc nitrate as a partial metal source. Qin et al.[141] crafted a 3-D porous polyoxometalate (POM)-based MOF with an open framework by connecting POM fragments as nodes with organic ligands. Similarly, Zhong et al.[142] synthesized two distinct MOFs, BMM-11 and BMM-12, using cobalt nitrate metal salts and organic linkers (H_4BPTC) via a solvothermal process, both demonstrating potential as direct electrocatalysts.

REFERENCE

1. Roy, S.; Titi, H. M.; Tripuramallu, B. K.; Bhunia, N.; Verma, R.; Goldberg, I. *Cryst. Growth Des.* **2016**, *16*, 2814−2825.
2. Coronado, E.; Giménez-Marqués, M.; Gómez-García, C. J.; Espallargas, G. M. *Inorg. Chem.* **2012**, *51*, 12938−12947.
3. Foo, M. L.; Matsuda, R.; Kitagawa, S. *Chem. Mater.* **2014**, *26*, 310–322.
4. Liang, X.; Cai, K.; Zhang, F.; Liu, J.; Zhu, G. *CrystEngComm.* **2017**, *19*, 6325–6332.
5. Deka, R.; Rajak, R.; Kumar, V.; Mobin**,** S. M. *Inorg. Chem.* **2023**, *62*, 3084–3094.
6. Unnikrishnan, V.; Zabihi, O.; Ahmadi, M.; Li, Q.; Blanchard, P.; Kiziltasb, A.; Naebe, M. *J. Mater. Chem. A* **2021**, *9*, 4348–4378.
7. Cook, T. R.; Zheng, Y. -R.; Stang, P. J. *Chem. Rev.* **2013**, *113*, 734−777.
8. Ma, S.; Zhoub, H. -C. *Chem. Commun.* **2010**, *46*, 44–53.
9. Li, J. -R.; Kuppler, R. J.; Zhou, H. -C. *Chem. Soc. Rev.* **2009**, *38*, 1477–1504.

10. Gong, W.; Xie, Y.; Pham, T. D.; Shetty, S.; Son, F. A.; Idrees, K. B.; Chen, Z.; Xie, H.; Liu, Y.; Snurr, R. Q.; Chen, B.; Alameddine, B.; Cui, Y.; Farha, O. K. *J. Am. Chem. Soc.* **2022**, *144*, 3737–374.
11. Li, M. -X.; Wang, H.; Liang, S. -W.; Shao, M.; He, X.; Wang, Z. -X.; Zhu, S. -R. *Cryst. Growth Des.* **2009**, *9*, 4626–4633.
12. Jensen, S.; Tan, K.; Lustig, W. P.; Kilin, D. S.; Li, J.; Chabal, Y. J.; Thonhauser, T. *Chem. Mater.* **2019**, *31*, 7933−7940.
13. Lustig, W. P.; Mukherjee, S.; Rudd, N. D.; Desai, A. V.; Li, J.; Ghosh, S. K. *Chem. Soc. Rev.* **2017**, *46*, 3242–3285.
14. Amo-Ochoa, P.; Castillo, O.; Gómez-García, C. J.; Hassanein, K.; Verma, S.; Kumar, J.; Zamora, F. *Inorg. Chem.* **2013**, *52*, 11428−11437.
15. Liu, K.; Zhang, X.; Meng, X.; Shi, W.; Cheng, P.; Powell, A. K. *Chem. Soc. Rev.* **2016**, *45*, 2423–2439.
16. Li, B.; Lei, Q.; Wang, F.; Zhao, D.; Deng, Y.; Yang, L.; Fan, L.; Zhang, Z. *J. Solid State Chem.* **2021**, *298*, 122117.
17. Zhu, L.; Xiao, C.; Dai, X.; Li, J.; Gui, D.; Sheng, D.; Chen, L.; Zhou, R.; Chai, Z.; –Schmitt, T. E. A.; Wang, S. *Environ. Sci. Technol. Lett.* **2017**, *4*, 316–322.
18. Tian, Y.; Liang, G.; Fan, T.; Shang, J.; Shang, S.; Ma, Y.; Matsuda, R.; Liu, M.; Wang, M.; Li, L.; Kitagawa, S. *Chem. Mater.* **2019**, *31*, 8494−8503.
19. Ma, S.; Han, W.; Han, W.; Dong, F.; Tang, Z. *J. Mater. Chem. A,* **2023**, *11*, 3315-3363.
20. Maity, D. K.; Otake, K.; Ghosh, S.; Kitagawa, H.; Ghoshal, D. *Inorg. Chem.* **2017**, *56*, 1581–1590.
21. Yoon, M.; Suh, K.; Kim, H.; Kim, Y.; Selvapalam, N.; Kim, K. *Angew. Chem. Int. Ed.* **2011**, *123*, 7870–7873.
22. Tomic, E. A. *J. Appl. Polym. Sci.* **1965**, *9*, 3745–3752.
23. O"Keeffe, M. *Chem. Soc. Rev.* **2009**, *38*, 1215–1217.
24. Janiak, C. *Dalton Trans.* **2003**, 2781–2804.
25. Bailar, J. C. Prep. *Inorg. React.* **1964**, *1*, 1–27.
26. Buser, H. J.; Schwarzenbach, D.; Petter, W.; Ludi, A. *Inorg. Chem.* **1977**, *16*, 2704– 2710.
27. Steed, J. W.; Atwood, J. L. *Supramolecular Chemistry, 2nd ed.; Wiley:Chichester, UK*, **2009**, 538–589.
28. Yaghi, O. M.; Li, H. *J. Am. Chem. Soc.* **1995**, *117*, 10401–10402.
29. Xiong, Y.; Li, B.; Gu, Y.; Yan, T.; Ni, Z.; Li, S.; Zuo, J. -L.; Ma, J.; Jin, Z. *Nature Chemistry*. **2023**, *15*, 286–293.
30. Lin, Z.; Richardson, J. J.; Zhou, J.; Caruso, F. *Nature Reviews Chemistry*. **2023**, *7*, 273–286.
31. Hou, Y.; Xu, Z.; Chu, F.; Gui, Z.; Song, L.; Hu, Y.; Hu, W. *Composites Part B.* **2021**, *221*, 109014.
32. Vukotic, V. N.; Loeb, S. J. *Chem. Eur. J.* **2010**, *16*, 13630 – 13637.
33. Zeng, M. H.; Feng, X. L.; Zhang, W. X.; Chen, X. M. *Dalton Trans.* **2006**, 5294–5303.
34. Zhou, Y. -L.; Wu, M. -C.; Zeng, M. -H.; Liang, H. *Inorg. Chem.* **2009**, *48*, 10146–10150.

35. Qi, Y.; Che, Y. X.; Batten, S. R.; Zheng, J. M. *CrystEngComm* **2008**, *10*, 1027–1030.
36. Zeng, M. H.; Gao, S.; Chen, X. M. *Inorg. Chem. Commun.* **2004**, *7*, 864–867.
37. Zeng, M. H.; Hu, S.; Chen, Q.; Xie, G.; Shuai, Q.; Gao, S. L.; Tang, L. Y. *Inorg. Chem.* **2009**, *48*, 7070–7079.
38. Zhou, W.; Huang, D.-D.; Wu, Y.-P.; Zhao, J.; Wu, T.; Zhang, J.; Li, D.-S.; Sun, C.; Feng, P.; Bu, X. *Angew. Chem., Int. Ed.* **2019**, *58*, 4227– 4231.
39. Gholipour-Ranjbar, H.; Soleimani, M.; Naderi, H. R. *New J. Chem.* **2016**, *40*, 9187– 9193.
40. Mei, H.; Mei, Y.; Zhang, S.; Xiao**,** Z.; Xu, B.; Zhang, H.; Fan, L.; Huang, Z.; Kang, W.; Sun**,** D. *Inorg. Chem.* **2018**, *57*, 17, 10953–10960
41. Raja, D. S.; Chuah, X. -F.; Lu, S. -Y. *Adv. Energy Mater.* **2018**, *8*, 1801065.
42. Zhou, W.; Xue, Z.; Liu, Q.; Li, Y.; Hu, J.; Li, G. *ChemSusChem* **2020**, *13*, 5647– 5653.
43. Eddaoudi, M.; Kim, J.; Rosi, N.; Vodak, D.; Wachter, J.; O'keeffe, M.; Yaghi, O. M. *SCIENCE*, **2002**, *295*, 469-472.
44. Martin, R. L.; Lin, L. -C.; Jariwala, K.; Smit, B.; Haranczyk, M. *J. Phys. Chem. C* **2013**, *117*, 23, 12159–12167.
45. Yang, N. -N.; Fang, J. -J.; Sui, Q.; Gao, E. -Q. *ACS Appl. Mater. Interfaces* **2018**, *10*, 2735–2744.
46. Peterson, G. W.; Moon, S. -Y.; Wagner, G. W.; Hall, M. G.; DeCoste, J. B.; Hupp, J. T.; Farha, O. K. *Inorg. Chem.* **2015**, *54*, 9684−9686.
47. Ji, J.; Lou, W.; Shen, P. *International Journal of Hydrogen Energy* **2022**, *47*, 39443-39469.
48. Qiu, L. -G.; Gu, L. -N.; Hu, G.; Zhang, L. -D. *J. Solid State Chem.* **2009**, *182*, 502-508.
49. Zhang, J. -P.; Zhou, H. -L.; Zhou, D. -D.; Liao, P. -Q.; Chen, X. -M. *National Science Review.* **2018**, *5*, 907–919.
50. Elsaidi, S. K.; Mohamed, M. H.; Banerjee, D.; Thallapally, P. K. *Coord. Chem. Rev.* **2018**, *358*, 125-152.
51. Wang, Z.; Cohen, S. M. *Chem. Soc. Rev.* **2009**, *38*, 1315-1329.
52. Mandal, S.; Natarajan, S.; Mani, P.; Pankajakshan, A. *Adv. Funct. Mater.* **2021**, *31*, 2006291.
53. M. Kalaj, M. Cohen**,** *ACS Cent. Sci.* **2020**, 6, 1046–1057.
54. Cui, Y.; Zou, W.; Song, R.; Yu, J.; Zhang, W.; Yang, Y.; Qian, G. *Chem. Commun.* **2014**, *50*, 719–721.
55. Roy, S.; Chakraborty, A.; Maji, T. K. *Coord. Chem. Rev.* **2014**, *273*, 139–164.
56. Tranchemontagne, D. J.; Mendoza-Cortes, J. L.; O"Keeffe, M.; Yaghi, O. M. *Chem. Soc. Rev.* **2009**, *38*, 1257–1283.
57. Sun, C.; Xi, R.; Fei**,** H. *Acc. Chem. Res.* **2023**, *56*, 452–461.
58. Wang, D.; Li, T. *Acc. Chem. Res.* **2023**, *56*, 462–474.
59. Chai, H.; Yu, K.; Zhao, Y.; Zhang, Z.; Wang, S.; Huang, C.; Zhang, X.; Zhang**,** G. *Anal. Chem.* **2023**, *95*, 10785–10794.
60. Ahmed, I.; Mondol, M. H.; Jung, M. -J.; Lee, G. H.; Jhung, S. H. *Coord. Chem. Rev* **2023**, *475*, 214912
61. Zhao, X. -L.; Sun, W. -Y. *CrystEngComm*, **2014**, *16*, 3247-3258.

62. Meng, F.; Zhang, M.; Shen, K.; Li, Y.; Zheng, H. *Dalton Trans.* **2015**, *44*, 1412-1419.
63. Gagnon, K. J.; Perry, H. P.; Clearfield, A. *Chem. Rev.* **2012**, *112*, 1034–1054.
64. Wang, C.; Guo, G.; Wang, P. *J. Mol. Struct* **2013**, *1032*, 93-99.
65. Zhao, W.; Fan, J.; Okamura, T. -a.; Sun, W. -Y.; Ueyama, N. *J. Solid State Chem.* **2004**, *177*, 2358-2365.
66. Zhang, K. -L.; Liang, W.; Chang, Y.; Yuan, L. -M.; Ng, S. W. *Polyhedron* **2009**, *28*, 647-652
67. Teixeira, F. J.; Flores, L. S.; Escobar, L. B. L.; dos Santos, T. C.; Yoshida, M. I.; Reis, M. S.; Hill, S.; Ronconi, C. M.; Corrêa, C. C. *Inorganica Chimica Acta* **2020**, *511*, 119791.
68. Hu, J. -S.; Shang, Y. -J.; Yao, X. -Q.; Qin, L.; Li, Y. -Z.; Guo, Z. -J.; Zheng, H. -G.; Xue, Z. -L. *Cryst. Growth Des.* **2010**, *10*, 4135–4142.
69. Li, J. -X.; Qin, Z. -B.; Li, Y. -H.; Cui, G. -H. *Polyhedron*, **2018**, *151*, 530-536.
70. He, Y. -P.; Tan, Y. -X.; Zhang, J. *Coord. Chem. Rev* **2020**, *420*, 213354.
71. Hu, J. -S.; Shang, Y. -J.; Yao, X. -q.; Qin, L.; Li, Y. -Z.; Guo, Z. -J.; Zheng, H -G.; Xue, Z. -L. *Cryst. Growth Des.* **2010**, *10*, 2676–2684.
72. Karmakar, A.; Rúbio, G. M. D. M.; da Silva, M. F. C. G.; Hazra, S. Pombeiro, A. J. L. *Cryst. Growth Des.* **2015**, *15*, 4185−4197.
73 Bhattacharya, B.; Halder, A.; Maity, D. K.; Ghoshal, D. *CrystEngComm* **2016**, *18*, 4074– 4083.
74. Dua, M.; Li, C. –P.; Liub, C. –S.; Fang, S. –M. *Coord. Chem. Rev.* **2013**, *257*, 1282–1305.
75. Kundu, T.; Wahiduzzaman, M.; Shah, B. B.; Maurin, G.; Zhao, D. *Angew. Chem. Int. Ed.* **2019**, *58*, 8073–8077.
76. Hou, J. -J.; Li, X. -Q.; Gao, P.; Sun, H. -Q.; Zhang, X. -M. *Cryst. Growth Des.* **2017**, 17, 3724–3730.
77. Greathouse, J. A.; Ockwig, N. W.; Criscenti, L. J.; Guilinger, T. R.; Pohl, P.; Allendorf, M. D. *Phys. Chem. Chem. Phys.* **2010**, *12*, 12621-12629.
78. Abdelhameed, R. M.; Nabil, M.; El-Medani, S. M.; Elantabli, F. M. Environmental Nanotechnology, Monitoring & Management **2023**, *20*, 100858.
79. Jana, A.; Mandal, J.; Mondal, S. S.; Patra, R.; Bhunia, A. *Inorganica Chimica Acta* **2023**, *549*, 121409.
80. Ghoshal, D.; Maji, T. K.; Mostafa, G.; Lu, T. -H.; Ray Chaudhuri, N. *Cryst. Growth Des.* **2003**, *3*, 9–11.
81. Ghosh, A. K.; Ghoshal, D.; Lu, T. -H.; Mostafa, G.; Ray Chaudhuri, N. *Cryst. Growth Des.* **2004**, *4*, 851–857.
82. Jung, J. H.; Lee, J. H.; Silverman, J. R.; John, G. *Chem. Soc. Rev.* **2013**, *42*, 924-936.
83. Long, L. S. *CrystEngComm* **2010**, *12*, 1354–1365.
84. Li, C. P.; Yu, Q.; Chen, J.; Du, M. *Cryst. Growth Des.* **2010**, *10*, 2650–2660.
85. Wang, H.; Wang, Y. Y.; Yang, G. P.; Wang, C. J.; Wen, G. L.; Shi, Q. Z.; Batten, S. R. *CrystEngComm* **2008**, *10*, 1583–1594.
86. Sun, Y. -X.; Sun, W. -Y. *Chin. Chem. Lett* **2014**, *25*, 823-828.
87. Wang, H.; Warren, M.; Jagiello, J.; Jensen, S.; Ghose, S. K.; Tan, K.; Yu, L.; Emge, T. J.; Thonhauser, T.; Li, J. *J. Am. Chem. Soc.* **2020**, *142*, 20088–20097.

88. Huang, Y.; Zhang, L.; Ji, J.; Cai, C.; Fu, Y. *Energy Storage Mater.* **2024**, *64*, 103065.
89. He, H.; Hashemi, L.; Hu, M. -L.; Morsali, A. *Coord. Chem. Rev* **2018**, *376*, 319-347.
90. Adarsh, N. N.; Kumar, D. K.; Dastidar, P. *CrystEngComm* **2009**, *11*, 796-802.
91. Kumar, K.; Das, A.; Dastidar, P. *CrystEngComm* **2006**, *8*, 805-814.
92. Adarsh, N. N.; Kumar, D. K.; Dastidar, P. *CrystEngComm* **2008**, *10*, 1565-1573.
93. Lee, G.; Yoo, D. K.; Ahmed, I.; Lee, H. J.; Jhung, S. H. *Chemical Engineering Journal* **2023**, *451*, 138538
94. Hu, X.; Zuhra, Z.; Ali, S..; Zhou, Y.; Zhang, L.; Duan, X.; Zhao, Z.; *New J. Chem.* **2023**, *47*, 3306-3311.
95. Walton, K. S.; Snurr, R. Q. J. Am. Chem. Soc. **2007**, *129*, 8552–8556.
96. Koh, K.; Wong-Foy, A. G.; Matzger, A. J. *J. Am. Chem. Soc.* **2009**, *131*, 4184–4185.
97. Lu, X.; Tang, Y.; Yang, G.; Wang, Y. -Y. *CrystEngComm*, **2023**, *25*, 896-908.
98. Li, H. -W.; Zhang, J. -L.; Xue, R.; An, Z. -W.; Wu, W.; Liu, Y.; Hu, G. -H.; Zhao, H. *Separation and Purification Technology*, **2023**, *320*, 124145.
99. Banerjee, R.; Phan, A.; Wang, B.; Knobler, C.; Furukawa, H.; O'Keeffe, M.; Yaghi, O. M. *Science* **2008**, *319*, 939–943.
100. Kevitiyagala, N. *Science* **2009**, *325*, 1644–1645.
101. Yeh, J. T.; Resnik, K. P.; Rygle K.; Pennline, H. W. *Fuel Process. Technol.* **2005**, *86*, 1533–1546.
102. Maiti, A; Dinda, S.; Halder, A.; Das, P.; Ghoshal, D. *Cryst. Growth Des.* **2023**, *23*, 1860−1867.
103. Zhang, G.; Liang, Y.; Cui, G.; Dou, B.; Lu, W.; Yang, Q.; Yan, X. *Energy Reports* **2023**, *9*, 2852–2860.
104. Zhu, Z. W.; Zheng, Q. R. *International Journal of Hydrogen Energy*, **2023**, *48*, 5166-5174.
105. Maity, D. K.; Halder, A.; Pahari, G.; Haque, F.; Ghoshal, D. *Inorg. Chem.* **2017**, *56*, 713-716.
106. Maiti, A.; Maity, D.; Halder, A.; Ghoshal, D. *Inorg. Chem.* **2023**, *62*, 12403-12412.
107. Sengupta, D.; Melix, P.; Bose, S.; Duncan, J.; Wang, X.; Mian, M. R.; Kirlikovali, K. O.; Joodaki, F.; Islamoglu**,** T.; Yildirim**,** T.; Snurr, R. Q.; Farha, O. K. J. *Am. Chem. Soc.* **2023**, *145*, 37, 20492-20502.
108. Farrando-Pérez, J.; Rodríguez-Castillo, M.; Martínez-Escandell, M.; Monge, M.; Silvestre-Albero, J. *International Journal of Hydrogen Energy* **2023**, *48*, 36474-36484.
109. Maity, D. K.; Halder, A.; Pahari, G.; Haque, F.; Ghoshal, D. *Inorg. Chem.* **2017**, *56*, 713−716.
110. Wu, Y.; Chen, H.; Xiao, J.; Liu, D.; Liu, Z.; Qian, Y.; Xi, H. *ACS Appl. Mater. Interfaces* **2015**, *7*, 26930−26940.
111. Tang, Y.; Dubbeldam, D.; Tanase, S. *ACS Appl. Mater. Interfaces* **2019**, *11*, 41383−41393.
112. Wang, S. -M.; Liu, H. -R.; Zheng, S. -T.; Lan, H. -L.; Yang, Q. -Y.; Zheng, Y. -Z. *Separation and Purification Technology* **2023**, *304*, 122378.
113. Jiang, M.; Weng, Y. -G.; Zhou, Z. -Y.; Ge, C. -Y.; Zhu, Q. -Y.; Dai, J. *Inorg. Chem.* **2020**, *59*, 10727–10735.

114. Dawood, S.; Dorris, A.; Davis, K.; Hammer**,** N. I.; Rathnayake**,** H. *J. Phys. Chem. C* **2021**, *125*, 792–802.
115. Haldar, R.; Ghosh, A.; Maji, T. K. *Chem. Commun.* **2023**, *59*, 1569-1588.
116. Jafarzadeh**,** M. *ACS Appl. Mater. Interfaces* **2022**, *14*, 24993–25024.
117. Tang, Y.; Ji, G.; Li, H.; Gao, H.; He, C.; Zhao, L.; Duan, C. *Inorg. Chem. Front.* **2023**, *10*, 5439-5451.
118. Tan, B.; Wu, Z. -F.; Jia, M. -Z.; Zhang**,** J.; Yang, G. -Y. *Inorg. Chem.* **2023**, *62*, 6688–6695.
119. Li, Q.; Wu, Z. -Q.; Li, D.; Liu, T. -H.; Yin, H. -y.; Cai, X. -B.; Zhu, W.; Fan, Z. -L.; Li, R. -Z. *J. Mater. Chem. A* **2023**, *11*, 2957-2968.
120. Zhao, Y.; Zhai, X.; Shao, L.; Li, L.; Liu, Y.; Zhang, X.; Liu, J.; Meng, F.; Fu, Y. *J. Mater. Chem. C* **2021**, *9*, 15840-15847.
121. Chen, G.; Huang, S.; Kou, X.; Zhu, F.; Ouyang, G. *Angew.Chem.Int.Ed.* **2020**, *59*, 13947–13954.
122. Sánchez, F.; Gutiérrez**,** M.; Douhal, A. *ACS Appl. Mater. Interfaces* **2023**, *15*, 56587–56599.
123. Fu, P. -Y.; Yi, S. -Z.; Pan**,** M.; Su, C. -Y. *Acc. Mater. Res.* **2023**, *4*, 939–952.
124. Guo, Y.; Cai**,** Z.; Yan, F.; Lei, D.; Guo, Y.; Zhang**,** S.; Dou, X. *Anal. Chem.* **2023**, *95*, 9014–9024.
125. Chen, J.; Huang, Y.; Gao, J.; Fan, C.; Gao, Y.; Yu, H.; Yang, X.; Tan, F.; Wang, X. *Sensors and Actuators B: Chemical* **2023**, *393*, 134301.
126. Goodman, J.; Brus, L. E. *J. Am. Chem. Soc.* **1978**, *100*, 7472.
127. Weller, *Elektrochemie* **1952**, *56*, 662.
128. Weller, Prog. *React. Kinet.* **1961**, *1*, 187.
129. Bhattacharya, B.; Halder, A.; Paul, L.; Chakrabarti, S.; Ghoshal, D. *Chem. Eur. J.* **2016**, *22*, 14998.
130. Halder, A.**;** Bhattacharya, B.**;** Haque, F.**;** Dinda, S.; Ghoshal, D. *Chem. Eur. J.* **2019**, *25*, 12196–12205**.**
131. Li, Y. -P.; Zhu, X. -H.; Li, S. -N.; Jiang, Y. -C.; Hu, M. -C.; Zhai, Q. -G. *ACS Appl. Mater. Interfaces* **2019**, 11, 11338.
132. Lin, Z..; Han, Z.; O'Connell, G. E. P.; Wan, T.; Zhang, D.; Ma, Z.; Chu, D.; Lu, X. *Adv. Mater.* **2024**, *2312797*, 1-10.
133. Fang, C.; Tang, X.; Yi, Q. *Applied Catalysis B: Environmental* **2024**, *341*, 123346.
134. Ejsmont, A.; Darvishzad, T.; Słowik, G.; Stelmachowski, P.; Goscianska, J. *Journal of Colloid and Interface Science* **2024**, *653*,1326-1338.
135. Jiang, H.; Zhao, Z.; Li, G.; Wang, M.; Chen, P.; Liu, X.; Tu, X.; Hu, Y.; Shen, Z.; Wu, Y. *Adv. Sci.* **2024**, *11*, 2306919.
136. Feng, C.; An, Q.; Zhang, Q.; Huang, L.; Wang, N.; Zhang, X.; Xu, Y.; Xie, M.; Wang, R.; Jiao, Y.; Chen, J. *International Journal of Hydrogen Energy* **2024**, *55*, 189–198.
137. Kashif, M.; Thangarasu, S.; Murugan, N.; Magdum, S. S.; Kim, Y. A.; Kurkuri, M.; Oh, T. -H. *Journal of Energy Storage* **2024**, *81*, 110348.
138. Zhao, T.; Zhong, D.; Fang, Q.; Zhao, X.; Du, R.; Hao, G.; Liu, G.; Li, J..; Zhao, Q. *Journal of Materials Science & Technology*, **2024**, *189*, 183-190.

139. Cui, X.; Lin, L.; Xu, T.; Liu, J.; Tang, M.; Wang, Z. *International Journal of Hydrogen Energy* **2024**, *49*, 1446-1457.
140. Yang, H.; Song, X.; Yang, T.; Liang, Z.; Fan, C.; Hao, X. *RSC Adv.* **2014**, *4*, 15720-15726.
141. Zhou, S.; Yue, P.; Huang, J.; Wang L.; She, H.; Wang, Q. *ChemEng J.* **2019**, 371, 885-892.
142. Zhong, L.; Ding, J.; Wang, X.; *Inorg Chem.* **2020**, *59*, 2701–2710.

CHAPTER-1B

Section B: Summary of Work

Chapter 1. This chapter is divided into two sections: Chapter 1A focuses on a brief survey regarding metal organic frameworks and their multifunctional behavior, while Chapter 1B provides a summary of various research works.

Chapter 1A. This chapter begins with an introduction to coordination polymers and metal-organic frameworks. It then explores into strategies for achieving multifunctionality within a single metal-organic framework. Finally, it touches upon diverse synthesis methods, potential applications, and the role of dynamic frameworks in relation to these properties.

Chapter 1B. It summarizes the topic of each chapter, incorporated in this thesis.

Chapter 2. This chapter explores into a series of mixed-ligand Zn(II) coordination polymers (CPs) formed by altering the relative ratio of two ligands. It employs a linear N,N′-donor ligand, trans 4,4′-azobispyridine (azbpy), and a sodium salt of tricarboxylic acid, 1,3,5-benzenetricarboxylate (btc), in different proportions, alongside a Zn(II) salt. This synthesis results in three distinct multifunctional hydroxy-bridged CPs: $\{[Zn_2(\mu_2\text{-}OH)(azbpy)(btc)(H_2O)].(H_2O)(MeOH)\}_n$ (**1**), $\{[Zn_2(\mu_3\text{-}OH)(azbpy)_{1.5}(btc)(H_2O)].(azbpy)_{0.5}(H_2O)_4\}n$ (**2**), and $\{[Zn_{2.5}(azbpy)(Hbtc)_2(\mu_2\text{-}OH)(H_2O)_2].(H_2O)_{3.5}(MeOH)\}n$ (**3**). Comprehensive characterization using single crystal X-ray diffraction (SCXRD), elemental analysis, infrared (IR) spectroscopy, thermogravimetric (TG) analysis, UV-visible spectroscopy, and powder X-ray diffraction (PXRD) has been conducted for all CPs **1**, **2**, and **3**. The desolvated frameworks of CPs **1** and **2** exhibit superior adsorption of CO_2 compared to N_2, while complex **3** shows the opposite behaviour. Furthermore, solid-state luminescence studies of these CPs reveal distinct fluorescence emissions at room temperature. This chapter highlights observed changes in these properties and elucidates their structural correlations.

Chapter 3. The chapter delves into two d^{10} metal complexes, $\{Zn_2(fum)_2(dim)_2(MeOH)\}_n$ (**1**) and $\{Cd_2(fum)_2(dim)_2(H_2O)\}n$ (**2**), synthesized using fumarate (fum) and di(1H-imidazol-1-yl)methane (dim) in methanol and water solutions. These complexes exhibit distinct structural architectures and interactions with the lattice solvent methanol. The single crystal of complex **1**

demonstrates a reversible, selective elimination of lattice methanol at room temperature, transforming into $\{Zn(fum)(dim)\}_n$ (**1a**). However, the polycatenated framework of complex **2** doesn't undergo such a solvent-induced transformation at room temperature. Instead, it showcases reversible dissolution-recrystallization structural transformation (DRST) through slow evaporation of methanol molecules, resulting in the creation of $\{Cd(dim)_2(H_2O)_2(H_2O)_2\}_n$ (**2a**). The selective solvent-induced reversible structural transformation of complex **1** and the reversible DRST of complex **2** at room temperature have been confirmed through PXRD and luminescence studies. Additionally, gas sorption studies with H_2, N_2, and CO_2 have been conducted for these compounds, revealing a higher hydrogen uptake in the polycatenated framework.

Chapter 4. This work focuses on modifying ligands to synthesize a pair of mixed-ligand d^{10} metal-organic framework (MOF) materials based on a previously published compound. The original compound, a Zn(II)-MOF, $\{[Zn(4\text{- bpdh})(H_2dht)]\cdot(MeOH)(H_2O)\}_n$ (1), featuring a five-fold interpenetrated framework, displayed high dynamic behaviour. In the first modification, the central metal was replaced by Cd(II), resulting in a rigid compound with the same framework formula as the base material but lacking interpenetration. The second modification involved substituting the 4,4'-coordinating N,N′- donor ligand with an isomeric 3,3'-coordinating N,N′- donor linker, rejuvenating the dynamism within the compound. The dynamic nature of these modifications was further confirmed through extensive PXRD studies, revealing a characteristic 'step-shaped' gas/solvent adsorption behaviour for CO_2, water, and ethanol. Moreover, these 3D MOFs exhibit excited-state intramolecular proton transfer (ESIPT) phenomena and demonstrate water-sensing properties in various organic solvents. Notably, the ease of water sensing is directly linked to the framework's dynamic behaviour, extensively studied in terms of structural correlations.

Chapter 5. Here, the growing demand for advanced switches and sensors has been addressed, prompting a keen interest in smart materials capable of swift, stimulus-triggered changes in their physical properties. Specifically, exploring alterations in the photophysical properties of materials, particularly in solid-state, aims to create intelligent on-off switches. Materials exhibiting external stimuli-responsive changes, such as excited-state intramolecular proton transfer (ESIPT), hold promises for these applications. While solid-state ESIPT phenomena are not novel in material chemistry, especially in organic molecules, its observation within coordination polymers (CPs) has been unprecedented. Prior instances of ESIPT in CPs required solvents as suspension media,

relying on a solvent-assisted ESIPT phenomenon. However, the emergence of solvent-independent ESIPT-enabled CPs offers distinct advantages. Their well-defined periodic arrangement ensures consistent property changes, and the sturdy coordination bonds between metal nodes and ligands guarantee durability even in harsh environments. Addressing this gap, we introduce the pioneering solid-state, solvent-free, and solvent-independent ESIPT-active coordination polymer (CP). Remarkably, this CP displays temperature-dependent ESIPT on-off behaviour, highlighting its potential as an innovative material in the realm of cutting-edge switches and sensors.

Chapter 6. Detection and sensing of amine through enhanced fluorescence emission is always challenging in aqueous solution. The range of different Lewis basicities, shape and sizes as well as the different structural arrangement of amines is responsible for their less specificity in aqueous solution. Here we have designed a highly fluorescent emissive 2D+2D→3D inclined polycatenated $–NO_2$ functionalized flexible metal organic framework (MOF) for selective segregation of electron rich aromatic primary amines from electron deficient amines in aqueous solution showing different emission behavior. The inclined polycatenated 2D+2D→3D MOF having asymmetric unit $\{[Cd(dim)(2\text{-nta})(H_2O)](H_2O)(MeOH)\}_n$ (**1**) has been synthesized by slow diffusion process and characterized thoroughly by single crystal and powder X-ray diffraction, as well as other physicochemical methods. The desolvated species of **1** (referred as ref. MOF) is found stable and has been characterized by PXRD and adsorption study. The fluorescence profile of the ref. MOF shows selective enhancement in presence of electron rich primary aromatic amines, while the same shows quenching for electron deficient amines in aqueous solution. The ref. MOF reported here consist of flexible space between the two 2D layers that is responsible for different orientation for different analyte PAAs with different sizes. The above findings are also supported by time resolved fluorescence spectroscopy as well. The respective fluorescence enhancement and quenching have been explained by the interaction between the CB of MOF and LUMO of amines. Therefore, this work is representing an operable method for the sensing of PAAs using a single compound, which is a polycatenated MOF.

Chapter 7. This work presents incorporation of potassium ions in a structurally flexible Co(II) metal organic framework (MOF) through post synthetic modification (PSM) for electrocatalytic oxygen evolution reaction (OER)application. The bimetallic 3D MOFs, where coordinated Co(II) ions are entirely surrounded by potassium ions, which assists to get an exceptional topological

arrangement. The formation of potassium ion containing 1D chain and its immense attraction toward water enables such system to get stabilized and carrying hydroxide ions in solutions and existence of catalytically active metal hydroxide slices, which is the key factor for electrocatalytic OER. Therefore, maintaining proper orientation and concentration of potassium ions in such bimetallic square MOFs based system, their structural stability can be maintained in alkaline medium as well as their electrocatalytic OER activity can also be tuned. Here it has been demonstrated that how the potassium ion introduction in $\{K_2[Co(H_2O)_2(CO_3)_2]\}_n$ (**2**) and $\{K_2[Co(2,6\text{-dcp})_2](H_2O)_7\}_n$ (**3**) 3D MOFs can exhibit the excellent potential for electrocatalytic OER, both in terms of catalytic efficacy as well as structural stability. Interestingly, compound **3** shows a low overpotential of 292 mV (at 10 mA cm^{-2}) and a small Tafel slope of 50 mV dec^{-1}; with a remarkable long-term electrochemical stability for the OER. The turn over frequency (TOF) of compound **3** has the value of 1.96 s^{-1}, which is ~27% greater than the commercially available cobalt oxide (Co_3O_4) catalyst for the OER performed under identical condition.

CHAPTER-2

Concentration Mediated Structural Modulation in a Family of Mixed-Ligand Coordination Polymers: Structure, Sorption and Luminescence Study

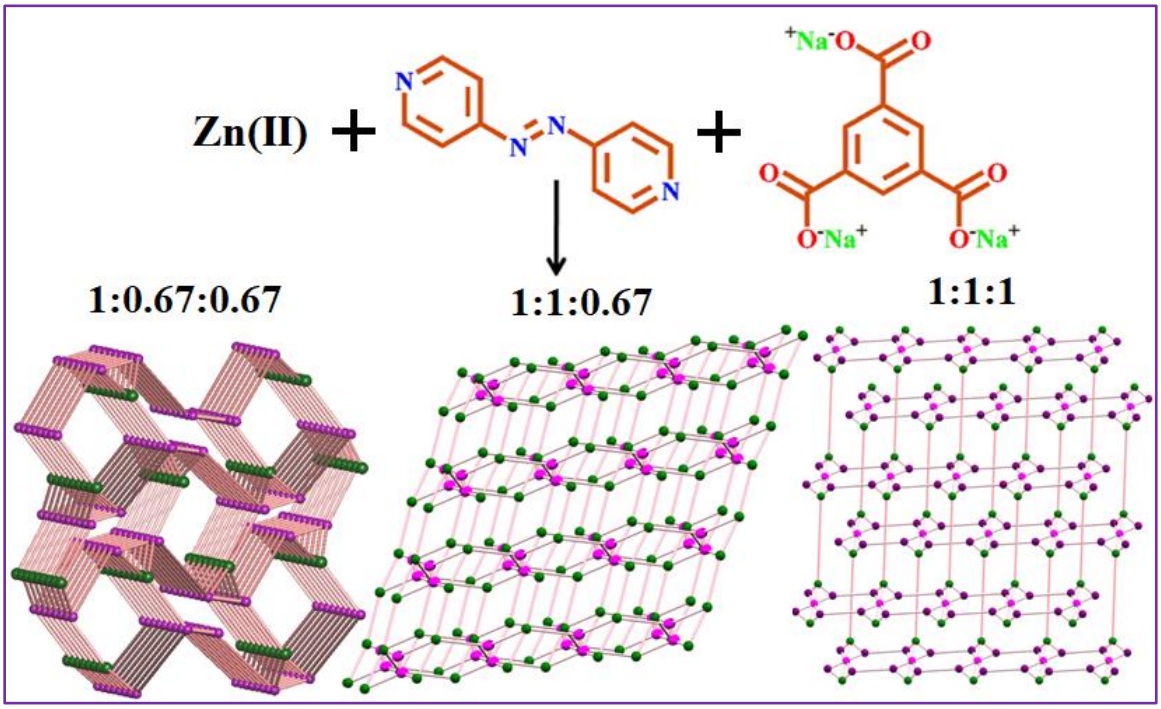

CHAPTER-2

Concentration Mediated Structural Modulation in a Family of Mixed-Ligand Coordination Polymers: Structure, Sorption and Luminescence Study

2.1. INTRODUCTION

Since the inception of the research related to the coordination polymers (CPs), their structural design has been established as an important area of exploration due to the strong structure-property relationship of such materials in the field of gas storage/separation, conductivity, catalysis, luminescence, and lot more[1-10]. Towards long journey of this topic, the general reaction condition based controlling factors like temperature, solvent, pressure, pH of the reaction medium[11-18]; along with the ratio of metal and ligands became a textbook topic nowadays. Despite extensive exploration in the field, practical applications often encounter unexpected variations in stoichiometry within resulting CPs that may not be commensurate with the reactant ratio and most of the time these discrepancies are not properly addressed and/or magnified in terms of understanding. Several factors can contribute to this, including inadequate fulfillment of reaction conditions, possibility of partial reactions, solubility limitations of reagents, and other variables[19]. These issues are especially prevalent when reactions are conducted under mild conditions, like slow diffusion techniques at room temperature[20-22]. The understanding is particularly necessary for the designing of specific materials by tuning the ligand ratio/s to imprint or enhance celebrated properties in such extended coordination networks[23-29].

Therefore, in order to address the aforesaid lacuna, related to the synthesis of CPs, here we have performed a case study using varying ratio of organic linkers in a same reaction condition keeping the concentration of the metal ion fixed. In this study, the Zn(II) are taken as the metal node along with two bridging ligand 4,4′-azobispyridine (azbpy) and 1,3,5-benzenetricarboxylate (btc). The NaOH solution is also used for the effective deprotonation of the btc. Among these two ligands, azbpy is a linear bidentate linker but the btc can bridge two and/or three metal centers simultaneously, depending on availability of metal coordination sites (Scheme 1). At sub-molar equal concentration of both the linkers (0.67 mmol for both) with respect to Zn(II) (1 mmol), resultant compound is $\{[Zn_2(\mu_2\text{-}OH)(azbpy)(btc)(H_2O)].(H_2O)(MeOH)\}_n$ (**1**) which is a binodal 3D structure with an appreciable volume of solvent filled pores. Keeping the concentration of btc (0.67 mmol) and Zn(II) (1 mmol) unaltered, the concentration of azbpy is increased to 1 mmol, [$Zn_2(\mu_3$-

OH)(azbpy)$_{1.5}$(btc)(H_2O)].(azbpy)$_{0.5}$(H_2O)$_4$}$_n$ (**2**) is obtained which is a trinodal 3D framework where half of azbpy ligand occupies the pores reducing solvent accessibility. In both **1** and **2** btc acts as a bridging tridentate linker, connecting three Zn(II) centers. Finally increasing the concentration of btc to 1 mmol, following Zn(II):azbpy:btc = 1:1:1 ratio, {[$Zn_{2.5}$(azbpy)(Hbtc)$_2$(μ_2-OH)(H_2O)$_3$].(H_2O)$_{3.5}$ (MeOH)}$_n$ (**3**) is formed where btc is bridging in bidentate fashion due to its higher concentration with respect to the metal ion in comparison to the previous two. This change in bridging fashion[30] leads to the formation of 2D structure without any potential voids.

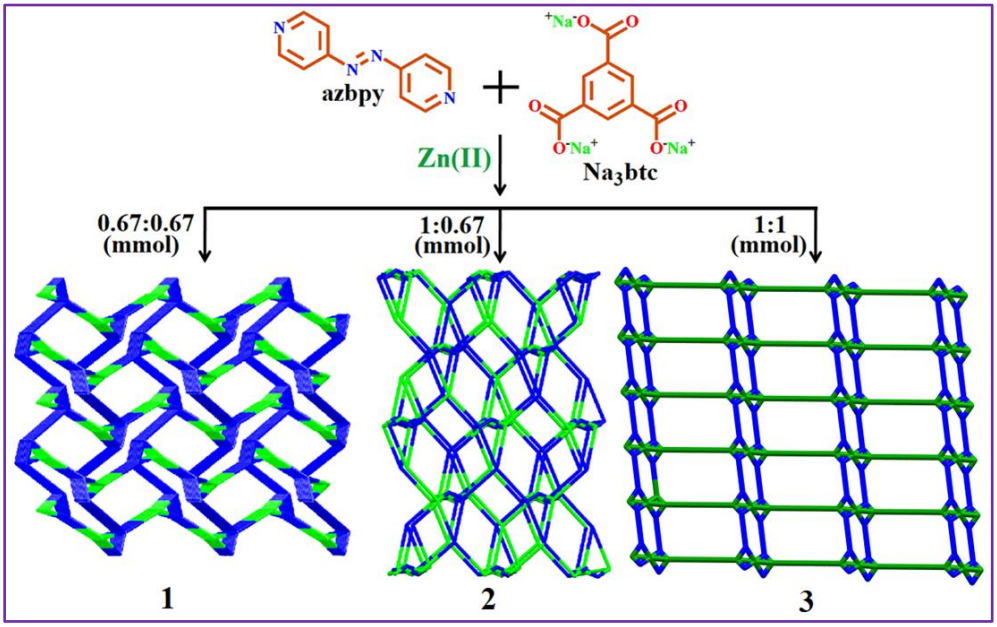

Scheme 1. Synthesis route of compounds **1**, **2**, and **3** with their topological representation

All the compounds are well characterized by elemental analysis, single crystal X-ray crystallography (Table 1), powder X-ray diffraction (PXRD), UV-vis spectroscopy, infrared (IR) spectroscopy, and thermogravimetric (TG) analyses. The dehydrated state of compounds **1**, **2** and **3** exhibit permanent porosity and therefore studied for various (CO_2 and N_2) gas adsorption, which found corroborative with their structures. In addition to that, all the compounds also exhibit solid-state ligand-based luminescence, which is discussed in detail in this chapter with a comparison with the constituent ligands.

2.2. EXPERIMENTAL SECTION

2.2.1. Materials

Trans 4,4′-azobispyridine (azbpy) was synthesized by oxidative coupling of 4-aminopyridine.[31] High purity Zn(II) nitrate hexahydratate and 1,3,5-benzenetricarboxylic acid were purchased from

the Sigma-Aldrich Chemical Company Inc. and used as received. All other chemicals were of AR grade and were used as received.

2.2.2. Physical Measurements. Elemental analyses (C, H, N) have been performed using a Heraeus CHNS elemental analyzer. FT-IR spectra have been obtained on a PerkinElmer spectrometer (Spectrum II) with the samples. PerkinElmer STA8000 thermal analyzer has been used for thermogravimetric analysis (TGA) with a ramp rate of 10 °C/min from room temperature to 600 °C under nitrogen flow. Powder X-ray diffraction (PXRD) data were collected on a Bruker D8 Discover instrument with Cu-Kα radiation (λ = 1.5406 Å), operating at 40 kV and 40 mA. UV-vis spectra are collected in PerkinElmer Lambda 35 instrument with integrating sphere attachment. Fluorescence measurements were done using Horiba FluoroMax 4 spectro fluorimeter.

2.2.3. Measurement of Gas Adsorption. Ambient pressure volumetric gas adsorption measurements were performed at 77K for N_2, maintained by a liquid nitrogen bath, with pressures ranging from 0 to 1 bar using a Quantachrome Autosorb-iQ adsorption instrument. CO_2 adsorption measurements were performed at 195 K (dry ice-acetone cold bath) with same pressure range and on same instrument. Highly pure gases were used for the adsorption measurements (nitrogen, 99.999%; carbon dioxide, 99.95%). The adsorbates were placed into the sample tubes, and then the change of the pressure was monitored, and the degree of adsorption was determined by the decrease in pressure at the equilibrium state. All operations were computer-controlled and automatic.

2.2.4. Synthesis

{[Zn_2(μ_2-OH)(azbpy)(btc)(H_2O)].(H_2O)(MeOH)}$_n$ (1). A methanolic solution (18 ml) of 4,4′-azobipyridine (azbpy) (0.225 g, 0.67 mmol) was mixed to an aqueous solution (18 ml) of tri sodium salt of 1,3,5-benzenetricarboxylic acid (btc) (0.177 g, 0.67 mmol) [prepared by the mixing of 0.67 mmol of 1,3,5-benzenetricarboxylic acid with 2 mmol of NaOH in aqueous solution] and stirred for 20 min to mix it well. $Zn(NO_3)_2 \cdot 6H_2O$ (0.296 g, 1 mmol) was dissolved in H_2O (18 mL), and this Zn(II) solution was slowly and carefully layered with the above mixed-ligand solution by using a solvent mixture (5 mL; 1:1 of H_2O and MeOH). After one-week, red block single crystals suitable for X-ray diffraction analysis were obtained (Yield 80%). Elemental analysis, calculated for $C_{19}H_{18}N_4O_{10}Zn_2$ (M_r = 591.11): C 38.47; H 3.06; N 9.45. Found: C 38.28; H 3.15; N 9.41. IR spectra (in cm^{-1}): ν(N=N), 1616; ν(C-O), 1310-1240; ν(CH-Ar), 3100-2900 and ν(C=C), 1620-1420.

{[$Zn_2(\mu_3$-OH)(azbpy)$_{1.5}$(btc)(H_2O)].(azbpy)$_{0.5}$(H_2O)$_4$}$_n$ (2) The process is same as described in the above synthesis procedure, only the concentration of 4,4′-azobipyridine (azbpy) ligands has been changed. Instead of 0.67 mmol of N,N′-donor ligands, 1 mmol has been taken in 18ml MeOH. After 8 days, red block crystals, suitable for single crystal X-ray diffraction, has been obtained (Yield 65%). Elemental analysis, calculated for $C_{29}H_{19}N_8O_{12}Zn_2$ (M_r = 802.30): C 38.47; H 3.06; N 9.45. Found: C 38.28; H 3.15; N 9.41. IR spectra (in cm^{-1}): ν(N=N), 1617; ν(C-O), 1309-1239; ν(CH-Ar), 3100-2900 and ν(C=C), 1620-1420.

{[$Zn_{2.5}$(azbpy)(Hbtc)$_2(\mu_2$-OH)(H_2O)$_3$].(H_2O)$_{3.5}$(MeOH)}$_n$ (3) The process is same as described the synthesis for complex **2**, instead of trisodium salt of 1,3,5-benzenetricarboxylic acid disodium salt has been used, which prepared by mixing of 2 mmol NaOH with 1 mmol btc. So here the concentration of two different ligands, 4,4′-azobipyridine (azbpy) and 1,3,5-benzenetricarboxylic acid (btc) are same as the concentration of Zn(II). 1 mmol of both the ligands have been taken in 18ml MeOH and H_2O solvents respectively. After 7 days, red block single crystals for X-ray diffraction analysis were observed (Yield 62%). Elemental analysis, calculated for $C_{29}H_{22}N_4O_{20}Zn_{2.5}$ (M_r = 917.98): C 38.47; H 3.06; N 9.45. Found: C 38.28; H 3.15; N 9.41. IR spectra (in cm^{-1}): ν(N=N), 1618; ν(C-O), 1310-1240; ν(CH-Ar), 3100-2900 and ν(C=C), 1620-1420.

2.2.5. Crystallographic Data Collection and Refinement. The X-ray single-crystal data for complexes **1**, **2**, **3** have been collected at room temperature in a Bruker made APEX II diffractometer. At first, single crystals of all the compounds have been isolated and then mounted on the glass fibre tip using commercial super glue. Mo−Kα radiation (λ = 0.71073 Å) from a sealed tube X-ray source has been used. The raw data have been integrated using the SAINT[32] and by utilizing SADABS,[33] the absorption corrections were performed. The structures have been solved by SHELXL-2016/6,[34] and full-matrix least-squares refinements on F^2 for all non-hydrogen atoms were performed by SHELXL-2016/6,[34] with anisotropic displacement parameters. For the data collection, all the hydrogen atoms have been fixed at their ideal position except bridging hydroxy group, and coordinated and lattice solvent molecules due to thermal disorder. All the calculations and molecular graphics were done by SHELXL-2016/6,[34] PLATON v1.15,[35] WinGX system Ver-1.80,[36] Diamond v3.2, Mercury,[37] and TOPOS.[38,39] All the crystallographic data and structural refinement parameters for all the compounds **1**, **2** and **3** have been mentioned in Table 1.

Table 1. Data Collection and Refinement Parameters for Single Crystal Analysis for **1**, **2** and **3**

	1	**2**	**3**
Formula	$C_{20}H_{20}N_4O_{10}Zn_2$	$C_{29}H_{30}N_8O_{12}Zn_2$	$C_{29}H_{38}N_4O_{20.5}Zn_{2.5}$
Formula Weight	607.11	813.30	933.90
Crystal System	Orthorhombic	Triclinic	Triclinic
Space Group	*Pna*2$_1$	*P*$\bar{1}$	*P*$\bar{1}$
a/ Å	14.7381(10)	10.531(2)	9.740(5)
b/Å	15.352(1)	11.096(2)	10.073(5)
c/ Å	10.0276(7)	16.286(3)	10.621(5)
α/°	90	96.769(5)	71.453(5)
β/°	90	91.777(5)	65.657(5)
γ/°	90	116.577(4)	86.564(5)
V/ Å3	2268.8(3)	1682.6(5)	897.0(8)
Z	4	2	1
D_c/ g cm^{-3}	1.751	1.584	1.692
μ /mm^{-1}	2.179	1.499	1.755
F(000)	1196	810	459
θ range/°	1.9- 27.5	2.1- 27.4	2.1- 27.6
Reflections Collected	35039	12947	15358
Unique Reflections	5143	7428	4122
Reflections $I > 2\sigma(I)$	3270	4730	3396
R_{int}	0.171	0.072	0.033
Goodness-of-Fit (F^2)	1.03	0.99	1.07
R_1 ($I > 2\sigma(I)$) [a]	0.0547	0.0776	0.0565
wR_2($I > 2\sigma(I)$) [a]	0.1438	0.2221	0.1811

$^{a}R_1 = \Sigma \big| |F_o| - |F_c| \big| / \Sigma |F_o|$, $wR_2 = [\Sigma (w (F_o^2 - F_c^2)^2) / \Sigma w (F_o^2)^2]^{1/2}$

2.3. RESULTS AND DISCUSSION

2.3.1. Structural description

{[Zn$_2$(μ$_2$-OH)(azbpy)(btc)(H$_2$O)].(H$_2$O)(MeOH)}$_n$ (1)

Compound **1** crystallizes in the orthorhombic system, space group *Pna*2$_1$; X-ray structure analysis revealed that the formation of a 3D structure where the asymmetric unit is constituted by two crystallographically independent Zn(II) centers [Zn1 and Zn2] along with a bridging btc, one μ_2-OH group and azbpy linker shown in Figure. 1a. Here both Zn1 and Zn2 are five-coordinated in square pyramidal geometry, but their coordination environments are entirely different. Square pyramidal coordination environment of Zn1 is furnished by O4^a and O5^a oxygen atoms (where *a* = 3/2-x, 1/2+y, -1/2+z) from one chelated carboxylate group of one btc, one oxygen atom (O1) of μ_2-OH group, one coordinated water (O1W) molecule and one nitrogen atom (N1) of pyridyl group

from azbpy linker. Here Zn1-O bond lengths are in the range of 1.907-2.535 Å and Zn1-N is of 2.057 Å (Table S1). Similarly, coordination around Zn2 is provided by two oxygen atoms ($O6^b$ and $O7^b$ where b = 3/2-x, 1/2+y, 1/2+z) of one chelated carboxylate group, one oxygen atom (O2) of bridging monodentate carboxylate group, one oxygen atom (O1) of μ_2-OH group and one nitrogen atom ($N4^c$ where c = 1/2+x, 1/2-y, -1+z) of bridging azbpy ligand. Here, Zn2-O bond distances vary from 1.932-2.724 Å and Zn2-N is of 2.049 Å (Table 2). The Zn···Zn contact distance across the dinuclear unit is 3.378Å. Here each btc acts as bridge, to link three Zn(II) ions, in which two carboxyl groups chelate two Zn(II) centers, and the other carboxyl group ligates one Zn(II) center via bridging monodentate mode, respectively.

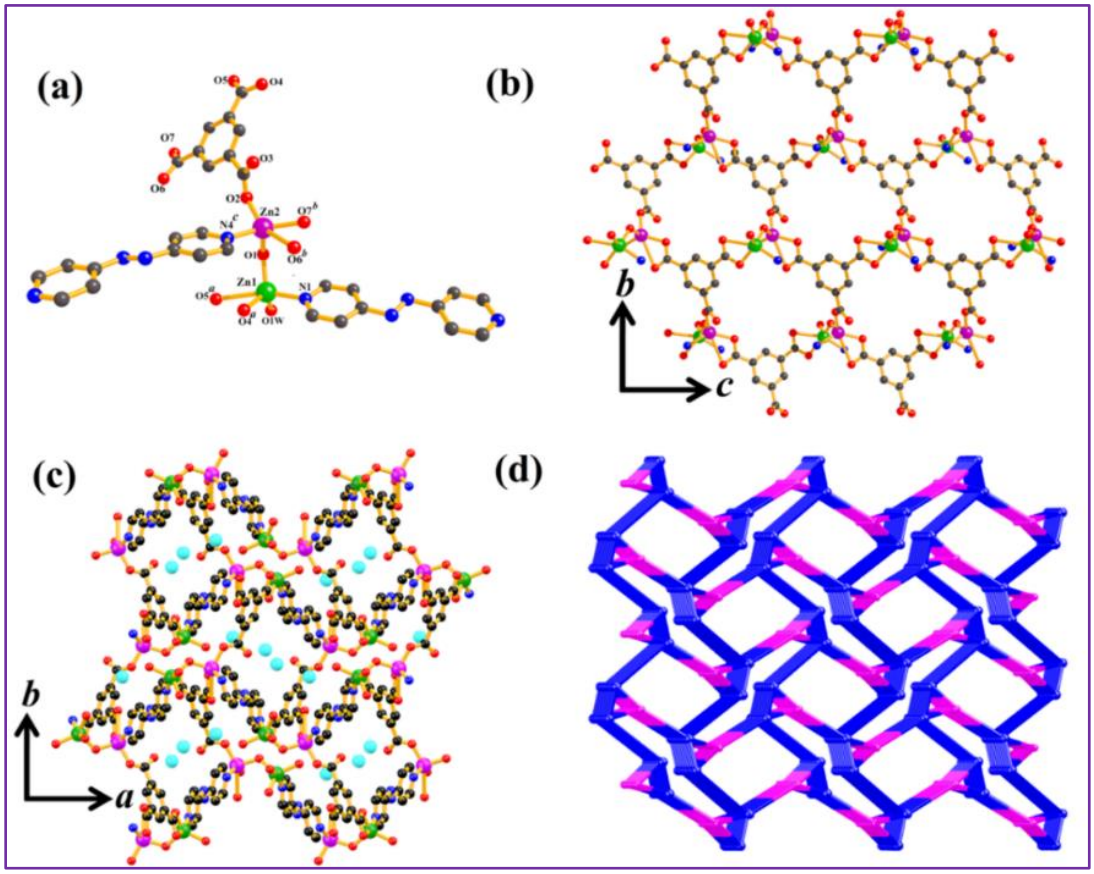

Figure. 1. Crystal structure of $\{[Zn_2(\mu_2\text{-}OH)(azbpy)(btc)(H_2O)].(H_2O)(MeOH)\}_n$(**1**) (Zn1 green, Zn2 magenta, O red, N blue, C black and solvents cyan) (a) view of the coordination environment; (b) view of metal carboxylate 2D net along the *ab* plane (c) view of 3D framework along the *ab* plane with 1D water filled channels; (d) topological representation of **1**

Thus, two crystallographically independent Zn(II) centers along with btc and hydroxyl group create a 2D arrangement in the crystallographic *bc* plane (Figure. 1b). The linear azbpy linker connects these 2D sheets to create a 3D arrangement with 1D channels along the crystallographic

c axis, which is occupied by lattice guest water and methanol molecules (Figure. 1c). The topology[38,39] of the 3D framework suggests a binodal 4,6 connected net with stoichiometry (4-c)(6-c) and the corresponding Schläfli symbol of the net is $\{3.5^2.6^2.7\}\{3^2.5^3.6^6.7^4\}$ (Figure. 1d). Artificial removal of solvent molecules from the framework suggests that there is about 17.5% void space to the crystal volume as calculated by the PLATON[35] crystallographic software. In the crystal packing, the btc ligands are also involved in π-π interactions (Table 3) with azbpy ligand, giving more stabilization to the overall 3D framework (Figure. 2).[40,41] Close packing space fill model shows that no multidirectional effective pore was present in the structure (Figure. 2).

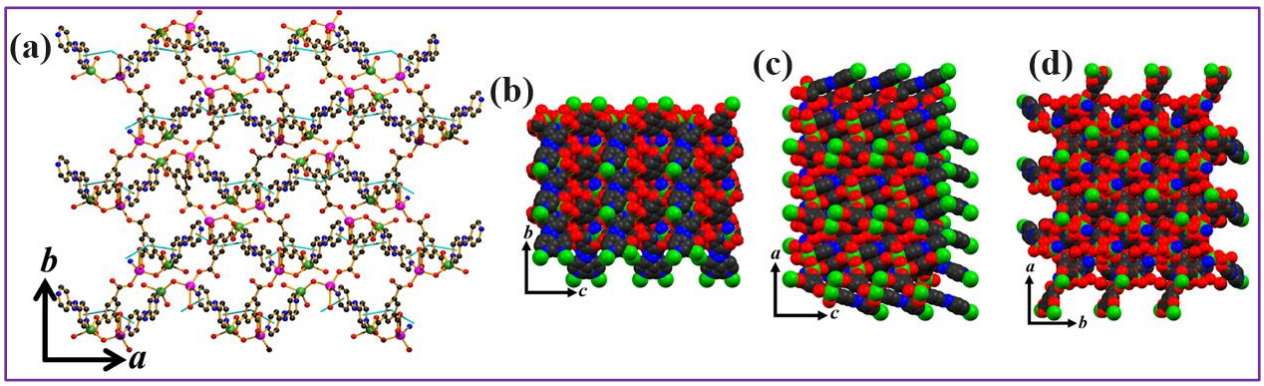

Figure 2. (a) π-π interactions, (b)-(c) space fill model of compound **1**

Table 2. Selected Bond Lengths (Å) and Bond Angles (°) for **1**

Zn1-O1	1.907(6)	Zn1-O1W	2.005(8)
Zn1-N1	2.057(8)	Zn1-O4^{d}	1.966(8)
Zn1-O5^{d}	2.535(8)	Zn2-O1	1.932(6)
Zn2-O2	1.962(7)	Zn2-O6^{e}	2.724(8)
Zn2-O7^{e}	2.000(7)	Zn2-N4^{g}	2.049(8)
O1-Zn1-O1W	115.1(3)	O1-Zn1-N1	104.7(3)
O1-Zn1-O4^{d}	116.0(3)	O1-Zn1-O5^{d}	93.2(3)
O1W-Zn1-N1	96.8(3)	O1W-Zn1-O4^{d}	119.0(3)
O1W-Zn1-O5^{d}	89.5(3)	O4^{d}-Zn1-N1	100.2(3)
O5^{d}-Zn1-N1	156.1(3)	O4^{d}-Zn1-O5^{d}	57.0(3)
O1-Zn2-O2	99.2(3)	O1-Zn2-O6^{e}	111.5(3)
O1-Zn2-O7^{e}	104.0(3)	O1-Zn2-N4^{g}	104.9(3)
O2-Zn2-O6^{e}	148.1(3)	O2-Zn2-O7^{e}	112.8(3)
O2-Zn2-N4^{g}	96.6(3)	O6^{e}-Zn2-O7^{e}	52.2(3)
O6^{e}-Zn2-N4^{g}	84.3(3)	O7^{e}-Zn2-N4^{g}	134.3(3)

Symmetry code: *d* = 3/2-x, 1/2+y, -1/2+z; *e* = 3/2-x, 1/2+y, 1/2+z; *g* = 1/2+x, 1/2-y, -1+z.

Table 3. π-π interaction in **1**

Ring(i) → Ring(j)	Distance of centroid(i) from ring(j),(Å)	Dihedral angle (i,j) (deg)	Distance between the (i,j) ring centroids,(Å)
R(1) → R(3)^{i}	4.150(7)	21.6(6)	3.665(5)
R(2) → R(3)^{ii}	3.916(7)	7.5(6)	3.468(5)
R(3) → R(1)^{iii}	4.151(7)	21.6(6)	3.534(5)
R(3) → R(2)^{iv}	3.915(7)	7.5(6)	3.600(5)

Symmetry code: (i) = 3/2-x, 1/2+y, 1/2+z; (ii) = 1-x, -y, 1/2 +z; (iii) = 3/2-x, -1/2+y, -1/2+z; (iv) = 1-x, -y, -1/2+z.

R(i)/R(j) denotes the ith/jth rings: R(1) = N(1)/C(10)/C(11)/C(12)/C(13)/C(14); R(2) = N(4)/C(17)/C(16)/C(15)/C(19)/C(18); R(2) = C(2)/C(3)/C(4)/C(5)/C(6)/C(7)

{[$Zn_2(\mu_3$-OH)(azbpy)$_{1.5}$(btc)(H_2O)].(azbpy)$_{0.5}$(H_2O)$_4$}$_n$ (2)

The X-ray analysis exhibits that the compound **2** crystallizes in the triclinic system with space group *P*$\bar{1}$; forms 3D structure and the asymmetric unit is contracted by two crystallographically independent Zn(II) centers [Zn1 and Zn2] along with one bridging btc, one μ_2-OH group and one azbpy linker shown in Figure. 3a. Here Zn1 and Zn2 are five and six coordinated with distorted square pyramidal and distorted octahedral geometry respectively. Distorted square pyramidal Zn1 center is furnished by O3^{b} and O5^{c} oxygen atoms from one chelated carboxylate group and free carboxylate group of second btc, two oxygen atoms (O7, O7^{a}) of two μ_3-OH groups, one nitrogen atom (N1) of pyridyl group from azbpy linker where Zn1-O bond lengths are in the range of 1.949-2.272 Å and Zn1-N is of 2.201 Å (Table 4). Similarly, coordination around Zn2 is provided by three oxygen atoms (O3^{b}, O1^{a} and O6^{d}) of one chelated carboxylate group and two oxygen atoms of bridging monodentate carboxylate group, one oxygen atom (O7^{a}) of μ_3-OH group, one water molecule (O1W) and one nitrogen atom (N4^{c} where *c* = 1/2+x, 1/2-y, -1+z) of bridging azbpy ligand. Here, Zn2-O bond distances vary from 1.998-2.536 Å and Zn2-N is of 2.157Å (Table 4). The Zn$\cdots$Zn contact distance across this dinuclear unit is 3.433 Å. Here each btc acts as bridge, to link three Zn(II) centers, in which two carboxyl groups chelate two Zn(II) centers, and the other carboxyl group ligates one Zn(II) center via bridging monodentate mode. Thus, two crystallographically independent Zn(II) centers adjoined by btc and hydroxyl group create a 2D arrangement in the crystallographic *ab* plane (Figure. 3b). The linear azbpy linker connects the 2D sheets to create a 3D arrangement with 1D channels along the crystallographic *c* axis, which is occupied by lattice guest water molecules and azbpy ligands (Figure. 3c). The topology[38,39] of the 3D framework suggests a trinodal 3,8,8 connected net with stoichiometry (3-c)(4-c)(4-c)(4-c) and

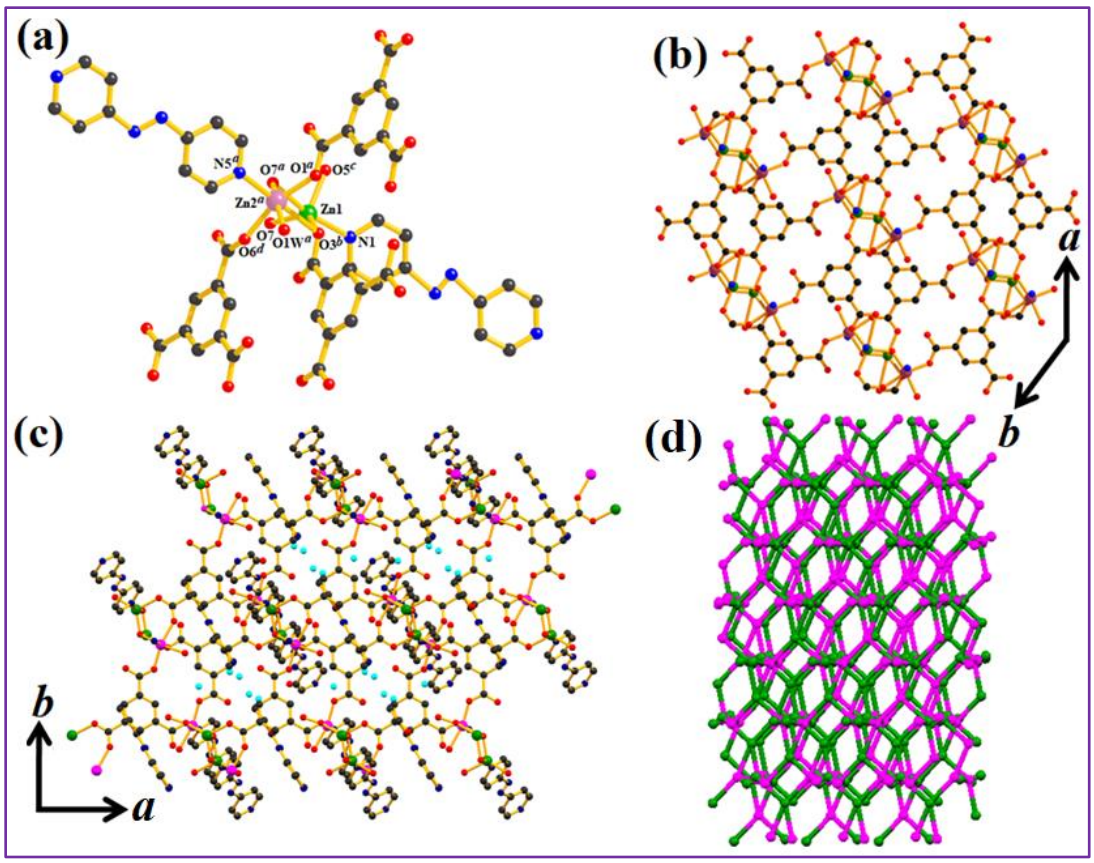

Figure 3. Crystal structure of {[$Zn_2(\mu_3$-OH)$(azbpy)_{1.5}(btc)(H_2O)$].$(azbpy)_{0.5}(H_2O)_4\}_n$ (**2**) (Zn1 green, Zn2 magenta, O red, N blue, C black and solvents cyan) (a) view of the coordination environment (b) view of metal carboxylate 2D net along the *ab* plane; (c) view of 3D framework along the *ab* plane with 1D water and azbpy ligand filled channels (d) topological[31,32] representation of **2**

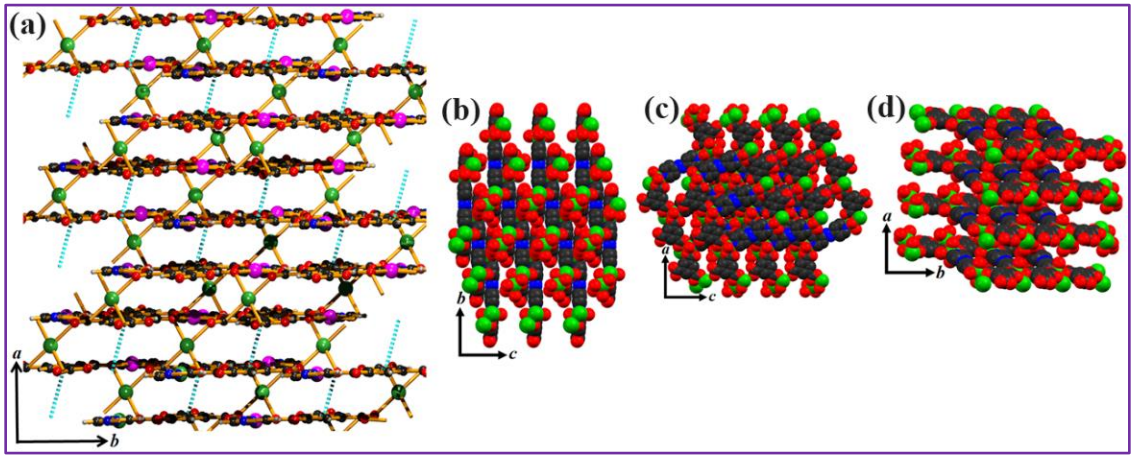

Figure 4. (a) π-π interactions, (b)-(d) space fill model of compound **2**

the corresponding Schläfli symbol of the net is $\{4.6.8^4\}\{4.6^2.8^3\}\{4^2.6.8^3\}\{4^2.6\}$ (Figure. 3d). Artificial removal of water molecules from the framework gives ~13.7% void space to the crystal volume as suggested by the PLATON[35] crystallographic software. In the crystal packing, the azbpy ligands are also involved in π-π and C-H-π interactions (Table 5) with azbpy ligand, giving the more stabilization of 3D framework (Figure. 4)[40,41]. The space fill model along *a* axis has some pore, otherwise in *ac* and *ba* plane has no pore (Figure. 4).

Table 4. Selected bond lengths (Å) and bond angles (°) for **2**

Zn1-O7	1.949(4)	Zn1-N1	2.201(5)
Zn1-O5^{c}	1.992(5)	Zn1-O3^{d}	2.001(5)
Zn1-O7^{f}	2.272(3)	Zn2-O1	2.007(4)
Zn2-O1W	2.049(5)	Zn2-O7	1.998(4)
Zn2-N5	2.157(5)	Zn2-O6^{c}	2.111(4)
Zn2-O3^{e}	2.536(5)	O7-Zn1-N1	106.76(19)
O5^{c}-Zn1-O7	108.29(19)	O3^{d} -Zn1-O7	126.69(18)
O7-Zn1-O7^{f}	84.59(14)	O5^{c}-Zn1-N1	89.9(2)
O3^{d}-Zn1-N1	92.5(2)	O7^{f}-Zn1-N1	167.80(19)
O3^{d}-Zn1-O5^{c}	121.23(17)	O5^{c}-Zn1-O7^{f}	82.09(18)
O3^{d}-Zn1-O7^{f}	83.85(18)	O1-Zn2-O1W	87.32(18)
O1-Zn2-O7	97.74(18)	O1-Zn2-N5	99.24(19)
O1-Zn2-O6^{c}	162.82(19)	O1-Zn2-O3^{e}	82.64(17)
O1W-Zn2-O7	164.80(17)	O1W-Zn2-N5	93.5(2)
O1W-Zn2-O6^{c}	80.92(17)	O1W-Zn2-O3^{e}	89.24(17)
O7-Zn2-N5	99.81(18)	O6^{c}-Zn2-O7	90.74(17)
O3^{e}-Zn2-O7	77.29(14)	O6^{c}-Zn2-N5	93.95(19)
O3^{e}-Zn2-N5	176.78(18)	O3^{e}-Zn2-O6^{c}	84.72(16)

Symmetry code: *a* = -1+x,-1+y,z; *b* = x,-1+y,z; *c* = x,1+y,z; *d* = 1+x,1+y,z; *e* = -x,-1-y,-z; *f* = 1-x,-y,-z.

Table 5. π-π and C-H- π interaction in **2**.

Ring(i) → Ring(j)	Distance of centroid(i) from ring(j),(Å)	Dihedral angle (i,j) (deg)	Distance between the (i,j) ring centroids,(Å)
R(1) → R(2)^{i}	4.042(6)	8.9(5)	3.459(4)
R(1) → R(3)^{ii}	3.605(5)	5.4(5)	3.459(4)
R(2) → R(3)^{iii}	3.811(6)	7.2(5)	3.707(5)
C-H ring(j)	H...R distance (Å)	C-H...R angle (deg)	C...R distance (Å)
C(20)-H(20)→ R(4)^{ii}	2.80	2145	3.595(10)

Symmetry code: (i) = 2-X,1-Y,1-Z; (ii) = X,Y,Z; (iii) = 1-X,-Y,1-Z;
R(i)/R(j) denotes the ith/jth rings: R(1) = N(1)/C(10)/C(11)/C(12)/C(13)/C(14); R(2) = N(2)/C(15)/C(16)/C(17)/C(18)/C(19); R(2) = N(5)/C(21)/C(20)/C(24)/C(23)/C(22) ; R(4) = N(7)/C(25)/C(26)/C(27)/C(28)/C(29).

{[$Zn_{2.5}$(azbpy)$(Hbtc)_2$(μ_2-OH)$(H_2O)_3$].$(H_2O)_{3.5}$(MeOH)}$_n$ (3)

X-ray structure analysis revealed that compound **3** crystallizes in the triclinic system with space group *P*$\bar{1}$ same as the compound **2**, but it has a 2D structure unlike other two compounds. Here also the framework consists of two symmetry-independent Zn(II) centers. The asymmetric unit constitutes by two Zn1, half Zn2, two btc, one μ_2-OH group and one azbpy along with three coordinated water molecules, three and half lattice water molecules and half of methanol molecules (Figure. 5a). Like the other two compounds, one Zn(II) center is pentacoordinated and another is hexacoordinated with although they are with distorted trigonal bipyramidal and distorted octahedral geometry respectively. Distorted trigonal bi pyramidal coordination geometry of Zn1 is furnished by O1 and $O3^c$ oxygen atoms from one chelated carboxylate group and mono-dentate carboxylate group of btc ligand, one oxygen atom (O7) of μ_2-OH group, one coordinated water (O1W) molecule and one nitrogen atom (N1) of pyridyl group of azbpy linker, where Zn1-O bond lengths are in the range of 1.988-2.009 Å and Zn1-N is of 2.063 Å (Table 6).

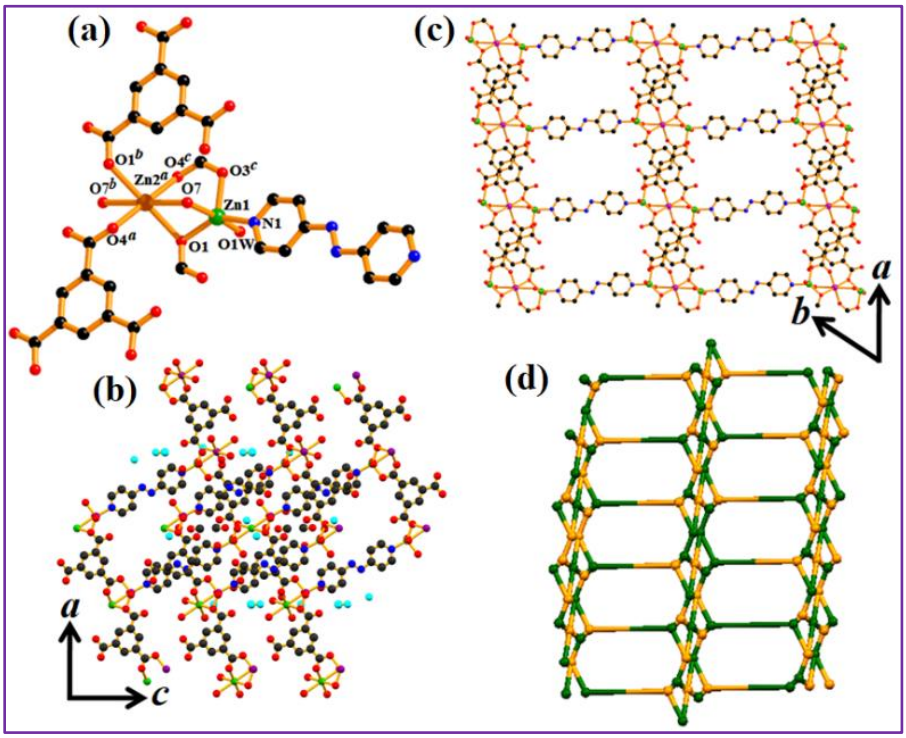

Figure 5. Crystal structure of {[$Zn_{2.5}$(azbpy)$(Hbtc)_2$(μ_2-OH)$(H_2O)_3$].$(H_2O)_{3.5}$(MeOH)}$_n$(**3**) (Zn1 green, Zn2 purple, O red, N blue, C black and solvents cyan) (a) view of the coordination environment (b) view of metal carboxylate 2D net along the *ab* plane (c) view of 2D framework along the *ac* plane with 1D water and methanol filled channels (d) topological[38,39] representation of **3**

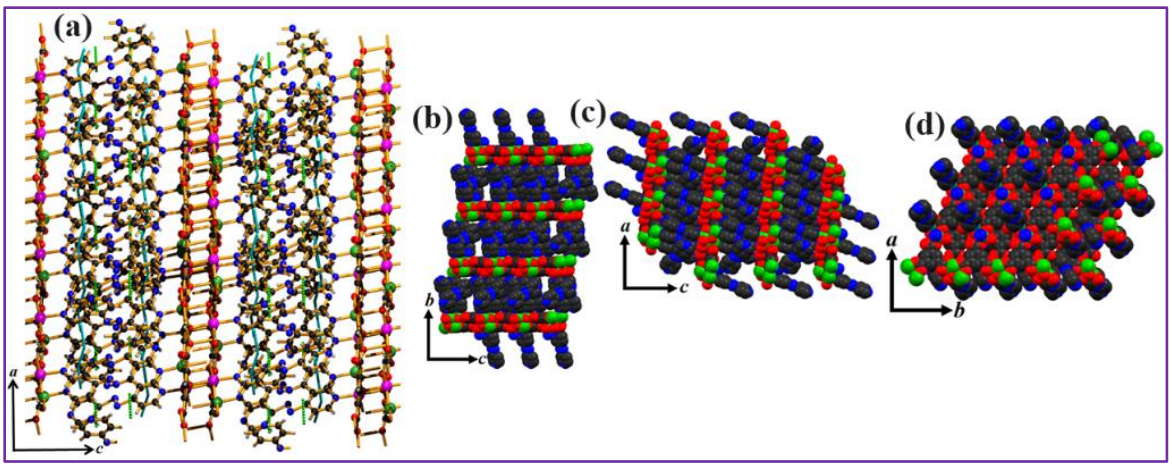

Figure 6. (a) π-π interactions, (b)-(d) space fill model of compound **3**

Table 6. Selected bond lengths (Å) and bond angles (°) for **3**

Zn1-O1	1.988(3)	Zn1-O1W	2.089(4)
Zn1-N1	2.063(3)	Zn1-O3^{a}	2.009(3)
Zn1-O7	2.227(3)	Zn2-O1^{b}	2.401(3)
Zn2-O4	2.290(4)	Zn2-O7^{b}	2.511(3)
Zn2-O1^{d}	2.401(3)	Zn2-O4^{e}	2.290(4)
O2W^{d}-Zn2-O4^{e}	86.55(11)	O1-Zn1-O1W	89.28(16)
O1-Zn1-O2W	83.49(13)	O1-Zn1-N1	137.12(14)
O1-Zn1-O3^{a}	123.51(12)	O1W-Zn1-O7	172.00(13)
O1W-Zn1-N1	94.10(14)	O1W-Zn1-O3^{a}	93.71(17)
O2W-Zn1-N1	93.54(11)	O2W-Zn1-O3^{a}	87.48(14)
O3^{a}-Zn1-N1	98.95(14)	O1^{b}-Zn2 -O4	78.41(12)
O2W^{b}-Zn2 -O4	86.55(11)	O1^{d}-Zn2-O4	101.59(12)
O2W^{d} -Zn2-O4	93.45(11)	O4-Zn2-O4^{e}	180.00
O1^{b}-Zn2-O7^{b}	69.80(10)	O1^{b}-Zn2-O1^{d}	180.00
O1^{b}-Zn2-O7^{d}	110.20(10)	O1^{b}-Zn2-O4^{e}	101.58(12)
O1^{d}-Zn2-O7^{b}	110.20(10)	O7^{b}-Zn2-O^{d}	180.00
O2W^{b}-Zn2-O4^{e}	93.45(11)	O1^{d}-Zn2-O7^{d}	69.80(10)
O1d-Zn2-O4^{e}	78.42(12)		

Symmetry code: *a* = -1+x,y,z; *b* = 1+x,y,z; *c* = 1-x,-y,2-z; d = 3-x,1-y,-z; e = 4-x,1-y,-z.

Table 7. π-π interaction in **3**

Ring(i) → Ring(j)	Distance of centroid(i) from ring(j),(Å)	Dihedral angle (i,j) (deg)	Distance between the (i,j) ring centroids,(Å)
R(1) → R(2)^{i}	3.553(3)	0.00(19)	3.3761(16)

Symmetry code: (i) = 3-X,1-Y,-Z. R(i)/R(j) denotes the ith/jth rings: R(1) = C1/ C2/C3/C4/C5/C6.

Similarly, coordination around Zn2 is created by four oxygen atoms (O1, O1^{b}, O4^{a}, and O4^{c}) of carboxylate group and two oxygen atoms (O7, O7^{b}) of μ_2-OH group. Here, Zn2-O bonds distance vary from 2.290-2.401Å (Table 6). The Zn···Zn contact distance across the dinuclear unit is 3.365Å. Here one of the carboxyl group of btc linker stays uncoordinated, although each btc connects three Zn(II) ions, in which one carboxyl group chelate two Zn(II) centers, and another carboxyl group ligates one Zn(II) center via bridging monodentate mode. Thus, unlike other two compounds, here btc and hydroxyl group connect two crystallographically independent Zn(II) centers to extend the structure along only one direction, *a* axis. The linear azbpy linker connects these 1D arrangements to create a 2D structure. (Figure. 5b), solvents filled 2D framework represents in Figure. 5c. The topology[38,39] of these 2D framework suggests a trinodal 3,4,6 connected net with stoichiometry (3-c)(4-c)(6-c) and the corresponding Schläfli symbol of the net is $\{3^2.4.5^2.6\}\{3^2.4.6^2.7\}\{3^4.4^4.5^4.6^3\}$(Figure. 5d). In the crystal packing, the Hbtc ligands are involved in π-π interactions (Table 7) with Hbtc ligands, giving the supramolecular 3D framework (Figure. 6)[40,41] with 1D channels along the crystallographic *c*-axis, which is occupied by guest water and methanol molecules. Upon artificial removal of water molecules from the framework there is about 6.6% void space to the crystal volume as suggested by the PLATON[35] crystallographic software. Space fill model shows that only surface pore has present (Figure. 6).

2.3.2. Framework Stability

Framework stability of **1**, **2**, and **3** has been determined by the thermogravimetric analysis (TGA) (Figure. 7a, 7b and 7c) and powder X-ray diffraction studies (PXRD) (Figure. 8). We have performed dynamic thermogravimetric analysis (TGA) by changing the temperature at constant rate. The temperature increases from 30 ^{o}C to 600 ^{o}C at the rate of 5 ^{o}C/min. The whole experiment was carried out at nitrogen environment. The weight of all the samples have been taken more 10 mg for the experiment. Thermogravimetric analysis of the crystalline powder sample of compound **1** has been performed in the temperature range 30-600°C (Figure. 7a). The TGA of compound **1** (Figure. 7a) shows a gradual weight-loss step of 9.63% (40–110°C), which corresponds to the escape of guest water, methanol and coordinated solvent molecules. The dehydrated framework of **1** is stable up to ~280°C. This is followed by a sharp weight loss, caused by unrecognized products probably due to the decomposition of the frameworks.

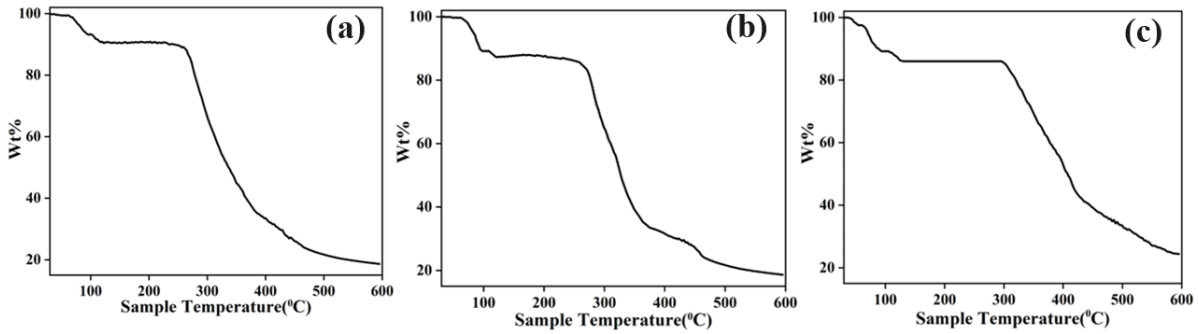

Figure. 7 TGA of compound **1** (a), **2** (b) and **3** (c)

In the case of compounds compound **2** (Figure. 7b) and **3** (Figure. 7c), closely resemble weight loses of 15.8% and 16.2% observed respectively in the temperature range of 60°C to 120°C and 40°C to 125°C. This weight loss is for lattice and coordinated solvent molecules. No significant weight loss is found up to 270°C and 300°C for compounds **2** and **3** respectively, signifying high thermal stability for both compounds.

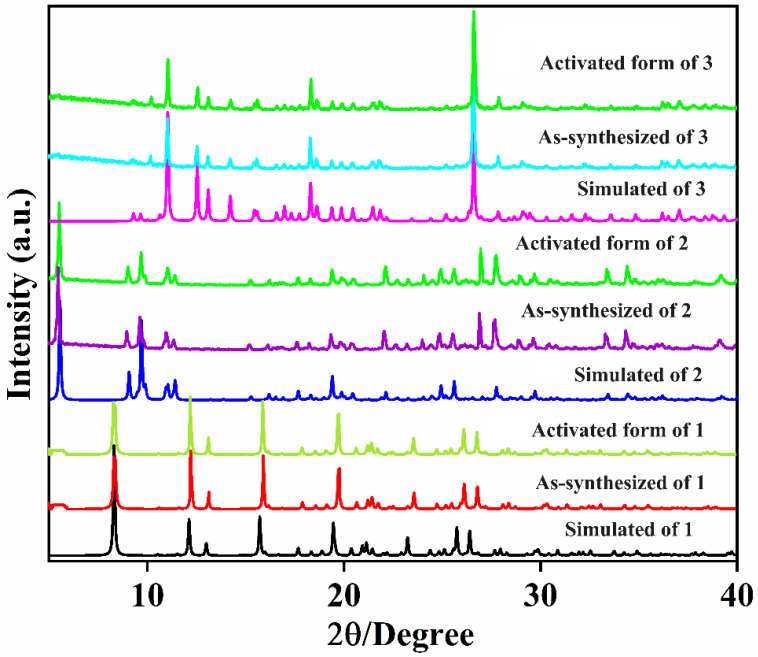

Figure 8. PXRD patterns of compound **1, 2** and **3**

The powder X-ray diffraction patterns show that simulated pattern of compounds **1**, **2**, and **3** exactly similar to their as-synthesized PXRD pattern (Figure. 8), which indicates the bulk purity of these compounds. Further, the powder x-ray diffraction of activated forms of compounds **1**, **2** and **3** have been performed, which show similar peak position with simulated pattern (Figure. 8).

2.3.3. Uv-Visible and IR Spectra

The solid state Uv-vis spectra of azbpy ligand, compound **1**, **2** and **3** (Figure 9) have been studied. Each samples show two maxima. The maxima of azbpy and compound **1** are 330nm (1st maxima) and 470nm (2nd maxima) each. In case of compounds **2** and **3** two maxima are 300nm and 530nm each. FT-IR spectra with the samples has been presented in Figure 10.

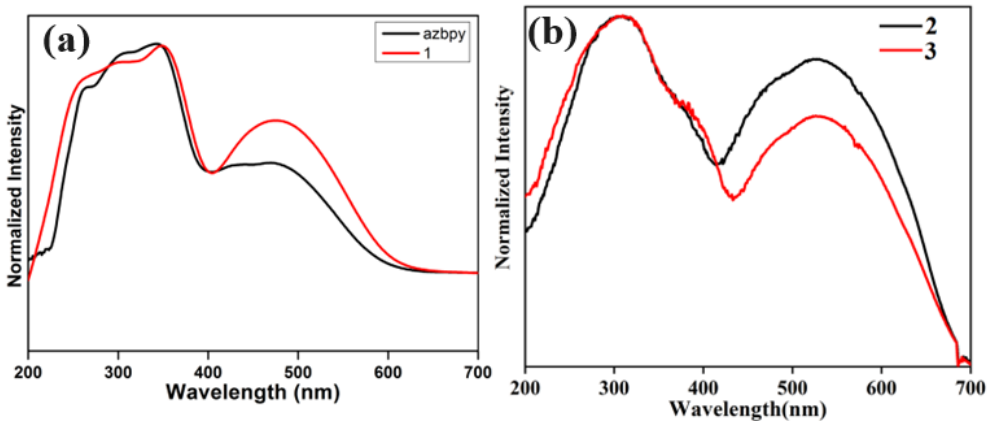

Figure 9. Uv-vis spectra of organic linker and compound **1, 2** and **3**

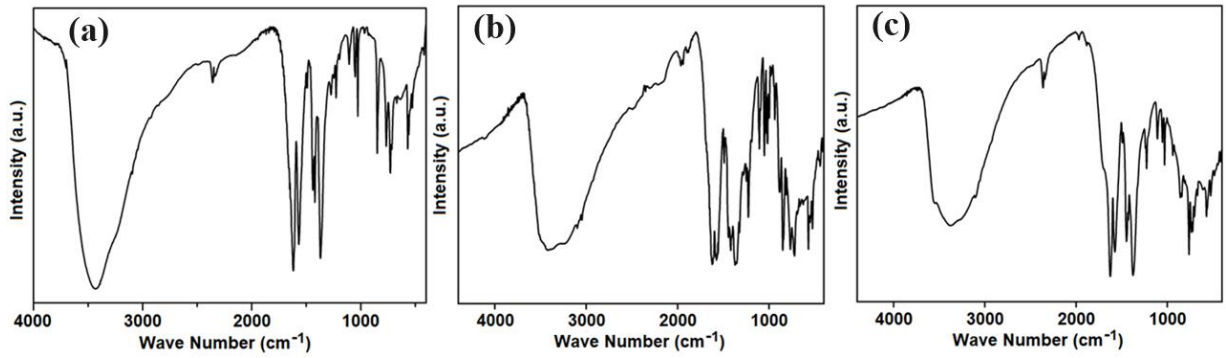

Figure 10. IR spectra of compound **1** (a), **2** (b) and **3** (c)

2.3.4. Permanent porosity and gas storage properties

The different framework tropology with highest dimensions (3D) of two compounds and frameworks stability and structural rigidity of all compounds **1**, **2** and **3** inspired us to perform gas adsorption studies. The complex **1** and **2** are with three-dimensional structures having void pore sizes 17.5% and 13.7%, which can capture the gases like carbon dioxide and nitrogen. The kinetic diameters of N_2 (3.65 Å) and CO_2 (3.40 Å), which are comparable with the pores of compound **1** and **2**. Also, the presence of unsaturated coordination sites in both the compounds along with the presence electron rich nitrogen atoms of azo (-N=N-) bonds in azo pyridine-based ligands present inside the pores, usually show interactions with adsorbing gas molecules. The N_2 adsorption

isotherms performed (77 K) on all the compounds exhibits nonporous behavior. At 1 bar pressure and 77 K temperature, **1** (Figure. 11a) adsorb ~12 mL/g (0.00054 mol/g) of N_2, **2** absorb ~18 mL/g (0.0008 mol/g) and 3 adsorb ~13 mL/g (0.00058 mol/g) (Figure. 11b). The pore size distribution analysis from N_2 sorption data at 77 K has been calculated by applying the non-local density functional theory (NL-DFT) method, which suggests the pore volumes for compounds **1**, **2** and **3** to be 0.093 cc/g, 0.028 cc/g and 0.015 cc/g respectively. Along with that the surface area of compounds **1**, **2** and **3** has been calculated from N_2 sorption, which are 56.47 m^2/g, 33.074 m^2/g and 12.045 m^2/g (Table 8). The CO_2 adsorption of compounds **1** and **2** at the temperature 195 K show interesting features with type II adsorption profile, at first it shows a sharp uptake due to unrestricted monolayer formation, followed by a relatively slow uptake signifying gradual multilayer formation by overlapping of monolayer coverage up to 1 bar. CO_2 uptake observed for the compound **1** is ~42 mL/g (0.0019 mol/g) and compound **2** is ~38 mL/g (0.00169 mol/g), as pressure reaches 1 bar. The presence of the hysteresis in adsorption-desorption isotherms of CO_2 sorption in both the compounds **1** and **2** indicate that polar CO_2 molecules interact strongly with the framework. Stronger interaction can be attributed to the presence of -N=N- group in azbpy on the pore walls which can interact effectively with the CO_2 molecules as the carbon atom in CO_2 is electron deficient (Lewis acid) in nature and for this there is a tendency to retain in the frameworks.

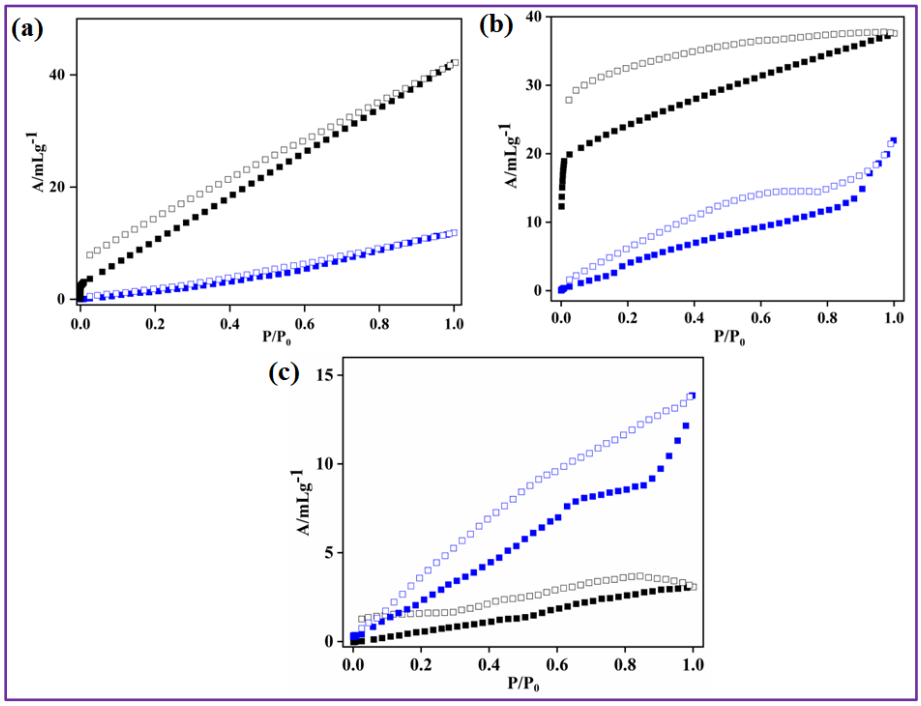

Figure 11. Gas sorption isotherms of **1** (a), **2** (b) and **3** (c) at low temperature, N_2 at 77 K (blue) and CO_2 at 195 K (black)

The relative CO_2 sorptions follows their percentages of void in the frameworks, **1** has greater void than **2**, shows higher uptake of CO_2. Complex **3** (Figure. 11c) has dense 2D framework, it has only free surface area to sorption. The value of CO_2 is ~4 mL/g (0.00018 mol/g), which is very negligible because of the small pore size 2D framework. To explore the affinity of the activated frameworks toward the CO_2 molecules, isosteric heat of adsorption (Q_{st}) was calculated[42] of compounds **1** and **3** from CO_2 adsorption data at two different temperatures i.e., 273K and 298K (Figure. 12a, 12b and 12c) using the Clausius-Clapeyron equation, which is $(d\ln p/dT) = Q_{st}/RT^2$ (Figure. 12d, 12e), values 60.53 kJ/mol and 44.51 kJ/mol.

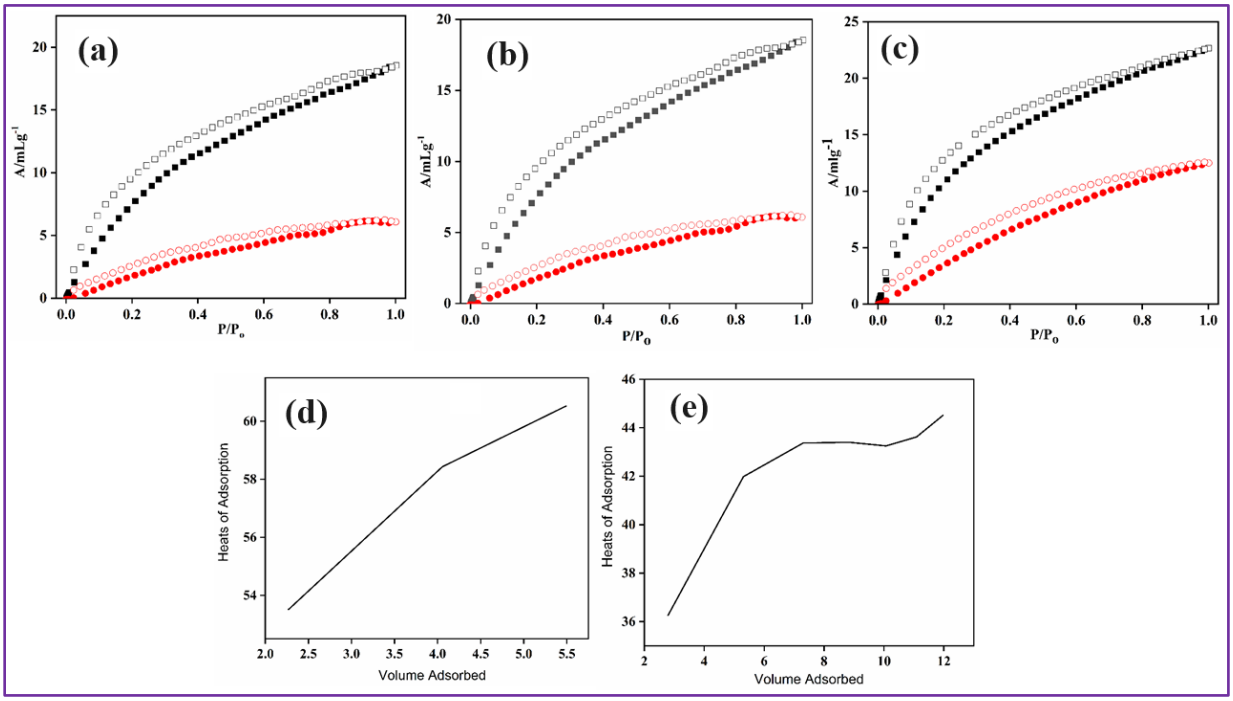

Figure 12. CO_2 sorption of compound **1** at 273 K (black) and 298 K (red), **(b)** CO_2 sorption of compound **2** at two temperatures 273 K (black) and 298 K (red), **(c)** CO_2 sorption of compound **3** at two temperatures 273 K (black) and 298 K (red). **(d)** Heat of adsorption plot of compound **1**, **(e)** Heat of adsorption plot of compound **3**

Table 8. Adsorption capacity of N_2 gas, surface area and pore volume of compounds **1**, **2** and **3**

Compound	Adsorption capacity of N_2 (mL/g)	Surface area (m^2/g)	Pore volume (cc/g)
1	12	56.47	0.093
2	18	33.074	0.028
3	13	12.045	0.015

2.3.5 Photoluminescent Study

CPs with d^{10} metal centers and organic ligands are promising candidates for photoactive materials with various potential applications. The solid-state luminescence spectra of azbpy ligand, compound **1, 2** and **3** have been investigated at room temperature (Figure. 13a, 13b). Free azbpy ligand in the solid state shows an emission band maximum at 361 nm on excitation at 270 nm, which can be assigned to the n→π* or π→π* transitions. Upon photoexcitation, **1**, **2** and **3** display the maximum emission peak at 401nm (λ_{ex} = 330nm), 390nm (λ_{ex} = 300nm), 335nm (λ_{ex}= 300nm). The similar emissions of free azbpy ligand and the compounds were not attributed to the dicarboxylate ligands. The emissions are significantly red-shifted (40nm, 29nm) for complexes **1** and **2**, compare to the free azbpy ligand, where it is blue-shifted (26nm) for compound **3** compared with that of the free azbpy ligand. The emissions are neither metal-to-ligand charge transfer (MLCT) nor ligand-to-metal charge transfer (LMCT). These results indicate that the fluorescence of **1**, **2** and **3** may be attributed to a mix-characteristic of intra-ligand and ligand-to-ligand charge transitions, as reported for other d^{10} metal complexes with N-donor ligands.

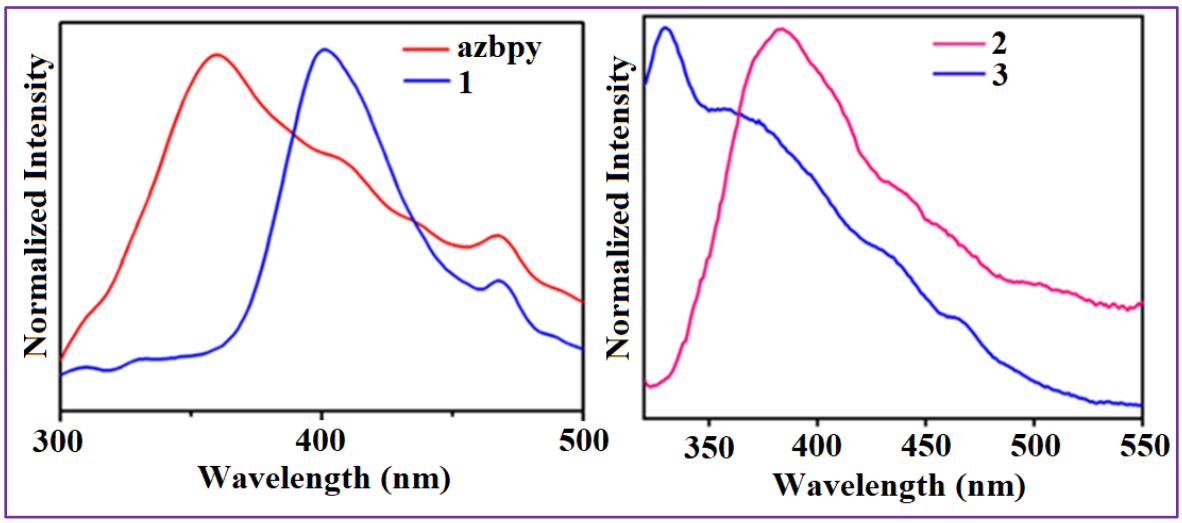

Figure 13. (a) Solid state luminescence study of organic ligand (azbpy) (Red) and complex **1** (Blue) (b) Solid state luminescence study of complex **2** (Magenta) and complex **3** (Blue)

2.4. CONCLUSION

Three new multifunctional metal-organic frameworks of Zn(II) from trans 4,4′-azobispyridine(azbpy) and 1,3,5-benzenetricarboxylate (btc) has been synthesized using different molar ratios of the reactants. All the complexes have unique bridging hydroxide, which connected

multiple metal centers. Two 3D frameworks have been formed with the same concentration of acidic linker, but higher concentration of acidic linker decreases the dimension to 2D due to change of coordination mode of acidic linker tripodal to bipodal. Here two 3D CPs show better gas adsorption than the 2D one. Furthermore, three compounds have fascinating luminescent properties with ability to red shift the emission except complex **3**. Overall, from this study it is evident that the change in the concentration of the constituent ligand/s can significantly change the structural outcome and associated properties. Thus, this kind of structural modulation can help to fabricate material with controlled and predefined functionality for realistic applications in the near future.

REFERENCES

1. Jayaramulu, K.; Narayanan, R.P.; George, S.J.; Maji, T.K. *Inorg. Chem.* **2012**, *51*, 10089−10091.
2. Ghosh, S.; Das, M.; Dinda, S.; Pahari, G.; Ray, P.P.; Ghoshal, D. *Cryst. Growth Des.* **2021**, *21* 4892−4903.
3. Haldar, R.; Maji, T. K. *CrystEngComm* **2013**, *15*, 9276–9295.
4. Lee, J. Y.; Farha, O. K.; Roberts, J.; Scheidt, K. A.; Nguyen, S. B. T.; Hupp, J. T. *Chem. Soc. Rev.* **2009**, *38*, 1450–1459.
5. Mallick, A.; Saha, S.; Pachfule, P.; Roy, S.; Banerjee, R. *J. Mater. Chem.* **2010**, *20*, 9073–9080.
6. Sahoo, S.C.; Kundu, T.; Banerjee, R. *J. Am. Chem. Soc.* **2011**, *133*, 17950–17958.
7. Gole, B.; Bar, A. K.; Mallick, A.; Banerjee, R.; Mukherjee, P. S. *Chem. Commun.* **2013**, *49* 7439–7441.
8. Dutta, S.; Let, S.; Shirolkar, M. M.; Desai, A. V.; Samanta, P.; Fajal, S.; More, Y. D.; Ghosh, S. K. *Dalton Trans.* **2021**, *50*, 10133-10141.
9. He, H.; Zhang, D. -Y.; Guo, F.; Sun, F. *Inorg. Chem.* **2018**, *57*, 7314−7320.
10. Chand, S.; Elahi, S. M.; Pal, A.; Das, M. C. *Chem.Eur.J.* **2019**, *25*, 6259 –6269.
11. Kanoo, P.; Gurunatha, K. L.; Maji, T. K. *Cryst. Growth Des.* **2009**, *9*, 4147−4156.
12. Dinda, S.; Pahari, G.; Maiti, A.; Ghoshal, D. *CrystEngComm* **2023**, *25*, 1116–1125.
13. Maity, D. K.; Haque, F.; Halder, A.; Ghoshal, D. *Cryst. Growth Des.* **2020**, *20*, 7667–7674.
14. Desai, A.V.; Sharma, S.; Roy, A.; Ghosh, S. K. *Cryst. Growth Des.* **2019**, *19*, 7046−7054.
15. Zhu, L.; Liu, N.; Yu, L.; Jiang, X.; Li, X. *Inorganica Chim. Acta* **2020**, *510*, 119728.
16. Yang, S. -L.; Li, G.; Guo, M. -Y.; Liu, W. -S.; Bu, R.; Gao, E. -Q. *J. Am. Chem. Soc.* **2021**, *143*, 8838−8848.
17. Karmakar, A.; Paul, A.; Mahmudov, K. T.; Fa´tima, M. C.G.D. Silva, A.J.L. Pombeiro, *New J. Chem.* **2016**, *40*, 1535—1546.
18. Im, J.; Seoung, D.; Hwang, G. C.; Jun, J. W.; Jhung, S. H.; Kao, C. -C.; Vogt, T.; Lee, Y. *Chem. Mater.* **2016**, *28*, 5336−5341.

19. Mckinstry, C.; Cathcart, R. J.; Cussen, E. J.; Fletcher, A. J.; Patwardhan, S. V.; Sefcik, J. *J. Chem. Eng.* **2016**, *285*, 718–725.
20. Maity, D. K.; Ghosh, S.; Otake, K. -I.; Kitagawa, H.; Ghoshal, D. *Inorg. Chem.* **2019**, *58*, 12943−12953.
21. Safaei, M.; Foroughi, M. M.; Ebrahimpoor, N.; Jahani, S.; Omidi, A.; Khatami, *M. Trends in Analytical Chemistry* **2019**, *118*, 401−425.
22. Halder, A.; Bhattacharya, B.; Haque, F.; Dinda, S.; Ghoshal, D. *Chem.Eur.J.* **2019**, *25* 12196–12205.
23. Allendorf, M. D.; Stavila, V.; Witman, M.; Brozek, C. K.; Hendon, C. H. *J. Am. Chem. Soc.* **2021**, *143*, 6705−6723.
24. Maza, W. A.; Padilla, R.; Morris, A. J. *J. Am. Chem. Soc.* **2015**, *137*, 8161−8168.
25. Luan, X. -J.; Cai, X. -H.; Wang, Y. -Y.; Li, D. -S.; Wang, C. -J.; Liu, P.; Hu, H.-M.; Shi, Q.-Z.; Peng, S.-M. *Chem. Eur. J.* **2006**, *12*, 6281 – 6289.
26. Liu, P. -P.; Cheng, A. -L.; Yue, Q.; Liu, N.; Sun, W. -W.; Gao, E. -Q. *Cryst. Growth Des.* **2008**, *8*, 1668–1674.
27. Wu, Y. -P.; Li, D. -S.; Fu, F.; Dong, W. -W.; Zhao, J.; Zou, K.; Wang, Y. -Y. *Cryst. Growth Des.* **2011**, *11*, 3850–3857.
28. Carlucci, L.; Ciani, G.; Maggini, S.; Proserpio, D. M. *Cryst. Growth Des*. **2008**, *8*, 162–165.
29. Yin, P. -X.; Zhang, J.; Qin, Y. -Y.; Cheng, J. -K.; Li, Z. -J.; Yao, Y. -G. *CrystEngComm* **2011**, *13*, 3536–3544.
30. Halder, A.; Bhattacharya, B.; Haque, F.; Ghoshal, D. *Cryst. Growth Des.* **2017**, *17*, 6613−6624.
31. Kennedy, A. R.; Brown, K. G.; Graham, D.; Kirkhouse, J. B.; Kittner, M.; Major, C.; McHugh, C. J.; Murdoch, P.; Smith, W. E. *New J. Chem.* **2005**, *29*, 826–832.
32. SMART (V 5.628), SAINT (V 6.45a), XPREP, SHELXTL; Bruker AXS Inc.: Madison, WI, **2004.**
33. Sheldrick, G. M. University of Göttingen: Germany, **2002**.
34. Sheldrick, G. M. *Acta Cryst.* **2015**, *A71*, 3-8.
35. Spek, A. L. Acta Crystallogr. Sect. D. **2009**, *68*, 148–155.
36. Farrugia, L. J. *J. Appl. Crystallogr*. **1999**, *32*, 837–838.
37. Macrae, C. F.; Edgington, P. R.; McCabe, P.; Pidcock, E.; Shields, G. P.; Taylor, R.; Towler, M.; Streek, J. V. D. *J. Appl. Cryst.* **2006**, *39*, 453–457.
38. Blatov, V. A.; Shevchenko, A. P.; Serezhkin, V. N. *J. Appl. Crystallogr*. **2000**, *33*, 1193.
39. Blatov, V. A.; Carlucci, L.; Ciani, G.; Proserpio, D. M. *CrystEngComm.* **2004**, *6*, 377–395.
40. Abbas, M.; Maceda, A. M.; Xiao, Z.; Zhou, H. -C.; Balkus Jr., K. J. *Dalton Trans.* **2023**, *52*, 4415–4422.
41. Dastidar, T. G.; Ghosh, K.; Drew, M. G. B.; Gomila, R. M.; Frontera, A.; Chattopadhyay, S. *Polyhedron* **2022**, *222*, 115862.
42. Qian, J.; Li, Q.; Liang, L.; Li, T. -T.; Hu, Y.; Huang, S. *Dalton Trans.* **2017**, *46*, 141002–141006.

CHAPTER-3

Solvent Induced Reversible Single-Crystal-to-Single-Crystal Structural Transformation in Dynamic Metal Organic Frameworks: A Case of Enhanced Hydrogen Sorption in Polycatenated Framework

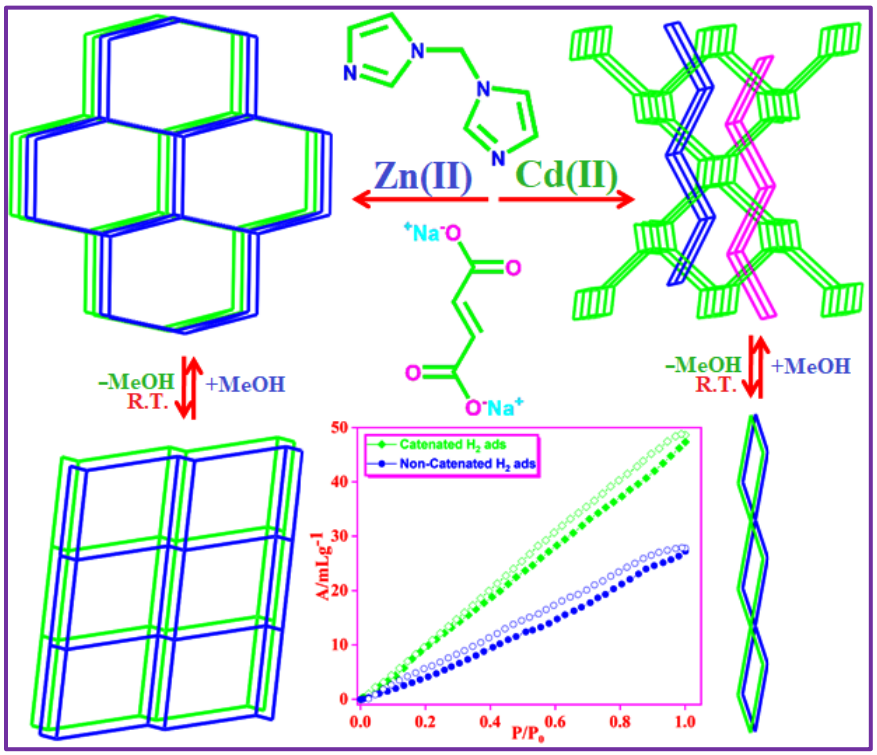

CHAPTER-3

Solvent Induced Reversible Single-Crystal-to-Single-Crystal Structural Transformation in Dynamic Metal Organic Frameworks: A Case of Enhanced Hydrogen Sorption in Polycatenated Framework

3.1. INTRODUCTION

Structural dynamism in metal organic frameworks (MOFs) is one of the affluent topics of research in the area of material science.[1-5] The structurally dynamic control of porosity in MOFs,[6] which is the principal concern of many various interesting properties.[7-10] This can be simply achieved by the proper framework designs and/or exploiting the structural transformation preferably in a single-crystal-to-single-crystal (SCSC) manner.[11-13] Such SCSC transformation[11-13] is very effective to obtain new functional MOFs in high yield and purity, which may not be formed under conventional procedures. However, a SCSC transformation of MOFs is still to some extent tricky and comparatively hard to achieve due to the simultaneous cleavage and formation of bonds[14] and high chances of losing crystallinity after the aforesaid solid-state rearrangement[11-12] of constituent atoms. In this context, dynamic or soft porous networks of MOFs have generated interests for the development of new materials for the selective gas sorption and separation.[10] For dynamic porous network SCSC[15] transformation generally occurs through external stimuli, like temperature, light and exchange of ions or solvent[16-18]. The exchange or elimination of guest solvent molecules[19-23] may transform the structure due to various facts like breathing effect,[24] sliding between layers,[25] variation of the packing mode, change in the spatial group and symmetry or redistribution of the pores in the network. Addition or elimination of lattice solvent[17,26] have a major role as it can make and break different supramolecular interactions[27] that may lead to new crystal structure. There are a few reported dynamic and flexible porous 2D framework[28,29], responds to the external stimuli and results structural transformation either *via* within the layer or between the layers.[25] Lattice solvent exchanged structural transformation generally triggered by high temperature, but the structural transformation due to selective solvent molecules elimination at room temperature is extremely rare. On the other hand, crystalline transformations through dissolution–recrystallization structural transformation (DRST),[30] solubility plays an important factor in rational transformation tuning. This process includes the dissolution and destruction of the initial complexes, consequence of formation and crystallization of new complexes in the solution phase

itself. Furthermore, the diversity of DRST[30] and SCSC[31] processes has been disclosed, but the mechanism behind the transformation process, such as the driving force and so on, were not been investigated systematically. Recently some studies of interpenetrated or polycatenated[32-34] MOFs having structural transformation features; shows greater hydrogen uptake not having the traditional factors for hydrogen uptake. In such cases, flexible interpenetration or framework catenation worked as an independent criterion, which is an important factor contributing to the high hydrogen uptake. In addition to that, the dynamic MOFs has also found promising as multifunctional luminescent materials,[35-37] and the changes of luminescence property in such cases with structural transformation is found also very much interesting.[37]

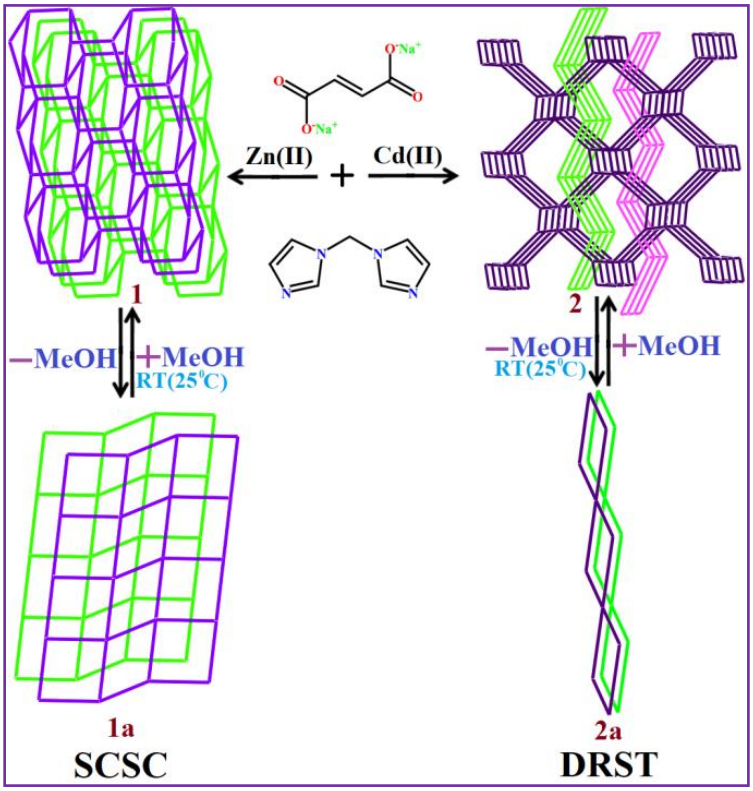

Scheme 1. Schematic presentation of selective solvent induced reversible SCSC in **1** and selective solvent induced reversible dissolution–recrystallization structural transformation (DRST) in **2** at room temperature

Considering these prospect of exploring structural transformation for better functionality in flexible MOFs, two d^{10} metals complexes $\{[Zn_2(fum)_2(dim)_2](H_2O)(MeOH)\}_n$ (**1**) and $\{[Cd_2(fum)_2(dim)_2(H_2O)](MeOH)\}_n$ (**2**) using fumarate (fum) and di(1H-imidazol-1-yl)methane (dim) has been synthesized in methanol-water solutions. Single crystal of complex **1** is a 2D MOF showing a solid state reversible transformation to form a different 2D structure of

{[Zn(fum)(dim)](H_2O)}$_n$ (**1a**) at room temperature (Scheme 1), whereas (**1a**) reversibly transformed to **1** upon immersion on methanol, which has been mentioned as **1′**. Here selective solvent induced reversible single crystal to single crystal transformation occurs at room temperature in 2D framework between squeezed and uncompressed structure. In contrast, the relatively more stable polycatenated 3D+2D→3D complex **2** does not undergo such solid-state transformation at room temperature in ambient condition; rather it undergoes slow dissolution–recrystallization structural transformation (DRST) in mother liquor itself. The said DRST converts **2** into a 1D framework of {[Cd(dim)$_2$(H_2O)$_2$](fum)(H_2O)$_2$}$_n$ (**2a**), which reverts back to **2** upon addition of methanol into the mother liquor, which has been denoted as **2′**. This selective solvent induced reversible SCSC structural transformation of **1** and the reversible DRST of complex **2**, both at room temperature; have been supported by PXRD, luminescence, TGA, IR, UV-Vis studies. Comparative H_2 gas sorption studies between complex **1a** of wavy 2D framework and complex **2** of polycatenated 3D+2D→3D framework has been performed along with CO_2, and N_2 sorption study.

3.2. EXPERIMENTAL SECTION

3.2.1. Materials

Immensely fresh $Zn(NO_3)_2 \cdot 6H_2O$, $Cd(NO_3)_2.4H_2O$, imidazole, dichloromethane, tetrabutylammonium chloride have been acquired from the Sigma-Aldrich Chemical Co. All other reagents and solvents have been bought from commercial sources and used except further purification. di(1H-imidazol-1-yl)methane[38] have been synthesized by a reaction between dichloromethane and imidazole in presence potassium hydroxide and tetrabutyl ammonium bromide(TBAB) at 40 ^oC in inert atmosphere condition. Na_2-fum had been synthesized by the sluggish collation of solid NaOH to the analogous acids (H_2-fum) in water in a 2:1 ratio and allowed to evaporate until dryness.

3.2.2. Physical Measurements

Elemental analyses (C, H, N) have been performed using a PerkinElmer 240C elemental analyzer. FT-IR spectra have been obtained on a PerkinElmer spectrometer (Spectrum II) with the samples. PerkinElmer STA8000 thermal analyzer has been used for thermogravimetric analysis (TGA) with a ramp rate of 10 °C/min from room temperature to 600 °C under nitrogen flow. Powder X-ray diffraction (PXRD) data were collected on a Bruker D8 Discover instrument with Cu-Kα radiation (λ = 1.5406 Å), operating at 40 kV and 40 mA. UV-vis spectra are collected in PerkinElmer

Lambda 35 instrument with integrating sphere attachment. Fluorescence measurements were done using HoribaFluoroMax 4 spectrofluorimeter.

3.2.3. Sorption Measurements

Quantachrome Autosorb–iQ adsorption instrument have been used to measured adsorption isotherms N_2 (77 K), CO_2 (195 K) and H_2 (77 K) for the dehydrated frameworks of **1a** and **2′′**. Very pure N_2 gas (99.999% purity), CO_2 gas (99.95%) and H_2 gas (99.999%) have been used for this measurement. The N_2 (at 77 K, liquid nitrogen bath), CO_2 (at 195 K, dry ice-acetone bath) and H_2 (at 77 K, liquid nitrogen bath) sorption measurements have been carried out in the pressure range 0–1 bar using dehydrated samples of **1a** and **2′′**. Before measurements, all the as-synthesized complexes (40 mg for each) have been dehydrated in the sample tube at 413 K for 3 h under a 1×10^{-1} Pa vacuum. By controlled introducing ultra-pure helium gas (99.999% purity) into the sample tube and allowing it to diffuse into the sample, the dead volume has been measured. The gas adsorption volume for each and every measurement has been calculated from the difference of pressure ($P_{cal}-P_e$), where P_{cal} signifies the calculated pressure without any gas adsorption and P_e indicates the observed pressure at equilibrium. The pressure change has been monitored by taking the adsorbent in the sample tube, and the degree of adsorption was calculated by observing the decrease in pressure at equilibrium.

3.2.4. Synthesis

{[Zn_2(fum)$_2$(dim)$_2$](H_2O)(MeOH)}$_n$ (1). After deprotonation of H_2-fumarate in aqueous solution by NaOH (2 mmol, 80 mg), the resulting 20 ml solution of Na_2-fum (1 mmol, 160 mg) was slowly mixed with a methanolic solution (20 mL) of di(1H-imidazol-1-yl)methane (1 mmol, 148 mg) and stirred for 20 min to mix well. slowly and carefully, 4ml aqueous solution of Zn(II) from 20 mL aqueous solution of $Zn(NO_3)_2\cdot6H_2O$ (1 mmol, 0.297 g) was layered with 6 mL of the aforesaid mixed-ligand solution by using 5 mL of mixed solvent (1:1 water/ MeOH mixture) as buffer. At the juncture of the solution colourless block-shaped single crystals appropriate for X-ray diffraction analysis were form in the layer tube after 4 days. The crystals were collected, washed with MeOH, and dried under air to separate for experiments. Yield: 82%. Elemental analysis, calculated for $C_{23}H_{26}N_8O_{10}Zn_2$ (705.29): C 39.13; H 3.68; N 15.87. Found: C 39.08; H 3.55; N 15.70. [IR spectra (KBr pellet, 4000−400 cm^{-1}): ν(O−H), 3479 (stretch, H-bonded); ν(C−H, imidazole), 3007 (stretch); ν(C−H, alkane), 2816 (stretch) and 1359 (bending); ν(C−C, imidazole), 1613−1516 (stretch); and ν(C−O), 1231 (stretch)].

{[Zn_2(fum)$_2$(dim)$_2$](H_2O)} (1a). Complex **1** undergoes selective solvent (methanol) elimination and structural transformation to complex **1a** at room temperature. Elemental analysis, calculated for $C_{11}H_{12}N_4O_5Zn$ (345.62): C 38.19; H 3.47; N 16.20. Found: C 38.06; H 3.40; N 16.15. [IR spectra (KBr pellet, 4000−400 cm^{-1}): ν(O−H), 3445 (stretch, H-bonded); ν(C−H, imidazole), 3027 (stretch); ν(C−H, alkane), 2819 (stretch) and 1359 (bending); ν(C−C, imidazole), 1615−1506 (stretch); and ν(C−O), 1232 (stretch)].

{[Zn_2(fum)$_2$(dim)$_2$](H_2O)(MeOH)}$_n$ (1′). Complex **1a** added to methanol solution for 30 minutes, resulting a new complex, which is complex **1**, denoted as **1′**. Elemental analysis, calculated for $C_{23}H_{26}N_8O_{10}Zn_2$ (705.19): C 39.13; H 3.68; N 15.87. Found: C 39.06; H 3.52; N 15.68. [IR spectra (KBr pellet, 4000−400 cm^{-1}): ν(O−H), 3479 (stretch, H-bonded); ν(C−H, imidazole), 3007 (stretch); ν(C−H, alkane), 2816 (stretch) and 1359 (bending); ν(C−C, imidazole), 1613−1506 (stretch); and ν(C−O), 1231 (stretch)].

{[Cd_2(fum)$_2$(dim)$_2$(H_2O)](MeOH)}$_n$ (2). By following the same procedure, instead of $Zn(NO_3)_2.6H_2O$, $Cd(NO_3)_2.4H_2O$ has been used. Suitable colorless crystals obtain at the junction of the solution after 1 week for X-ray diffraction analysis. The crystals were collected, washed with MeOH, and dried under air to separate for experiments. Yield 78%. Elemental analysis, calculated for $C_{23}H_{24}N_8O_{10}Cd_2$, (797.29): C 34.62; H 3.01; N 14.05. Found: C 34.58; H 2.94; N 14.01. [IR spectra (KBr pellet, 4000−400 cm^{-1}): ν(O−H), 3417 (stretch, H-bonded); ν(C−H, imidazole), 3011 (stretch); ν(C−H, alkane), 1396 (bending); ν(C−C, imidazole), 1582 (stretch); and ν(C−O), 1230 (stretch)].

{[Cd_2(fum)$_2$(dim)$_2$(H_2O)] (2a). After elimination of solvent (methanol) molecules in open air from the reaction mixture of **2**, dissolution–recrystallization structural transformation has been happened, formed complex **2a**. Elemental analysis, calculated for $C_{18}H_{20}N_8O_7Cd$ (587.81): C 34.75; H 3.40; N 19.05. Found: C 34.68; H 3.35; N 19.01. Anal. Cal. for, [IR spectra (KBr pellet, 4000−400 cm^{-1}): ν(O−H), 3180 (stretch, H-bonded); ν(C−H, imidazole), 3006 (stretch); ν(C−H, alkane), 2824 (stretch) and 1338 (bending); ν(C−C, imidazole), 1529 (stretch); and ν(C−O), 1238 (stretch)].

{[Cd_2(fum)$_2$(dim)$_2$(H_2O)](MeOH)}$_n$ (2′). Immersing the complex **2a** in methanol-water solvents for 6 days, converts to a similar structure of **2**, denoting as **2′**. Elemental analysis, calculated for $C_{23}H_{24}N_8O_{10}Cd_2$, (797.29): C 34.62; H 3.01; N 14.05. Found: C 34.58; H 2.94; N 14.01. [IR spectra (KBr pellet, 4000−400 cm^{-1}): ν(O−H), 3417 (stretch, H-bonded); ν(C−H, imidazole), 3011

(stretch); ν(C−H, alkane), 1396 (bending); ν(C−C, imidazole), 1582 (stretch); and ν(C−O), 1230 (stretch)].

3.2.5. Crystallographic Data Collection and Refinement

The X-ray single-crystal data for complexes **1**, **1a**, **1′**, **2**, **2a** and **2′** have been collected at room temperature in a Bruker made APEX III diffractometer. At first, single crystals of both the compounds have been isolated and then mounted on the glass fiber tip using commercial super glue. Mo−Kα radiation (λ = 0.71073 Å) from a sealed tube X-ray source has been used. The raw data have been integrated using the SAINT[39] program and by utilizing SADABS,[40] the absorption corrections were performed. The structures have been solved by SHELXL-2016/6,[41] and full-matrix least-squares refinements on F^2 for all non-hydrogen atoms were performed by SHELXL-2016/6,[41] with anisotropic displacement parameters.

Table 1. Data Collection and Refinement Parameters for Single Crystal Analysis for Complexes; **1**, **1a**, **1′**, **2**, **2a** and **2′**

	1	**1a**	**1′**	**2**	**2a**	**2′**
Formula	$C_{23}H_{26}N_8O_{10}Zn_2$	$C_{11}H_{12}N_4O_5Zn$	$C_{23}H_{26}N_8O_{10}Zn_2$	$C_{23}H_{24}N_8O_{10}Cd_2$	$C_{18}H_{24}N_8O_8Cd$	$C_{23}H_{24}N_8O_{10}Cd_2$
Formula Weight	705.24	345.62	705.19	797.29	592.84	797.29
Crystal System	Triclinic	Triclinic	Triclinic	Monoclinic	Triclinic	Monoclinic
Space Group	*P-1*	*P-1*	*P-1*	$P2_1/c$	*P-1*	$P2_1/c$
a/ Å	8.940(5)	8.1969(8)	8.7683(7)	10.80049(8)	8.4948(8)	10.8053(12)
b/Å	12.233(5)	9.3522(9)	12.2482(9)	15.8656(13)	8.8675(8)	15.8625(17)
c/ Å	14.394(5)	10.159(1)	14.4310(9)	16.4535(13)	9.1411(9)	16.4783(18)
α/°	87.621(5)	104.479(3)	87.618(2)	90	62.811(2)	90
β/°	72.178(5)	113.104(3)	72.671(2)	91.071(3)	72.947(2)	90.987(3)
γ/°	77.266(5)	105.177(3)	77.004(3)	90	87.063(2)	90
V/ Å^3	1461.2(11)	634.41(11)	1441.05(18)	2818.9(4)	582.78(10)	2824.0(5)
Z	2	2	2	4	1	4
D_c/ g cm^{-3}	1.587	1.799	1.593	1.869	1.681	1.866
μ /mm^{-1}	1.708	1.965	1.731	1.578	0.998	1.575
F_{000}	706	348	692	1560	297	1560
θ range/°	1.7, 27.5	2.4, 27.5	2.2, 27.5	1.8, 27.5	4.6, 28.8	1.8, 27.5
Reflections Collected	51656	21504	14385	101028	20860	89746
Unique Reflections	6702	2904	6504	6490	5717	6488
Reflections $I > 2\sigma(I)$	5215	2728	5100	5706	5711	5413
R_{int}	0.060	0.072	0.063	0.0230	0.029	0.086
Goodness-of-Fit (F^2)	1.09	1.12	1.02	1.13	1.09	1.06
R_1 ($I > 2\sigma(I)$) [a]	0.0517	0.0400	0.0911	0.041	0.0149	0.0379
$wR_2(I > 2\sigma(I))$ [a]	0.1270	0.1061	0.2615	0.0646	0.0406	0.1048
Δρ min / max /e Å^3	-0.39, 0.86	-0.73, 1.34	-2.18, 2.01	-0.42, 0.70	-0.24, 0.19	-1.28, 1.25

[a] $R_1 = \Sigma \left| \left| F_o \right| - \left| F_c \right| \right| / \Sigma \left| F_o \right|$, $wR_2 = [\Sigma (w (F_o^2 - F_c^2)^2) / \Sigma w (F_o^2)^2]^{1/2}$

All the calculations and molecular graphics were done by SHELXL-2016/6,[41] PLATON v1.15,[42] WinGX system Ver-1.80,[43] Diamond v3.2, Mercury,[44] and TOPOS.[45,46] All the crystallographic data and structural refinement parameters for the compounds **1**, **1a**, **1′**, **2**, **2a**, and **2′** have been mentioned in Table 1.

3.3. RESULTS and DISCUSSION

3.3.1. Crystal Structure Description

Structural Description of {[$Zn_2(dim)_2(fum)_2$](H_2O)(MeOH)}$_n$ (1). Single-crystal X-ray analysis reveals that complex **1** is a 2D framework of Zn(II). It crystallizes in the triclinic space group P-1. The asymmetric unit of **1** comprises of two crystallographically independent Zn(II) metal centers (tetra-coordinated Zn1 and Zn2), three di(1H-imidazol-1-yl)methane ligands, four fumarates ligands, along with one guest water and methanol molecule. Each tetra coordinated Zn1 has a ZnO_2N_2 environment, which is surrounded by two oxygen atoms (O3 and O7) from two fumarate ligands, one pair of nitrogen atoms (N1 and N10^b) coming from two different fumarate ligands, composing a distorted tetrahedral geometry in all direction of the metal centre (Figure. 1a). The Zn1−O and Zn1−N distances around Zn1 are in between of 1.953(3)−1.984(4) and 1.993(3)−2.003(4) Å, respectively (Table 2). However, each tetracoordinated Zn2 has a ZnO_2N_2 environment, which is closed by two oxygen atoms (O2 and O5), from two acid linkers and two nitrogen atoms coming from two di(1H-imidazol-1-yl)methane linkers (N9^a and N5), composing a distorted tetrahedral geometry around the metal centre (Figure. 1a). Here the Zn2−O and Zn2−N bond lengths around Zn2 are in between of 1.940(3)−1.982(3) and 1.987(3)−2.025(3) Å, respectively (Table 2). All the bond angles surrounded Zn1 and Zn2 are in between of 100.60(12)°−114.37(11)° and 97.38(11)°−121.18(12)°, respectively (Table 2). Here one fumarate ligand bridges two different Zn(II) centers, Thus, both the geometrically similar Zn(II) centers join with each other via one di(1H-imidazol-1-yl)methane ligand to form a 1D chain (Figure. 1b). The di(1H-imidazol-1-yl)methane linkers connect the 1D metal−carboxylate sheets in a canted and criss-cross fashion to create a 2D arrangement (Figure. 1c) occupied by guest water and methanol molecules in *bc* plane. Total crystal structure has potential solvent accessible void volume of 239 Å^3 calculated using PLATON[42] which is 16.3% of the total crystal volume of 2414 Å^3.

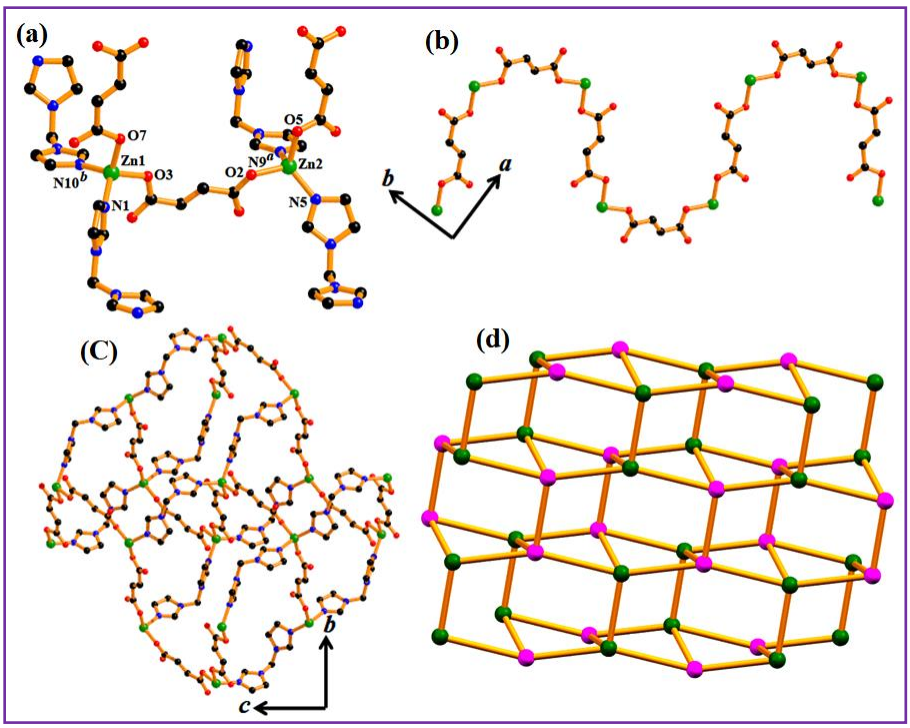

Figure 1. (a) Coordination environment around Zn(II) ions in **1**. Colors: tetracoordinated Zn1 (green) and Zn2 (green), C (gray), N (blue), O (red),. (b) The 1D chain constructed from Zn1 and Zn2 centers joined through fumarate ligands. (c) View of the 2D structure of **1** constructed by fumarate and dim linkers with Zn1 and Zn2 centers in bc plane. (d) Representation of the (4,4)-connected binodal net from TOPOS[45,46] of **1**

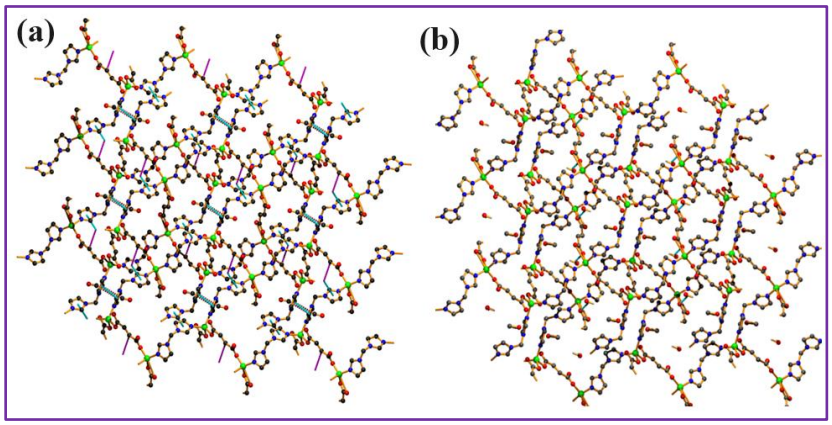

Figure 2. (a) Intermolecular π-π & C-H…π interactions in complex **1**, (b) Intermolecular H-bonding interactions in **1**

The 2D structure is further stabilized by intermolecular π−π and C−H…π interactions between imidazole rings and C-H bonds and imdazole rings respectively (Figure. 2a), forming a 3D network (Table 3). In the supramolecular structure, hydrogen bondings are

formed between hydrogen atoms of lattice water molecules and oxygen atoms of fumarate (Figure. 2b). In the framework, this hydrogen bonding in lattice water molecules given greater stabilization energy in comparison to the lattice methanol moieties, which are not stabilized by H-bonding (Table 4). Overall network analysis by using TOPOS[45,46] shows that the structure comprises of (4,4)-connected binodal diamonded nets, point symbol (Schlafli symbol) $\{4^2.6^4\}\{4^2.6^4\}$ (Figure. 1d).

Table 2. Selected Bond Lengths (Å) and Bond Angles (°) for complex **1**

Zn1-O3	1.953(3)	Zn2-O2	1.940(3)
Zn1 -O7	1.984(4)	Zn2-O5	1.982(3)
Zn1-N1	2.003(4)	Zn2-N5	1.987(3)
Zn1-N8^a	1.993(3)	Zn2-N4^c	2.025(3)
O3-Zn1-O7	100.60(12)	O2-Zn2-N5	114.99(11)
O3-Zn1-N1	111.83(12)	O2-Zn2-O5	97.38(11)
O3-Zn1-N8^a	108.74(13)	O2-Zn2-N4^c	106.16(11)
O7-Zn1-N1	108.34(13)	O5-Zn2-N5	121.18(12)
O7-Zn1-N8^a	112.14(12)	O5-Zn2-N4^c	106.47(11)
N1-Zn1-N8^a	114.37(11)	N4^c-Zn2-N5	109.23(14)

a = -1+x, y, 1+z , c =1+x, -1+y, z.

Table 3. Intermolecular π-π & C-H…π Interactions in Complex **1**

ring(i) → ring(j)	distance of centroid(i) from ring(j),(Å)	dihedral angle (i,j) (deg)	distance between the (i,j) ring centroids,(Å)
R(1)→R(1)^{i}	4.499(4)	0	3.259
R(2)→R(3)^{ii}	4.032(3)	4.2	1.985
R(3)→R(2)^{ii}	4.032(3)	4.2	2.169
C-H ring(j)	H...R distance (Å)	C-H...R angle (deg)	C...R distance (Å)
C(17)-H(17)→R(3)^{iii}	2.91	148	3.704(5)

Symmetry code: i = -X,1-Y,1-Z; ii = 2-X,1-Y,-Z; iii = 2-X,-Y,-Z;

R(i)/R(j) denotes the ith/jth rings in the corresponding structures: R(1) = N(1)/C(8)/C(9)/N(2)/C(10); R(2) = N(3)/C(12)/N(4)/C(23)/C(13); R(3) = N(7)/C(5)/C(24)/N(8)/C(6).

Table 4. Intermolecular H-bonding Interactions in **1**

D-H···A	D-H	H···A	D···A	∠D-H···A
O1W-H1WB···O5	0.96	2.11	2.897(7)	138

Structural Description of $\{[Zn(dim)(fum)](H_2O)\}_n$ (1a). Single-crystal X-ray analysis reveals that compound **1a** is a 2D framework of Zn(II) that crystallizes in the triclinic space group P-1. The asymmetric unit of **1a** comprises of Zn(II) metal center (tetracoordinated Zn1), two di(1H-

imidazol-1-yl)methane ligands, two fumarates ligands, along with one guest water molecules. Tetracoordinated Zn1 has a ZnO_2N_2 environment, which is surrounded by two oxygen atoms (O1 and O3) coming from two fumarate ligands, one pair of nitrogen atoms (N1 and N4^a) coming from two different di(1H-imidazol-1-yl)methane ligands, composing a distorted tetrahedral geometry (Figure. 3a). The Zn1−O and Zn1−N distances around Zn1 are in the ranges of 1.945(4)−1.965(3) Å and 2.026(4)−2.049(4)Å, respectively and the angles around Zn1 are in ranges of 103.83(16)°−117.94(14)° (Table 5). The fumarate linkers are linked by Zn(II) centers to form a 1D arrangement in *a* direction (Figure. 3b), which are linked by di(1H-imidazol-1-yl)methane linkers to form 2D sheet in *bc* plane (Figure. 3c) occupied by only guest water molecules.

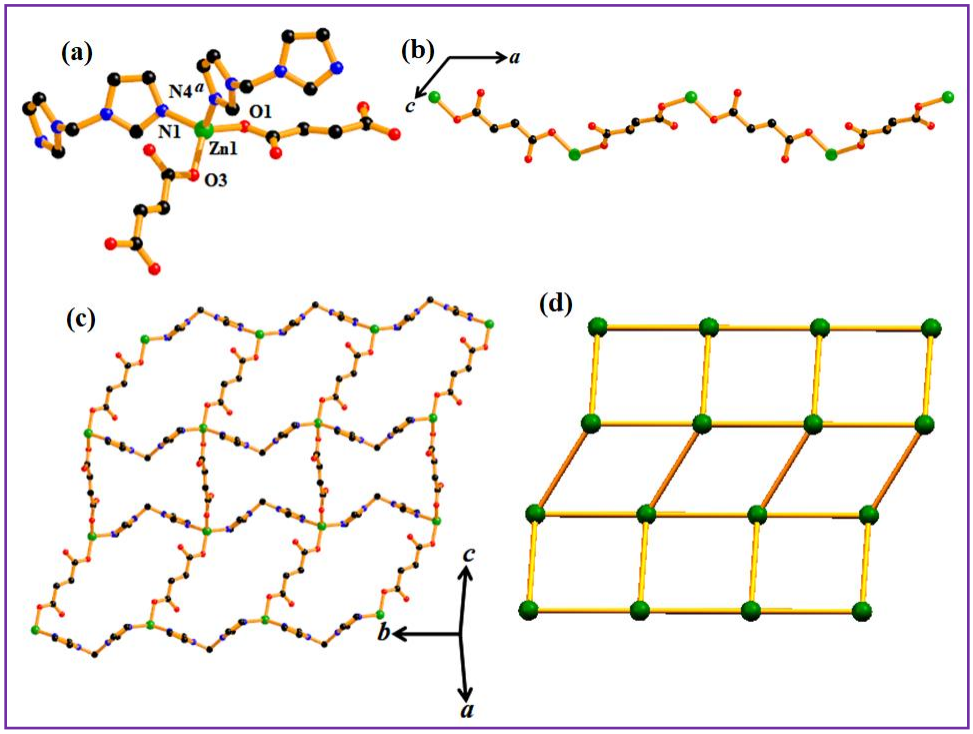

Figure 3. (a) Coordination environment around Zn(II) ion in **1a**. Colors: tetracoordinated Zn1 (green), C (gray), N (blue), O (red),. (b) View of the 1D chain constructed from Zn1 linked with fumarate linkers in *a* direction. (c) View of the 2D stair like structure of **1a** constructed by fumarate and dim linkers with Zn1 center. (d) Representation of the 4-connected uninodal net from TOPOS[45,46] of **1a**

Total potential solvent accessible void volume is 27 Å^3 calculated using PLATON,[42] which is 4.3% of the total crystal volume of 614 Å^3. Similar to **1** here also the 2D structure is stabilized by intermolecular π−π interactions and C−H…π interactions to form a supramolecular 3D framework (Figure 4a, Table 6). Hydrogen bonding also is also present here in similar fashion like **1** (Figure. 4b, Table 7), which further stabilizes the structure. Overall network analysis using TOPOS[45,46]

shows that the structure comprises of 4-connected uninodal square nets with the point symbol (Schlafli symbol) $\{4^2.6^4\}$ (Figure. 3d).

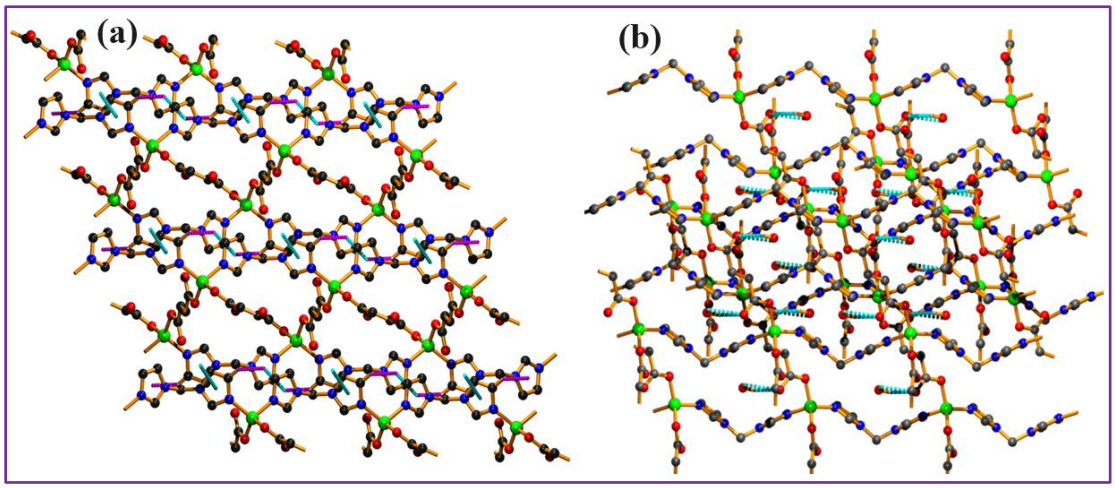

Figure 4. (a) Intermolecular π-π & C-H…π interactions in complex **1a**, (b) Intermolecular H-bonding interactions in **1a**

Table 5. Selected Bond Lengths (Å) and Bond Angles (°) for Complex **1a**

Zn1-O1	1.945(4)	Zn1-N1	2.026(4)
Zn1-O3	1.965(3)	Zn1-N4^b	2.049(4)
O1-Zn1-O3	117.94(14)	O1-Zn1-N1	110.24(17)
O1-Zn1-N4^b	103.83(16)	O3-Zn1-N1	109.97(16)
O3-Zn1-N4^b	105.84(16)	N1-Zn1-N4^b	108.40(15)

b = x, 1+y, z

Table 6. Intermolecular π-π & C-H…π Interactions in Complex **1a**

ring(i) → ring(j)	distance of centroid(i) from ring(j),(Å)	dihedral angle (i,j) (deg)	distance between the (i,j) ring centroids,(Å)
R(1)→R(1)^i	4.192(3)	0	1.903
R(2)→R(2)^{ii}	3.983(3)	0	1.816
C-H ring(j)	H...R distance (Å)	C-H...R angle (deg)	C...R distance (Å)
C(2)-H(2)→R(2)^i	2.92	137	3.660(5)

Symmetry code: i = 2-X,1-Y,1-Z; ii = 1-X,-Y,1-Z;

R(i)/R(j) denotes the ith/jth rings in the corresponding structures: R(1) = N(1)/C(1)/N(2)/C(3)/C(2); R(2) = N(3)/C(5)/C(6)/N(4)/C(11).

Table 7 Intermolecular H-bonding Interactions in Complex **1a**

D-H···A	D-H	H···A	D···A	∠D-H···A
O1W-H1WA···O2	0.85	2.52	2.87(3)	106
O1W-H1WB···O2	0.85	2.43	2.87(3)	112

Structural Description of {[$Cd_2(fum)_2(dim)_2(H_2O)$][(MeOH)}$_n$ (2). Complex **2** crystallizes in the monoclinic $P2_1/c$ space group (Z = 4) and the structural analysis reveals the formation of a polycatenated 2D+3D→3D pillared-layer framework structure. The asymmetric unit of **2** contains two crystallographically independent Cd(II) centers (Cd1 and Cd2). The five-coordinated Cd1 with CdO_3N_2 environment shows distorted trigonal bipyramidal geometry where the equatorial sites are occupied by three oxygen atoms ($O5^a$, $O6^b$ and O10) from three different fumarate ligands and two nitrogen atoms (N1 and $N10^c$) from two different dim linkers occupy the axial positions (Figure. 5a). However, the heptacoordinated Cd2 shows distorted pentagonal bipyramidal geometry with CdO_5N_2 environment (Figure. 5a). The equatorial positions of Cd2 are occupied by five oxygen atoms (O1, O2, $O3^a$, $O4^a$ and O1W) from two different fumarate and one water molecule, two nitrogen atoms (N5 and $N8^b$) from two different dim linkers occupy the axial positions (Figure. 5a). Selected bond angles and bond lengths are reported in Table 8.

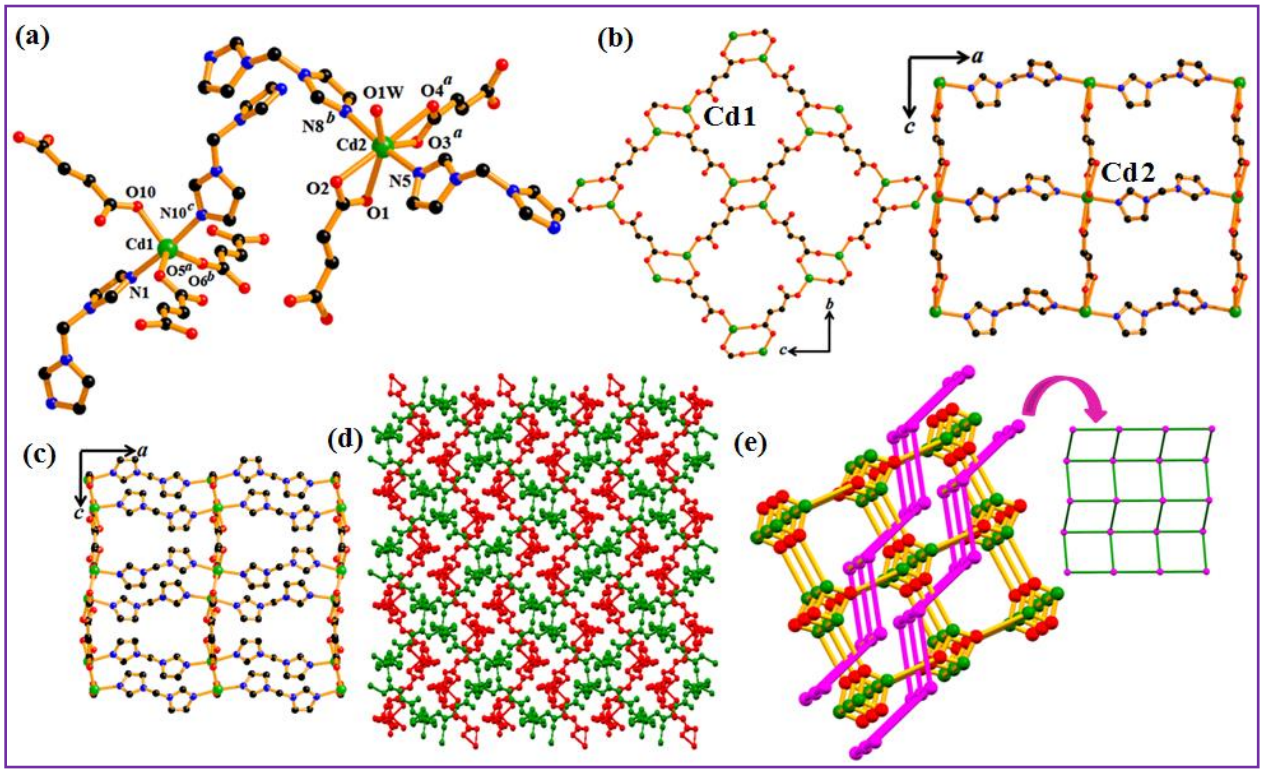

Figure 5. (a) Coordination environment around Cd(II) Colors: pentacoordinated Cd1 and heptacoordinated Cd2 (green), N (blue), O (red), C (gray). (b) View of the 2D sheet and 2D arrangement of Cd2 center. (c) View of the 3D arrangement of Cd1 center. (d) The overall 3D representation of **2**. (e) Topological representation[45,46] of of Cd1 and Cd2

In case of Cd1, each fumarate ligands connects the adjacent three Cd(II) centers by bis-chelation and mono oxo-bridging fashion to produce a planar metal-carboxylate 2D layer (Figure. 5b) in the

crystallographic bc plane, where carboxylate behave as 3-connected nodes (Figure. 5c). The linear dim linkers connect the 2D metal-carboxylate sheet to create a bi-pillared 3D structure (Figure. 5d). On the other hand, for Cd2, each fumarte ligand connects adjacent two Cd(II) centers through bridging bidented fashion to form almost linear 1D metal-carboxylate layer. These 1D layers are also coordinated by linear dim linkers to form a wavy 2D (Figure. 5b) structure in *ac* plane. 3D bi-pillared lattice and 2D wavy lattice for Cd1 and Cd2 are catenated to each other forming 2D+3D→3D polycatenated structure (Figure. 5d). The intermolecular π−π interactions and C−H…π interactions are in between imidazole rings and C-H bonds-imdazole rings respectively (Figure 6a, Table. 9) have also stabilizes the structure. Hydrogen bonding also formed here between hydrogen atoms of water and methanol molecules with oxygen atoms (Figure 6b, Table 10). Unlike **1** here the participation of hydrogen atom of water as well as methanol molecules, stabilizes both the solvents molecules in the crystal lattice. The structure of **2** is found to be microporous with total solvent accessible estimated void calculated using PLATON[42] of 207.0 $Å^3$ which is 7.3 % of the total crystal volume (2818 $Å^3$). The TOPOS[45,46] analysis reveals that the structure of **2** can be represented as a (3,5) connected bi-nodal net $\{4.6^2\}\{4.6^6.8^3\}$ and 4-c uniconnected uninodal net, point symbol $\{4^4.6^2\}$ (Figure. 5e) polycatenated net (Figure. 5e).

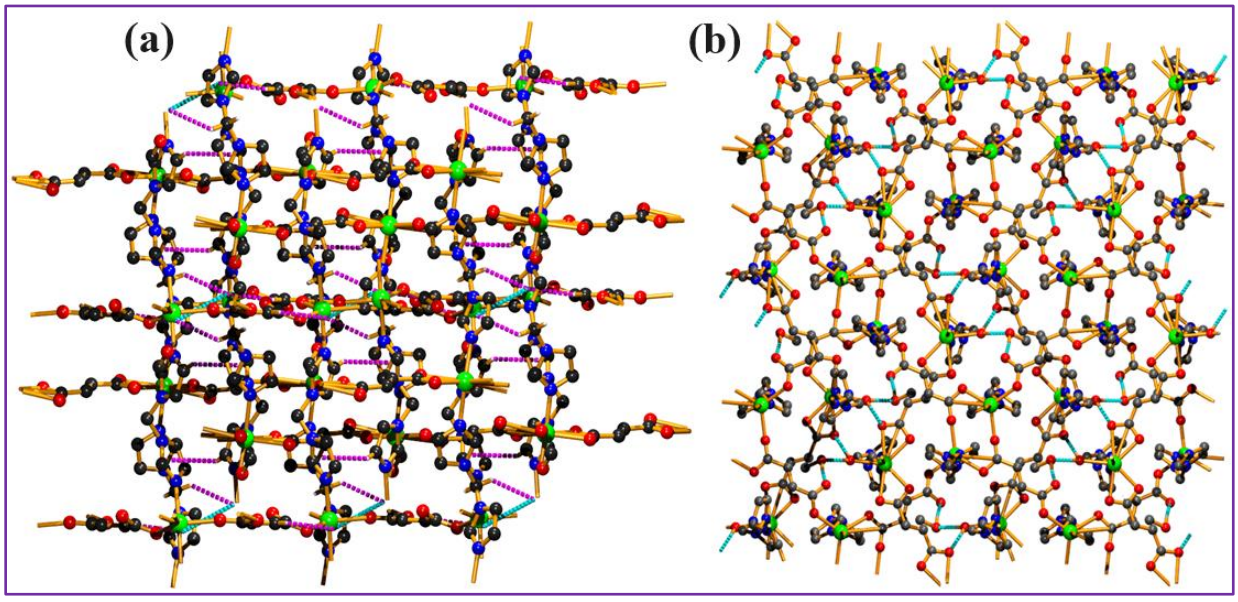

Figure 6. (a) Intermolecular π-π & C-H…π interactions in complex **2**, (b) Intermolecular H-bonding interactions in **2**

Table 8. Selected Bond Lengths (Å) and Bond Angles (°) for Complex **2**

Cd1-O10	2.252(2)	Cd2-O2	2.464(2)
Cd1-N1	2.256(2)	Cd2-N5	2.302(2)
Cd1-N10^{e}	2.252(2)	Cd2-O3^{c}	2.351(2)
Cd1-O5^{g}	2.268(2)	Cd2-N11^{a}	2.295(2)
Cd1-O6^{k}	2.287(3)	Cd2-O4^{c}	2.561(2)
O10-Cd1-N1	86.76(8)	Cd2-O1W	2.421(2)
O10-Cd1-N10^{e}	86.13(8)	Cd2-O1	2.360(2)
O5^{g} -Cd1-O10	118.62(9)	O1W-Cd2-O4^{c}	79.80(7)
O6^{k}-Cd1-O10	116.89(10)	O2-Cd2-N5	89.02(8)
N1-Cd1 -N10^{e}	171.75(9)	O2-Cd2-N11^{a}	91.45(8)
O5^{g} -Cd1-N1	91.91(8)	O2-Cd2-O3^{c}	139.72(7)
O6^{k} -Cd1-N1	87.46(10)	O2-Cd2-O4^{c}	166.75(7)
O5^{g}-Cd1-N10^{e}	95.16(8)	N5-Cd2-N11^{a}	166.73g(9)
O6^{k}-Cd1-N10^{e}	92.03(10)	O3^{c}-Cd2-N5	101.49(8)
O5^{g}-Cd1-O6^{k}	124.35(10)	O4^{c}-Cd2-N5	83.89(8)
O3^{c}-Cd2-N11^{a}	86.65(8)	O4^{c}-Cd2-N11^{a}	92.92(8)
O3^{c}-Cd2-O4^{c}	53.13(7)	O1W-Cd2-O3^{c}	131.89(7)
O1-Cd2-N11^{a}	102.03(8)	O1W-Cd2-O2	88.00(7)
O1W-Cd2-N5	80.41(8)	O1W-Cd2-N11^{a}	86.35(8)

a =-1+x, y, 1+z, *c* =1+x, -1+y, z.

Table 9. Intermolecular π-π & C-H…π Interactions in **2**

ring(i) → ring(j)	distance of centroid(i) from ring(j),(Å)	dihedral angle (i,j) (deg)	distance between the (i,j) ring centroids,(Å)
R(1)→R(1)^{i}	4.2485(19)	0	2.484
C-H ring(j)	H...R distance (Å)	C-H...R angle (deg)	C...R distance (Å)
C(20)-H(20)→R(1)^{ii}	2.86	159	3.726(3)
C(19)-H(19)→R(1)^{i}	2.72	140	3.526(4)
C(8)-H(8)→R(2)^{iii}	2.85	148	3.593(3)

Symmetry code: i = 3-X,-Y,-Z; ii = 2-X,1/2+Y,1/2-Z; iii = 2-X,-Y,1-Z;
R(i)/R(j) denotes the ith/jth rings in the corresponding structures: R(1) = N(7)/C(100)/C(131)/N(11)/C(102); R(2) = N(1)/C(1)/N(2)/C(2)/C(3).

Table 10. Intermolecular H-bonding interactions in complex **2**

D-H···A	D-H	H···A	D···A	∠D-H···A
O1W-H1WA···O1S	0.82	1.94	2.758(3)	177
O1S-H1S···O20	0.88	1.85	2.686(4)	157
O1W- H2WB···O4	0.78	2.05	2.834(3)	176

Structural Description of $\{[Cd(dim)_2(H_2O)_2](fum)(H_2O)_2\}_n$ (2a) The compound **2a** is a 1D framework of Cd(II) ions which is revealed from its X-ray structure. It crystallizes in the triclinic space group P-1. The asymmetric unit of **2a** comprises of hexacoordinated Cd(II) metal center (Cd1), four di(1H-imidazol-1-yl)methane ligands and two water molecules. Hexacoordinated Cd1 has a CdO_2N_4 environment, which is closed by two oxygen atoms (O1W and O2W^a) coming from two different water molecules, four pair of nitrogen atoms (N1, N1^a, N4^b and N4^c) coming from two different di(1H-imidazol-1-yl)methane ligands, composing a distorted octahedral geometry (Figure. 7a). The Cd1−O distances are 2.358(8) Å and 2.380(8) Å and Cd1−N distances around Cd1 are in the ranges of 2.303(6)−2.332(6)Å (Table 11). The angles around Cd1 are in ranges of 85.3(3)°− 177.7(2)° (Table 11). The dim linkers are dubly linked the Zn(II) centers to form a 1D chains running along the diagonal of *bc* plane (Figure. 7b). The fumarate linkers are arranged along the 1D chain in lattice without coordinating to the metal centers (Figure. 7c)

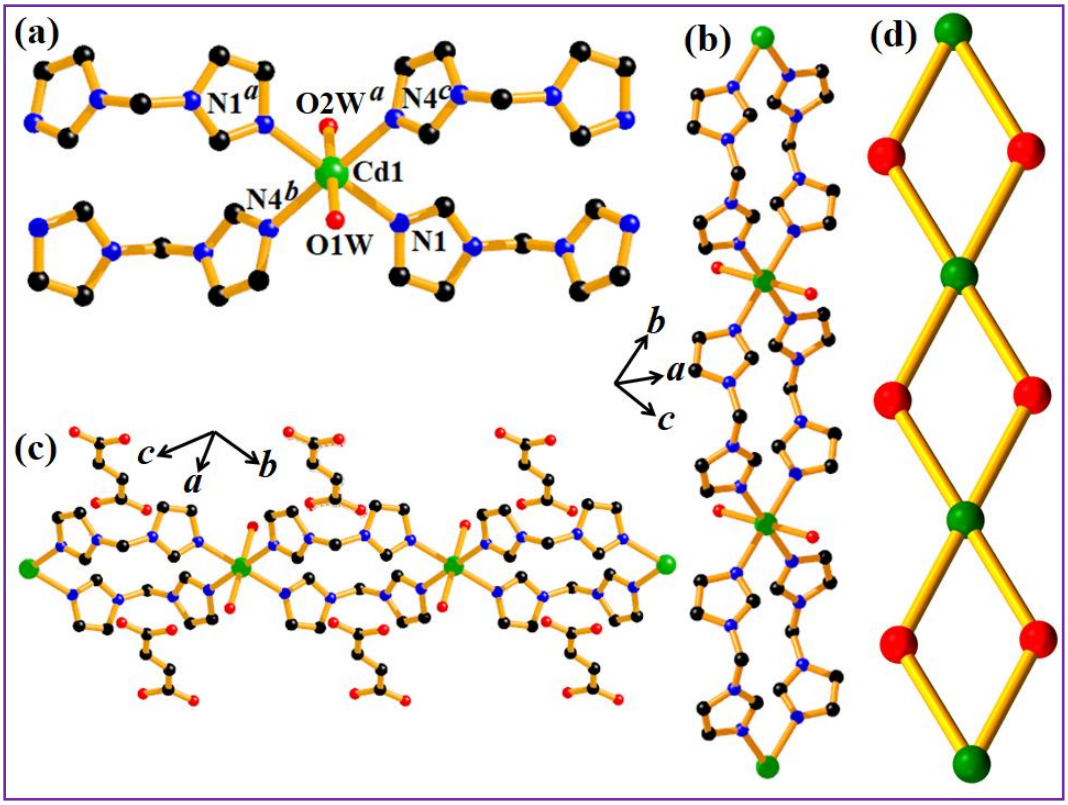

Figure 7. (a) Coordination environment around Cd(II) ion in **2a**. Colors: hexacoordinated Cd1 (green), C (gray), N (blue), O (red),. (b) View of the 1D chain constructed from Cd1 linked with di(1H-imidazol-1-yl)methane ligands. (c) View of the 1D chain structure of **2a** constructed by dim linkers surrounded by fumarate liners. (d) Schematic representation[45,46] of the 4,2-connected binodal net of **2a**

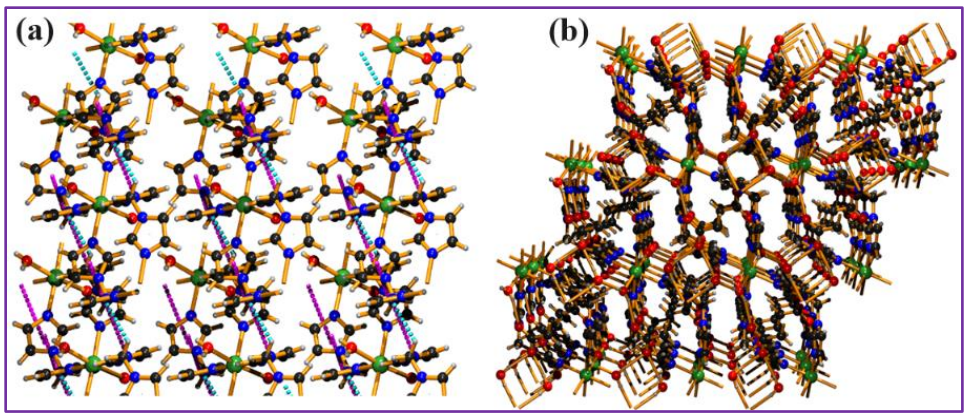

Figure 8. (a) Intermolecular π-π & C-H…π interactions in complex **2a**, (b) Intermolecular H-bonding interactions in **2a**

Table 11. Selected Bond Lengths (Å) and Bond Angles (°) for Complex **2a**

Cd1-O1W	2.358(8)	Cd1-O2W	2.380(8)
Cd1-N1	2.327(6)	Cd1-N5	2.332(6)
Cd1-N4^b	2.303(6)	Cd1-N8^b	2.303(9)
O1W-Cd1-O2W	173.9(3)	O1W-Cd1-N1	94.3(3)
O1W-Cd1-N5	87.4(2)	O1W-Cd1-N4^b	91.3(2)
O1W-Cd1-N8^b	87.9(3)	O2W-Cd1-N1	89.6(3)
O2W-Cd1-N5	88.1(2)	O2W-Cd1-N4^b	93.2(2)
O2W-Cd1-N8^b	88.4(3)	N1-Cd1-N5	86.0(2)
N1-Cd1-N4^b	93.9(2)	N1-Cd1-N8^b	177.7(2)
N4^b-Cd1-N5	178.7(2)	N5-Cd1-N8^b	94.9(3)
N4^b -Cd1-N8^b	85.3(3)		

b = x,1+y,-1+z.

Table 12. Intermolecular π-π & C-H…π Interactions in **2a**

ring(i) → ring(j)	distance of centroid(i) from ring(j),(Å)	dihedral angle (i,j) (deg)	distance between the (i,j) ring centroids,(Å)
R(1)→R(4)^{i}	3.560(5)	1.6	1.443
R(2)→R(3)^{ii}	4.151(5)	2.2	2.366
C-H ring(j)	H...R distance (Å)	C-H...R angle (deg)	C...R distance (Å)
C(11)-H(11B)→R(2)^{iii}	2.85	118	3.414(9)

Symmetry code: I= X,Y,-1+Z, ii= X,-1+Y,Z, iii= X,1+Y,Z.

R(i)/R(j) denotes the ith/jth rings in the corresponding structures: R(1) = N1/ C1/N2/C3/C2 ; R(2) = N3/C5/ N4/ C7/ C6; R(3) = N5/ C8/C10/N6/C9; R(4) = N7/C12/C14/ N8/C13.

Table 13. Intermolecular H-Bonding Interactions in Complex **2a**

D-H···A	D-H	H···A	D···A	∠D-H···A
O2W --H2WA···O1	0.73(3)	2.03(3)	2.734(11)	160(4)
O2W --H2WB···O4W	0.77(3)	1.98(3)	2.745(12)	169(4)
O4W --H4WA···O2	0.83(3)	1.93(3)	2.750(10)	178(3)
O4W --H4WB···O4	0.87(4)	2.04(4)	2.888(11)	167(3)

The 1D structure is also stabilized by intermolecular π−π interactions and C−H…π interactions between imidazole rings and C-H bonds-imdazole rings respectively (Figure. 8a), forming a 2D arrangement (Table 11). Hydrogen bonding is formed between hydrogen atoms of water molecules and oxygen atoms (Figure 8b) of acidic ligand to hydrogen atom of dim ligands, which stabilizes the solvents molecules and fumarate in the lattice, forming a supramolecular 3D structure (Table 12). The network analysis using TOPOS[45,46] shows that the structure comprises of 4-connected and 2-connected binodal nets with the point symbol (Schlafli symbol) $\{4^2.6^4\}$ (Figure. 7d).

3.3.2. Powder X-ray Diffraction (PXRD) Analysis and Thermal Framework Stability

To ensure the phase purity of the bulk materials to the simulated pattern of crystals, powder X-ray diffraction (PXRD) experiments have been carried out at room temperature (25 °C) using the as-synthesized powder samples of **1**, **1a**, **1′** (**1′** i.e. **1**) and **2**, **2a**, **2′** (**2′** i.e. **2**) depicted in Figure 9. Good resemblance of all the peak positions with their analogous simulated patterns, which indicates the phase purity of all the as-synthesized form of all the compounds (Figure 9a, 9b). The PXRD pattern of **1a** showed completely different peak positions compared to PXRD pattern of complex **1**. Interestingly, **1a** comes back into the mother form (**1′** i.e. **1**) upon dipping it in MeOH for 30 minutes, indicating low energy involvement in the reversible transformation, which has been further confirmed by single crystal analysis as well as fluorescence spectra study of **1′**. The above resolvated form **1′** shows identical peak positions with the PXRD pattern of its mother form **1**, proving framework flexibility and reversibility in solid state structural transformation. In case of **2**, the as-synthesize PXRD pattern showed resembles of peak positions compared to stimulated PXRD pattern, indicates the bulk purity. Similarly for compound **2a** also has similar PXRD pattern of stimulated and as-synthesized forms. Unlike the previous case, **2a** comes back into the mother form of **2′** (i.e., **2**) upon dipping it in MeOH:H_2O (1:1) for 7 days, indicating reversible transformation, which is confirmed by single crystal analysis as well as fluorescence spectra study of **2′**. Therefore the framework of **2** is more rigid towards the reversible transformation and that is due to the larger Cd(II) metal ion and polycatenated structure of **2**. To through some more light into the temperature dependent transformation of **1** and **2** variable temperature (30°C to 150°C) PXRD studies have been performed with the as-synthesized crystals of **1** and **2** (Figure 10a, 10b). The VTPXRD pattern of as-synthesized powder sample of complex **1** (Figure 10a)**,** shows exactly similar peak position with the simulated pattern up to 45°C. At 60°C, due to the complete

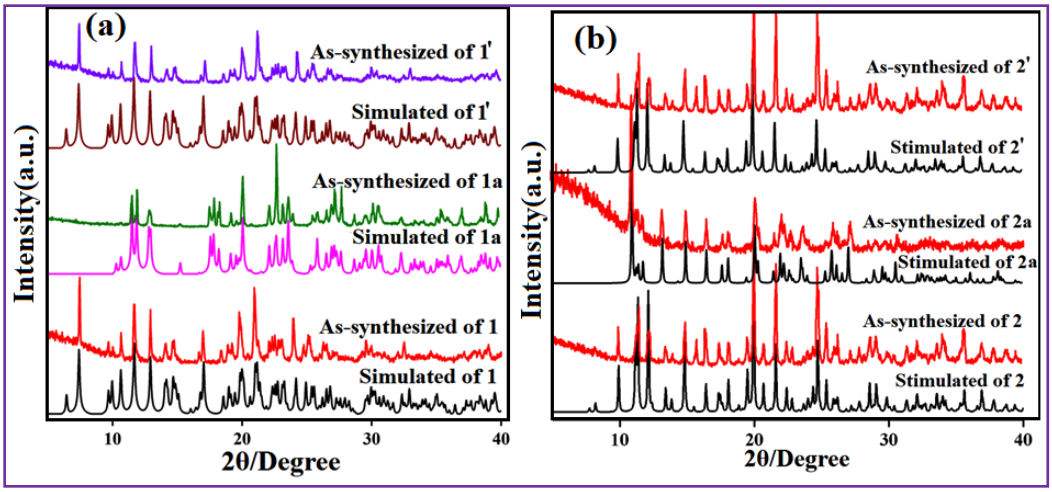

Figure 9. (a) PXRD pattern of complexes **1**, **1a** and **1′** in different phase. (b) PXRD pattern of complexes **2**, **2a** and **2′** in different phase

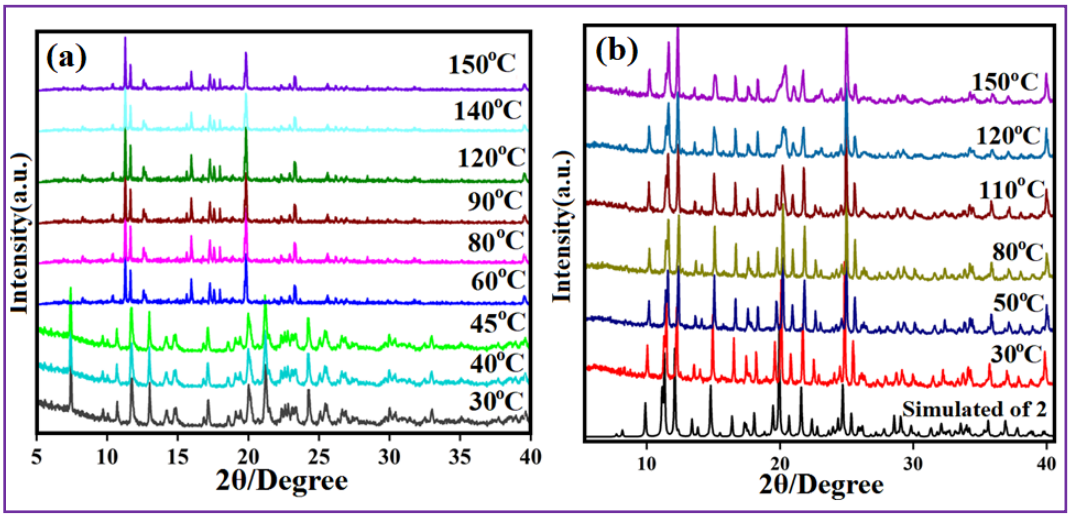

Figure 10. (a) VTPXRD of complex **1** (b) VTPXRD of complex **2**

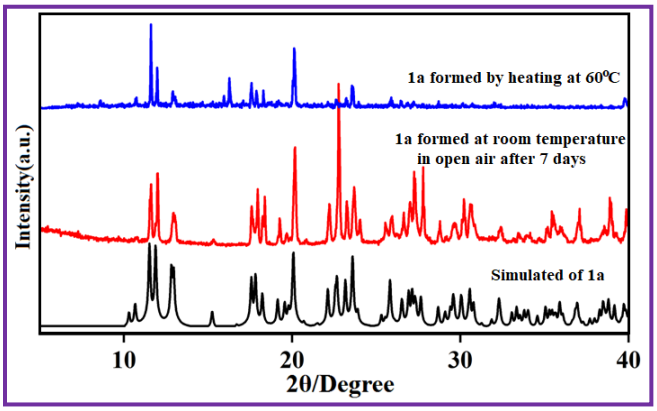

Figure 11. Comparison of PXRD pattern of simulated form, formed in open air at room temperature and formed by heating at 60°C of complex **1a**

elimination of lattice methanol molecules complex **1** transform to complex **1a** and remains same up to 150 ^{o}C. The PXRD pattern of transformed structure of **1** in open atmosphere at room temperature after 7 days has also the similar peak position with the transformed structure obtained through heating at 60^{o}C (Figure 11). VTPXRD pattern of **2** exhibits an identical peak position to their resembling as-synthesized PXRD pattern upto 110°C of the mother form (Figure 10b), indicates the framework stability after complete removal of all guest methanol molecules. A change in VTPXRD pattern has been observed at 120°C, which indicates the release of coordinated water molecules.

Thermogravimetric analysis (TGA) of the complexes **1** (Figure. 12a), **2** (Figure. 12b), **1a** (Figure. 12c) and **2a** (Figure. 12d) have been performed at the temperature range 30−600 °C with a heating rate of 5 °C min^{-1}. The TGA data of complex **1** shows 3% weight loss within the temperature range of 45^{o}C to 60^{o}C due to the loss of lattice methanol molecules, which influences the rearrangement of the framework to **1a**, which has been corroborated by VTPXRD data. After that, in the temperature range of 80^{o}C to 120^{o}C, weight loses for elimination of lattice water from the framework. The framework stable up to 300^{o}C, after that collapsed into unknown products.

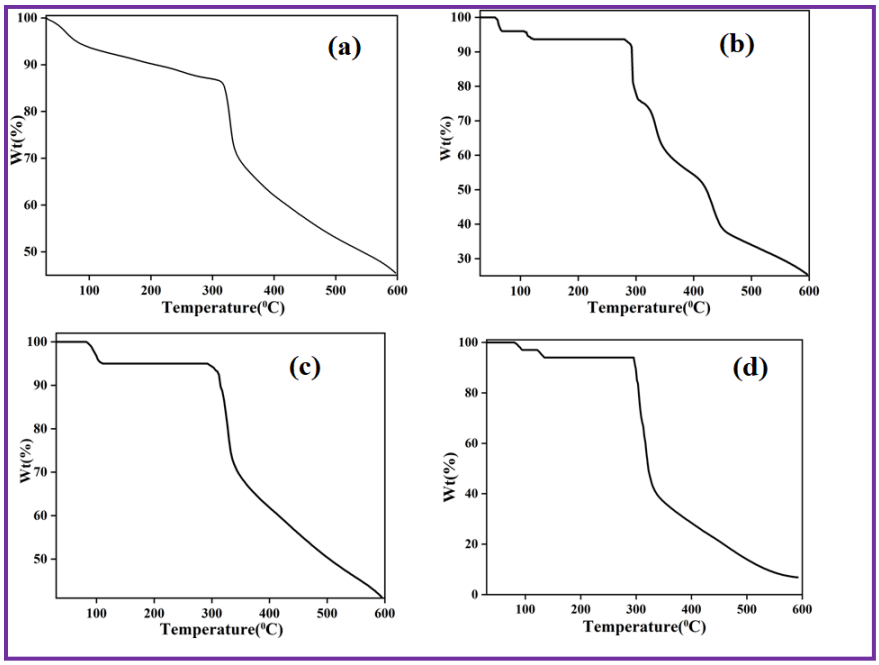

Figure 12. TGA of (a) Complex **1** (b) Complex **2** (c) Complex **1a** (d) Complex **2a**

Complex **2** shows two weight losses at 70°C and 112°C. At 70°C, 4% weight loss shows for stabilized lattice methanol water, and 3.2% weight loss happens for coordinated one water molecule per asymmetric unit. The framework then collapses into an unidentified product at

280°C. It has been observed that complex **1a** shows a weight loss of 5% (calcd. 5.3%) at 95°C for the loss of one strongly hydrogen bonded lattice water molecule per asymmetric unit. The dehydrated framework was stable up to 300°C like **1**; after that it collapsed into an unidentified product upon further heating. For complex **2a**, two loses (3% each) are observed at 80°C and 120°C for lattice and coordinated water molecules, completely collapses at 300°C like **2**.

3.3.3 FT-IR and Uv-Vis Spectroscopy Study

FT-IR spectra of complexes **1**, **1a**, **1′**, **2**, **2a**, and **2′** (Figure 13) have been studied in KBr pellet. The pinch of solid sample of crystal puts in a mortar pastel with the pinch of dry KBr, paste the mixture to powder, forms a transparent KBr plate, through which the radiate passes with in the ranges of 4000cm^{-1} to 400cm^{-1}. UV-visible spectroscopy of complexes **1**, **1a**, **1′**, **2**, **2a**, **2′** and di(1H-imidazol-1-yl)methane have been measured in reflectance mode with integrating sphere attachment instrument. The solid sample of crystal puts in a holder with specific quartz attached, transfers Uv-vis radiation within ranges of 200nm to 500nm through the sample. The absorption maxima have been observed at 330nm wavelength for compound **1**, **1a**, and **1′**. The absorption maxima of compound **2**, **2a**, and **2′** and have been observed at 300nm, 340nm and 300nm wavelength respectively (Figure 14).

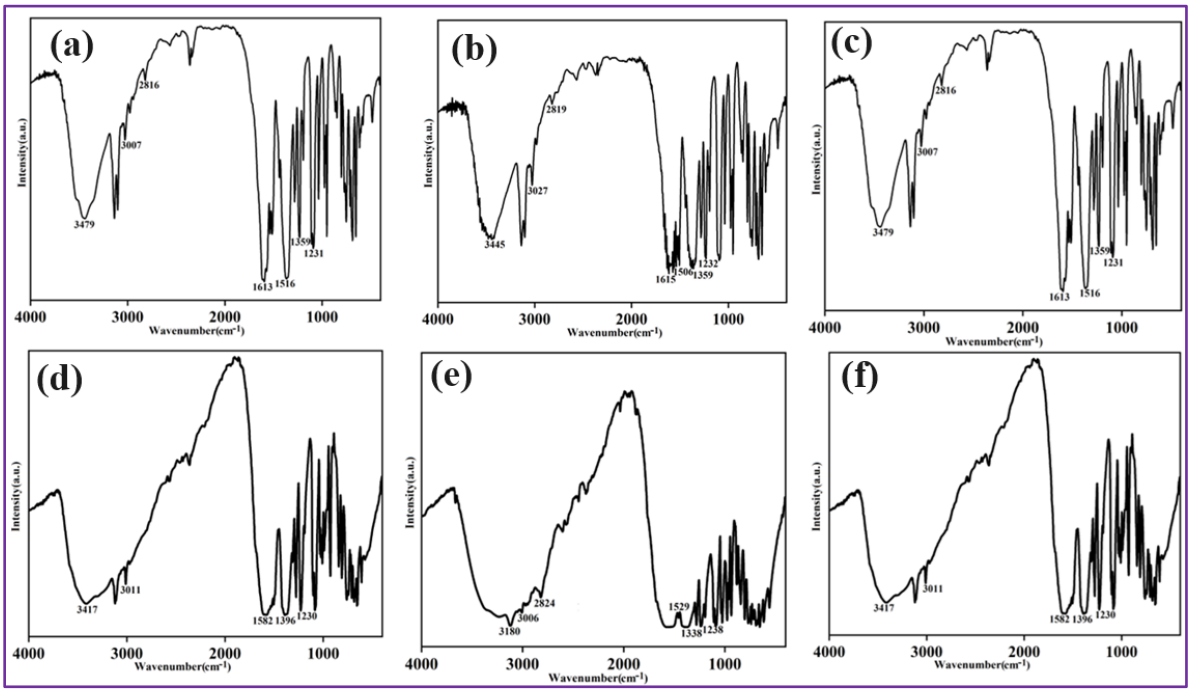

Figure 13. (a) IR of complex **1** (b) IR of complex **1a** (c) IR of complex **1′** (d) IR of complex **2**. (e) IR of complex **2a**. (f) IR of complex **2′**

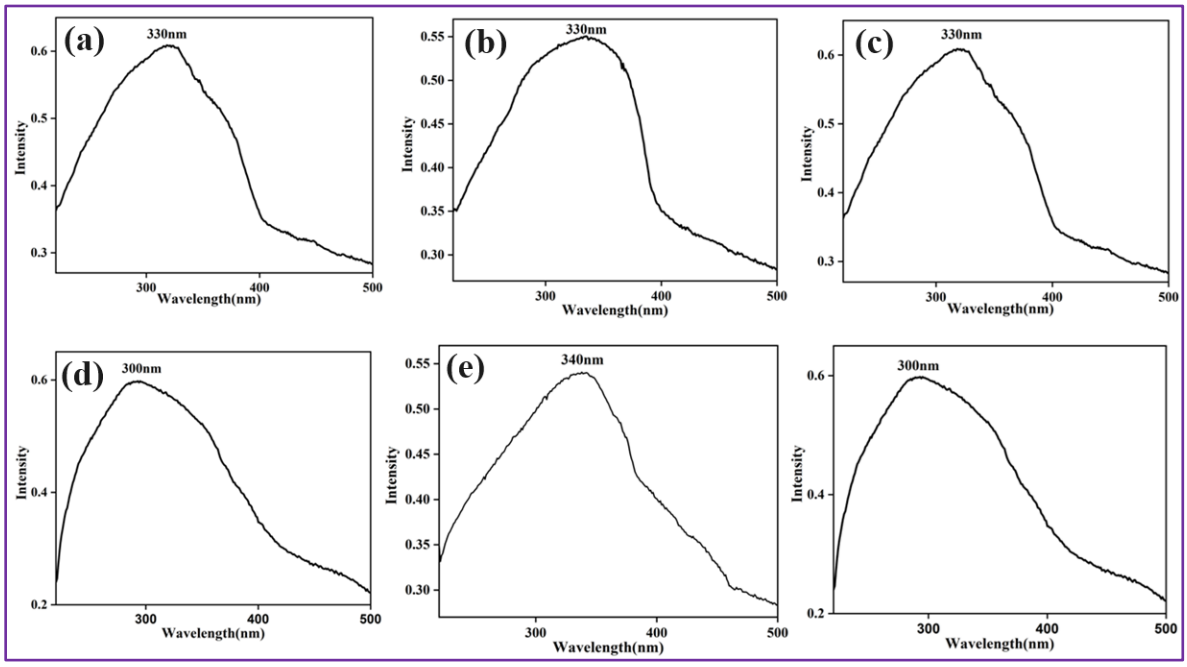

Figure 14. Uv-Vis spectra of (a) Complex **1** (b) Complex **1a** (c) Complex **1′** (d) Complex **2**. (e) Complex **2a**. (f) Complex **2′**

3.3.4. Discussion for Reversible Structural Transformation

Transformations of coordination polymers are commonly divided into two types, namely, solid-state structural transformation (SSST)[11-13] and dissolution–recrystallization structural transformation (DRST),[30] Single-crystal-to-single-crystal (SCSC)[11-13,15] transformations are one kind of common transformation in SSST, sustaining the macroscopic integrity during reactions. Complex **1** contains weakly bound methanol molecules at lattice position, undergoes selective solvent (methanol) induced structural transformation to shrunk single crystal of complex **1a** at room temperature (25°C) by molecular rearrangement in solid state. This selective solvent elimination occurs may be due to weekly interacted methanol solvent than lattice water molecules which involves in intermolecular hydrogen bonding interaction with the framework structure. Also, this transformation occurs by heating of complex **1** at 60^{o}C for 5 minutes. Interestingly this converted complex **1a** returns back to mother complex **1** when soaked with methanol for 30 minutes, suggests from luminescence. This low energy reversible transformation indicates the flexible nature of complex **1** and **1a**. This is a case of selective solvent induced reversible single crystal to single crystal transformation occurs at room temperature in 2D framework between squeezed and uncompressed structure. On the other hand, complex **2** shows dissolution–

recrystallization structural transformation (DRST), resulting from slow evaporation of methanol molecules from reaction medium, which changes the 3D polycatenated framework to 1D chain **2a**. This is possibly due to the fact that in increased of the concentration of all the constituents, the flexible N,N′-donor shows greater binding ability towards metal centers than the dicarboxylate. This results the formation of 1D chain, which has fumarate linkers in the lattice. On addition of methanol to the aforesaid concentrated reaction mixture reverts the 1D chain to the 3D polycatenated framework, as the reaction condition is also reverted back.

3.3.5. Sorption Measurements

Due to the high thermal stability for both the complexes **1a** and **2**, the sorption experiment was performed for different gases (e.g., N_2 and H_2 at 77 K and CO_2 at 195 K). The dehydrated framework of **1a** shows no residual solvent accessible voids or pore channel with considerable dimension. So, it is quite obvious to exhibit a negligible amount (up to ~6 mL/g at 77 K and 1 bar pressure) (Figure. 15a) of adsorption for large-sized N_2 gas molecules (kinetic diameter of N_2 = 3.6 Å). A similar trend is also observed for CO_2 sorption which is almost negligible (at 195 K and 1 bar pressure). The H_2 sorption experiment shows surface adsorption with a total uptake up to 27 mL/g at 77 K and 1 bar pressure (Figure. 15a), which is relatively high. This is possibly due to adheration of tiny H_2 over the 2D surface and possible coordination of dihydrogen to the coordinately unsaturated Zn(II).[47] This is further supported by the high pressure H_2 gas adsorption showing fewer uptakes than the ambient pressure study which indicates the non adheration of H_2 over 2D surface at high pressure (Figure 16a). The desolvated framework of **2** exhibits a lower N_2 adsorption 10 mL/g at $P/P_0 \approx 0.99$ and also shows a negligible CO_2 sorption (Figure. 15b). It exhibits appreciably high H_2 adsorption with a maximum value of 44 mL/g at 77 K 1 bar of pressure (Figure. 15b). The high uptake for H_2 compare to compound **1a** may be attributed to the opening of the polycatenated nets due to the structural transformation of **2** as discussed above. In addition to that, formation of open coordination site upon desolvation, may also acts for greater H_2 sorption. Hence, it clearly reveals that the optimum opening of the polycatenated[32-34] framework occurs when it was degassed at 70°C. The reported GCMC simulation[48,49] reveals that the small pores created by catenation play an active role in confining the H_2 molecules more closely, indicating that the catenated MOFs have higher H_2 uptake than the non-catenated MOFs at low pressure. However, the high pressure H_2 adsorption[31-33] study shows comparatively less uptake of H_2 due to partial breakdown of the structures at 10 bar (Figure16b). This is further

supported by the PXRD pattern of **2** after high-pressure sorption measurement, showing fewer peaks having lesser intensity compared to the PXRD pattern taken after ambient pressure H_2 adsorption measurement (Figure 16c).

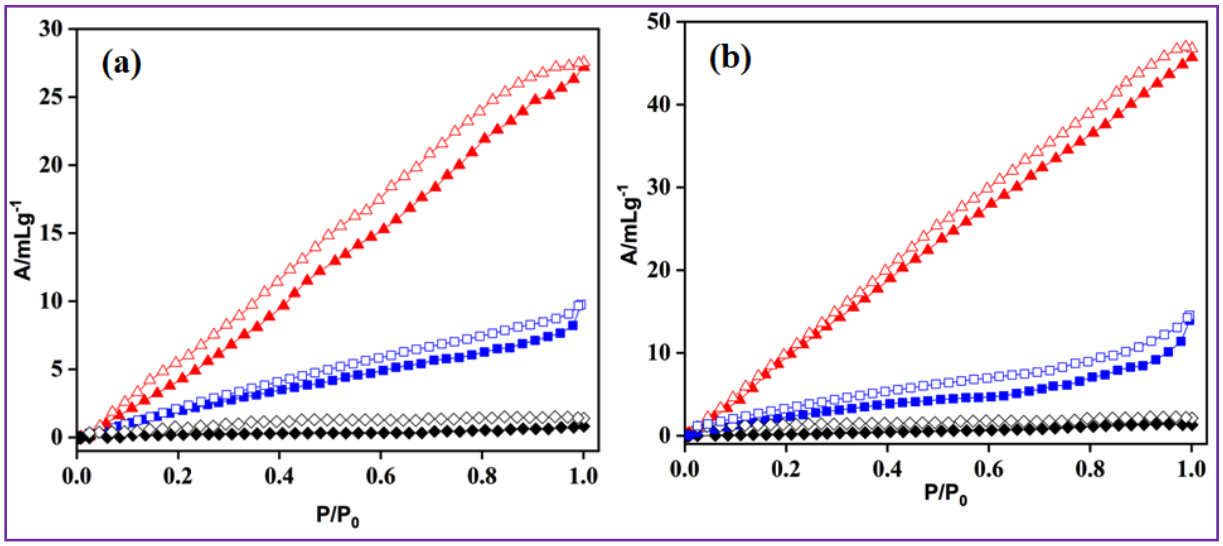

Figure 15 (a) Gas adsorption plot of complex **1a**, H_2 (Red), N_2 (blue), CO_2 (black). (b) Gas adsorption plot of complex **2**, H_2 (Red), N_2 (blue), CO_2 (black).

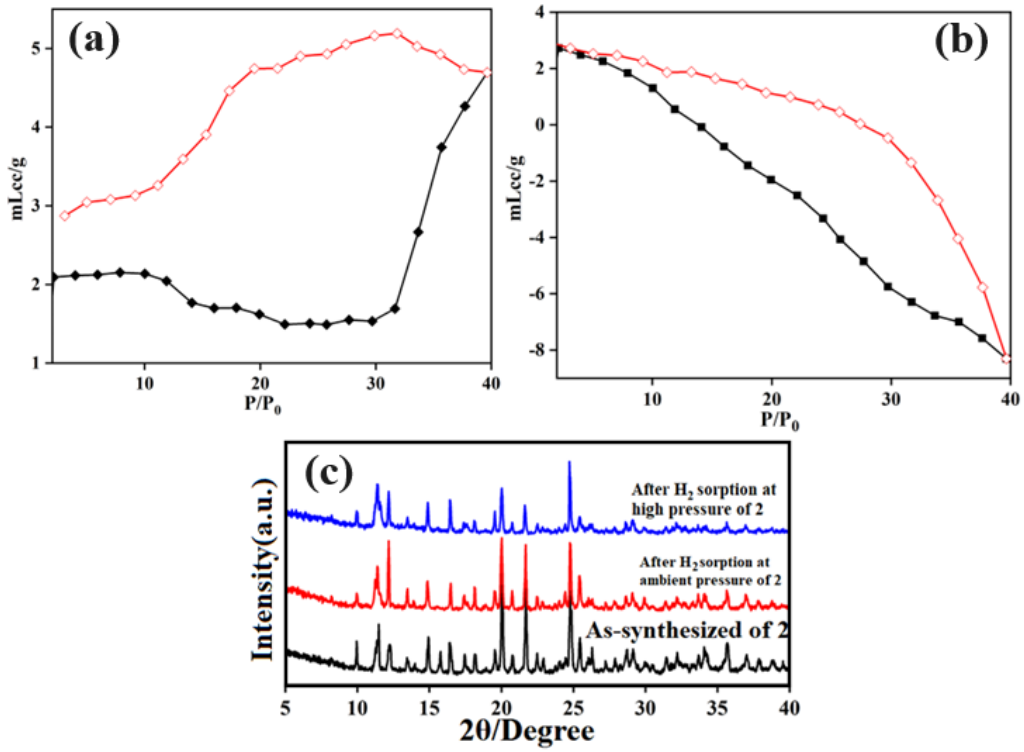

Figure 16. (a) High pressure gas adsorption of complex **1a**, (b) **2**, (c) PXRD pattern of complexes **2** after H_2 sorption

3.3.6. Luminescence Study.

Optical properties of MOFs with d^{10} metal centers and recent successful use of them in various applications[34-36] have brought them one more time under the spotlight of interest of researchers. Liquid state photoluminescence study of the d^{10} complexes **1** and **1a** (Figure. 17a) were performed at room temperature. The compound **1** and **1a** in ACN show emission maxima at 363 nm (λex = 330 nm) and 452 nm (λex = 330 nm) (Figure. 17a). After adding few drops of methanol in ACN solution of compound **1a**, PL data has been collected within 2 minutes, similar emission maxima have been observed, but after 30 minutes later the emission spectra change to spectra of compound **1′**, emission maxima 363 nm (λex = 330 nm).

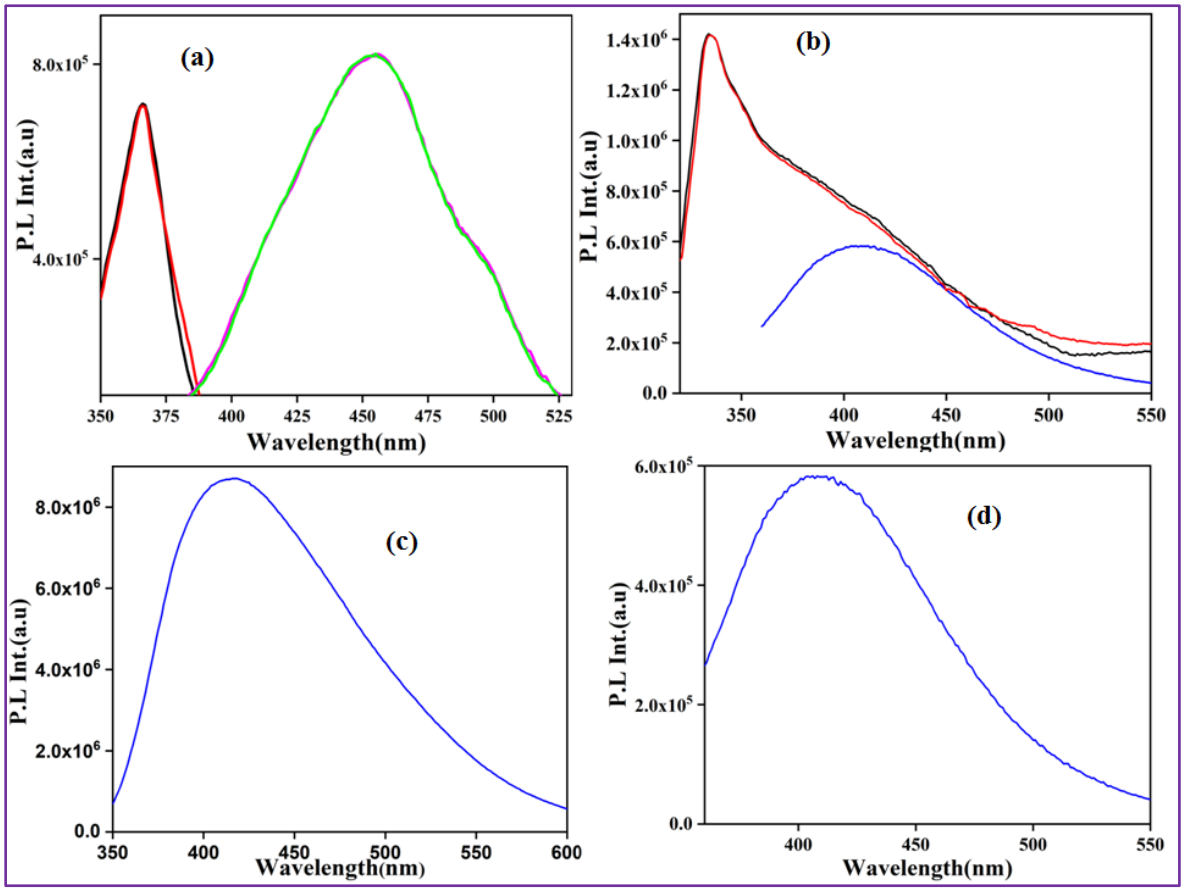

Figure 7. (a) Emission spectra of complex **1** in ACN solvent (black), complex **1a** in ACN solvent (purple), complex **1a** in ACN with few drops of methanol within 2 minutes (cyan), complex **1a** in ACN with few drops of methanol after 30 minutes (red). (b) Emission spectra of complex **2** in ACN solvent (black), complex **2a** in ACN solvent (blue), complex **2′** in ACN solvent (red). (c) Emission spectra of di(1H-imidazol-1-yl)methane in ACN solvent (blue). (d) Emission spectra of complex **2′** in ACN solvent (blue).

It indicates the structural change from compound **1a** to **1′**. Since the d^{10} metal ions are difficult to be reduced or oxidized there is less possibility for the metal-associated MLCT/LMCT charge transfer[34,35] to occur. Thus, the emission property of these compounds may be allocated primarily to the intraligand charge transition (ILCT) and ligand-to-ligand charge transfer (LLCT). Similarly, fluorescence spectra of complex **2, 2a** (Figure 17b) have been studied in ACN solvent, emission maxima at 340 nm (λex = 300 nm) and at 420 nm (λex = 300 nm) observed. N,N'- donor di(1H-imidazol-1-yl)methane ligand shows fluorescence spectra, emission maxima at 410 nm (λex = 320 nm) (Figure 17c).

3.4. CONCLUSION

Herein, compounds **1** and **2** showed reversible structural transformation through solid state SCSC and DRST respectively, induced by lattice methanol solvent molecules. Precisely, structural flexibility of complex **1** helped to reorganize the metal centers after elimination/addition of methanol molecules, exhibits a low energy structural transformation. It shows a rare reversible 2D to 2D SCSC transformation by squeezing a bulky 2D framework to a wavy 2D framework. On the contrary **2**, due to its framework rigidity, exhibit a reversible DRST from 3D to 1D framework by elimination/addition of methanol molecules. Interestingly, the addition of methanol in 1D framework of **2a** results a transformation into higher dimensional 3D framework and the said transformation is truly reversible. Clearly, it indicates the flexibility of the frameworks that help to transform in solid state and their rigidity bounds to transform in solvent by de-coordination and re-coordination process. Luminescence study in ACN and MeOH solvent also supports the structural transformation of the frameworks, hence the structural dynamism of the frameworks as well. Gas sorption study was found interesting, particularly the study with hydrogen gas. The hydrogen uptake in case of polycatenated 3D framework **2″** is much higher in comparison to the non-catenated 2D framework of **1a**. In a nutshell, the meticulous monitoring of these two different types of crystalline structural transformation will definitely help to understand different factors behind the complicated structural transformation in MOF. In addition to that, this work also reiterates the positive role of polycatenation and 3D structure for enhanced hydrogen uptake, for their prospective use in hydrogen storage.

REFERENCES

1. Chakrabarty, R.; Mukherjee, P. S.; Stang, P. J. *Chem. Rev.* **2011**, *111*, 6810–6918.
2. Halder, A. Ghoshal, D. *CrystEngComm* **2018**, *20*, 1322-1345.
3. Halder, A.; Maiti, A.; Dinda, S.; Bhattacharya, B.; Ghoshal, D. *Cryst. Growth Des.* **2021**, *21*, 6110−6118.
4. Kanoo, P.; Haldar, R.; Reddy, S. K.; Hazra, A.; Bonakala, S.; Matsuda, R.; Kitagawa, S.; Balasubramanian, S.; Maji, T. K. *Chem. Eur. J.* **2016**, *22*, 15864-15873.
5. Wu, Y.-N.; Li, F.; Zhu, W.; Cui, J.; Tao, C.-A.; Lin, C.; Hannam, P. M.; Li, G. *Angew. Chem.* **2011**, *123*, 12726–12730.
6. Peng, L.; Yang, S.; Jawahery, S.; Moosavi, S. M.; Huckaba, A. J.; Asgari, M.; Oveisi, E.; Nazeeruddin, M. K.; Smit, B.; Queen, W. L. *J. Am. Chem. Soc.* **2019**, *141*, 12397–12405.
7. Jiang, H.–L.; Xu, Q. *Chem. Commun.* **2011**, *47*, 3351-3370
8. Cui, Y.; Yue, Y.; Qian, G.; Chen, B. *Chem. Rev.* **2012**, *112*, 1126-1162.
9. Basu, O.; Mukhopadhyay, S.; Laha, S.; Das, S. K. *Chem. Mater.* **2022**, *34*, 6734–6743.
10. Sahoo, R.; Mondal, S.; Mukherjee, D.; Das, M. C. *Adv. Funct. Mater.* **2022**, *2207197*, 1-74.
11. Vittal, J. J. *Coord. Chem. Rev.* **2007**, *251*, 1781-1795.
12. Suh, M. P.; Cheon, Y. E. *Aust. J. Chem.* **2006**, *59*, 605-612.
13. Halder, G. J.; Kepert, C. J. *Aust. J. Chem.* **2006**, *59*, 597-604.
14. Takaoka, K.; Kawano, M.; Tominaga, M.; Fujita, M. *Angew. Chem. Int. Ed.* **2005**, *117*, 2189-2192.
15. Notash, B.; Rodbari, M. F.; Gallo, G.; Dinnebier, R. *Inorg. Chem.* **2021**, *60*, 9212−9223.
16. Kawano, M.; Fujita, M. *Coord. Chem. Rev.* **2007**, *251*, 2592-2605.
17. Nihei, M.; Han, L. Q.; Oshio, H. *J. Am. Chem. Soc.* **2007**, *129*, 5312-5313.
18. Park, J.; Koo, J. Y.; Choi, H. C. *Inorg. Chem.* **2021**, *60*, 5376−5382.
19. Li, X.–H.; Liu, Y.; Lin, H.–Y.; Xu, N.; Zhang, Z.; Liu, G.–C.; Wang, X.–L. *Cryst. Growth Des.* **2022**, *22*, 3845−3852.
20. Qian, J.–L.; Zhou, T.; Lu, X.; Xu, H.; Sun, J.–Y.; Zhang, C.–L.; Zheng, H.–G. *Inorg. Chem.* **2022**, *61*, 47−51.
21. Li, L.; Ma, H.; Zhang, J.; Zhao, E.; Hao, J.; Huang, H.; Li, H.; Li, P.; Gu, X.; Tang, B. Z. *J. Am. Chem. Soc.* **2021**, *143*, 3856−3864.
22. Pang, J.; Wu, M.; Qin, J.–S.; Liu, C.; Lollar, C. T.; Yuan, D.; Hong, M.; Zhou, H.–C. *Chem. Mater.* **2019**, *31*, 8787−8793.
23. Wang, Y.; Chen, R.; Jia, W.; Wang, Q.; Xue, C. –Y.; Fan, J. –H.; Qi, W. –R.; Qin, Y. –J.; Pan, Y. –H.; Yang, R. –R. *Inorg. Chem.* **2018**, *57*, 2381−2385.
24. Xiao, J.; Wu, Y.; Li, M.; Liu, B.–Y.; Huang, X.–C.; Li, D. *Chem. Eur. J.* **2013**, *19*, 1891-1895.
25. Maji, T. K.; Mostafa, G.; Matsuda, R.; Kitagawa, S. *J. Am. Chem. Soc.* **2005**, *127*, 17152-17153.
26. Kawano, M.; Fujita, M. *Coord. Chem. Rev.* **2007**, *251*, 2592-2605.
27. Supriya, S.; Das, S. K. *J. Am. Chem. Soc.* **2007**, *129*, 3464-3465.

28. Takaoka, K.; Kawano, M.; Hozumi, T.; Ohkoshi, S.; Fujita, M. *Inorg. Chem.* **2006**, *45*, 3976-3982.
29. Zeng, H.–M.; Wang, C.; Wu, W.–H.; Mao, W.–T.; Jiang, Z.–G.; Zhan, C.–H. *Nanoscale Adv.* **2021**, *3*, 4680-4684.
30. Zhang, X.–F.; Yan, T.; Wang, T.; Feng, J.; Wang, Q.; Wang, X.; Du, L.; Zhao, Q.–H. *CrystEngComm* **2018**, *20*, 570-577.
31. Ghosh, S. K.; Zhang, J. P.; Kitagawa, S. *Angew. Chem. Int. Ed.* **2007**, *46*, 7965-7968.
32. Ma, S.; Sun, D.; Ambrogio, M.; Fillinger, J. A.; Parkin, S.; Zhou, H.-C. *J. Am. Chem. Soc.* **2007**, *129*, 1858−1859.
33. Dybtsev, D. N.; Chun, H.; Kim, K. *Angew. Chem., Int. Ed.* **2004**, *43*, 5033−5036.
34. Maity, D. K.; Halder, A.; Pahari, G.; Haque, F.; Ghoshal, D. *Inorg. Chem.* **2017**, *56*, 713–716.
35. Molla, M. R.; Gehrig, D.; Roy, L.; Kamm, V.; Paul, A.; Laquai, F.; Ghosh, S. *Chem. Eur. J.* **2014**, *20*, 760 – 771.
36. Acharyya, K.; Mukherjee, P. S. *Chem. Commun.* **2014**, *50*, 15788-15791.
37. Garai, B.; Mallick, A.; Banerjee, R. *Chem. Sci.* **2016**, *7*, 2195-2200.
38. Diez-barra, E.; De la hoz, A.; Sanchez-migallon, A.; Tejeda, J. *Heterocyles(sendai).* **1992**, *34*, 1365-1373.
39. SMART (V 5.628), SAINT (V 6.45a), XPREP, SHELXTL; Bruker AXS Inc.: Madison, WI, **2004**.
40. Sheldrick, G. M. University of Göttingen: Germany, **2002**.
41. Sheldrick, G. M. *Acta Cryst.* **2015**, *A71*, 3-8.
42. Spek, A. L. *Acta Crystallogr. Sect. D*. **2009**, *65*, 148–155.
43. Farrugia, L. J. *J. Appl. Crystallogr*. **1999**, *32*, 837–838.
44. Macrae, C. F.; Edgington, P. R.; McCabe, P.; Pidcock, E.; Shields, G. P.; Taylor, R.; Towler, M.; Streek, J. V. D. *J. Appl. Cryst*. **2006**, *39*, 453–457.
45. Blatov, V. A.; Shevchenko, A. P.; Serezhkin, V. N. *J. Appl. Crystallogr*. **2000**, *33*, 1193.
46. Blatov, V. A.; Carlucci, L.; Ciani, G.; Proserpio, D. M. *CrystEngComm.* **2004**, *6*, 377–395.
47. Takaoka, K.; Kawano, M.; Hozumi, T.; Ohkoshi, S. –I.; Fujita, M. *Inorg. Chem.* **2006**, *45*, 3976–3982.
48. Han, S. S.; Mendoza-Cortes, J. L.; Goddard, W. A. *Chem. Soc. Rev.* **2009**, *38*, 1460−1476.
49. Jung, D. H.; Kim, D.; Lee, T. B.; Choi, S. B.; Yoon, J. H.; Kim, J.; Choi, K.; Choi, S.-H. *J. Phys. Chem. B.* **2006**, *110*, 22987−22990.

CHAPTER-4

Unraveling the Role of Structural Dynamism in Metal Organic Frameworks (MOF) for Excited-State Intramolecular Proton Transfer (ESIPT) Driven Water Sensing

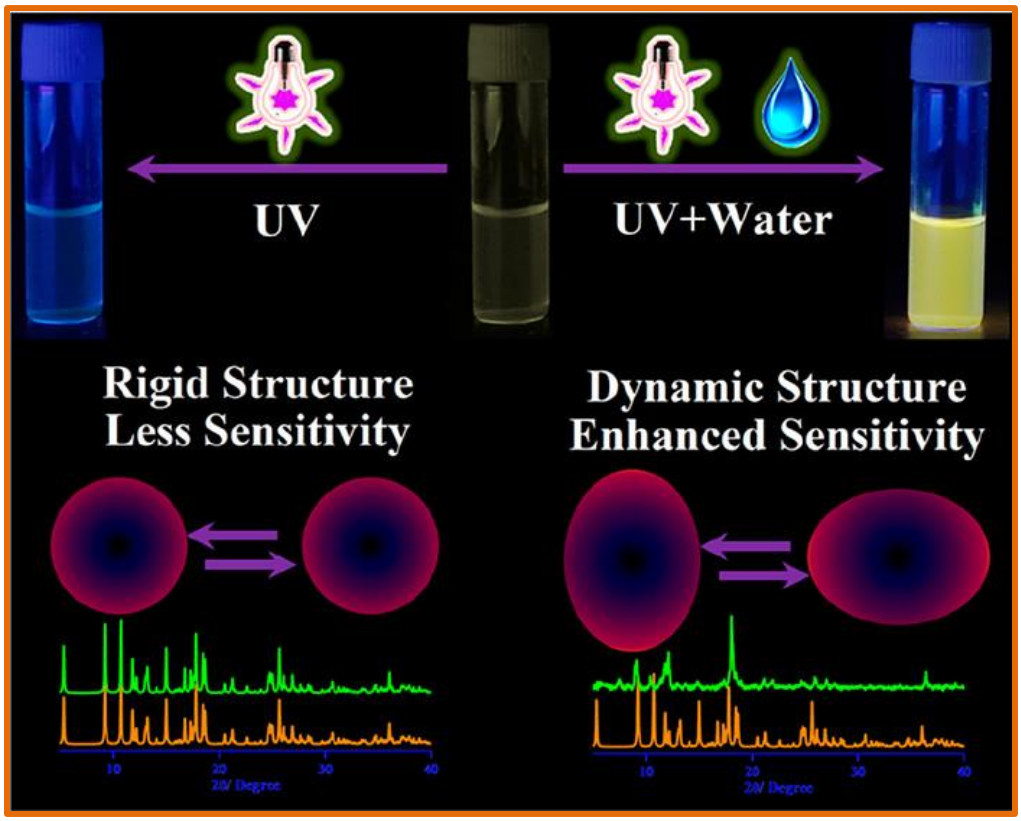

CHAPTER-4

Unraveling the Role of Structural Dynamism in Metal Organic Frameworks (MOF) for Excited-State Intramolecular Proton Transfer (ESIPT) Driven Water Sensing

4.1. INTRODUCTION

Dynamic materials are always a substance of interest due to their responsiveness towards specific stimulus/stimuli by facilitating structural transformations.[1,2] This structural transformation ability made such materials potential candidate for many modern interests like responsive smart optics,[3] molecular sensors,[4] selective capture/storage,[5,6] drug delivery,[7] thermo-chromic material,[8] photo-chromic material[9] etc. Various attempts have so far been performed for the control and manifestation of dynamism in a wide range of material. In between, many kinds of material, dynamism in metal-organic framework (MOF) materials is also studied extensively.[10–13] Metal-organic frameworks (MOFs) or porous coordination polymers (PCP) are already well established for their structural tunability[14–16] and structure dependent properties.[14–16] For these materials, by controlling the overall structure, properties and application can be moderated to a great extent.[14–16] MOFs are constructed by metal ions or clusters as nodes which are extended by multi-topic organic ligand/s. Variation in these building blocks[14–16] and/or any change in reaction parameters like reaction time[17,18] temperature[18] solvent media,[19] etc. can also bring immense variation in the overall architecture. This kind of structural tunability also enables step-by-step study of the effect of different parameters on the overall structure of a MOF and the structure dependent properties.[14–19] So far, a wide range of studies have been performed on the non-dynamic (rigid) MOFs by changing different parameters and/or the building blocks.[20–23] Likewise, in recent times, a wide range of dynamic MOFs has been reported and in many instances where the effects of different parameters are studied thoroughly.[19,24–29] Unfortunately, in most of the illustrations, the change in parameters results in a non-dynamic system.[12,25] Thus, still after a wide range of studies, it is still a mystery to find out a clear rational way for the introduction of dynamism in a MOF.[12,30] As there is still no straight forward way to introduce dynamism in a MOF, it may be an excellent move to use a previously known dynamic MOF as base material followed by a step-by-step structural modification to understand the thrive dynamism in the related structure. Considering this immediate thought, a previously reported[31] MOF has been used as a base material and modification has been performed on the building block/s to synthesize two new MOFs and their structural

behavior has been studied. This said base material is a Zn(II)-MOF, {[Zn(4-bpdh)(H_2dht)]·(MeOH)(H_2O)}$_n$ (**1**), [N,N′-bis(1-pyridin-4-yl-ethylidene)hydrazine = 4-bpdh and 2,5-dihydroxyterephthalic acid = H_4dht] which is a fivefold interpenetrated framework and highly dynamic in nature.[31] To study the effect of the size of the metal ion, Cd(II) ion is used instead of Zn(II). This results in, materials with the same framework formula, {[M(4-bpdh)(H_2dht)]}$_n$ [M = Zn(II) for **1** and Cd(II) for **2**] at their activated state. But this Cd(II) based, new compound is non-interpenetrated rigid framework. Further, when the 4,4'-coordinating linker 4-bpdh is replaced by an 3,3'-coordinating linker 3-bpdh (N,N′-bis(1-pyridin-3-yl-ethylidene) hydrazine), keeping the same metal ion; it result a 3D non-interpenetrated framework, {[Cd(3-bpdh)(dht)$_{0.5}$(H_2dht)$_{0.5}$(H_2O)] ·2H_2O}$_n$(**3**). Here it is interesting to note that, the framework (**3**) shows structural dynamism on dehydration/rehydration.[32] All the structure related analysis are performed for **2** and **3** and structural transformation features are compared with previously published[31] compound **1**. The effect of dynamism on different applications like adsorption and luminescence has also been thoroughly studied and discussed. Here both of these compounds show excited-state intramolecular proton transfer (ESIPT)[25,31] behavior and water sensing properties which are substantially influenced by the structural flexibility feature of the corresponding compounds.

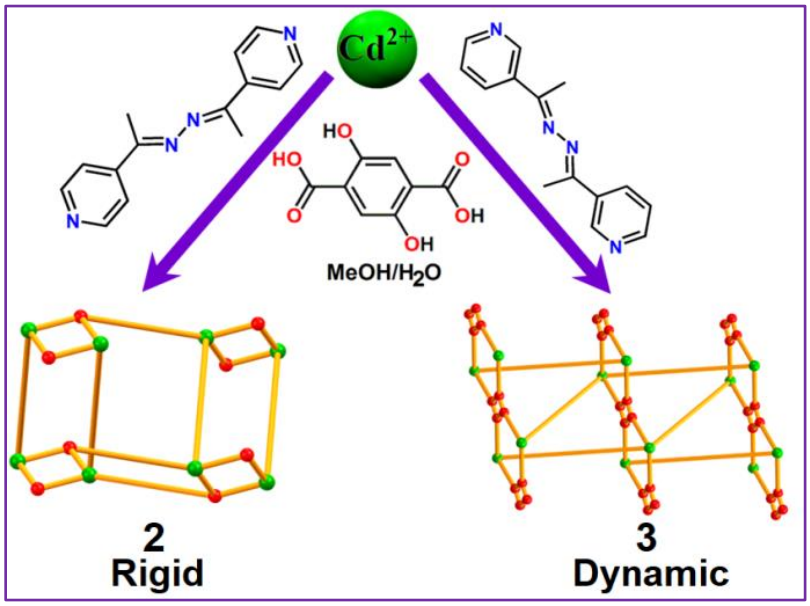

Scheme 1. Synthetic Scheme of Compounds **2** and **3**, where they are synthesized by slow diffusion technique at room temperature

4.2. EXPERIMENTAL SECTION

4.2.1. Materials and General Methods

All starting materials and solvents were purchased from the Sigma-Aldrich and used as received without further purification. Na_2H_2dht has been prepared by the slow addition of solid $NaHCO_3$ to suspended H_2dht in water up to the neutralization point and was allowed to evaporate until dryness. 3-bpdh and 4-bpdh has been prepared by usual Schiff base condensation reaction using a previously reported procedure from hydrazine hydrate and 3-acetyl pyridine[33] or 4-acetyl pyridine.[34] H_2dht, Hydrazine hydrate, 3-acetyl pyridine and 4-acetyl pyridine was purchased from Merck India and used without further purification. Elemental analyses (C, H, N) were performed using a PerkinElmer 240C elemental analyzer. FT-IR spectra were obtained on a Perkin Elmer spectrometer (Spectrum II) with the samples. PerkinElmer STA8000 thermal analyzer has been used for thermogravimetric analysis (TGA) with a ramp rate of 10 °C/min from room temperature to 600 °C under nitrogen flow. Powder X-ray diffraction (PXRD) data were collected on a Bruker D8 Discover instrument with Cu-Kα radiation (λ = 1.5406 Å), operating at 40 kV and 40 mA. UV-vis spectra are collected in PerkinElmer Lambda 35 instrument with integrating sphere attachment. Fluorescence measurements were done using HoribaFluoroMax 4 spectro fluorimeter.

4.2.2. Sorption Measurements

Ambient pressure volumetric N_2 gas (99.999% purity) adsorption study for **2** and **3** was carried out with the activated samples at 77 K, maintained by a liquid-nitrogen bath, in the pressures range 0 to 1 bar using a Quantachrome Autosorb-iQ adsorption instrument. CO_2 gas (99.99% purity) adsorption measurements were performed at 195 K (maintained by dry ice-acetone bath) in the same pressure range and in the same instrument. The vapor adsorptions studies with different solvents such as H_2O and dry EtOH, were performed in the vapor state by using the same instrument in range of partial pressure 0–0.9 at 298 K. To prepare the activated forms, a sample was taken in a sample holder and degassed at 120 °C under high vacuum (10^{-6} bar) for 4 h prior to the measurements. Afterwards the same sample tube has been placed to the analysis port of the instrument. Dead volume has been measured using ultra-pure helium gas (99.999% purity). Gas or solvent vapor is then allowed diffuse in the sample tube. Amount of adsorption is measured by the change of gas/vapor pressure at equilibrium state. Pore size distribution was determined from the N_2 isotherm at 77K, using the NL-DFT model.

4.2.3. Synthesis of Compounds

Synthesis of {[Cd(4-bpdh)(H_2dht)]}$_n$ (2).

An aqueous solution of Na_2dht (121 mg, 20 mL) was mixed with a methanolic solution of 4-bpdh (119 mg, 20 mL) and stirred to make a homogenous solution. In a thin crystal tube, 8mL of this mixed ligand solution was carefully layered over 4mL aqueous solution of $Cd(NO_3)_2 \cdot 6H_2O$ (154 mg, 20 mL) with a separation by 2mL of 1:1 water/MeOH buffer. After 7 days, needle like yellow crystals, suitable for single X-ray diffraction analysis, is obtained at the junction of the layer (yield = 76% based on Cd). Crystals are separated and washed with a small amount of cold 1:1 water/methanol solution. Anal. Cal. for $C_{22}H_{14}CdN_4O_6$ (543.99), **2**: C, 48.68; H, 2.60; N, 10.32. Found C, 48.46; H, 2.29; N, 10.89.

Synthesis of {[Cd(3-bpdh)(dht)$_{0.5}$(H_2dht)$_{0.5}$(H_2O)]·2H_2O}$_n$ (3).

Compound **3** is obtained in the same procedure and the same amount of ligand and metal salt in same solvent system, except the N,N′ donor ligand, here 3-bpdh (119 mg, 20 mL) is used instead of 4-bpdh. Block shaped pale yellow crystals suitable for X-ray studies were obtained after 15 days at the junction of the tube (yield = 76% based on Cd). Crystals are separated and washed with copious amount of 1:1 water/methanol solution. Anal. Cal. for $C_{22}H_{23}CdN_4O_9$ (599.85), **3**: C, 44.05; H, 3.86; N, 9.34. Found C, 43.92; H, 4.01; N, 9.47.

Bulk Synthesis of 2 and 3: In bulk scale, the compounds are synthesized by the same procedure as mentioned previously. After 3 weeks, crystals from the tube were manually separated and washed with copious amounts of cold 1:1 water/methanol solution. PXRD analysis is used to confirm their purity in bulk phase.

Synthesis of 3′: Freshly prepared crystals of **3** were collected and heated at 120 °C under reduced pressure. After 4h a yellow crystalline material of **3′** is obtained.

Synthesis of 1: Synthesized by the reported[35] synthetic procedure.

4.2.4. Single-Crystal X-ray Diffraction

The single crystals of **2** and **3** were mounted on the glass fiber with the use of commercially available super glue. X-ray single crystal diffraction data for the compounds was collected at room temperature using Bruker APEX II diffractometer, equipped with a normal focus, sealed tube X-ray source with graphite monochromated Mo-K radiation (λ= 0.71073Å). The data were integrated using SAINT program[36] and SADABS[37] program was used for the absorption corrections. The structure was solved by SHELXS 2018[38] using Patterson method and followed by successive

Fourier and difference Fourier synthesis. Full matrix least-squares refinements were performed on F^2 using SHELXL 2018[38] with anisotropic displacement parameters for all non-hydrogen atoms. For 2, phenoxy oxygen atoms are found with positional disorder. For every dicarboxylate ligands, phenoxy oxygen atoms are found with 0.5 occupancy and present over 4 carbon atoms instead of two. Before final refinement PART command is utilised to separate them. Potential solvent accessible area or void space was calculated using PLATON[39] multipurpose crystallographic software. All the hydrogen atoms were fixed geometrically by HFIX command and placed in ideal positions in case of both the structures. All other calculations were carried out using SHELXS 2018,[38] SHELXL 2018,[38] WinGX system Ver-1.80[40] and PLATON v1.15.[39] Mercury v3.6[40] and Diamond v3.2 are used to visualize and draw the figures for the structures. Detailed data collection strategy and structure refinement parameters along with crystallographic data are presented in Table 1.

Table 1. Crystallographic and Structural Refinement Parameters for 2 and 3

	2	**3**
Formula	$C_{22}H_{14}CdN_4O_6$	$C_{22}H_{23}CdN_4O_9$
Formula Weight	542.78	599.85
Crystal System	Monoclinic	Triclinic
Space group	$P2_1/c$	Pī
a/ Å	7.6677(1)	7.260(5)
b/Å	13.7419(2)	10.438(5)
c/ Å	20.1767(4)	17.320(5)
α/°	90	101.825(5)
β/°	92.354(1)	98.331(5)
γ/°	90	107.333(5)
V/ Å3	2124.20(6)	1196.2(11)
Z	4	2
D_c/ g cm^{-3}	1.697	1.654
μ /mm^{-1}	1.076	0.972
F(000)	1080	598
θ range/°	1.8-27.5	2.1–27.5
Reflections collected	35778	20070
Unique reflections	4884	5438
Reflections $I > 2\sigma(I)$	4384	4877
R_{int}	0.030	0.022
goodness-of-fit (F^2)	1.13	1.04
$R1$ ($I > 2\sigma(I)$) [a]	0.0363	0.0329
$wR2(I > 2\sigma(I))$ [a]	0.0942	0.0914
CCDC	2068191	2068192

[a] $R_1 = \Sigma \big| |F_o| - |F_c| \big| / \Sigma |F_o|$, $wR_2 = [\Sigma (w (F_o^2 - F_c^2)^2) / \Sigma w (F_o^2)^2]^{½}$

4.2.5. Emission Spectral Study and Water Titration

All the emission data are collected using HoribaFluoroMax 4 spectro fluorimeter at room temperature. Here we have studied the emission spectra of room temperature dried assynthesized compounds or desolvated compounds in different solvents (dry acetonitrile, dry ethanol, dry methanol, dry THF, dry DMF, dry acetone, dry toluene and water). For these, 2 mg of either assynthesized compounds or desolvated compounds are placed in 2 ml of individual solvents and emission data is taken after 2 minutes. For water titration in different dry solvents, 3 mg of each desolvated sample is placed in a closed container with 3 ml of individual solvent. Then it is sonicated for 5 minutes to have a uniform suspension. 1 ml of this suspension is placed on the spectrophotometer and emission data is collected after addition of a certain amount of water followed by mixing of the suspension by a dropper and 2 minutes wait time.

4.3. RESULTS AND DISCUSSION

4.3.1. Structural Description

Structural Description of {[Zn(4- bpdh)(H_2dht)]·(MeOH)(H_2O)}$_n$ (1)

[N,N′-bis(1-pyridin-4-yl-ethylidene)hydrazine = 4-bpdh and 2,5-dihydroxyterephthalic acid = H_4dht] which is a fivefold interpenetrated framework and highly dynamic in nature.[31]

Structural Description of {[Cd(4-bpdh)(H_2dht)]}$_n$ (2).

It is quite fascinating to note that the change in metal center, from Zn(II) to Cd(II) in **1** to **2**, a significant structural change has taken place. The metal center is shifted from 4 coordinated tetrahedral centers (for **1**) to 6 coordinated octahedral centers (for **2**) which are not so uncommon in case of Cd(II). Although, both are with 3D architecture and crystallizes in the same monoclinic crystal system (Table 1) but in a different space group, $P2_1/c$. The asymmetric unit of **2** comprises one Cd(II) atom, one H_2dht ligand, and one 4-bpdh linker (Figure 1a). Each metal atom is connected to four oxygen atoms (O1^b, O2, O3^c and O4^c where *b* = 2-x, -y, 2-z and *c* = 2-x, 1/2+y, 3/2-z) of three different bridging H_2dht ligands and two pyridyl nitrogen atoms (N1 and N4^a where *a* = 1+x, 1+y, z) of two different 4-bpdh ligand (Figure 1a). These two nitrogen atoms are present at almost trans to each other (angle between N1-Cd1-N4^a is ~166.13^o). All other relevant bond lengths and bond angles are presented in the Table 2. Both the phenoxy oxygen present in the dicarboxylate ligand, are with positional disorder and present on two carbons with 0.5 occupancy. Here, two adjacent metal ions are octahedrally coordinated by eight carboxylate oxygen atoms of

four H_2dht ligands and four nitrogen from bridging 4-bpdh ligand creating a $Cd_2(CO_2)_4N_4$ SBU where Cd(II) centers are separated by 4.587 Å. In a SBU, the H_2dht ligand connects two Cd(II) centers in bridging bidentate fashion at the one end of the carboxylate whereas the other end is connected to another Cd(II) center of adjacent SBU. Thus, each H_2dht ligand is connected to three Cd(II) centers forming a two-dimensional $[Cd_2(H_2dht)_2]_n$ sheet lying in the crystallographic *bc* plane (Figure 1b). Such two adjacent 2D sheets are further connected by 4-bpdh ligand forming three-dimensional (3D) pillared layer framework (Figure 1c). Topological analysis[43,44] shows that the simplified form of this 3D network can be represented as a (3,5)-connected net with Schläfli symbol $\{4.6^4.8^3.10^2\}\{4.8^2\}$ (Figure 1d). This 3D framework is farther stabilized by intramolecular face-to-face π···π interaction, present between the phenyl ring of H_2dht and pyridyl ring of 4-bpdh (Table 3, Figure 2a). It is also worth to mention that this framework does not contain any measurable solvent accessible voids or unidirectional channel (Figure 2b, 2c, 2d).

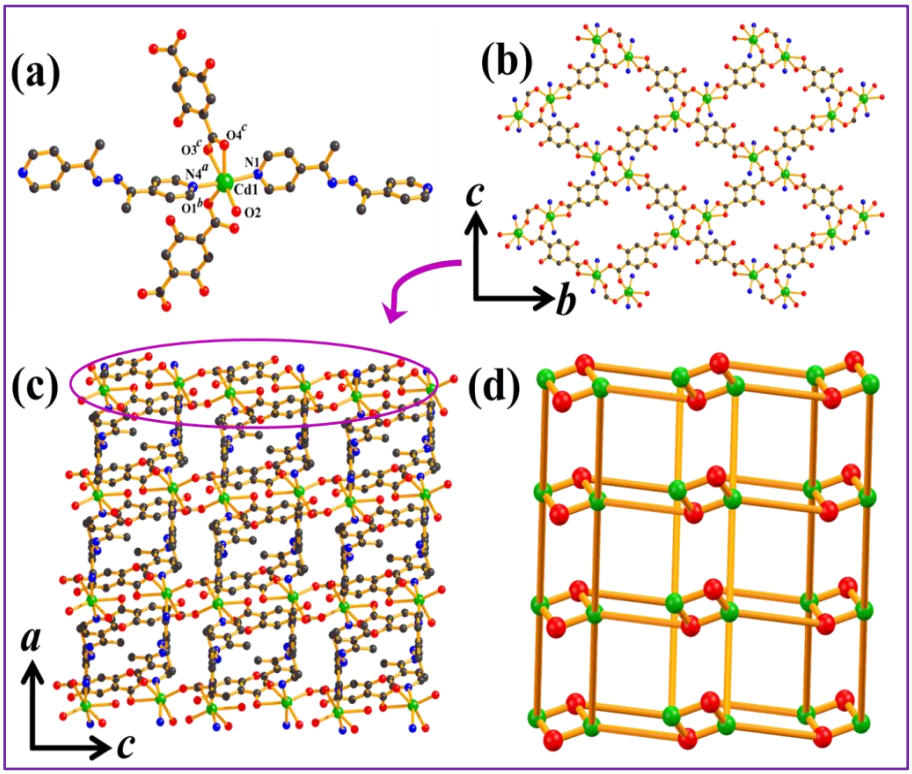

Figure 1 (a) Coordination environment around distorted octahedral Cd(II) center of **2**, (b) view of two-dimensional metal carboxylate sheet ($[Cd_2(H_2dht)_2]_n$) along crystallographic *bc* plane, (c) three dimensional structure of **2**, and (d) simplified presentation of the (3,5)-connected 3D network of **2**. Half of the disorder phenoxy oxygen atoms are omitted for clarity.

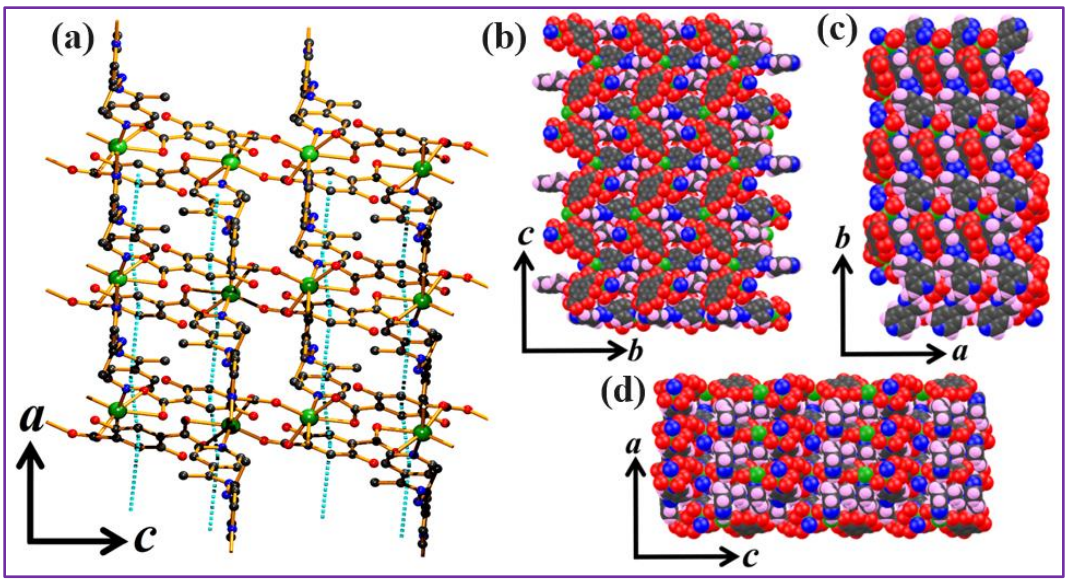

Figure 2 (a) View of π…π interaction in **2** along *a* axis. Cd(II) in green, C in black, N in blue, O in red, π…π interaction in cyan. Space fill view of compound **2** in crystallographic (a) *bc* plane, (b) *ab* plane and (c) *ac* plane. Cd(II) in green, C in black, N in blue, O in red, H in pink.

Table 2. Selected Bond Lengths (Å) and Bond Angles (°) for **2**.

Cd1-O2	2.302(3)	Cd1-N1	2.299(3)
Cd1-N4^{a}	2.381(3)	Cd1 -O3^{c}	2.374(3)
Cd1-O4^{c}	2.406(3)	Cd1-O1^{b}	2.254(3)
O2-Cd1-N1	91.54(10)	O2-Cd1-N4^{a}	84.37(10)
O2 -Cd1-O3^{c}	165.92(10)	O2-Cd1-O4^{c}	115.27(10)
O1^{b}-Cd1-O2	99.91(10)	N1-Cd1-N4^{a}	166.13(11)
O3^{c}-Cd1-N1	97.44(10)	O4^{c}-Cd1-N1	86.22(10)
O1^{b}-Cd1-N1	109.88(10)	O3^{c}-Cd1-N4^{a}	84.36(10)
O4^{c}-Cd1-N4^{a}	83.59(10)	O1^{b}-Cd1-N4^{a}	83.91(11)
O3^{c}-Cd1-O4^{c}	54.95(9)	O1^{b}-Cd1-O3^{c}	87.24(9)

Symmetry code: *a* = 1+x, 1+y, z; *b* = 2-x, -y, 2-z; *c* = 2-x, 1/2+y, 3/2-z.

Table 3. π-π Interactions in **2**

ring(i) → ring(j)	distance of centroid (i) from ring(j),(Å)	dihedral angle (i,j) (deg)	distance between the (i,j) ring centroids,(Å)
R(1)→ R(2)^{i}	4.415(2)	1.71(18)	3.4680(15)
R(1)→ R(2)^{ii}	3.594(2)	1.71(18)	3.3565(15)
R(2)→ R(1)^{ii}	3.594(2)	1.67(18)	3.3634(15)
R(2)→ R(1)^{iii}	4.415(2)	1.67(18)	3.4030(15)

Symmetry code: i = -1+x, y, z; ii = x, y, z; iii = 1+x, y, z.

R(i)/R(j) denotes the ith/jth rings: R(1) = N(1)/C(9)/C(10)/C(11)/C(12)/C(13); R(2) = C(2)/C(3)/C(4)/ C(5)/C(6)/C(7).

Structural Description of {[Cd(3-bpdh)(dht)$_{0.5}$(H$_2$dht)$_{0.5}$(H$_2$O)]·2H$_2$O}$_n$ (3).

Keeping all the ingredients same as **2**, but the 4,4'-coordinating 4-bpdh is replaced by the 3,3'-coordinating 3-bpdh ligand, **3** is synthesized where the framework appears as a 3D architecture as previous two structures. Unlike the other two (**1** and **2**), it crystallizes in a centrosymmetric triclinic crystal system with the *P*$\bar{1}$ space group (Table 1). The asymmetric group of **3** contains one hexa-coordinated Cd(II) ion, two half of 3,3'-coordinating 3-bpdh, half of dht (deprotonated phenoxo group), half of H$_2$dht, one coordinated water molecule and two guest water molecules (Figure 3a). Each of these Cd(II) centers with a CdN$_2$O$_4$ coordination environment are octahedrally surrounded by two pyridyl nitrogen atoms (N1 and N3) of two different 3-bpdh ligand along with four oxygen atoms (O1, O3, O5^a and O1W where *a*=-1+x, y, z) of one carboxylate oxygen atom of H$_2$dht, one carboxylate oxygen atom of dht ligand, one phenoxo oxygen from another dht ligand and one water molecule (Figure 3a). Here also two pyridyl nitrogen atoms are present at trans position (angle between N1-Cd1-N3 is ~172.28^o) (Table 4, Figure 3a). All the other bond lengths and bond angles around Cd(II) are provided in Table 4.

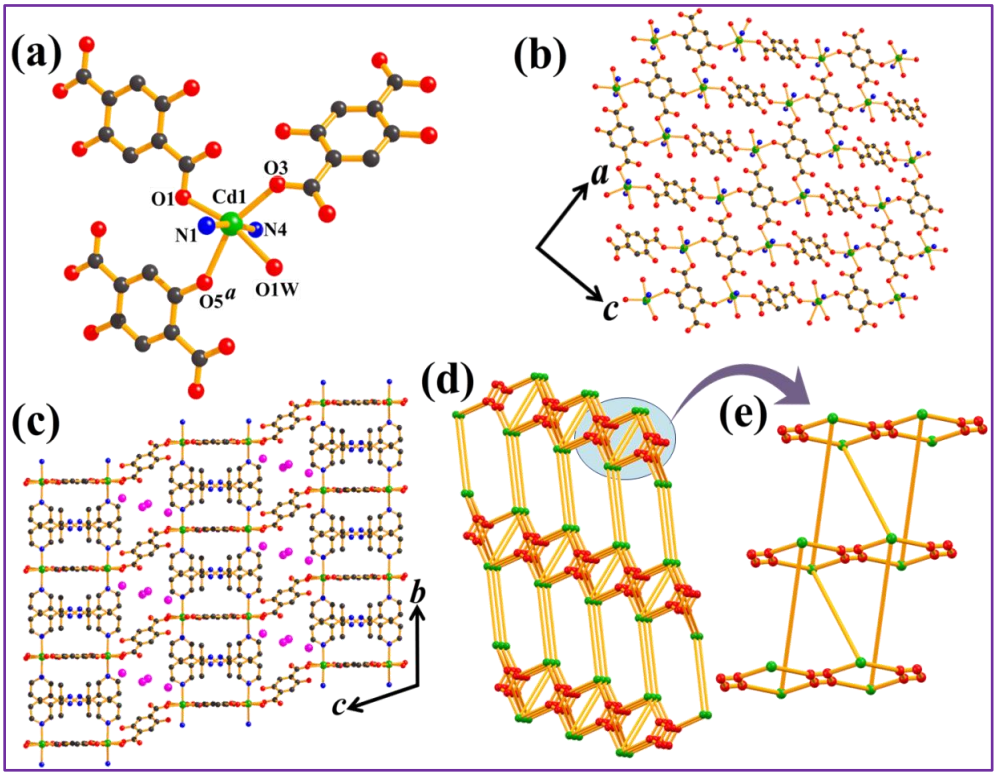

Figure 3 (a) Coordination environment around distorted octahedral Cd(II) center of **3**, (b) view of two-dimensional metal carboxylate sheet {[Cd(dht)$_{0.5}$(H$_2$dht)$_{0.5}$]}$_n$, (c) three dimensional structure of **3** where guest water molecules (color: magenta) are filled in the 1D channel, and (d,e) simplified presentation of the (3, 3, 5)-connected 3D network of **3**.

Thus each of the dht ligand is connected to four Cd(II) atoms and forms a 1D chain along the crystallographic *a* axis. These chains are interconnected by H_2dht ligand and form 2D metal carboxylate sheets (Figure 3b). These sheets are joined by 3-bpdh ligands and form a 3D architecture (Figure 3c). Network analysis by TOPOS[43,44] suggests that it is a (3, 3, 5)-connected tri-nodal net with point symbol $\{4.6.8\}2\{6^4.8^6\}$ (Figure 3d,e). This 3D structure is further stabilized by the intramolecular π…π interaction between the adjacent pyridyl rings (Table 5, Figure 4a) and intramolecular hydrogen bonding between phenoxy group, carboxy group and coordinated water molecule (Table 6, Figure 4b-c). Here in this compound, Cd…Cd distances through H_2dht ligand and 3-bpdh ligand is ~11.6Å and ~12.8Å respectively.

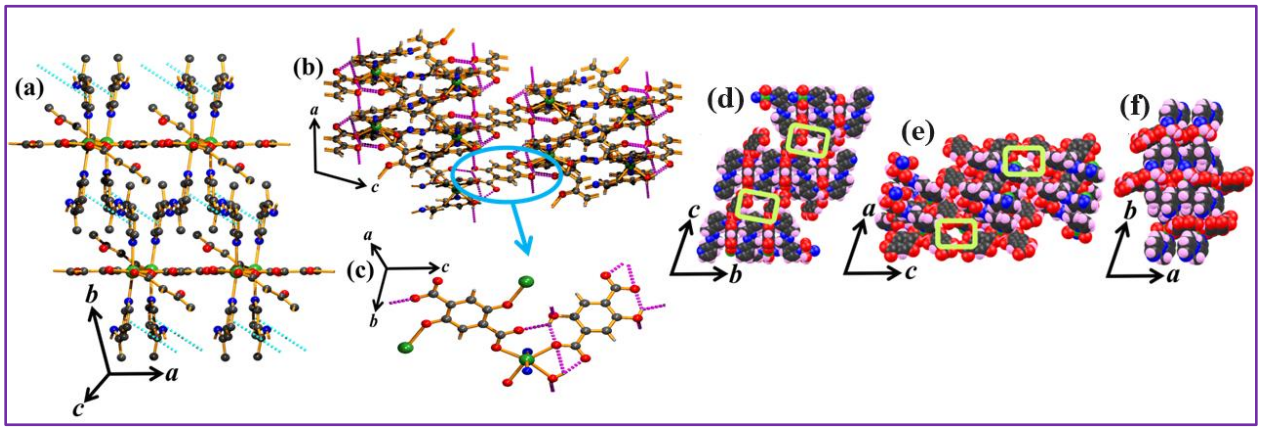

Figure 4 View of intermolecular weak interaction in **3**. (a) π…π interaction in cyan, (b) and (c) hydrogen bonding in magenta. Cd(II) in green, C in black, N in blue, O in red. Space fill view along (d) *a* axis, (e) *b* axis and (f) *c* axis, of the compound **3** showing directional channel along crystallographic *a* and *b* axis. Cd(II) in green, C in black, N in blue, O in red, H in pink.

Table 4. Selected Bond Lengths (Å) and Bond Angles (°) for **3**.

Cd1-O1	2.263(3)	Cd1-O1W	2.362(4)
Cd1-O3	2.308(3)	Cd1-N1	2.321(3)
Cd1-N3	2.343(3)	Cd1-O5^a	2.435(3)
O1-Cd1-O1W	164.59(10)	O1-Cd1-O3	115.56(8)
O1-Cd1-N1	92.00(8)	O1-Cd1-N3	93.46(8)
O1-Cd1-O5^a	89.24(7)	O1W-Cd1-O3	79.82(10)
O1W-Cd1-N1	85.64(10)	O1W-Cd1-N3	87.66(10)
O1W-Cd1-O5^a	75.48(9)	O3-Cd1-N1	93.99(9)
O3-Cd1-N3	88.57(9)	O3-Cd1-O5^a	154.94(7)
N1-Cd1-N3	172.28(11)	O5^a-Cd1-N1	88.37(9)
O5^a-Cd1-N3	86.25(9)		

Symmetry code: *a* = -1+x,y,z

Table 5. π-π Interactions in **3**

ring(i) → ring(j)	distance of centroid(i) from ring(j),(Å)	dihedral angle (i,j) (deg)	distance between the (i,j) ring centroids,(Å)
R(1)→ R(2)^{p}	4.371(4)	8.59(17)	3.7945(15)
R(1)→ R(2)^{q}	4.371(4)	8.59(17)	3.4276(15)

Symmetry code: p = x,1+y,z; q = x,-1+y,z.

R(i)/R(j) denotes the ith/jth rings: R(1) = N(1)/C(1)/C(2)/C(3)/C(4)/C(5); R(2) = N(3)/C(8)/C(9)/C(10)/C(11)/C(12).

Table 6 Hydrogen Bonding Interactions (Å, °) of **3**

D-H···A	D-H	H···A	D···A	∠D-H···A
O1W--H1WA..O3	0.85(5)	2.58(5)	2.997(5)	111(4)
O1W--H1WA..O4	0.85(5)	1.92(5)	2.763(5)	168(5)
O1W--H1WB..O6^{i}	0.67(9)	2.30(9)	2.934(5)	159(9)
O6--H6..O2	0.82	2.32	2.908(4)	129
O6--H6..O3	0.82	1.85	2.571(4)	145

Symmetry code: i = -1+x,y,z.

Such high inter-metal distances cause an appreciable size of void channels along the crystallographic *a* and *b* axis (Figure 3c, 4d-f). These channels are filled by the guest water molecules (Figure 3c). Analysis of void volume[39] by artificially removing the solvent molecules suggests that compound **3** contains ~150 Å^3 potential solvent accessible void which is ~12.5% of the total crystal volume.

4.3.2. Flexibility and Thermal Stability

Immediately after removing the crystals from the mother solvent, both the compounds are subjected to PXRD studies. Peak-to-peak matching for the simulated and as-synthesized PXRD pattern confirms the phase purity of the as-synthesized compounds (Figure 5). To understand the thermal stability of these compounds, thermogravimetric (TGA) analysis has been performed with both the samples (Figure 6). It is already seen that **2** do not have any lattice guest molecules, which consistent with the TGA curve; no significant weight loss up to ~ 350 °C and afterwards a rapid weight loss has been observed which signifies the breakdown of the framework into unrecognized products (Figure 6). For compound **3**, from the beginning of the thermogravimetric study, a steady weight loss has been observed and it ceases at the temperature ~75 °C with a total weight loss of ~7.23% which is equivalent to ~2.4 water molecules (Figure 6). Afterwards it is stable up to ~ 300 °C, which immediately suggests that the weight loss up to ~75 °C is probably due to the loss of both the lattice guest as well as coordinated water molecules. It is quite clear that the weight loss

has started from the beginning of the TGA study, so it is very logical to pretend that during the processing of the experiment, part of the lattice water has escaped, which is the reason behind discrepancy between the theoretical amount of water molecules and that of experimentally found number.

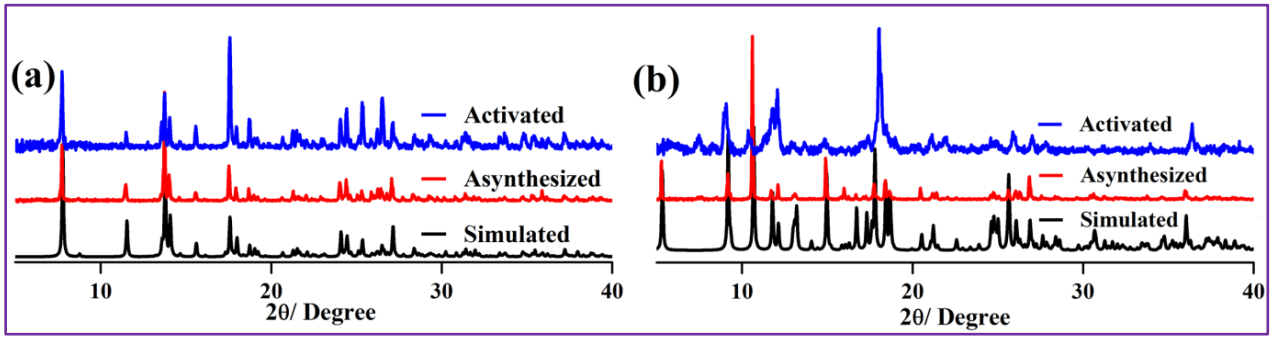

Figure 5 PXRD pattern of the compound (a) **2** and (b) **3** at their different phase, simulated (black), as-synthesized (red), activated (blue).

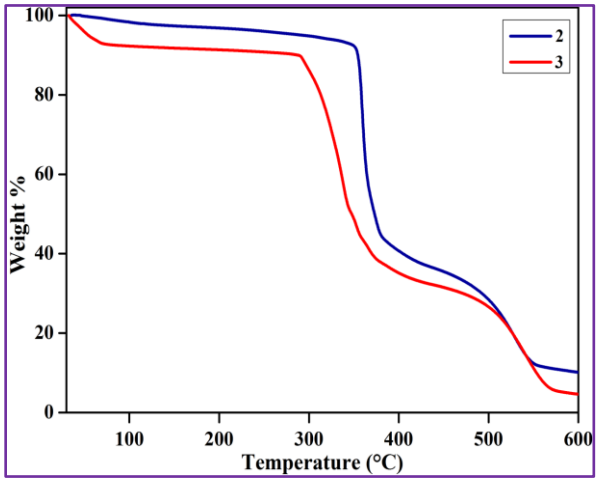

Figure 6 Thermogravimetric analysis curves for **2** (blue) and **3** (red).

To know the structural stability after loss of water molecules, compound **3** is desolvated at 120 °C under dynamic vacuum for 4h. PXRD of this desolvated compound shows substantial change in pattern with shift of peak position as well as emerging of new peaks (Figure 5b). It signifies that after the loss of water molecules a structural transformation has taken place. To analyze this phase transformation of **3**, variable temperature PXRD (VTPXRD) has been performed, which suggests, there is commencement of peak shifting started from 70 °C and after 80 °C (Figure 7b), there is a sudden change in the PXRD pattern indicating the formation of a new phase (**3′**). This new phase is found to be stable almost up to 280 °C (Figure 7b). In case of compound **2** no such structural

transformation has been observed (Figure 7a). To verify reversibility of these structural transformations, compound **3** at activated state (**3′**) have been immersed in different common solvents for one week and PXRD study has been performed (Figure 8c) after taking them out from the solvents immediately. It is interesting to note that only in water; **3′** can be reverting to its mother structure, **3**.

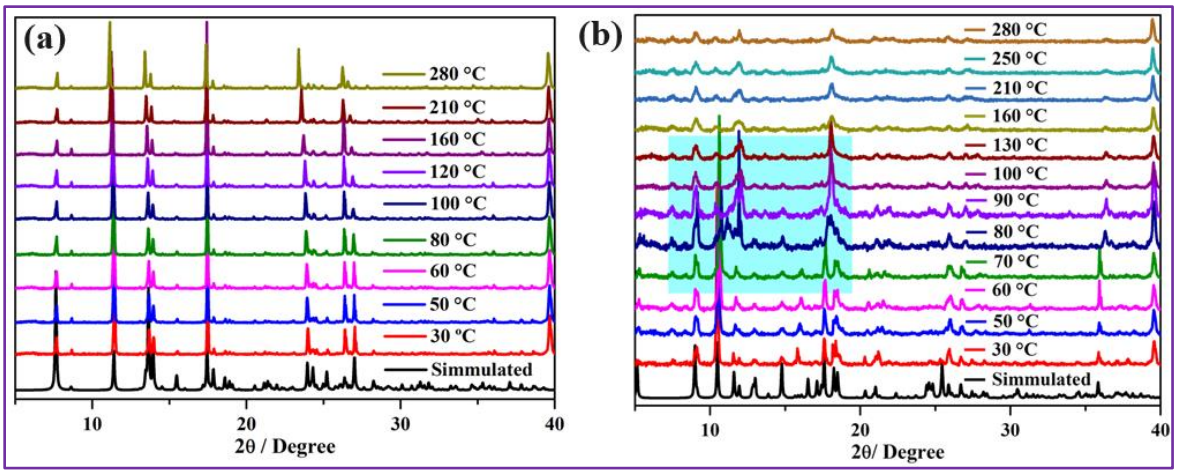

Figure 7. (a) Variable temperature PXRD pattern for the compound **2**. (b) Variable temperature PXRD pattern for the compound **3**, Highlighted portion signifies the major changes in the peak positions.

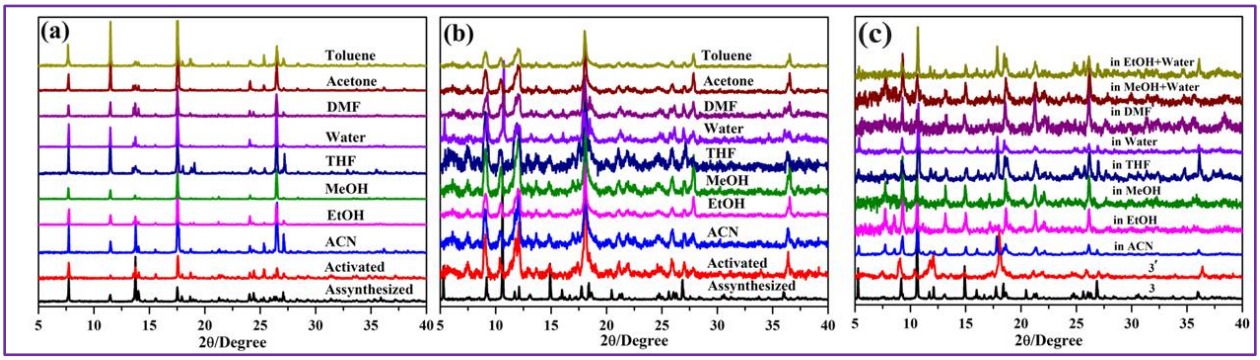

Figure 8. PXRD pattern of **3′** after soaking in different solvents.

This is a direct consequence of the fact that the losses of waters from the lattice have definitely triggered the transformation and the presence of water may have facilitated the reverse process. In all other solvent, like, dry EtOH, dry MeOH, dry THF, dry ACN and dry DMF etc., the transformed phase remained as the desolvated phase or any other unrecognized phases. Although in 1:1 water+EtOH or 1:1 water+MeOH, the peak positions are almost similar to the pristine phase which is quite expected due to the role of water molecules. Thus, compound **3** is completely dynamic in

nature with respect to the desolvation and resolvation in presence of water. During all these studies framework integrity is confirmed by the PXRD study of isolated samples immediately (within 1 hour) after emission experiments (Figure 8). It is worth to mention that all these PXRD patterns of such isolated compounds are similar with PXRD pattern of activated **3** (**3′**), except in water. Isolated **3′** from water shows some extra peaks in PXRD pattern than the activated state (Figure 8).

4.3.4. IR Spectroscopy Study

FT-IR analysis also supports the structural findings. The peak assignment are as follows.

IR spectra of compound **2** (4000–400^{-1}): 3417 (br), 3048 (m), 1612 (s), 1580 (s), 1499 (s), 1444(m), 1364 (m), 1234 (m), 1105 (s), 1063 (s), 1011 (s), 866 (s), 834 (s), 816 (s), 786 (s), 690 (s), 573 (s), 548 (s). IR spectra of compound **3** (4000−400 cm^{-1}):3418 (br), 1810 (m), 1630 (s), 1515 (s), 1443 (s), 1369 (s), 1320 (s), 1291 (s), 1261 (s), 1199 (s), 1135 (s), 1105 (s), 1041 (m), 927 (m), 865 (s), 805 (m), 689 (s), 641 (s), 606 (s), 541 (s). IR spectra of **3′** (4000−400 cm^{-1}): 3425 (br), 1786 (s), 1621 (m), 1513 (s), 1441 (s), 1367 (s), 1321 (m), 1260 (s), 1198 (s), 1136 (s), 1106 (s), 1028 (m), 897 (s), 861 (s), 790 (m), 694 (s), 644 (s), 607 (s), 541 (s).

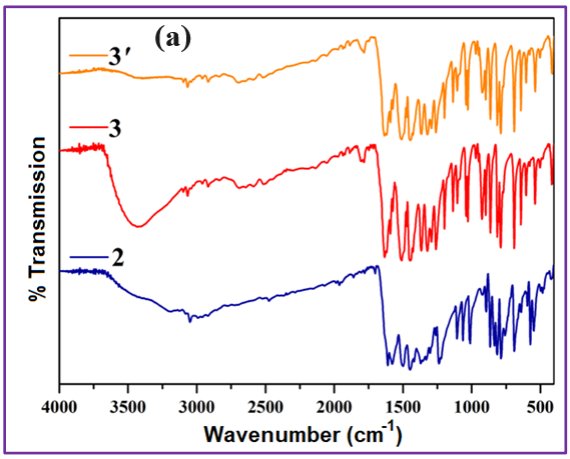

Figure 9. IR spectra of compound **2**, **3** and **3′**.

4.3.5. Adsorption Study

Vapor and gas sorption studies are performed for activated **2** and **3** (**3′**). Different adsorption profiles for **3′** are significantly commensurate with its dynamic nature. CO_2 adsorption for **3′** shows an initial steep uptake then a leveling of curve (up to partial pressure ~0.3) followed by another enhanced uptake is observed and final uptake amount is ~115 mL/gm (ca. 3 molecules of CO_2 per formula unit). Similar initial steep uptake also found for **1**, although it was only with this single step uptake.[31] This adsorption profile with initial step, is a clear indication of structural dynamism

(Figure 10a). For water sorption (at 298K), activated **3** (**3′**) also exhibit gate opening behavior which starts at P/P_0 ~ 0.1 and at P/P_0 ~ 0.3, saturation is set off with a maximum value of ~37 mL/gm equivalent to one water molecule per formula weight.

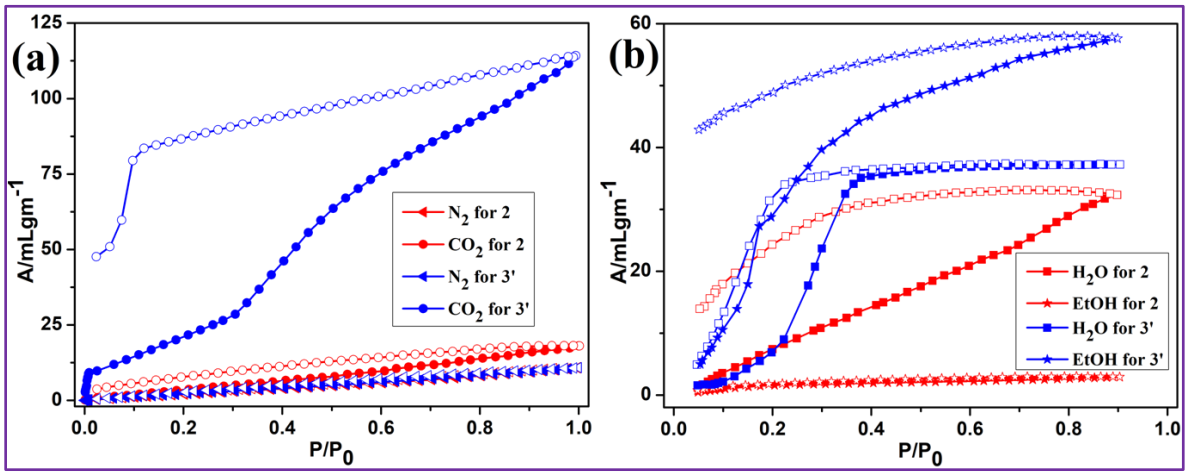

Figure 10. (a) Gas sorption and (b) vapor sorption isotherms for activated **2** (Red) and **3** (**3′**) (Blue); N_2 (triangle) CO_2 (circle) H_2O (square) and EtOH (star). Filled and open circles represent adsorption and desorption, respectively.

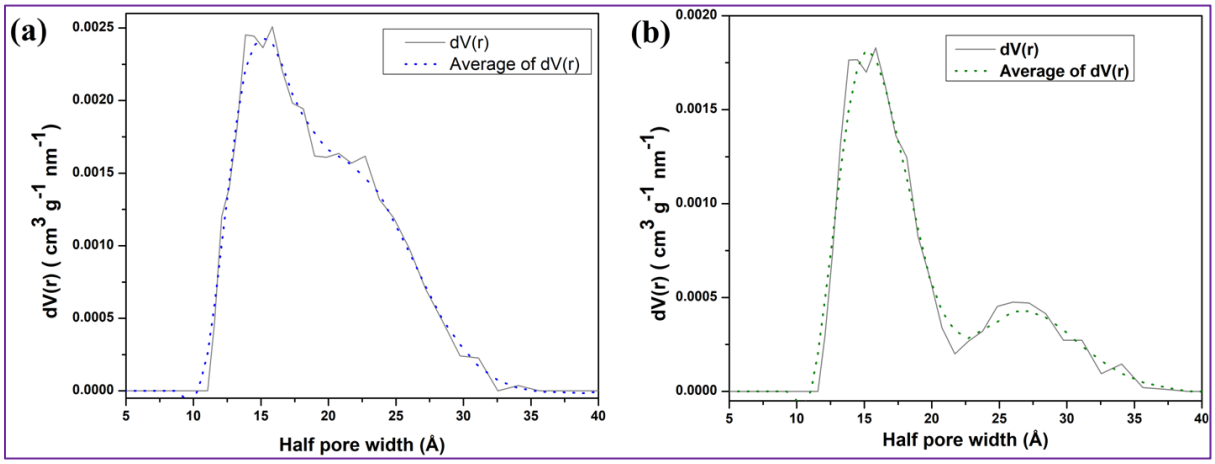

Figure 11. NL-DFT pore size distribution curve for (a) **2** and (b) **3**, obtained from the N_2 isotherm.

Gate opening behavior is also observed for EtOH vapor sorption. From the very initial pressure steep increase is observed which continues up to P/P_0 ~ 0.4 with an uptake value of ~45 mL/gm and ends with a maximum uptake of 58 mL/gm (ca. 1.5 molecules of EtOH per formula unit). For each of these sorption profiles, desorption curve does not concur with the adsorption curve, instead a large hysteresis is observed (Figure 10). It may be the kinetic delay of the transformed phase to return back to its original form. This retention property is found highest for ethanol sorption, where about one molecule of ethanol per formula remained in the system at the lowest pressure.

Although, no such gate opening phenomenon has been observed for **2** for CO_2, water and ethanol sorption profiles (Figure 10b), which is obvious for a rigid structure. Both of activated **2** and **3 (3′)** is nonporous towards N_2. It may be due to non-polar N_2 with kinetic diameter 3.6 Å, does not have enough force of attraction to remain in the surface or in the huge pore (maximum population of pore width at ~30Å for both **2** and **3′**) (Figure 11) of these compounds.

4.3.6. Excited-State Intramolecular Proton Transfer (ESIPT) and Water Sensing

Many different studies have already pointed out that MOF made of ESIPT enable ligand dht, can show many intriguing properties. Compound **1** shows fabulous dual emission behavior at λ_{ex}=350 nm[31] in presence of traces of water and this phenomenon is suitable for water sensing in common polar organic solvents. Here the Cd(II) version (**2**) of that Zn(II)-MOF, **1**[31], and then replaced the N,N′ donor ligand by a 3,3'-coordinating analogue in **3** is to study the structure-property relationship. Both the **2** and activated **3** (**3′**), exhibit similar trends of emission properties at λ_{ex}=350 nm. The solid-state emission studies show that, both the activated form of **2** and **3**, are with single emission maxima at 456 nm and 462 nm respectively (Figure 12a). Here, similar activation procedure as the sorption measurement has been performed on individual sample to get activated **2** and **3** (**3′**).

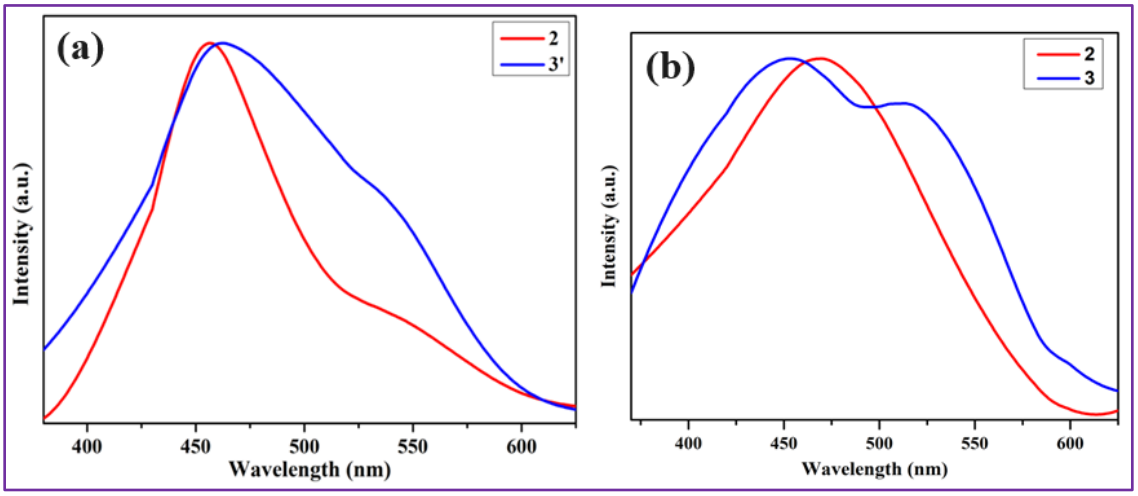

Figure 7. (a) The solid-state emission spectra for **2** and activated **3(3′)** at room temperature (λ_{ex}=350 nm). (b) The solid-state emission spectra for as-synthesized **2** and **3** at room temperature (λ_{ex}=350 nm).

Next, we have studied the emission spectra of these desolvated compounds in different solvents (dry acetonitrile, dry ethanol, dry methanol, dry THF, dry DMF, dry acetone, dry toluene and water) at room temperature by placing 2 mg of each activated compound in 2ml of individual

solvents and emission data is taken after 2 minutes. It is found that except for DMF and water, in all the dry solvents; both of these activated frameworks show either similar kind of emission maxima as they have in the solid state or they are being simply non-emissive in nature (Figure 13). In DMF and water, a distinct peak separation has been observed (Figure 13), similar to the base material **1**. This distinct dual broad peak is a clear indication of excited state intramolecular proton transfer.[44] Now, compound **3** contains lattice water molecules and these water molecules may have similar effect as the external solvent water molecules. To verify this, we have studied the solid-state emission property for the compounds has been studied without activating the samples. This study shows that compound **3**, at its pristine form shows dual emission peak with maxima at 453 nm and 513 nm (Figure 12b) instead a single peak at 462 nm (Figure 12a). Although no such dual emission is observed for compound 2 which does not contain any lattice water molecules.

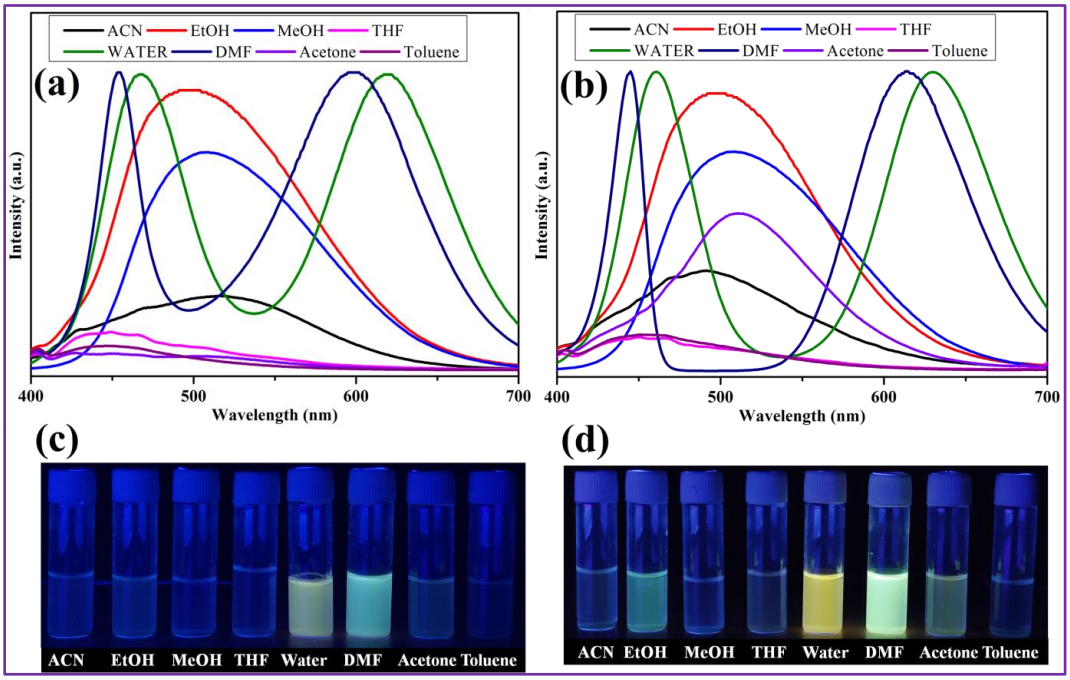

Figure 13. Emission spectra of the activated compounds (a) **2** and (b) **3 (3′)** in different dry solvents at λ_{ex}=350 nm; distinctly separated dual emission bands in water and DMF signifying the ESIPT phenomenon. Photographic images of the activated compounds (c) **2** and (d) **3 (3′)**, suspended in different dry solvents after photo-excitation with a 365 nm UV lamp.

Considering the correlation between previous studies about H_2dht embedded framework,[31] it is worth to say that the lower wavelength peak is coming from the enol tautomer of the carboxylate ligand and keto tautomer is the origin of higher wavelength peak.[31] A close look on the results suggests that these peaks are at a similar position as that of the mother compound, **3**. The dynamic

nature of the compound in water is only possible reason behind this partial revert back of the structure. Now both of these compounds show similar single maxima or weak emission in different dry solvent (ACN, ethanol, methanol, THF, acetone and toluene) and dual emission in water and DMF as our previously published compound **1**.[31] The water titration experiment is now performed in different dry solvents. For these experiments, 3 mg of each activated sample is placed in a closed container with 3 ml of individual solvent. Then it is sonicated for 5 minutes to have a uniform suspension. This suspension is placed on the spectrofluorometer and emission data is collected after addition of a certain amount of water followed by 2 minutes wait time. Dry acetonitrile, dry ethanol, dry methanol, dry THF and dry acetone; have been used for these studies (Figure 13, 14). These experiments clearly show that for all the solvents the emission intensity enhances at the beginning and afterwards it got divided into two maxima, i.e., it started exhibiting ESIPT behavior.

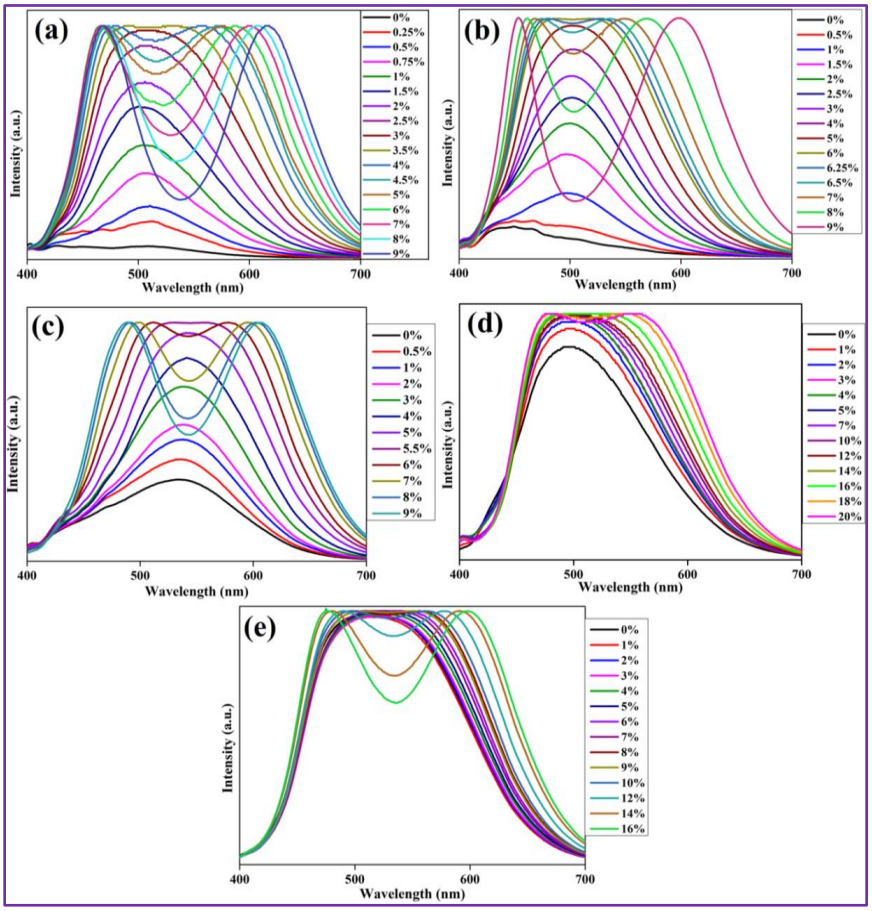

Figure 13. Water titration of activated compound **2** in different dry solvent; (a) Acetone, (b) THF, (c) ACN, (d) EtOH and (e) MeOH (λ_{ex}=350 nm).

For activated **2**, lowest titer amount found as 3.5 v/v % of water in acetone. On the other hand, for activated **3** (**3′**) lowest titer amount found as 1 v/v % of water in EtOH. For clarity, in different solvents, the lowest peak splitting with water percentage (%) is provided in table 1. Comparing the sensitivity in different solvent it is logical to comment that dht ligand is the reason behind all these different ESIPT phenomena when it is embedded in a framework. It is also clear that when the system moves from dynamic to rigid (i.e. from **1** to **2**), although the system is ESIPT active but here more water is needed for the system to promote the proton transfer phenomenon. Whereas on re-introduction of dynamism by the 3,3'-coordinating ligand, the sensitivity significantly enhances for almost in all the solvent. Thus, it is quite logical to comment that the ease of the sensitivity is related to the framework dynamism.

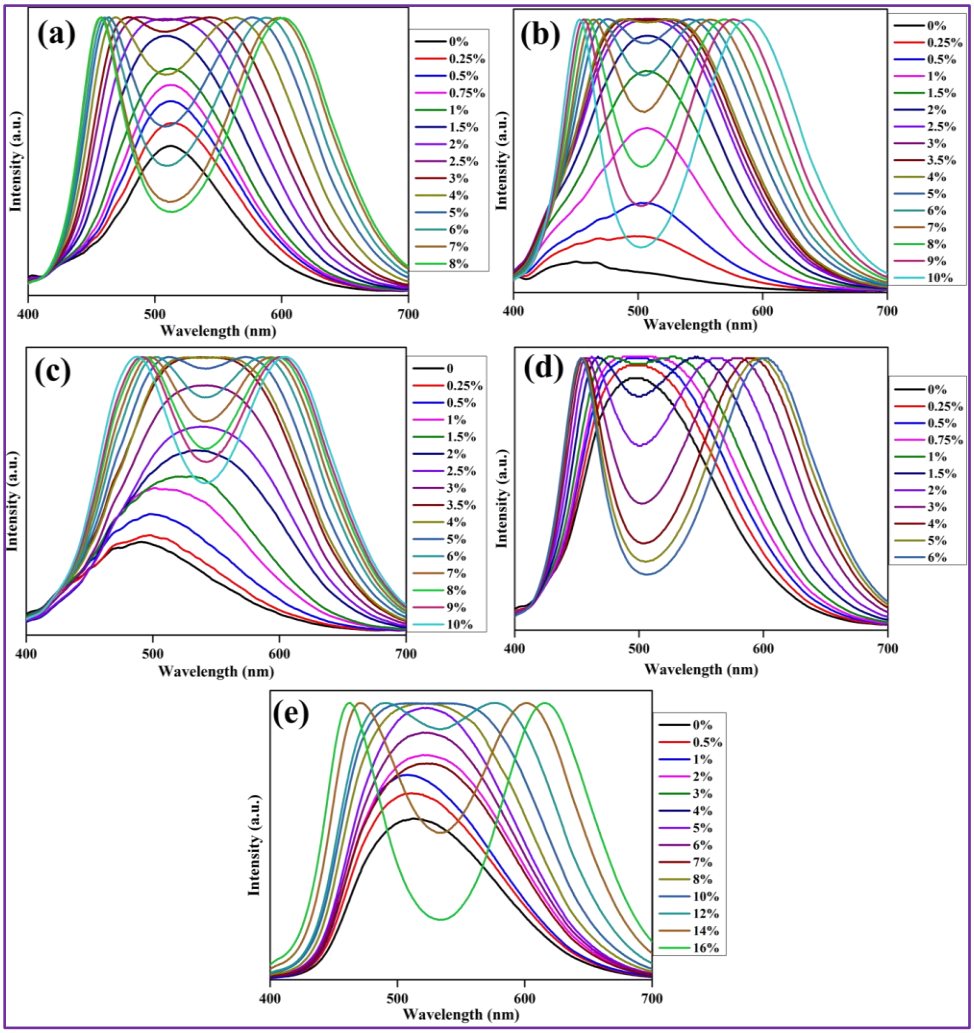

Figure 14. Water titration of activated compound **3** (**3′**) in different dry solvent; (a) Acetone, (b) THF, (c) ACN, (d) EtOH and (e) MeOH (λ_{ex}=350 nm).

Table 7. Minimum water percentage (v/v) required to facilitate ESIPT phenomenon in different dry solvent for activated **1** (**1′**), **2** (**2**) and **3** (**3′**)

	Acetone	THF	ACN	EtOH	MeOH
Activated **1** (**1′**); dynamic	2	1	4	4	0.25
Activated **2**; rigid	3.5	6	5.5	16	12
Activated **3** (**3′**); dynamic	2.5	3.5	4	1	10

4.3.7. Mechanism Behind Involvement of Water or DMF for ESIPT Process

The water titration study suggests that water is directly involved in the transfer of hydrogen from one donor to another accepter, as with increase of the water percentage the ease of ESIPT process in individual environment increases rapidly. It is evident that on addition of water or DMF, the incoming solvent molecules are making hydrogen bond with enol hydrogen. A possible mechanism for the involvement of water in ESIPT may be drawn on the basis of the hypothesis that hydrogen bonded water is minimizing the transition state energy during concerted proton transfer occurring in between carboxylate oxygen and keto/enol oxygen (Scheme 2). Now with increase of the water percentage, there is more population of water molecules in the system which probably enhances the probability for the fluorophore to find a water molecule to facilitate tautomerism readily. Same phenomenon may be also happening for DMF molecules. It is also making hydrogen bond with enol hydrogen and responsible for stabilization of the transition state energy.

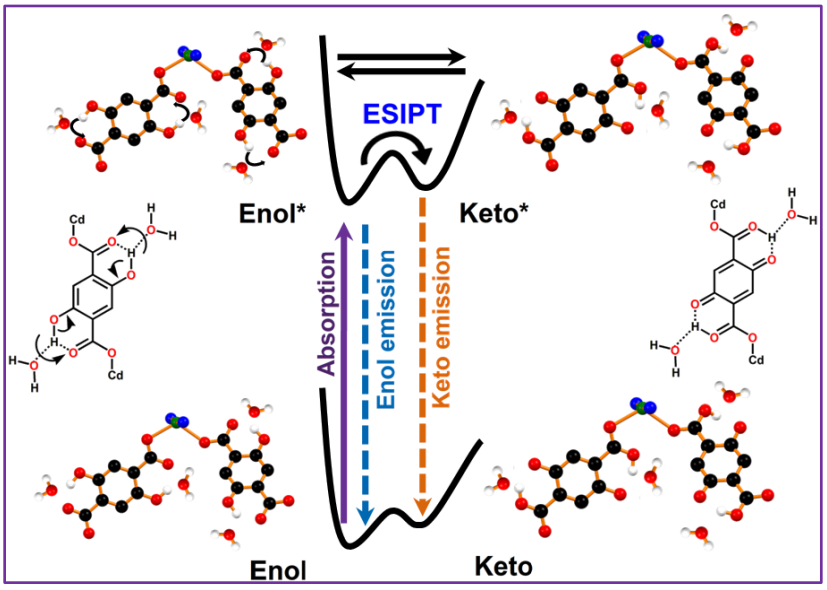

Scheme 2. Possible mechanism behind the involvement of the water molecules behind the ESIPT process.

4.4. CONCLUSION

Here two new Cd(II) MOF has been synthesized by the synthetic modification of a published Zn(II) based MOF to understand the structural tuning. First to study the effect of the size of metal ions on overall structure, property and structural dynamism, Cd(II) is used instead of Zn(II). The resultant system is non-dynamic in nature. Next modification is performed in the N,N′-donor ligand. A 3,3'-coordinating isomeric ligand is used instead of 4,4'-coordinating N,N′-donor ligand and here the dynamism is regained in the system. The dynamism in the system is established on the basis of extensive PXRD studies. Different gas and vapor adsorption studies also correlate the dynamic behavior. Due to presence of ESIPT fluorophore, both these systems are with dual emission behavior. Also like the previously published base material, both of these compounds show water sensing property in different organic solvent. Interestingly this study shows that the ease of water detection is directly related to the dynamism of the system. Here it has also been witnessed that the dynamic materials can detect water at a much lower percentage, when we compared it with a rigid non-dynamic compound, even having similar framework moieties. Therefore, this work is not only stands for a properly engineered framework structure with step-by-step modification but also it portrays clear understanding regarding the introduction of structural dynamism in MOFs. Last but not the least, this work is also stands for another verification tool to prove the efficacy of dynamic material over the rigid one; in the way to design of smart responsive materials.

REFERENCES

1. Mohammed, J. S.; Murphy, W. L. *Adv. Mater*. **2009**, *21*, 2361–2374.
2. Houck, H. A.; Blasco, E.; Du Prez, F.E.; Barner-Kowollik, C. *J. Am. Chem. Soc*. **2019**, *141*, 12329−12337.
3. Pallavi, P.; Kumar, V.; Hussain, W.; Patra, A. *ACS Appl. Mater. Interfaces* **2018**, *10*, 44696–44705.
4. Kreno, L. E.; Leong, K.; Farha, O. K.; Allendorf, M.; Duyne, R. P. V.; Hupp, J. T. *Chem. Rev*. **2012**, *112*, 1105–1125.
5. Sikdar, N.; Bonakala, S.; Haldar, R.; Balasubramanian, S.; Maji, T. K. *Chem. Eur. J*. **2016**, *22*, 6059–6070.
6. Wang, H.; Warren, M.; Jagiello, J.; Jensen, S.; Ghose, S. K.; Tan, K.; Yu, L.; Emge, T. J.; Thonhauser, T.; Li, J. *J. Am. Chem. Soc*. **2020**, *142*, 20088–20097.
7. Sponchioni, M.; Palmiero, U. C.; Moscatelli, D. *Mater. Sci. Eng. C.* **2019**, *102*, 589–605.
8. Yan, Z.-H.; Li, X.-Y.; Liu, L.-W.; Yu, S.-Q.; Wang, X.-P.; Sun, D. *Inorg. Chem*. **2016**, *55*, 1096–1101.

9. Verma, P.; Singh, A.; Maji, T. K. *Chem. Sci.* **2021**, *12*, 2674–2682.
10. Lee, J. H.; Jeoung, S.; Chung, Y.G.; Moon, H. R. *Coord. Chem. Rev*. **2019**, *389*, 161–188.
11. Li, G.-L.; Liu, G.-Z.; Ma, L.-F.; Xin, L.-Y.; Lia, X.-L.; Wang, L.-Y. *Chem. Commun*. **2014**, *50*, 2615–2617.
12. Halder, A.; Ghoshal, D. *CrystEngComm* **2018**, *20*, 1322–1345.
13. Sarkisov, L.; Martin, R. L.; Haranczyk, M.; Smit, B. *J. Am. Chem. Soc*. **2014**, *136*, 2228–2231.
14. Desai, A. V.; Sharma, S.; Let, S.; Ghosh, S. K. *Coord. Chem. Rev*. **2019**, *395*, 146–192.
15. Robison, L.; Drout, R. J.; Redfern, L. R.; Son, F. A.; Wasson, M. C.; Goswami, S.; Chen, Z.; Olszewski, A.; Idrees, K. B.; Islamoglu, T.; Farha, O. K. *Chem. Mater*. **2020**, *32*, 3545–3552.
16. Halder, A.; Bhattacharya, B.; Haque, F.; Ghoshal, D. *Cryst. Growth Des.* **2017**, *17*, 6613–6624.
17. Cheng, L.; Zhang, L.; Cao, Q.; Gou, S.; Zhanga, X.; Fanga, L. *CrystEngComm* **2012**, *14*, 7502–7510.
18. Cheetham, A. K.; Kieslich, G.; Yeung, H. H.-M. *Acc. Chem. Res*. **2018**, *51*, 659–667.
19. Bhattacharya, B.; Halder, A.; Maity, D. K.; Ghoshal, D. *CrystEngComm***2016**, *18*, 4074-4083.
20. Khatua, S.; Bar, A. K.; Konar, S. *Chem. Eur. J*. **2016**, *22*, 16277–16285.
21. Desai, A. V.; Sharma, S.; Roy, A.; Ghosh, S. K. *Cryst. Growth Des.***2019,***19*, 7046–7054.
22. J. Cornelio, J.; T.-Y. Zhou, T.-Y.; Alkaş, A.; Telfer, S. G. *J. Am. Chem. Soc*. **2018**, *140*, 15470–15476.
23. Goswami, A.; Ghosh, D.; Chernyshev, V. V.; Dey, A.; Pradhan, D.; Biradha, K. *ACS Appl. Mater. Interfaces* **2020**, *12*, 33679–33689.
24. Krause, S.; Hosono, N.; Kitagawa, S. *Angew. Chem. Int. Ed*. **2020**, *59*, 15325–15341.
25. Halder, A.; Bhattacharya, B.; Haque, F.; Dinda, S.; Ghoshal, D. *Chem. Eur. J*. **2019**, *25*, 12196–12205.
26. Cepeda, J.; Pérez-Mendoza, M.; Calahorro, A. J.; Casati, N.; Seco, M. J. M.; Aragones-Anglada; Moghadam, P. Z.; Fairen-Jimenez, D.; Rodríguez-Diéguez, A. *J. Mater. Chem. A* **2018**, *6*, 17409–17416
27. Wannapaiboon, S.; Schneemann, A.; Hante, I.; Epp, M. Tu, K.; Semrau, A. L.; Sternemann, C.; Paulus, M.; Baxter, S. J.; Kieslich, G.; Fischer, R. A. *Nat. Commun*. **2019**, *10*, 346.
28. Coudert, F.-X. *Chem. Mater*. **2015**, *27*, 1905–1916.
29. Maity, D. K.; Halder, A.; Pahari, G.; Haque, F.; Ghoshal, D. *Inorg. Chem*. **2017**, *56*, 713–716.
30. Férey, G.; Serre, C. *Chem. Soc. Rev*. **2009**, *38*, 1380–1399.
31. Bhattacharya, B.; Halder, A.; Paul, L.; Chakrabarti, S.; Ghoshal, D. *Chem. Eur. J*. **2016**, *22*, 14998–15005.
32. Halder, A.; Bhattacharya, B.; Dey, R.; Maity, D. K.; Ghoshal, D. *Cryst. Growth Des.***2016**, *16*, 4783–4792.
33. Dong, Y.-B.; Smith, M. D.; Loye, H.-C. Z. *Inorg. Chem*. **2000**, *39*, 4927–4935.
34. Kennedy, A. R.; Brown, K. G.; Graham, D.; Kirkhouse, J. B.; Kittner, M.; Major, C.; McHugh, C. J.; Murdoch, P.; Smith, W. E. *New J. Chem*. **2005**, *29*, 826–832.
35. Bhattacharya, B.; Halder, A.; Paul, L.; Chakrabarti, S.; Ghoshal, D. *Chem. Eur. J*. **2016**, *22*, 14998–15005.

36. SMART (V 5.628), SAINT (V 6.45a), XPREP, SHELXTL; Bruker AXS Inc.: Madison, WI, **2004**.
37. Sheldrick, G. M. SADABS, Version 2.03; University of Göttingen: Germany, **2002**.
38. Sheldrick, G. M. University of Göttingen: Germany, **2002**.
39. Sheldrick, G. M. *Acta Cryst.* **2015**, *A71*, 3-8.
40. Farrugia, L. J. *J. Appl. Crystallogr*. **1999**, *32*, 837–838.
41. Macrae, C. F.; Edgington, P. R.; McCabe, P.; Pidcock, E.; Shields, G. P.; Taylor, R.; Towler, M.; Streek, J. V. D. *J. Appl. Cryst*. **2006**, *39*, 453–457.
42. Blatov, V. A.; Shevchenko, A. P.; Serezhkin, V. N. *J. Appl. Crystallogr*. **2000**, *33*, 1193.
43. Blatov, V. A.; Carlucci, L.; Ciani, G.; Proserpio, D. M. *CrystEngComm* **2004**, *6*, 377–395.
44. Sedgwick, A. C.; Wu, L.; Han, H.-H.; Bull, S. D.; He, X.-P.; James, T. D.; Sessler, J. L.; Tang, B. Z.; Tian, H.; Yoon, J. *Chem. Soc. Rev*. **2018**, *47*, 8842–8880.

CHAPTER-5

Solid-State Solvent-Free Excited State Intramolecular Proton Transfer (ESIPT) in a Coordination Polymer and Its Temperature Dependence

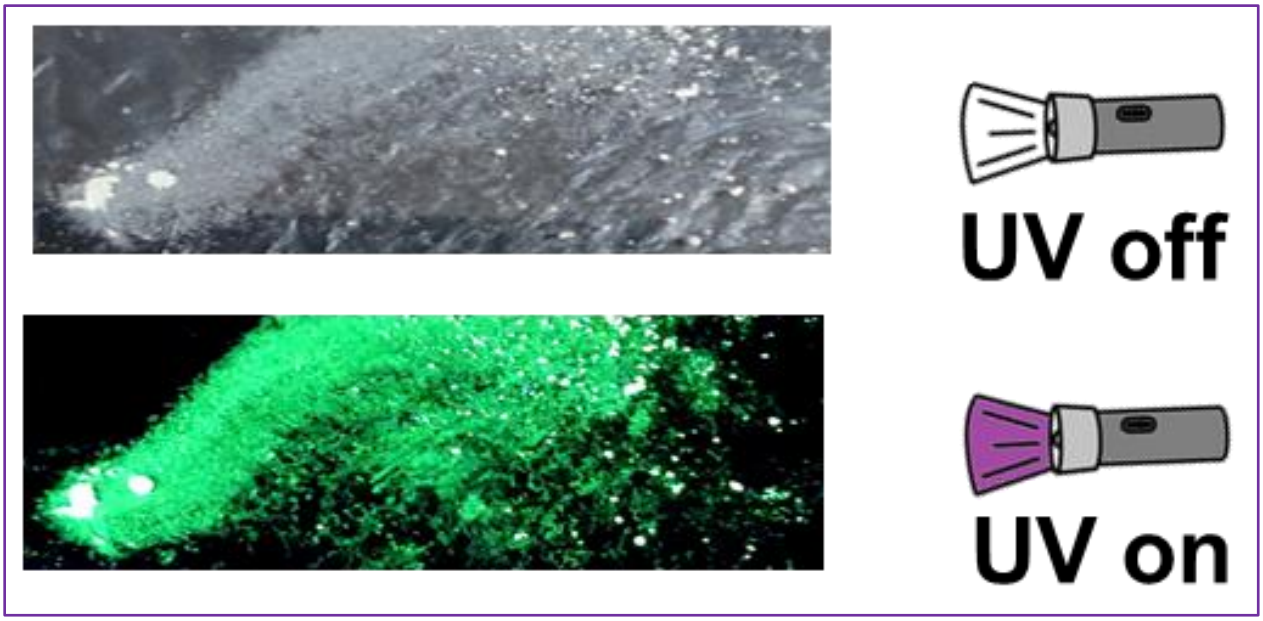

CHAPTER-5

Solid-State Solvent-Free Excited State Intramolecular Proton Transfer (ESIPT) in a Coordination Polymer and Its Temperature Dependence

5.1. INTRODUCTION

Luminogenic materials have engrossed a foremost role both in photophysical science as well as in optoelectronic industry due to their versatile use as sensors and/or imaging agent.[1–3] Generally, luminogenic materials exhibit an extreme change in emission behavior in presence of external stimuli like molecular sorption,[4] mechanical force,[5,6] and temperature,[7,8] to name a few. If the continuous change in a particular luminogenic behavior can be monitored against a particular external stimulus, the material can be used as the imaging or sensing agent.[9–11] Conversely, materials with an abrupt distinctive change of photo-physical behavior in presence of suitable external stimuli can be used as an on-off switch for different applications.[8,12] Among different photophysical phenomena, photo-induced structural isomerism (tautomerism) coupled ultra-fast intramolecular proton transfer could happen in a suitable system. This process is categorically known as excited state intramolecular proton transfer (ESIPT) (Scheme 1a), which is an interesting phenomenon to investigate in the context of aforesaid applications.[1,13] In an ESIPT process, two different excited states are formed, one from normal excitation of the parent molecule (N* of Scheme 1a) and another from the excited state proton transferred species (T* of Scheme 1a). [1,13] Consequently, from these two excitation states, two different emission maxima (dual emission) could be observed with large stroke-shift, which may be beneficial to eliminate any unwanted self-reabsorption and inner filter effects.[1,13] Among diverse tautomerism enabled molecules, ESIPT phenomenon is mostly observed and studied in hydrogen bonded keto-enol tautomeric systems (Scheme 1b).[13] A huge number of investigations, both in experimental and theoretical aspects, were performed for different objectives. So far, most studies are carried out in a solution phase, and these studies unambiguously contributed to essential understanding at the fundamental level. But due to aggregation-caused quenching (ACQ) or aggregation-induced emission enhancement (AIEE),[14,15] any luminogenic behavior is found to be highly concentration-dependent and always necessitates a range of operating concentrations for functionalities.[15,16] Additionally, for a particular application, solution phase long term stability of the active motif in the appropriate solvent often faces a great challenge. This makes solid-state ESIPT active systems as reasonable

choice for their possible application in different mechanical or temperature-sensitive switches,[17] organic light emitting diodes (OLEDs),[18] optical sensing[19] and laser applications[20] where the solution based ESIPT have shortcomings. Some external or internal environmental effects can even persist in a solid-state ESIPT active system (e.g. moisture from environment) which can alter intramolecular proton donation ability which in turn could change/terminate the ESIPT behavior.[20] Also, a system may reorient and/or reorganize under certain temperature and pressure swing conditions,[21] causing unpredictable ESIPT phenomena. Thus, this process demands a stable and structurally robust sustainable system where external environment has minor effect on the ESIPT phenomenon. In this connection, coordination polymer (CP) can pave the way for the purpose. Although a wide class of materials has been studied showing modular solid-state ESIPT behavior,[19,20] it is never observed in a coordination polymer (CP). CPs are already well-known for different celebrated applications and their specific application oriented structural modulation[22–26] which enables embedding of an ESIPT active motif. Due to well-defined periodic arrangement of the ligands in CPs, there are less possibilities of aggregation caused quenching phenomena.[14,15]

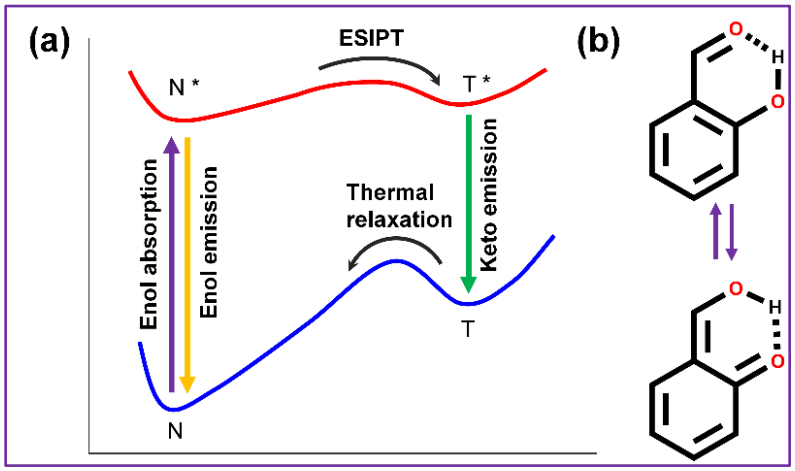

Scheme 1. (a) Schematic representation of ESIPT process which involves four level photo-cycles. **N** represents the normal ground state molecule at enol tautomer which populated to **N*** state on photoexcitation. **N*** can return to ground state by normal enol emission or it can transform to excited cross over keto form **T***. This **T*** eventually returns to the ground state by keto-emission followed by a thermal relaxation to enol form, **N**. (b) An example of mostly studied ESIPT active hydrogen bonded keto-enol tautomeric fragments. Here keto-enol tautomerism is shown in a representative molecule, salicylaldehyde.

Moreover, coordination bonds could impose extra stability on the ESIPT active ligands, even in a harsh condition. With intuitive design ingenuity an appropriate ligand can be employed to

construct the CP and structural modularity, can be leveraged for the structural screening to induce solid-state ESIPT phenomena. In this screening endeavor, we previously synthesized five CPs with suspension phase ESIPT behavior which strongly influenced by external environment; three of them[27,28] ([Zn(4-bpdh)(H_2dht)]·(MeOH)(H_2O)], [Cd(4-bpdh)(H_2dht)], and[Cd(3-bpdh)(dht)$_{0.5}$(H_2dht)$_{0.5}$(H_2O)]}; 4-bpdh=N,N'-bis(1-pyridin-4-yl-ethylidene) hydrazine,3-bpdh=N,N-bis(1-pyridin-3-yl-ethylidene)hydrazine and H_4dht=2,5-dihydroxyterephthalic acid) can show ESIPT behavior in presence of water and N,N dimethyl formamide (DMF) (Fig. 1a,b,c). Rest two compounds[29] ([Cd(bpe)$_{1.5}$(H_2dht)·Solvent] and [Cd(bpe)$_{1.5}$(H_2dht)]; bpe=1,2-bis(4-pyridyl)ethane and H_4dht=2,5-dihydroxyterephthalic acid) (Fig. 1d,e) show ESIPT in presence of commonly available polar solvents.

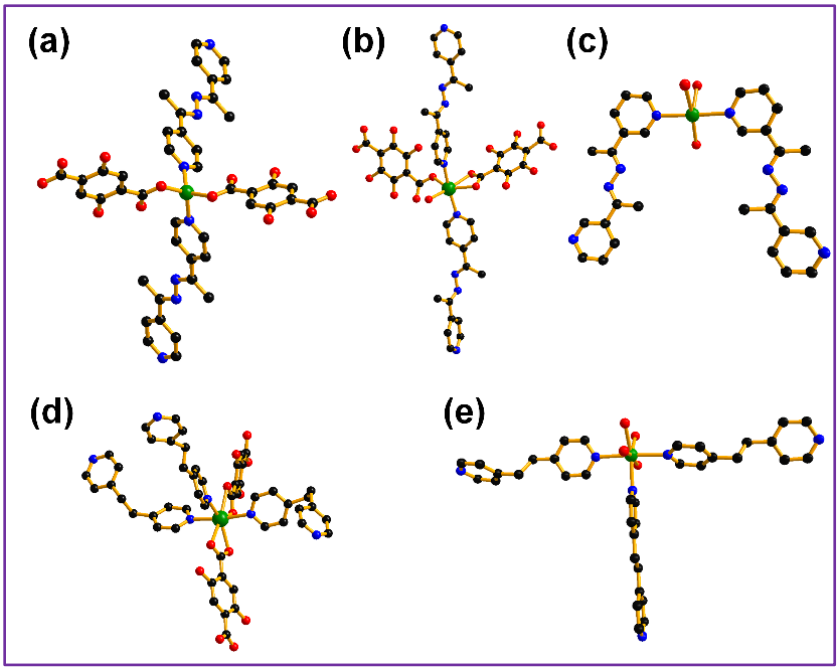

Figure 1. Coordination environment of five previously published (adapted from reference 27–29) solvent assisted ESIPT active coordination polymers. (a) ([Zn(4-bpdh) (H_2dht)]·(MeOH)(H_2O)], (b) [Cd(4-bpdh)(H_2dht)], (c) [Cd(3-bpdh)(dht)$_{0.5}$(H_2dht)$_{0.5}$ (H_2O)]}, (d) ([Cd(bpe)$_{1.5}$(H_2dht)·Solvent] and (e) [Cd(bpe)$_{1.5}$(H_2dht)]; 4-bpdh=N,N'-bis(1-pyridin-4-yl-ethylidene)hydrazine, 3-bpdh=N,N-bis(1-pyridin-3-yl-ethylidene)hydrazine,bpe=1,2-bis(4-pyridyl) ethane, and H4dht=2,5-dihydroxyterephthalic acid. Here d^{10} metal ion, Zn(II) for (a) and Cd(II) for (b)–(e),green sphere; carbon, black sphere; nitrogen, blue sphere and oxygen, red sphere. Hydrogen atoms are omitted for clarity.

For the first three CPs, –C=N-N=C– group is present in between two pyridine rings which are relatively more polar system than the connector –C–C– present in other two CPs.[27–29] Although there is no adequate evidence to claim that this connector systems are responsible for generalized (water and DMF to any polar solvent) solvent dependent ESIPT phenomenon for the last two CPs; but it may have influenced the ease of proton transfer for H_4dht. Considering this thought, here we have studied ESIPT phenomenon on a similar reported CP with formula [Zn(bpp)(H2dht)] (**1**) which has more carbons in the C–C chain[30] has been explored. Here –C–C– is replaced by –C–C–C– and 1,3-bi(4-pyridyl)propane (bpp) is used along with common building blocks, Zn(II) and H_4dht. Details luminogenic study of this CP show that this material does have a solid-state ESIPT phenomenon. Different solvent effects on this property were also studied. Different physiochemical studies are also performed on this material to determine the stability of the material under different conditions.

5.2. EXPERIMENTAL SECTION

5.2.1. Materials

All the used chemicals are reagent grade and were purchased from commercial sources. Highly pure $Zn(NO_3)_2{\cdot}6H_2O$ (98%), 1,3-bis(4-pyridyl)propane (bpp) (98%) and 2,5 dihydroxy terephthalic acid (H_4dht) were purchased from the Merck Sigma-Aldrich Chemical Company. All the solvents except dry solvents were purchased from Merck Millipore were used without further purification. Dry N,N-dimethylformamide (DMF) (99.8%), dry tetrahydrofuran (THF) (99.9%), dry acetonitrile (ACN) (99.8%), dry methanol (99.9%), dry ethanol (99.9%), and dry toluene (99.8%) were purchased from Merck Sigma-Aldrich Chemical Company and stored over molecular sieves to keep in their anhydrous condition. Highly pure, helium (99.999%), nitrogen (99.999%) carbon dioxide (99.95%) and hydrogen (99.99%) were used for all the adsorption experiments. Same grade nitrogen with additional silica absorber was used for the thermogravimetric analyses.

5.2.2. Physical Measurements.

Fourier-transform infrared (FTIR) spectra (4000–400 cm^{-1}) were taken on KBr pellet, using PerkinElmer Spectrum BX-II IR spectrometer. Thermo gravimetric analysis (TGA) and Differential thermal analysis (DTA) were carried out on a PerkinElmer STA 8000 thermal analyzer under nitrogen atmosphere (flow rate: 20 cm^3 min^{-1}) at the temperature range 30–600º C with a heating rate of 5º C/min. X-ray powder diffraction (PXRD) patterns for the sample were recorded

at room temperature using a Bruker D8 Discover instrument using Cu-Kα radiation (λ=1.5406) operating at 40mA and 40 kV. UV-visible spectroscopic analyses were performed on a PerkinElmer Lambda 35 spectrophotometer. A separate attachment, integrating sphere is used to measure the solid-state UV/vis spectra.

5.2.3. Sorption Measurements

All the adsorption studies were performed in a Quantachrome (now Anton Paar Quantachrome) Autosorb-iQ adsorption instrument. For all isotherms, ~ 40 mg of the air dried powder sample was placed in a pre-weighed analysis tube and placed to the out-gassing port of the adsorption instrument. Prior to an experiment, sample was degassed at 120 °C for 4 hour. Due to lack of any guest solvent molecules, outgas reached desired pressure (which is outgas rate < 3 militorr/min) very fast. After 4 hours, evacuated sample tube was removed from the out-gassing port and weight is taken to determine the mass of the degassed sample. Then this tube was transferred to the analysis port and ambient pressure volumetric N_2, H_2 and CO_2 gas adsorption studies were performed in the ambient pressure condition, ranging from 0 to 1 bar. N_2 and H_2 isotherms are collected at 77 K maintained by a liquid-nitrogen bath, whereas CO_2 isotherm was performed at 195 K (dry ice-acetone cold bath). Helium gas is used for the measurement of the void volume. During adsorption isotherm data collection, analysis gas was allowed to diffuse to the sample tube by opening the appropriate valve and degree of adsorption was determined by the change in the pressure at the equilibrium state. All operations were computer-controlled and automatic.

5.2.4. General Strategy for Emission Data Collection

All the emission spectra of the compound were studied either in solid state or suspended in the solvents are collected in Horiba FluoroMax 4. Solid state measurements were performed by filling the sample holder sample and a quartz plate was used to guard the sample from falling down. Then, it is placed in the instrument with installed solid state data collector. In a typical suspended state measurement, 3 mg of the sample is added to 3mL of solvent and sonicated for 10 minutes to get a good suspension. Then 2 mL of this suspension was transferred to the measuring cell and was placed in the instrument. Data collection was started after ~2 minutes of waiting time for all the samples.

For temperature-dependent emission spectral measurement, we have used Hahntech (DC-3006) circulation bath, an external setup with Horiba FluoroMax 4 has been used and collected the emission data from 0°C to 50° C.

5.2.5. Emission Life-Time Measurements.

Emission lifetime measurements were carried out by using time-correlated single photon counting set up from Horiba Jobin-Yvon. The luminescence decay data were collected on a Hamamatsu MCP photomultiplier (R3809) and were analyzed by using EZ time software. For photoexcitation, a delta-diode of 370 nm has used as the light source. For temperature-dependent lifetime measurements, a Peltier of Quantum Northwest external setup with Horiba Jobin-Yvon has been used and collected the emission data from 0°C to 50° C.

5.2.6. Synthesis

Synthesis of {[Zn(bpp)(H_2dht)]}$_n$ (1). Bulk compound is synthesized using a modified procedure than the reported procedure[1] by adding aqueous Zn(II) solution (1 mmol $Zn(NO3)_2 \cdot 6H_2O$ in 10 ml water) to the equimolar mixed ligand MeOH/H_2O solution (1 mmol Na_4dht and 1 mmol bpp in 20 ml MeOH/H_2O). Immediately a yellowish precipitate appeared and this solution was stirred over magnetic stirrer for 24 hours at room temperature. After 24 hours, polycrystalline powder of the compound was isolated by normal gravity filtration and washed with water (3 X 20 ml) and MeOH (3 X 20 ml) to remove any unreacted starting material. The polycrystalline product is then air dried by leaving it in the ambient environment.

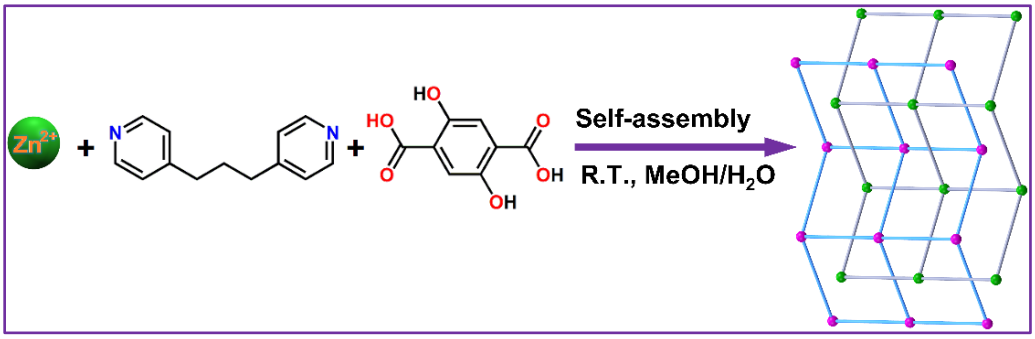

Scheme 2. General synthetic strategy for **1**, [Zn(bpp)(H_2dht)], with a topological representation of the structure determined by SC-XRD (adapted from reference 30). Here each sphere represents Zn(II) node, and the lines are representative of either bpp or H_2dht ligand**.**

5.3. RESULT AND DISCUSSION

5.3.1. Structural Description of Compound 1

This Zn(II) based coordination polymer crystalizes in orthorhombic *Pbca* space group and X-ray single crystal structural analysis suggest that each asymmetric unit consist of one Zn(II) ion, one bpp ligand and one H_2dht ligand (Figure 2a). The central metal ion forms a distorted tetrahedral geometry with ZnO_2N_2 donor set where two nitrogen atoms are from two different bpp ligands and

two oxygen atoms are from two different H_2dht ligand. Here H_2dht ligand connects Zn(II) centers to form one dimensional chain along crystallographic *c* direction and this chains are further connected by bpp ligands to form a 2D wavy net in the crystallographic *ac* plane (Figure 2b).

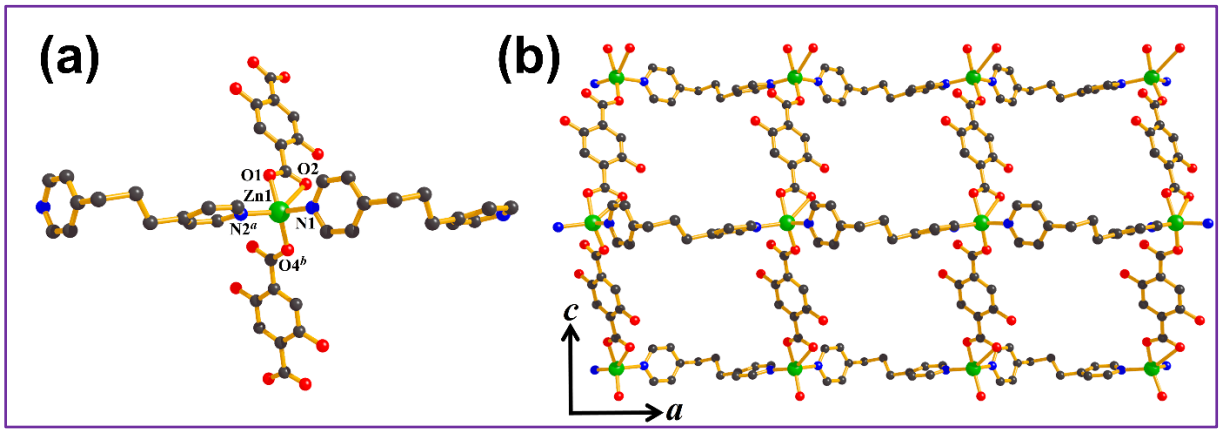

Figure 2. (a) Asymmetric unit of **1**, comprises of Zn(II) ion, one H_2dht and one bpp ligands. (b) Individual ligands connect two Zn(II) centers to form one dimensional (1D) chain along crystallographic *a* axis by bpp ligand and along crystallographic *c* axis by H_2dht ligands. These two 1D chains cooperatively form two dimensional (2D) wavy sheets along *ac* plane. Representation: Zn(II), green sphere; carbon, black sphere; nitrogen, blue sphere and oxygen, red sphere.

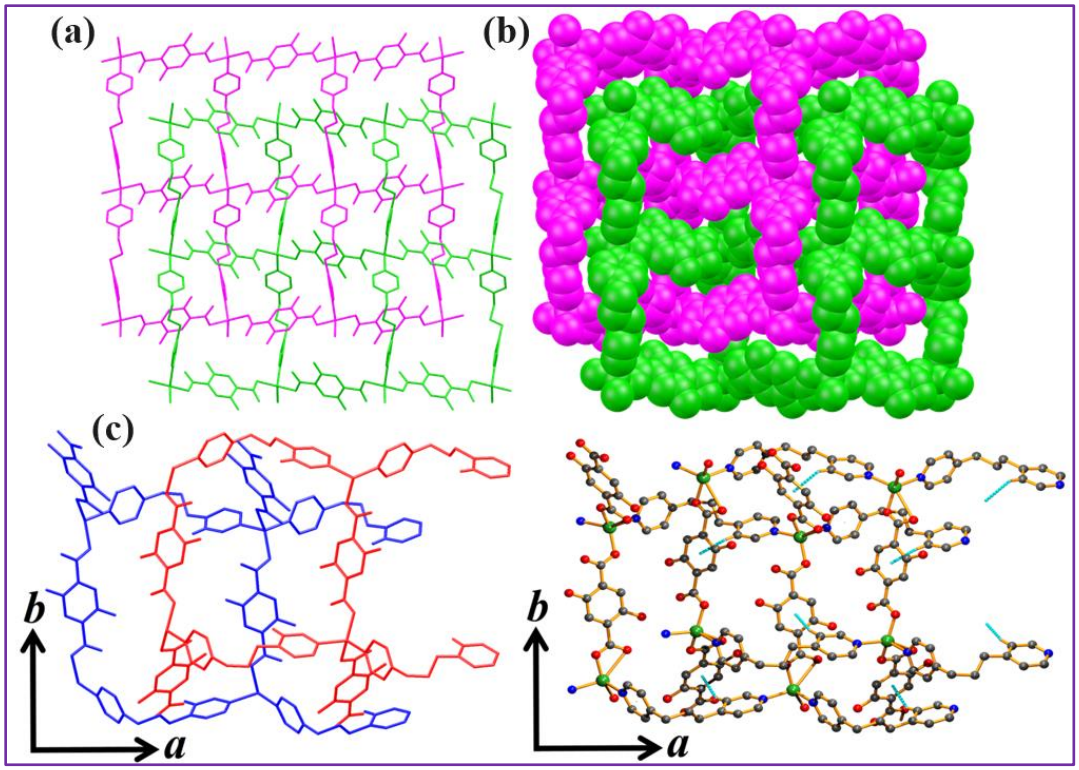

Figure 3. Inter-woven structure of compound **1**, (a) wireframe model and (b) space fill model.

Such two equivalent networks are catenated in the same direction to form two-fold inter-woven networks (Figure. 3). One intramolecular weak C–H…π interaction (Figure 4 and Table 1) in between C–H of a bpp ligand and aromatic ring of H_2dht ligand provides extra stability in the individual net. Whereas two different chains are held together by π…π interaction in between aromatic rings of two different ligands (Fig. 4 and Table 1).Representation of two inter-woven framework of **1** in *ab* plane, (c) without showing any weak interactions and (d) with intermolecular, also inter-framework, C–H…π interactions present between C–H from the bpp ligand and π cloud of the H_2dht ligand adapted from reference 1. Zn(II) is represented by green sphere, carbon as black sphere, nitrogen as blue sphere and oxygen as red sphere. Hydrogen atoms are omitted for clarity except the hydrogen atoms involved in C–H…π bond are presented here with white colored spheres. Here cyan dotted lines are representative of C–H…π bond present between hydrogen atoms to center of gravity of the π ring.

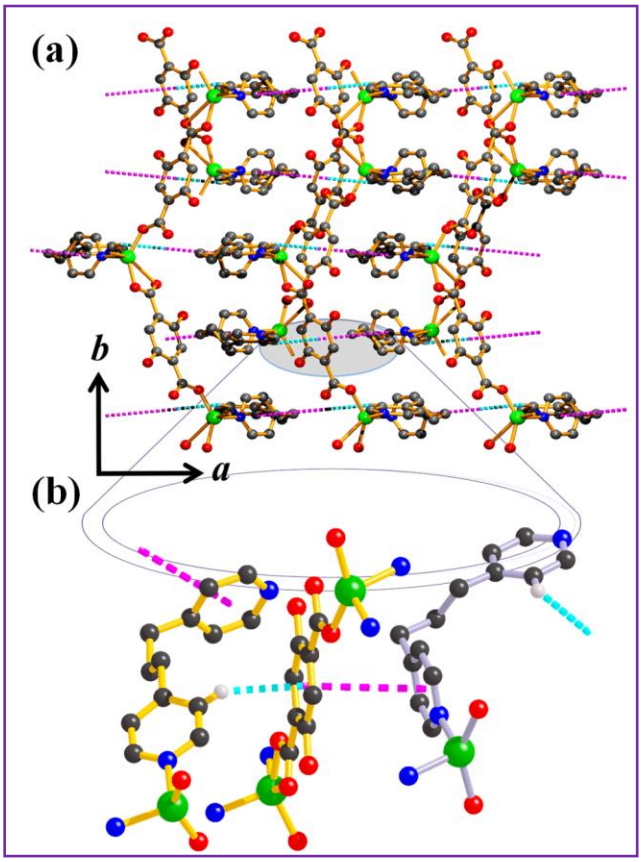

Figure 4. Weak interaction presents in **1**; (a) overall framework and (b) zoomed in view of the two different weak interactions adapted. Zn(II) is represented by green sphere, carbon as black sphere, nitrogen as blue sphere and oxygen as red sphere. Hydrogen atoms are omitted for clarity except the hydrogen atoms involved in C–H…π bond are presented here with white colored spheres.

Individual two-dimensional frameworks (with yellow colored bond in the zoomed in figure) are held together by C–H…π interactions (cyan colored bonds) (Table 1) between C–H from the bpp ligand and π cloud of the H_2dht ligand to forms inter-woven architectures. Such inter-woven architectures are connected to similar adjacent architecture (presented in magenta-colored bonds in the zoomed in figure) by π…π interaction (magenta-colored bonds) in between bpp linker (Table 1) and H_2dht ligand. This interaction enhances the structural dimension along *b* axis and forms a 3D supramolecular arrangement.

Table 1 π-π and C-H···π interactions in **1**.

ring(i) → ring(j)	distance of centroid(i) from ring(j),(Å)	dihedral angle (i,j) (deg)	distance between the (i,j) ring centroids, (Å)
R(1)→ R(2)^{i}	4.088(3)	10.9(3)	3.719(2)
R(2)→ R(1)^{ii}	4.088(3)	10.9(3)	3.829(2)
C-H→ ring(j)	H...R distance (Å)	C-H...R angle (deg)	C...R distance (Å)
C23–H23→ R(2)^{iii}	2.71	149	3.544(5)

Symmetry code: i =2-x,-1/2+y,1/2-z; ii =2-x,1/2+y,1/2-z; iii=1/2+x,y,1/2-z.
R(i)/R(j) denotes the ith/jth rings: R(1) = N(1)/C(9)/C(10)/C(11)/C(12)/C(13);
R(2) = C(2)/C(3)/C(4)/C(5)/C(6)/C(7).

5.3.2. Phase Purity and Thermal Stability

The material is synthesized herein by a different procedure than the previously published method.[30] So, to check the phase purity of the material, the polycrystalline powder is subjected to the PXRD study (Figure 5). The overlapping peak positions of simulated pattern to the pattern for as-synthesized material establish the bulk phase purity of the material.

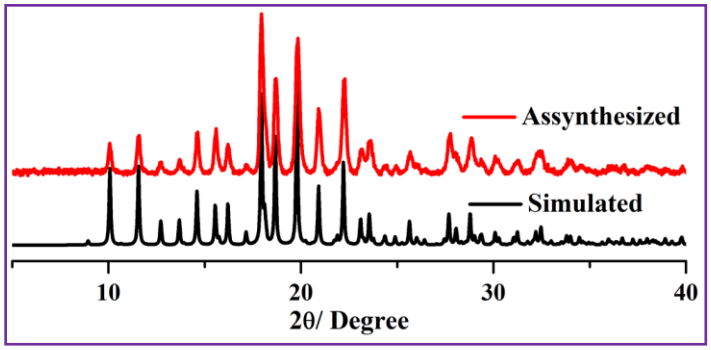

Figure 5 Powder X-ray diffraction (PXRD) pattern for the as-synthesized **1**, collected under ambient condition.

The stability of **1**, in different solvents is verified by PXRD studies after 24 h (Figure 6); which is equivalent to the PXRD patterns of solvent dipped samples with the as-synthesized **1**. In the thermogravimetric study (Figure 7), an initial loss of mass is observed which is related to the residual solvent from the wet sample and then no loss in the mass is observed up to 240 °C. But after ~240 °C, a steady loss of mass is observed which is associated with the decomposition of the material into unrecognized products. In support of this hypothesis, we have performed consecutive DSC runs on the same sample. In the solvent free second run, there is a clear endothermic hump between ~40 and 60 °C. Although in this range there is no mass loss in TGA trace which supports an internal phenomenon like breakdown of the hydrogen bonding at this temperature (Figure 8).

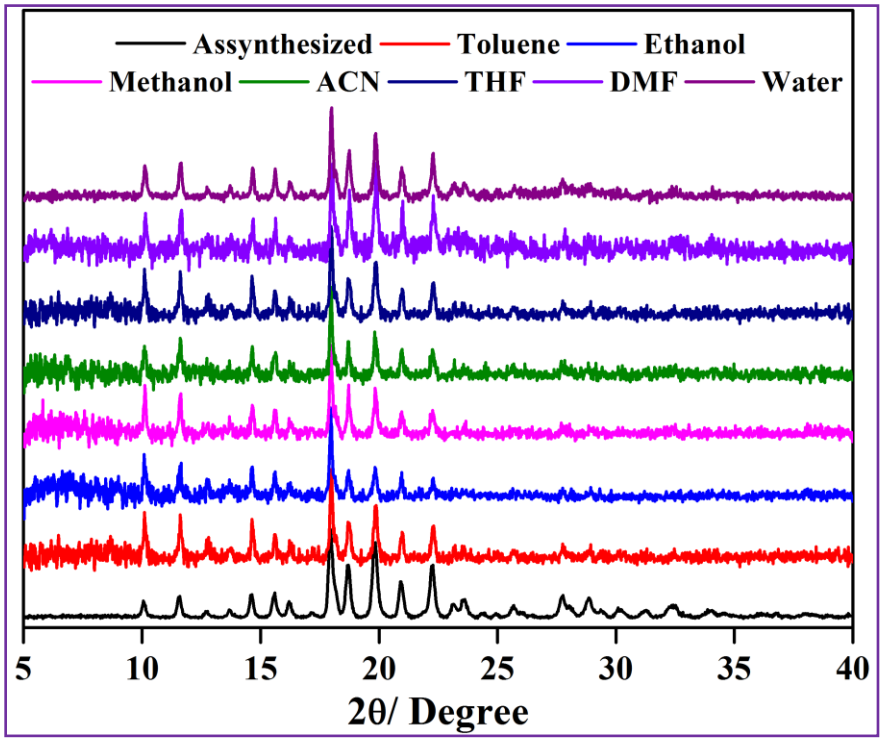

Figure 6 Powder X-ray diffraction patterns of recovered compound **1** from different solvents after emission spectral study. After emission study the compound **1** was left in the different analysis solvent for 24 hour. Then it is filtered and air dried to perform PXRD experiment. Here black colored pattern is for as-synthesized where as others are for different solvents. Peak to peak matching of recovered compound's pattern with the assynthesized pattern suggests structural integrity of the material. In the first run, there is some endothermic peak due to removal of residual solvent molecules (Figure 8).

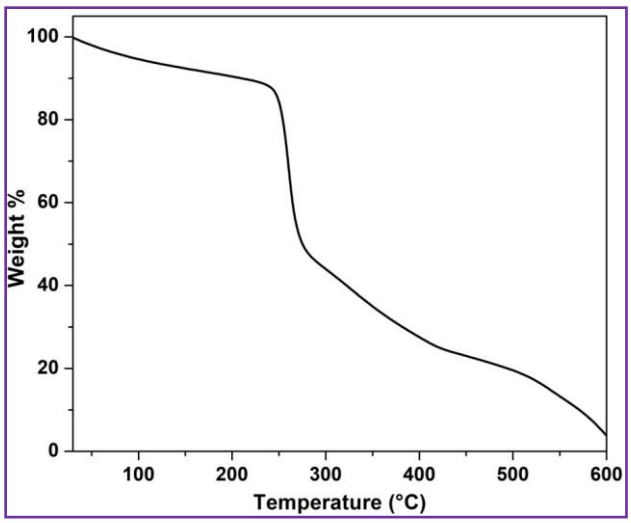

Figure 7 Thermogravimetric analysis of air dried compound **1**. The analysis conducted using a PerkinElmer STA 8000 thermal analyzer under nitrogen atmosphere (flow rate: 20 cm^3 min^{-1}) at the temperature range 30–600º C with a heating rate of 5º C/min. Mass correction is not performed due to buoyancy effects. Rapid mass loss after 240 °C is likely happened thermal decomposition of the framework.

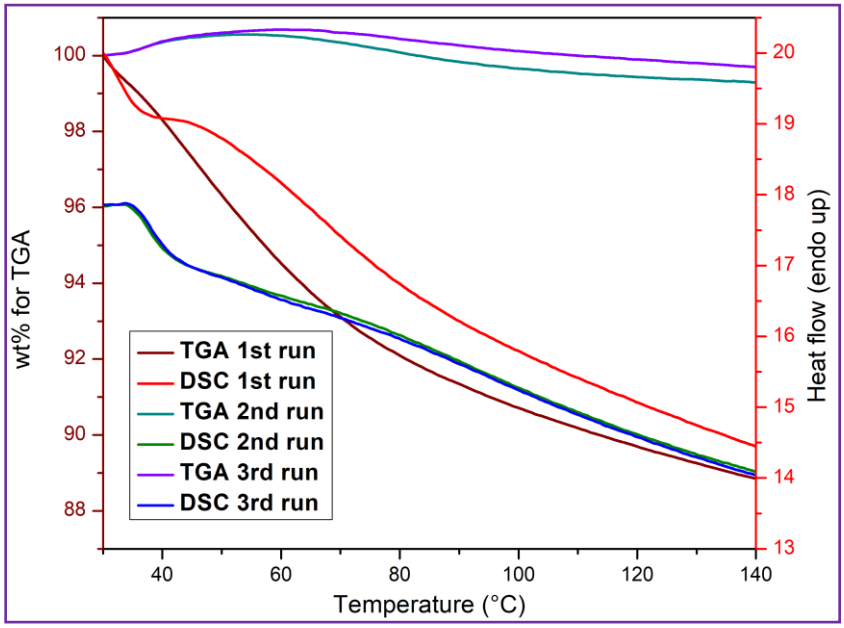

Figure 8. Multiple TGA and DSC curves for same sample of **1**. Change of slope in 2nd or 3rd DSC curve can be observed around 40 °C where there is no weight loss is observed in that region for 2nd or 3rd TGA curve. These combined observations suggest that it is associated with some internal phenomenon, possibly breakdown of the intra molecular hydrogen bonding. Equivalent curve pattern for multiple runs on same sample suggest structural integrity for the compound, in this operating temperature region. The difference in the 1st run is due as a MeOH/water washed sample is used without drying.

5.3.3. Fourier-Transform Infrared Spectroscopy (FTIR) on KBr Palate:

Fourier-transform infrared (FTIR) spectra (4000–400 cm^{-1}) were taken on KBr pellet, UV-visible spectroscopic analyses were performed on a PerkinElmer Lambda 35 spectrophotometer. A separate attachment, integrating sphere is used to measure the solid-state UV/vis spectra.

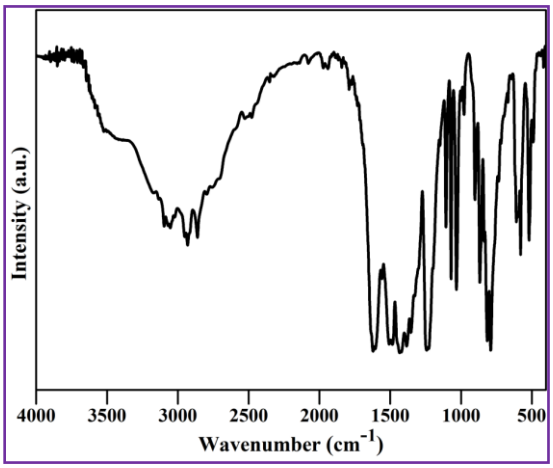

Figure 9 Fourier-transform infrared spectroscopic (FTIR) data for the bulk phase of **1** on KBr pellets.

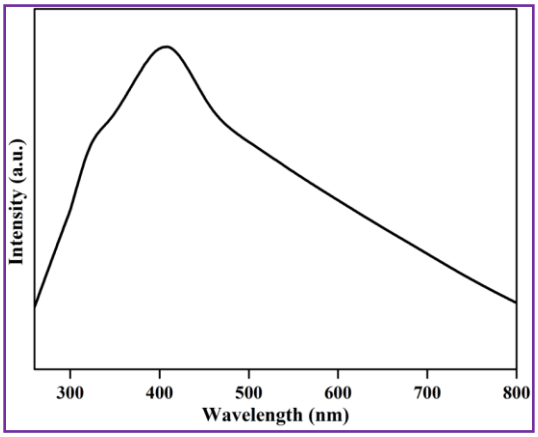

Figure 10 UV-Vis spectrum of compound **1** at solid state, collected by PerkinElmer Lambda 35 spectrophotometer with integrating sphere attachment to measure UV/vis spectra solid state. Around 40 mg of the sample was loaded in the sample holder which was then placed in the solid-state attachment and UV/vis spectra is collected in reflectance mode using default software for the instrument.

5.3.4. Different Gas Adsorption Isotherms

Multipurpose crystallographic software PLATON suggests that the material does not content significant void space which is also supported by different gas adsorption analyses (N_2, CO_2 and H_2) where the material shows non-porous nature (Figure 11) to all these gas molecules with negligible uptake amount.

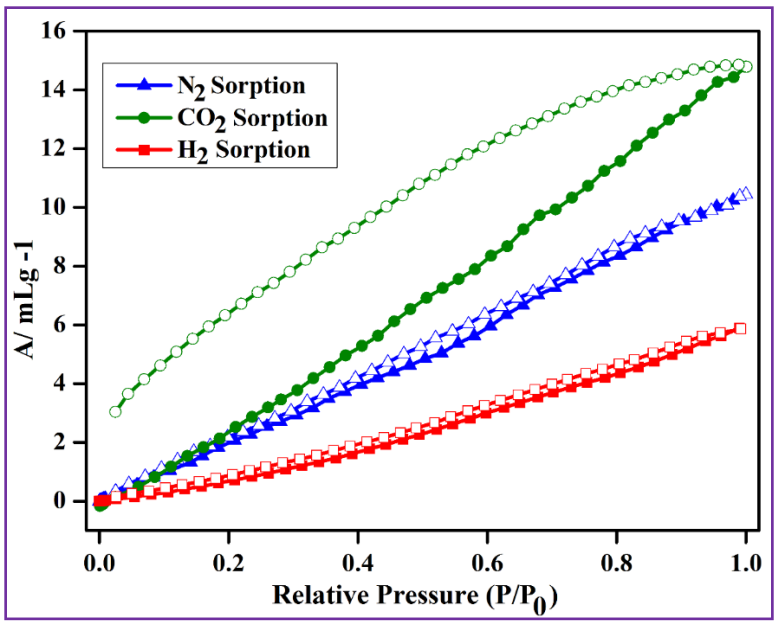

Figure 11 N_2 (blue triangle), CO_2 (green circle) and H_2 (red square) sorption isotherms of degassed **1**, measured at 77 K for N_2 and H_2 and 195 K for CO_2. Filled and open triangles represent adsorption and desorption respectively. Lines connecting data points are only guidelines for eyes and they do not represent any mathematical fits. Low adsorption value for all the analysis gasses indicates non-porous nature of the material which is accordance with the structure obtained from single XRD data.

5.3.5. Luminescence Behavior and Solid-State ESIPT

Most interesting feature for compound **1** is discovered when accidentally a sample vial is opened under UV light (365 nm); dry air-borne compound glows in an intense green color. This event has been captured and the video is provided as supporting material (VSI). On exposure of **1** to UV light (commercially available UV sources of 365 nm and 395 nm), an intense green emission from the compound was observed (Fig. 12a–d). Luminogenic behavior, responsible for this highly intense emission phenomenon, became clear from detailed excitation-wavelength-dependent emission spectral measurements, within the domain of 340–400 nm at room temperature (Figure 12e). The presence of well-defined broad dual emission peaks (at ~435 nm and ~615 nm) without altering their maxima throughout the measurement suggests that the present material has solid-state ESIPT behavior. Here it is worth mentioning that Ghoshal et. al. and some others have already demonstrated that coordination polymers with dht ligand exhibit intriguing luminescence properties and interesting ESIPT phenomenon.[27–29] But for all of them, the material needs to be in a suspension state and without any solvent used for the suspension; the material has shown only a single maximum emission behavior without any ESIPT behavior.

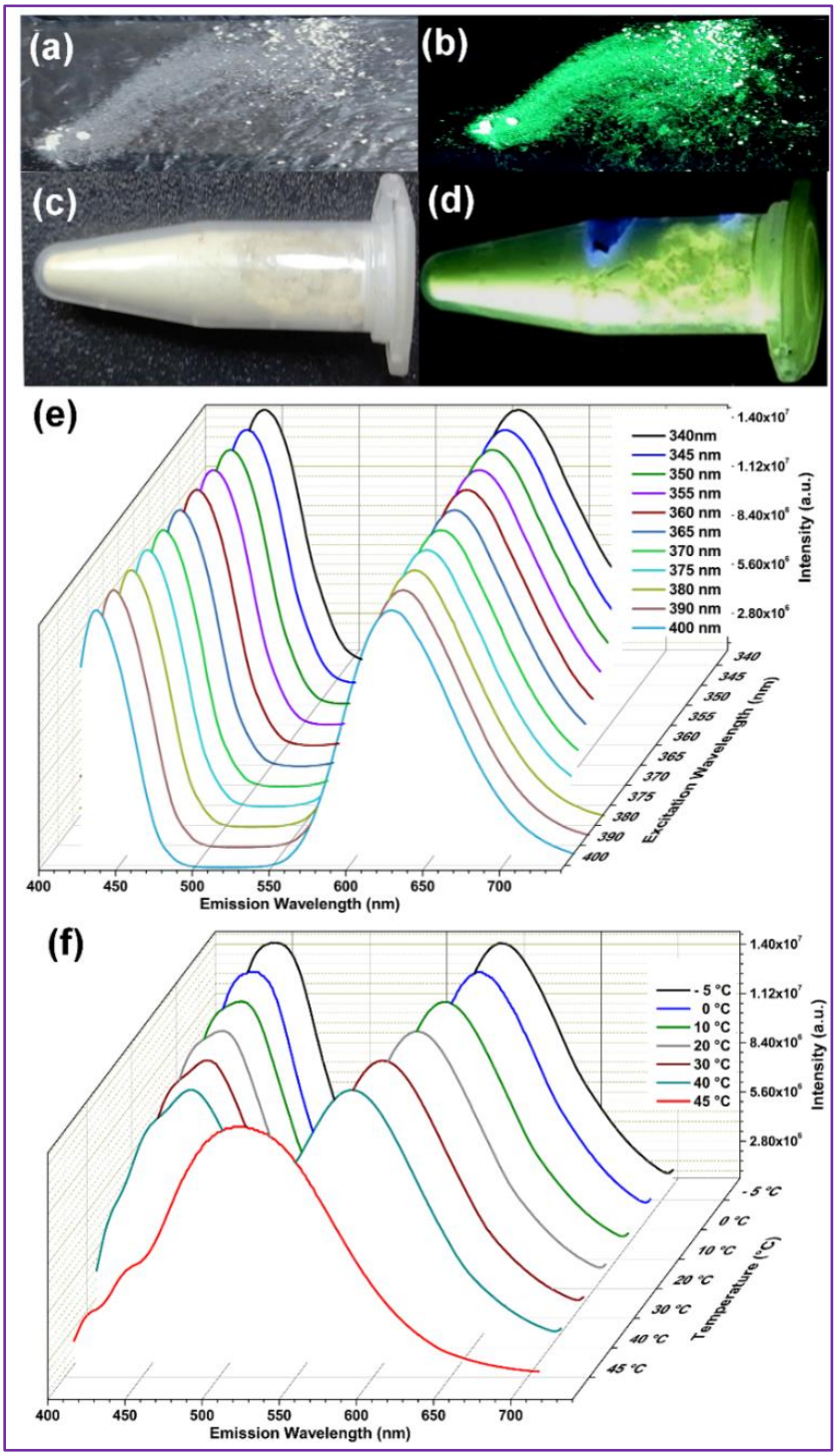

Figure 12. Real time photograph of compound **1** (a) under normal light, (b) under UV light (Philips made 365 nm UV lamp) and (c) under normal light in a sample vial and (d) under UV light in a sample vial. (e) Emission spectra of compound **1** at solid state with different excitation wavelengths in the range of 340–400 nm. (f) Temperature dependent emission.

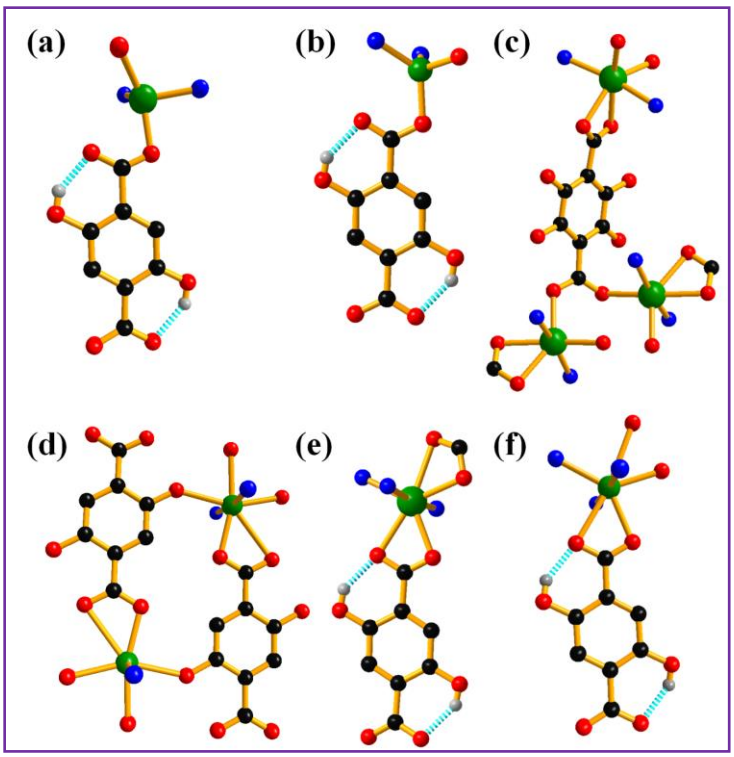

Figure 13 Coordination environment around H_2dht ligand and intramolecular hydrogen bonding in **1** and other 5 discussed compound, generated from reference; (a) **1**, (b) ([Zn(4-bpdh)(H_2dht)]·(MeOH)(H_2O)], (b) [Cd(4-bpdh)(H_2dht)], (c) [Cd(3-bpdh)(dht)$_{0.5}$(H_2dht)$_{0.5}$(H_2O)]}, (d) ([Cd(bpe)$_{1.5}$(H_2dht)·Solvent] and (e) [Cd(bpe)$_{1.5}$(H_2dht)], whereas 4-bpdh=N,N'-bis(1-pyridin-4-yl-ethylidene)hydrazine,3-bpdh=N,N-bis(1-pyridin-3-yl-ethylidene)hydrazine, bpe=1,2-bis(4-pyridyl)ethane and H_4dht=2,5-dihydroxyterephthalic acid. Here Zn(II) or Cd(II) is represented by green sphere, carbon as black sphere, nitrogen as blue sphere and oxygen as red sphere. Hydrogen atoms are omitted for clarity except the hydrogen involved in intra-molecular hydrogen bonding are presented here with white colored spheres.

Interestingly, for this current system, it does not need any solvent support for the ESIPT phenomenon and possibly this is the first report of solid-state ESIPT active CP. When we were searching for the probable reason behind this ESIPT phenomenon, it observed that one crucial intramolecular interaction is active in all these systems with dht ligand, *viz*. hydrogen bonding between hydroxyl group and carboxylic oxygen atom (Figure 13) of H_2dht ligand. A comparison of distance between hydroxyl hydrogen and carboxylic oxygen suggests that for compound **1**, it is ~1.8 Å which is at least 0.3 Å lower than our previously published five CPs (Figure 13, Table 2).[27–29] This stronger intramolecular H-bond strength in this present system compared to other similar systems (Figure 13, Table 2) is probably the reason behind the efficient proton transfer resulting spontaneous ESIPT event.[31] From previously published reports, it is worth to mention

that H_4dht (H_2dht^{2-} in the CP) is the origin of the ESIPT phenomenon and the enol form shows the lower wavelength emission (~435 nm) whereas the keto form shows higher wavelength peak (~615 nm) (Figure 11e). Thus, only excitation energy from UV source (360 nm) is sufficient to facilitate proton transfer or the tautomerism process and no solvent assistance is required here, like in other CPs. This is further supported by the solid-state emission spectroscopic study carried out in different excitation wavelengths (Figure 12e). Additional strong hydrogen bonding interaction present in this CP makes the atoms of H_4dht co-planner which is probably responsible for the observed spontaneous ESIPT.

Table 2. Intra-molecular hydrogen bonding present in the coordinated H_2dht ligand of the six ESIPT enabled CPs. Values are calculated from cif adapted from reference.

CP	D – H distance (Å)	D...A distance (Å)	D - H...A distance (Å)	D - H...A angle (deg))
([Zn(4-bpdh)(H_2dht)]·(MeOH)(H_2O)])[27]	0.82	1.83	2.553(6)	146
([Cd(4-bpdh)(H_2dht)])[28]	Hydroxyl hydrogen is not fixed			
([Cd(3-bpdh)(dht)$_{0.5}$(H_2dht)$_{0.5}$(H_2O)])[28]				
([Cd(bpe)$_{1.5}$(H_2dht)·Solvent])[28]	0.82	1.83	2.547(4)	145
[Cd(bpe)$_{1.5}$(H_2dht)][29]	0.82	1.86	2.578(6)	145
1, ([Zn(bpp)(H_2dht)]), Present work	0.82	1.80	2.533(8)	147

Here ‘D’ stand for donor oxygen and ‘A’ stand for acceptor oxygen atoms in the ground state (enol form) of the dht moiety. 4-bpdh=N,N'-bis(1-pyridin-4-yl-ethylidene)hydrazine,3-bpdh=N,N-bis(1-pyridin-3-yl-ethylidene)hydrazine, bpe=1,2-bis(4-pyridyl)ethane, bpp=1,3-bis(4-pyridyl)propane and H_4dht=2,5-dihydroxyterephthalic acid. To evaluate the solvent effect, emission spectrum of **1** under suspension condition in different dry common solvents has also recorded (Figure 14). In all solvents, except ACN and DMF, the enol emission appeared within 420–435 nm whereas keto emission within the emission window of 605–625 nm (Figure 14) which are very close to the spectra observed in the solid-state (Figure 12e). This constancy in the luminogenic behavior suggests that ease of proton transfer is independent of adjacent solvent molecules. This confirms the stability of **1** under highly solvated condition as well. Thus, other than the small discrepancy in DMF and ACN, the ESIPT behavior of **1** persists under excess solvent exposure, suggesting potential usability of this CP as a solid-state ESIPT emitter under extremely harsh solvent environment. In DMF, the two peaks are closer than other solvents (enol

at ~480 nm and keto ~590 nm), whereas in ACN two maxima almost merge to one (enol at ~490 nm and keto at ~590 nm) (Figure 14). The proton acceptor capability of nitrogen(s) present in those two solvents may have shown stronger affinity towards the protons in the CP and that may responsible for the difference in ESIPT behavior in above two solvents.

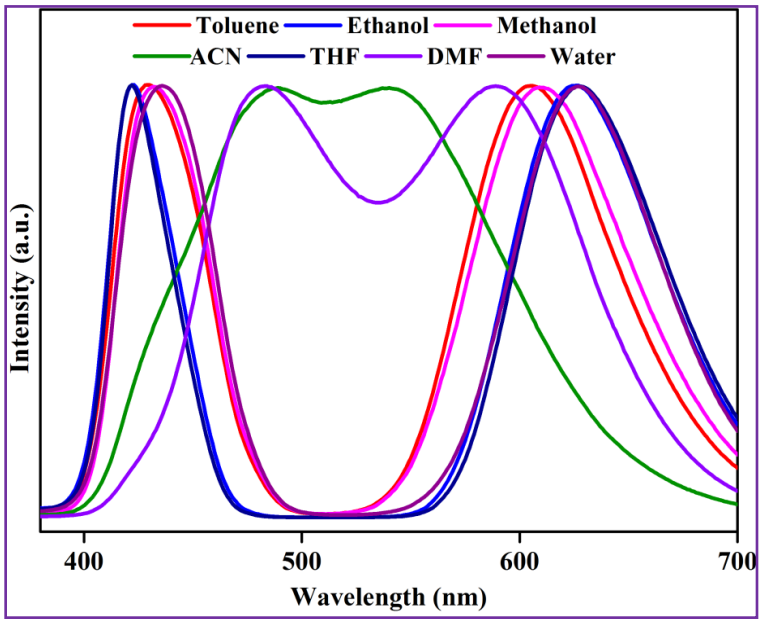

Figure 14 Emission spectra of **1** at suspension state in different solvent, water, dry N,N-dimethylformamide (DMF), dry tetrahydrofuran (THF), dry acetonitrile (ACN), dry methanol, dry ethanol, and dry toluene. During all these studies excitation wavelength was 360 nm.

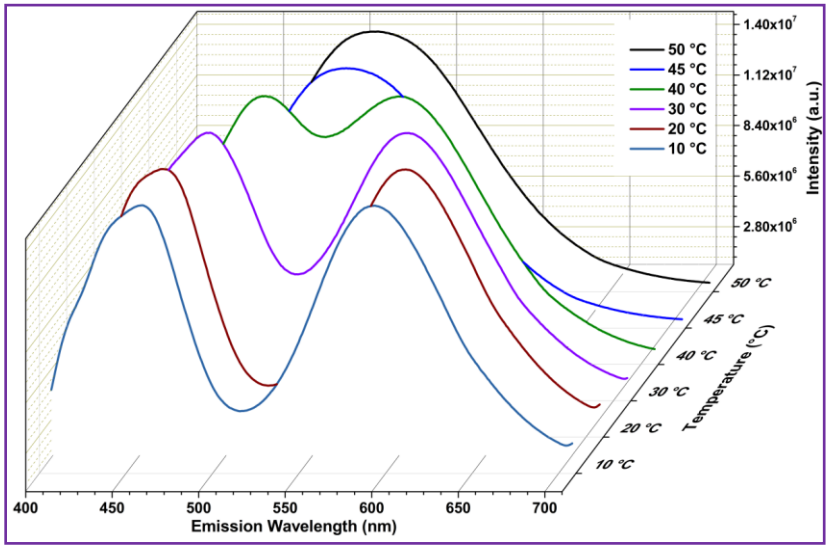

Figure 15. With decrease of temperature single peak divided into two separate peaks. From the temperature up scan and back scan it is very clear that ESIPT phenomenon is reversible in nature for this compound. During all these studies excitation wavelength was 360 nm.

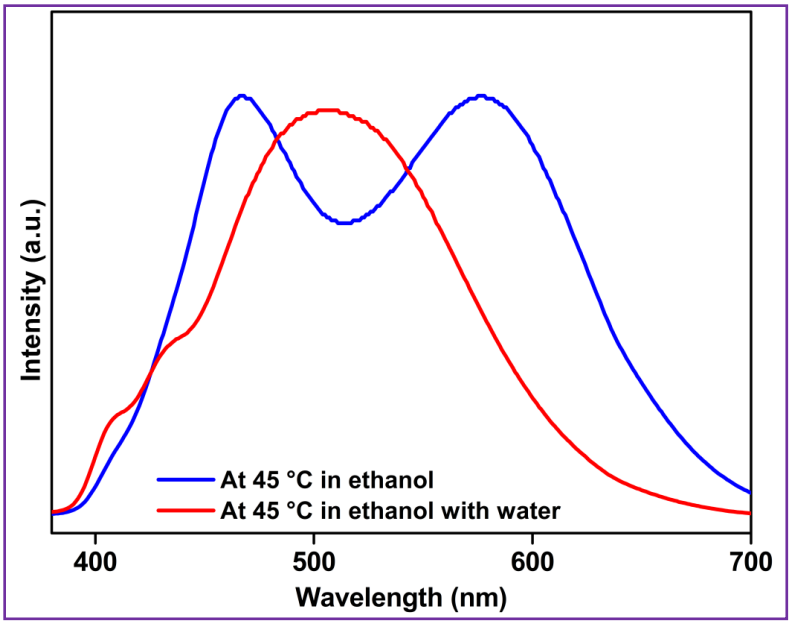

Figure 16 Emission spectra of compound **1** at 45 °C in dry ethanol suspension (red) and for the same suspension after addition of water (blue). During all these studies excitation wavelength was 360 nm.

Finally, to evaluate the range of operating temperatures of this ESIPT phenomenon, variable temperature steady-state and time-resolved emission spectroscopic studies are performed. Considering instrument compatibility, and equivalent peak position and performance in ethanol as in the solid state, this study is performed with ethanolic suspension of **1**. The study shows that even at lower temperatures like –5 °C, **1** shows profound ESIPT behavior that continues up to ~ 45 °C (Figure 3f). After that, no dual peak is observed. In this regard, our hypothesis is that at ~ 45 °C, the intramolecular hydrogen bonding interaction collapses, causing no further ESIPT afterwards. It is observed that irrespective of temperature, overall lifetime and decay profile is very similar at both the monitoring wavelengths. Similar endothermic curve at multiple DSC runs suggest that on decrease of temperature every time the hydrogen bonding is restored which is also evident from the emission data after decrease of temperature, where sample started to show dual emission after cooling down below ~40 °C (Figure 15). Interestingly, at higher temperature (>45 °C), dual emission is reappeared in presence of trace amount of water (Figure 16) which further supports that above the mentioned temperature, ESIPT is not happening due to unfavorable hydrogen transfer which can be reactivated with solvent assistance.[32]

5.3.5. Life Time Study

Lifetime measurement in both the emission maxima via TCSPC also indicates the existence of two types of emitting species, the species with lower emission maximum decays in a bi-exponential manner with lifetime of τ_1=1.5 ns (30%) and τ_2=5.8 ns (70%), while species having higher emission maximum decays in a mono exponential way with τ=5.7 ns (Figure 17).

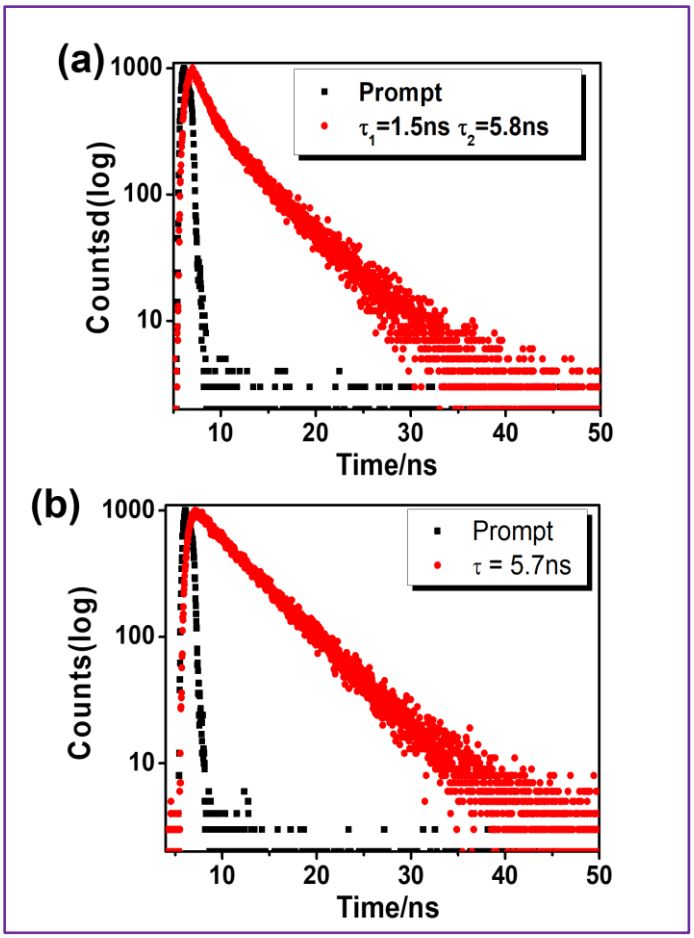

Figure 17. Excited state decay profiles for **1** in EtOH at room temperature upon monitoring emission at 450 nm (a) and at 590 nm (b). Photoexcitation was done by using delta flex of 370 nm as light source. Insets of the profile show lifetime values.

Temperature-dependent lifetime measurements were performed with 370 nm excitation source and emission decays are monitored at both wavelengths (450 and 590 nm) within the temperature range of 0–50 °C (Figure 18). Additionally, contribution of initial short-lived component of 450 nm emission steadily decreases with concomitant increase of second long-lived component upon increase of temperature and becomes almost mono exponential at ~50 °C.

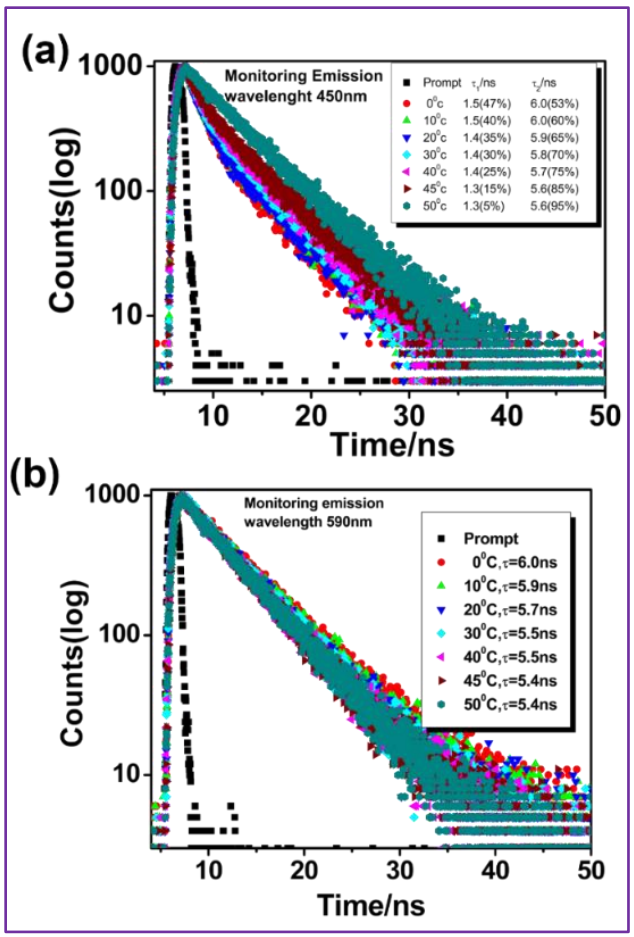

Figure 18. Change of excited state decay profile for **1** in EtOH upon variation of temperature within the range of 0–50 °C at the monitoring emission wavelength of (a) 450 nm, and (b) 590 nm. Photoexcitation was done by using delta-flex of 370 nm light source. Insets of the profile show lifetime values.

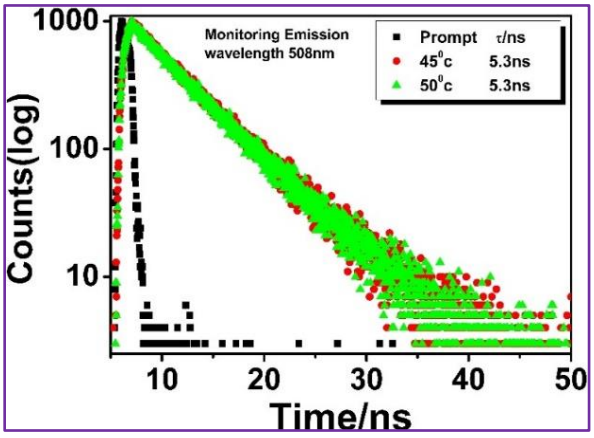

Figure 19. Change of excited state decay profile for **1** in EtOH upon variation of temperature 45 and 50^{0}C at the monitoring emission wavelength of 508 nm. Photoexcitation was done by using delta-flex of 370 nm as light source. Insets of the profile show lifetime values.

The bi-exponential decay for shorter wavelength emission probably indicates the existence of hydrogen-bonded structure in the enol form of the CP and gradual increase of temperature induces systematic rupture of hydrogen bond, as evidenced by systematic decrease of initial decay component. Interestingly, a mono-exponential decay at 508 nm has also observed where two emission maxima merged above 45 °C (Figure 19).

5.4. CONCLUSION

The solid state ESIPT behavior of a previously published Zn(II) based coordination polymer along with studied the temperature dependency of the ESIPT behavior which is directly associated with the change in the intramolecular interaction inside the coordination polymer. This temperature-dependent intramolecular interaction and the associated changes in the photo-physical behavior could be a pathway for the fabrication of smart molecular switch. This kind of switch is convenient for fabrication of smart devices where upon reaching a specific temperature, certain operations, e.g., heater, can be turned-off or services like cooler could be turned-on and vice-versa. In addition, the solvent-independency of ESIPT behavior has also demonstrated which in turn could be useful to apply such materials for ESIPT- induced potential photo-molecular switches even under extreme solvent exposed conditions. This work being the first report of solid-state solvent independent ESIPT active coordination polymer can be a possible robust raw material for the aforesaid switches in the opto-electronic industries.

REFERENCES

1. Sedgwick, A. C.; Wu, L.; Han, H. H.; Bull, S. D.; He, X. P.; James, T. D.; Sessler, J. L.; Tang, B. Z.; Tian, H.; Yoon, J. *Chem Soc Rev* **2018**, *47*, 8842–8880.
2. Treiling, S.; Wang, C.; Förster, C.; Reichenauer, F.; Kalmbach, J.; Boden, P.; Harris, J. P.; Carrella, L. M.; Rentschler, E.; Resch-Genger, U.; Reber, C.; Seitz, M.; Gerhards, M.; Heinze, K. *Angew. Chem. Int. Ed.* **2019**, *58*, 18075–18085.
3. Wenger, O. S. A Bright Future for Photosensitizers. *Nat. Chem. 2020 12:4* **2020**, *12*, 323–324.
4. Li, Z.; Wang, G.; Ingxiang Ye, Y.; Li, B.; Li, H.; Chen, B. *Angew. Chem.* **2019**, *131*, 18193 18199.
5. Sagara, Y.; Yamane, S.; Mitani, M.; Weder, C.; Kato, T.; Sagara, Y.; Weder, C.; Yamane, S.; Mitani, M.; Kato, T. *Adv Mater* **2016**, *28*, 1073–1095.
6. Purba, P. C.; Maitra, P. K.; Bhattacharyya, S.; Mukherjee, P. S. *Inorg Chem* **2023**, *28*, 2023.
7. Wang, X. D.; Wolfbeis, O. S.; Meier, R. J. *Chem Soc Rev* **2013**, *42*, 7834–7869.
8. Deb, S.; Sahoo, A.; Mondal, P.; Baitalik, S. *Dalton Transactions* **2022**, *51*, 15601–15613.
9. Mrinalini, M.; Prasanthkumar, S. *Chempluschem* **2019**, *84*, 1103–1121.

10. Lustig, W. P.; Mukherjee, S.; Rudd, N. D.; Desai, A. V.; Li, J.; Ghosh, S. K. *Chem Soc Rev* **2017**, *46* (11), 3242–3285.
11. Mahato, D.; Fajal, S.; Samanta, P.; Mandal, W.; Ghosh, S. K. *Chempluschem* **2022**, *87*, 202100426.
12. Zhang, J.; Zou, Q.; Tian, H. *Adv Mater* **2013**, *25*, 378–399.
13. Kwon, J. E.; Park, S. Y. *Adv Mater* **2011**, *23*, 3615–3642.
14. Yuan, W. Z.; Lu, P.; Chen, S.; Lam, J. W. Y.; Wang, Z.; Liu, Y.; Kwok, H. S.; Yuguang, M.; Tang, B. Z. *Adv Mater* **2010**, *22*, 2159–2163.
15. Wang, D.; Tang, B. Z. *Acc Chem Res* **2019**, *52*, 2559–2570.
16. Hong, Y.; Lam, J. W. Y.; Tang, B. Z. *Chem Soc Rev* **2011**, *40*, 5361–5388.
17. Ahmed, A.; Seth, S.; Purewal, J.; Wong-Foy, A. G.; Veenstra, M.; Matzger, A. J.; Siegel, D. J. *Nat. Comm.* **2019**, *10*, 1–9.
18. Trannoy, V.; Léaustic, A.; Gadan, S.; Guillot, R.; Allain, C.; Clavier, G.; Mazerat, S.; Geffroy, B.; Yu, P. *New J Chem* **2021**, *45*, 3014–3021.
19. Chen, L.; Fu, P.-Y.; Wang, H.-P.; Pan, M.; Chen, L.; Wang, H.; Fu, P.; Pan, M. *Adv Opt Mater* **2021**, *9*, 2001952.
20. Padalkar, V. S.; Seki, S. *Chem Soc Rev* **2016**, *7*, 169–202.
21. Li, A.; Liu, H.; Song, C.; Geng, Y.; Xu, S.; Zhang, H.; Zhang, H.; Cui, H.; Xu, W. *Mater Chem Front* **2019**, *3*, 2128–2136.
22. Halder, A.; Klein, R. A.; Lively, R.; Mcguirk, C. M.; Li, R. *Chemical Communications* **2022**, *58*, 11394–11397.
23. Freund, R.; Canossa, S.; Cohen, S. M.; Yan, W.; Deng, H.; Guillerm, V.; Eddaoudi, M.; Madden, D. G.; Fairen-Jimenez, D.; Lyu, H.; Macreadie, L. K.; Ji, Z.; Zhang, Y.; Wang, B.; Haase, F.; Wöll, C.; Zaremba, O.; Andreo, J.; Wuttke, S.; Diercks, C. S. *Angew. Chem. Inter. Ed.* **2021**, *60*, 23946–23974.
24. Huang, P.; Liu, Y.; Karmakar, A.; Yang, Q.; Li, J.; Wu, F. Y.; Deng, K. Y. *Dalton Transactions* **2021**, *50*, 6901–6912.
25. Elahi, S. M.; Raizada, M.; Sahu, P. K.; Konar, S. *Chem. Eur. J.* **2021**, *27*, 5858–5870.
26. Bhattacharyya, S.; Maji, T. K. *Coord Chem Rev* **2022**, *469*, 214645.
27. Bhattacharya, B.; Halder, A.; Paul, L.; Chakrabarti, S.; Ghoshal, D. *Chem. Eur. J.l* **2016**, *22*, 14998–15005.
28. Halder, A.; Maiti, A.; Dinda, S.; Bhattacharya, B.; Ghoshal, D. *Cryst Growth Des* **2021**, *21*, 6110–6118.
29. Halder, A.; Bhattacharya, B.; Haque, F.; Dinda, S.; Ghoshal, D. *Chem. Eur. J.* **2019**, *25*, 12196–12205.
30. Wang, S. T.; Zheng, X.; Zhang, S. H.; Li, G.; Xiao, Y. *CrystEngComm* **2021**, 23, 4059–4068.
31. Sakai, K. I.; Takahashi, S.; Kobayashi, A.; Akutagawa, T.; Nakamura, T.; Dosen, M.; Kato, M.; Nagashima, U. *Dalton Transactions* **2010**, *39*, 1989–1995.
32. Mutai, T. *Advances in Organic Crystal Chemistry* **2020**, 271–298.

CHAPTER-6

Selective Detection of Primary Aromatic Amines Through Enhanced Luminescence of a 2D+2D Inclined Polycatenated Microporous Nitro Functionalized MOF

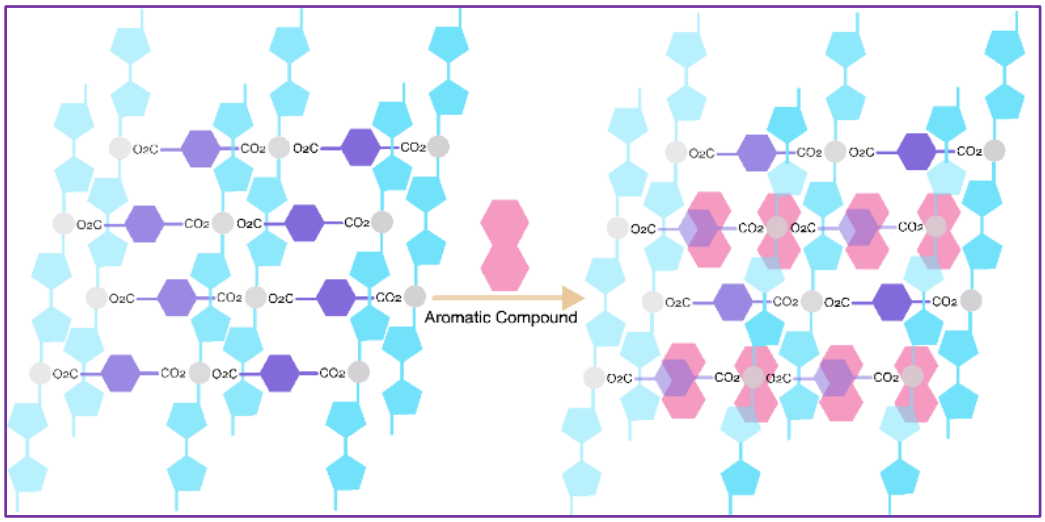

CHAPTER-6

Selective Detection of Primary Aromatic Amines Through Enhanced Luminescence of a 2D+2D Inclined Polycatenated Microporous Nitro Functionalized MOF

6.1. INTRODUCTION

In this era of polymers, the uses of amines have been extensively increased not only in the domain of polymers and textile manufacturing, but also it has been significantly used in other booming industries like pharmaceutical, chemical and fertilizers, food processing and defence.[1–3] Specifically, primary aromatic amines (PAAs), such as aniline (AN), p-phenylenediamine (PPD) are commonly used in manufacturing of rubber and soft polymers, hair dye and textile dye; fine chemical and agrochemical industries; all in a similar popularity.[4,5] Such massive use of these aforesaid PAAs increases the risk of its human exposer through food and water which may cause the damage of respiratory and cardiovascular system, encourage intense incendiary granulomas in the living body, affect the central nervous system and even trigger the growing of cancer cells.[6–9] Therefore the presence of free PAAs with other amines need to be critically monitored in industrial wastes as well as in agro product and that needs an extremely choosy and responsive identification of PAAs contaminants[10-12]. The widespread techniques for determination of PAAs in environmental samples, including spectrometry, GC, GC-MS, HPLC, capillary electrophoresis with amperometric detection etc. are associated with elaborated and time devouring pretreatments such as preconcentration and derivatization earlier to detection[13-17]. In contrast to that, the application of a fluorescent chemo sensor for the detection of PAAs is always a smarter option due to its high sensitivity, straightforward operation and fast response, which is absolutely necessary for real-time monitoring.[18-21] In this context, metal organic framework (MOF) based chemo sensors are studied extensively but most of them exhibit fluorescence quenching to the active materials by interaction with analytes.[22-26] There are few fluorescent MOF sensors as active materials for fluorescence recognition of PAAs have been developed[9,22] so far, but an enhance fluorescence emission with different intensity maxima observed with different primary aromatic amines has not yet been reported. Strategically, it is quite difficult to design fluorescent materials for preferential recognition of primary aromatic amines through π electron transfer between electron rich conjugated MOF and π^* of electron-rich amines. Herein the polycatenated MOF may

be a possible answer to overcome these aforesaid difficulties. A few polycatenated MOFs are utilized for sensing of nitro aromatic explosive[23-24] but all of them are recognized by fluorescence quenching and in such cases clear understanding of structure property relationship has not been explored properly. However, the catenated 2D+2D layers of MOF contains specific space between the layers and the pores which may be regulated by rearranging the layers[25-28] in presence of different analytes. Therefore, this can make such materials to act as a promising candidate for the detection of multiples PAA in water with accurate precession.

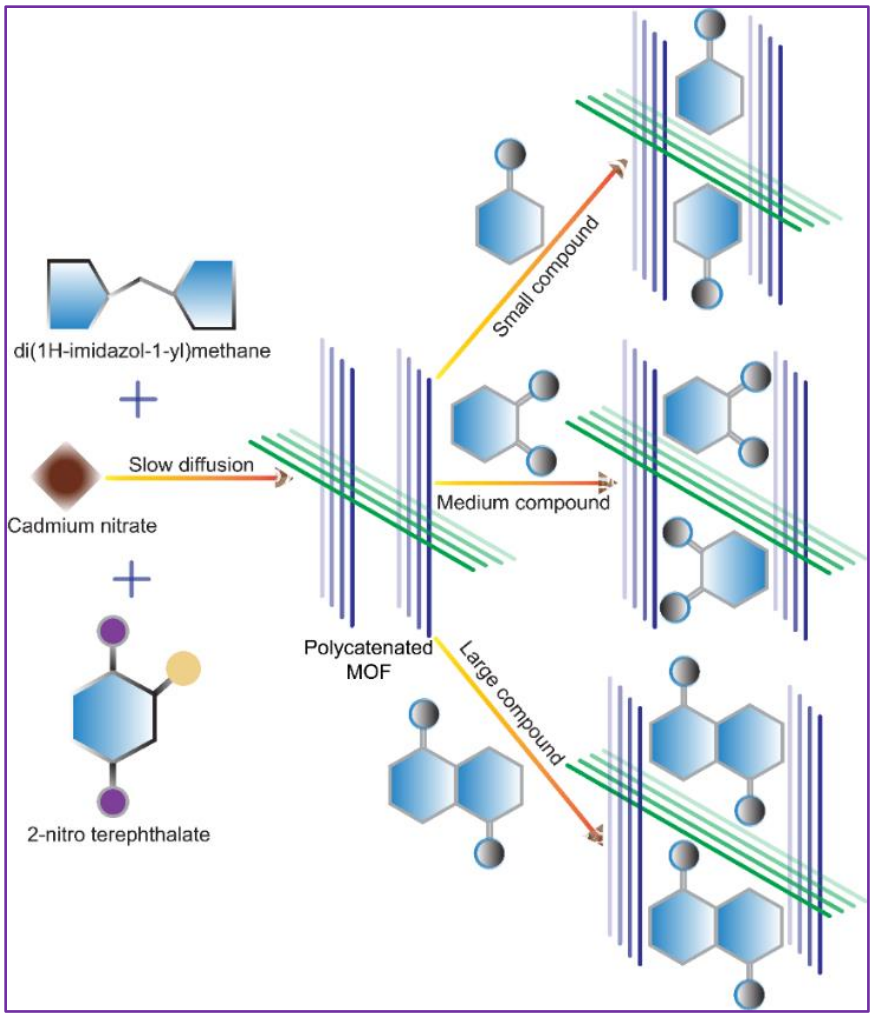

Scheme 1. Synthetic routs of MOF along with the schematic representation of pore expansion and compression of Ref. MOF depending on the size of the amines.

Here a model has been presented where an inclined polycatenated 2D+2D→3D nitro functionalized MOF for the selective detection of PAAs in water over other electron deficient amines in terms of different emissive response (Scheme 1). The MOF, {[Cd(dim)(2-

nta)(H_2O)](H_2O)(MeOH)}$_n$ (**1**) has been synthesized using cadmium (II) nitrate, di(1H-imidazol-1-yl)methane (dim) and 2-nitro terephthalate (2-nta) using slow diffusion process. The arrangement of 2D layers in catenated fashion can considerably tune the electronic transition energies and increase the luminous efficacy. Seventeen different aliphatic and aromatic amines have been selected as analytes and it has been observed that the present MOF at dehydrated condition, exhibit high fluorescence enhancement with different maxima towards different amine in specific. The mono –NH_2 group containing amine e.g. phenylamine (AN) shows blue shift fluorescence maxima and di –NH_2 groups containing amines show red shift with respect to the reference MOF. This shifting of emission maxima along with enhancement of intensity has been explored vividly to understand the precise sensing of PAA by polycatenated MOF.

6.2. EXPERIMENTAL SECTION

6.2.1. Materials

Immensely fresh $Cd(NO_3)_2.4H_2O$, imidazole, dichloromethane, tetrabutylammonium chloride have been acquired from the Sigma-Aldrich Chemical Co. All other reagents and solvents have been bought from commercial sources and used without further purification. di(1H-imidazol-1-yl)methane[29] have been synthesized by a reaction between dichloromethane and imidazole in presence of potassium hydroxide and tetrabutyl ammonium bromide (TBAB) at 40^0C in inert atmosphere condition. Na_2-2-nitroterephthalate have been prepared by the sluggish collation of solid NaOH to the analogous acids (H_2-2nta) in water in a 2:1 ratio and allowed to evaporate until dryness.

6.2.2. Physical Measurements

Elemental analyses (C, H, N) have been performed using a Heraeus CHNS elemental analyzer. FT-IR spectra have been obtained on a PerkinElmer spectrum BX-II IR spectrometer with the KBR plate of samples. PerkinElmer STA8000 thermal analyzer has been used for thermogravimetric analysis (TGA) with a ramp rate of 5 °C/min from room temperature (30 °C to 600°C under nitrogen flow. Powder X-ray diffraction (PXRD) data were collected on a Bruker D8 Discover instrument with Cu-Kα radiation (λ = 1.5406 Å), operating at 40 kV and 40 mA. UV-vis spectra are collected in PerkinElmer Lambda 35 instrument with integrating sphere attachment. Fluorescence measurements were done using Horiba FluoroMax 4 spectrofluorometer.

6.2.3. Sorption measurements

Quantachrome Autosorb– iQ adsorption instrument have been used to measured adsorption isotherms N_2 (77 K) for the dehydrated framework of compound **1,** i.e. Ref. MOF. Very pure N_2 gas (99.999% purity), has been used for this measurement. The N_2 (at 77 K, liquid nitrogen bath sorption measurements have been carried out in the pressure range 0–1 bar using dehydrated samples of **1**. Before measurements, all the as-synthesized complexes (40 mg for each) have been dehydrated in the sample tube at 413 K for 3 h under a 1×10^{-1} Pa vacuum. By controlled introduction of ultra-pure helium gas (99.999% purity) into the sample tube and allowing it to diffuse into the sample, the dead volume has been measured. The gas adsorption volume for each and every measurement has been calculated from the difference of pressure ($P_{cal}-P_e$), where P_{cal} signifies the calculated pressure without any gas adsorption and P_e indicates the observed pressure at equilibrium. The pressure change has been monitored by taking the adsorbent in the sample tube, and the degree of adsorption was calculated by observing the decrease in pressure at equilibrium.

6.2.4. Synthesis

To synthesisze compound **1**, 3ml 1 mmol aqueous solution of $Cd(NO_3)_2.6H_2O$, 5ml MeOH:H_2O (1:1) solution and equally mixed 3ml 1 mmol methanolic di(1H-imidazol-1-yl)methane solution and aqueous solution of 2-nitro terephthalate put in layer tube as sequence. Yellow crystalline material forms within seven days, which collects through washing with MeOH:H_2O (1:1) solution. The crystallographic arrangement figure outs by SCXRD, bulk purity confirms from PXRD. The TGA study conducts to evaluate framework stability. Yield: 98%. Elemental analysis, calculated for $C_{16}H_{17}CdN_5O_9$ (537.68): C 35.71; H 3.53; Cd 20.9; N 13.02; O 26.78. Found: C 35.65; H 3.5; Cd 20.85; N 13; O 26.72.

The Ref. MOF has been prepared by the elimination of lattice solvent molecules from compound **1** trough heating at 90 ^oC.

6.2.6. Crystallographic data Collection and Refinement

The X-ray single-crystal data for compound **1** has been collected at room temperature in a Bruker made APEX III diffractometer. At first, single crystals of both the compounds have been isolated and then mounted on the glass fiber tip using commercial super glue. Mo−Kα radiation (λ = 0.71073 Å) from a sealed tube X-ray source has been used. The raw data have been integrated using the SAINT[30] program and by utilizing SADABS,[31] the absorption corrections were

performed. The structures have been solved by SHELXL-2016/6,[32] and full-matrix least-squares refinements on F^2 for all non-hydrogen atoms were performed by SHELXL-2016/6,[32] with anisotropic displacement parameters. For complex **1**, due to thermal disorder hydrogen atom in C11, C13, C14 carbon atoms and along with that hydrogen atom of coordinated water molecule cannot be fixed. Also, hydrogen atoms in solvents molecules (methanol and water) cannot be fixed in complex **1** due to thermal disorder. All the calculations and molecular graphics were done by SHELXL-2016/6,[32] PLATON v1.15,[33] WinGX system Ver-1.80,[34] Diamond v3.2, Mercury,[35] and TOPOS.[36,37] All the crystallographic data and structural refinement parameters for the compound **1** has been mentioned in Table 1.

Table 1. Crystallographic data of compound **1**

	1
Formula	$C_{16}H_{19}CdN_5O_9$
Formula weight	537.68
Crystal system	Orthorhombic
Space group	*Pna2₁*
a/ Å	9.5012(8)
b/Å	18.2295(16)
c/ Å	11.5971(10)
α/°	90
β/°	90
γ/°	90
V/ Å^3	2008.6(3)
Z	4
D_c/ g cm^{-3}	1.742
μ /mm^{-1}	1.147
F_{000}	1036
θ range/°	3.1, 27.5
Reflections collected	68336
Unique reflections	4560
Reflections $I > 2\sigma(I)$	4527
R_{int}	0.031
Goodness-of-fit (F^2)	1.14
R_1 ($I > 2\sigma(I)$) [a]	0.0226
$wR_2(I > 2\sigma(I))$ [a]	0.0648
$\Delta\rho$ min / max /e Å^3	-1.08, 0.62

[a] $R_1 = \Sigma \big| |F_o| - |F_c| \big| / \Sigma |F_o|$, $wR_2 = [\Sigma (w (F_o^2 - F_c^2)^2) / \Sigma w (F_o^2)^2]^{1/2}$

6.3. RESULTS AND DISCUSSION

6.3.1. Structural Description

{[Cd(dim)(2-nta)(H_2O)](H_2O)(MeOH)}$_n$ (1)

Single-crystal X-ray diffraction analysis discloses that complex **1** is a catenated 2D+2D→3D framework of Cd(II) ion. It crystalizes in orthorhombic $Pna2_1$ space group and the asymmetric unit of **1** composes of one Cd(II) metal ion center, one di(1H-imidazol-1-yl)methane (dim) ligand, one 2-nitro terephthalate (2-nta) ligand and one coordinated water molecule, along with one guest water and methanol molecules. The hepta coordinated Cd1 is coordinated by four oxygen atoms (O2, O3, O6 and O7) coming from two different 2-nitro terephthalate ligands, one pair of nitrogen atoms (N1 and N4^a) of two different di(1H-imidazol-1-yl)methane ligands and one oxygen atom from water molecule (O1W), shaping a distorted pentagonal bipyramidal geometry (CdO_5N_2) (Figure 1a). The Cd1−O and Cd1−N distances around Cd1 are in the range of 2.257(3)−2.502(3) and 2.315(3)−2.317(3) Å, respectively (Table 2). The bond angles around Cd1 is in the range of 52.66(11)°−169.57(11)° (Table 2).

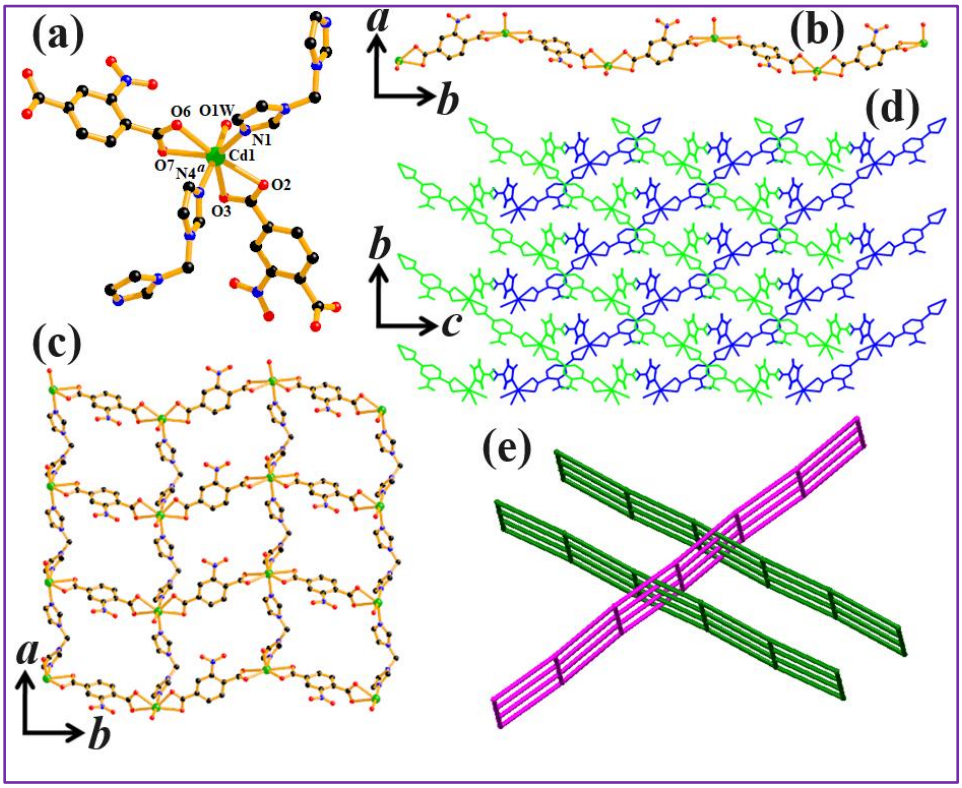

Figure 1. (a) coordination environment of compound **1**. Green (Cd) black (C), blue (N), red (O). (b) 1D chain in c direction (c) 2D wavy sheet in crystallographic *ab* plane. (d) Overall 3D porous framework through 2D+2D nets. (e) Topological[36,37] representation of **1**.

Thus, geometrically alike Cd(II) centers connect with each other via 2-nitro terephthalate ligands to form a 1D arrangement in the crystallographic *ab* plane (Figure 1b) in *c* direction. The di(1H-imidazol-1-yl)methane linkers connect to the 1D metal− carboxylate in *a* direction to create a 2D wavy arrangement (Figure 1c) in *ab* plane. These 2D layers organized through inclined catenation to appearance porous 3D framework, along *bc* plane in Figure 1d. The Cd…Cd distances through 2-nta and dim are~10 Å and~9 Å respectively, which is responsible for rectangular 1D void channel along *c* direction of crystallographic axis with channel dimension about ~4×3.5 $Å^2$. After the removal of lattice solvents molecules the total potential solvent accessible void volume is found 383 $Å^3$, which is 19.08% of the total crystal volume of 2008.6 $Å^3$ (Figure 2).

Table 2. Selected Bond Lengths (Å) and Bond Angles (°) for Complex **1**

Cd1-O1	2.435(3)	Cd1-O1W	2.257(3)
Cd1-O2	2.502(3)	Cd1-N1	2.317(3)
Cd1-N4^a	2.315(3)	Cd1-O3^d	2.499(4)
Cd1-O4^d	2.425(4)	O1-Cd1-O1W	95.32(12)
O1-Cd1-O2	52.97(9)	O1-Cd1-N1	82.02(11)
O1-Cd1-N4^a	85.55(11)	O1-Cd1-O3^d	162.35(11)
O1-Cd1-O4^d	143.57(11)	O1W-Cd1-O2	84.41(11)
O1W -Cd1-N1	92.99(11)	O1W -Cd1-N4^a	169.57(11)
O1W-Cd1-O3^d	92.12(12)	O1W-Cd1-O4^d	87.26(12)
O2-Cd1-N1	134.23(10)	O2-Cd1-N4^a	87.88(10)
O2-Cd1-O3^d	144.02(10)	O2-Cd1-O4^d	91.37(10)
N1-Cd1-N4^a	97.42(11)	O3^d-Cd1-N1	81.64(12)
O4^d -Cd1-N1	134.24(11)	O3^d-Cd1-N4^a	90.00(12)
O4^d-Cd1-N4^a	85.92(12)	O3^d-Cd1-O4^d	52.66(11)

Table 3. Intermolecular π-π interactions in **1**

ring(i) → ring(j)	distance of centroid(i) from ring(j),(Å)	dihedral angle (i,j) (deg)	distance between the (i,j) ring centroids,(Å)
R(1)→R(2)^i	3.870(2)	16.4(2)	1.914
R(2)→R(1)^{ii}	3.870(2)	16.4(2)	1.766

Symmetry code: i = 1/2+X,-1/2-Y,Z; ii = 1/2+X,1/2-Y,Z;
R(i)/R(j) denotes the ith/jth rings in the corresponding structures: R(1) = N3/C5/C6/N4/C9; R(2) = N1/C1/C3/N2/C2.

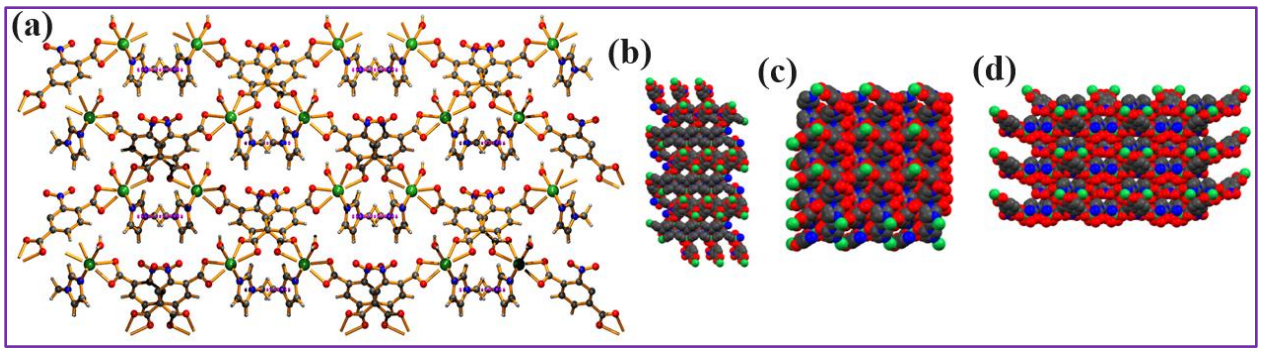

Figure 2. (a) π-π interaction in compound **1**, (b), (c) and (d) Space fill model of Ref. MOF (after elimination of lattice solvents molecules from compound **1**).

The catenated 3D structure is also stabilized by intermolecular π…π interactions between the imidazole rings of two inclined 2D sheet (Figure 2, Table 3), which gives stability to the overall 3D framework. Network analysis using TOPOS[36,37] revealed that the two inclined 2D nets are consists of 4-c uninodal square nets with the point symbol (Schlafli symbol) $\{4^4.6^2\}$ (Figure 1e).

6.3.2. Stability and purity

The thermal stability of the compound **1** has been checked by thermogravimetric analysis. The test has been performed at 5°C/min heating rate from 30°C to 600°C range. The lattice solvents molecules loss within 80°C, approximately 9.2% of total weight, this lattice solvent removed forms consider as Ref. MOF, after that within 110°C the coordinated water molecule losses with 3.6% weight from the framework. Stability of the framework remains unchanged up to 280°C, after that speedy break down starts (Figure 3).

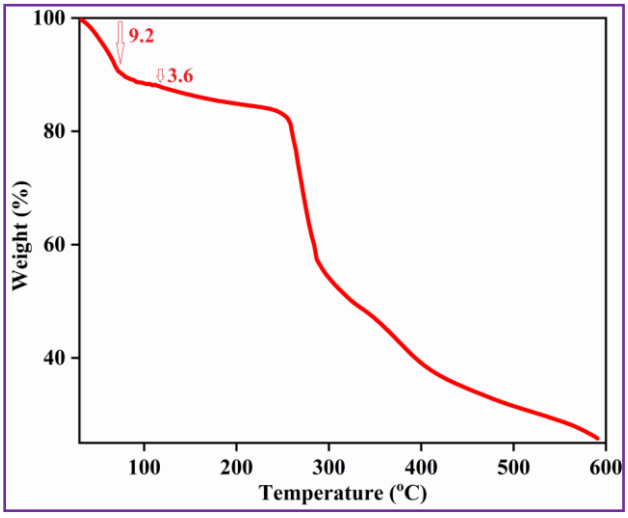

Figure 3. TGA graph of compound **1**

The bulk purity and framework stability of compound **1** has been proved by the powder x-ray diffraction study. The similar peak position has been viewed between stimulated and as-synthesis form of compound **1**. The PXRD pattern of Ref. MOF (lattice solvents removed form of compound **1**) has similar peak position with the simulated form of compound **1** (Figure 4). The framework stability of Ref. MOF has been studied in eight different solvents, DMF, water, chloroform, DCM, MeOH, EtOH, DMSO and THF. The intensity of different peak has different values for different solvent, but the overall peak position is same (Figure 4), that indicates the huge stability of the framework in different organic solvent including polar solvent like water. The framework stability in DMF and water is very crucial for the study.

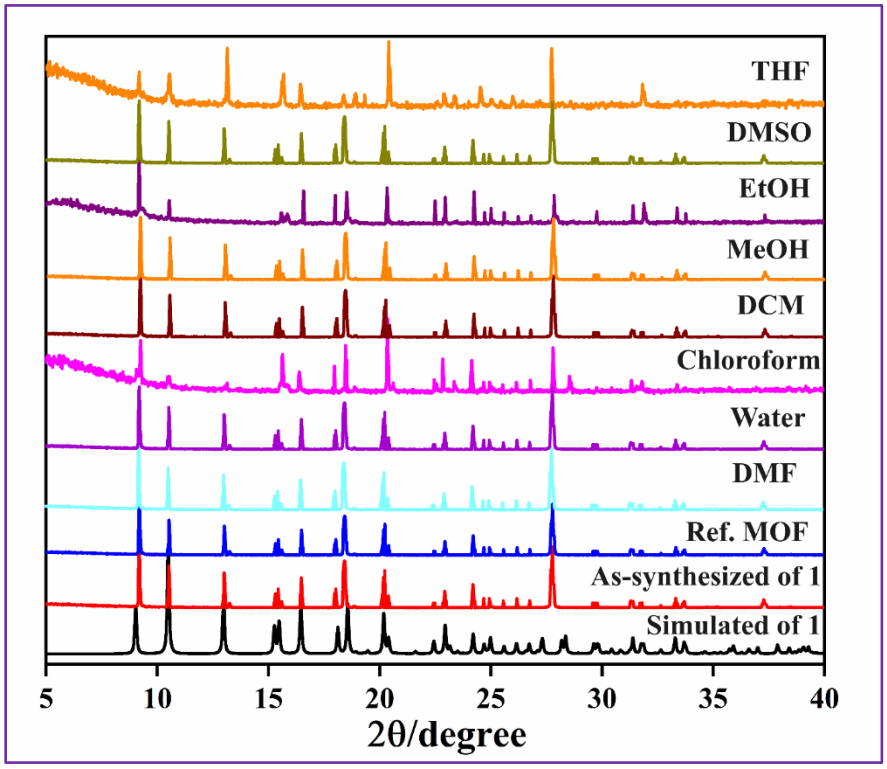

Figure 4. PXRD patterns of simulated form of compound 1 (black), lattice solvent removed form of compound **1** i.e., Ref. MOF in red, along with PXRD patterns of Ref. MOF in different solutions mentioned in figure.

6.3.3. IR Study and UV-visible spectroscopy study

IR spectra has been presented in Figure 5. IR spectra (KBr pellet, 4000−400 cm^{-1}): ν(O−H), 3479 (stretch); ν(C−H, imidazole), 3030 (stretch); ν(C−H, alkane), 2816 (stretch) and 1359 (bending); ν(C−C, imidazole), 1613−1516 (stretch); and ν(C−O), 1231 (stretch).

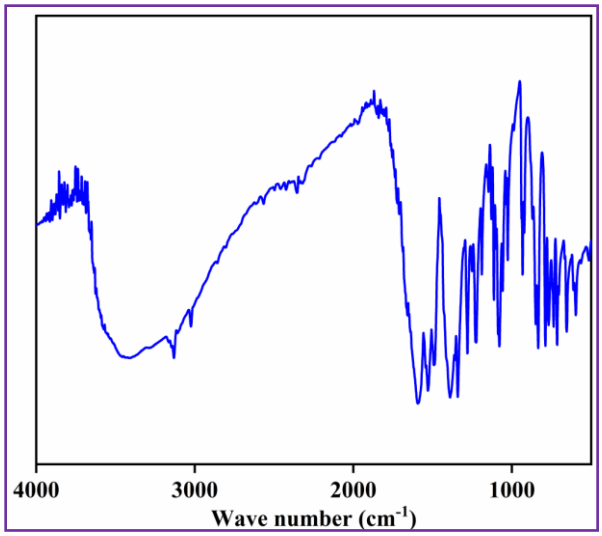

Figure 5. IR spectra of compound **1**

UV-visible spectroscopy of Ref. MOF has been studied in PerkinElmer Lambda 35 instrument with integrating sphere attachment instrument in DMF:H_2O (20:1) solvent mixture with 0.024mmol concentration. The absorption maximum has been observed at 280 nm wavelength (Figure 12 in set).

6.3.4. Optical properties of compound Ref. MOF

To understand the luminescence properties of microporous 3D nitro functionalized MOF, the fluorescence performance of the ligands, i.e. di(1H-imidazol-1-yl)methane (dim) and two 2-nitro terephthalate (2-nta) were studied first. To compare the fluorescence properties of dim and *2-nta* the experiment was done using same solution concentration (0.024 mmol) in same DMF/H_2O solvents (vide infra) using the excitation wavelength of 280 nm. The 2-nta ligand shows four different maxima of fluorescence emissions 340nm, 390nm, 430nm and 465nm, whereas dim ligand shows two maxima of emission at 415nm and 435nm. All the maxima of these two ligands have huge lower intensity with different peak position than Ref. MOF, which show the unique high fluorescence nature of the Ref. MOF. To select the proper solvent for sensing study of Ref. MOF, eight different solvents viz. DMF, water, EtOH, MeOH, THF, chloroform, dichloromethane, DMSO has been checked, taking the equal concentration (0.024 mol) of the compound in each case. To replicate the exact condition of sensing study, a trace amount of water (one drop in 1 ml i.e. DMF:H_2O, 20:1) is also added with all non-aqueous solvents; as during sensing study the analyte amines are dissolved in water same ratio of water and solvents, has been

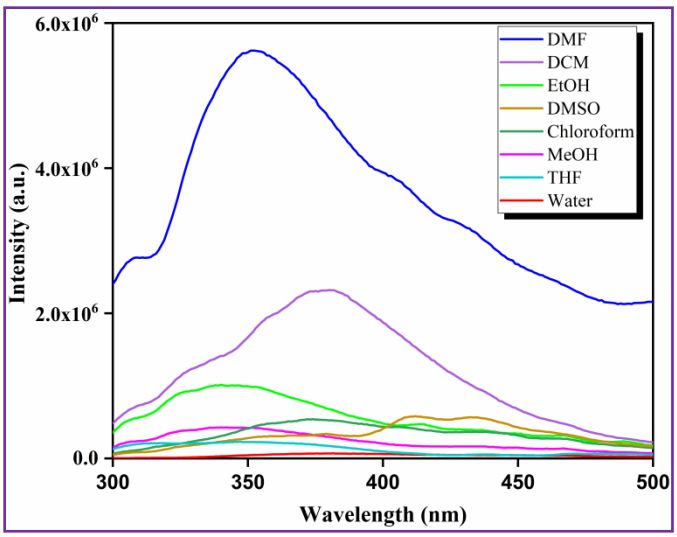

Figure 6. The fluorescence spectra of Ref. MOF in different solutions [0.024 mmol concentration in solvent:water (20:1) mixture]

checked. The intensity of emission spectra of Ref. MOF shows higher value in DMF/H_2O as compared to other solvents with well resolved emission maxima at 352nm (Figure 6). Therefore, DMF has been selected as the preferred solvent for detection of the amines from aqueous solution. In addition to the above criteria, DMF also has the advantage of good water miscibility, low volatility/toxicity and high boiling point.

6.3.5. Nitrogen Gas sorption and Porosity calculation

As stated earlier in the structural description, the compound under investigation possesses a coordinated water molecule along with one lattice methanol and lattice water molecule, resulting in an open metal site and lattice pore with a pore volume of 383 $Å^3$ upon activation at temperatures exceeding 110°C. This observation is also substantiated by a thermogravimetric analysis (TGA) experiment, revealing a total weight loss of 12.8%, attributed to the removal of both lattice and coordinated solvent molecules. Inspired by the relevance of porous MOFs featuring open metal sites and a pore-centric orientation of polar functional groups, as emphasized in previous literature outlining key factors for enhanced sorption of hydrogen (H_2) and carbon dioxide (CO_2), sorption measurements have been conducted for these two gases at temperatures of 77 K and 195 K, respectively. Moreover, for the determination of pore size using the non-local density functional theory (NL-DFT) method and the assessment of surface area, nitrogen (N_2) sorption measurements were conducted at 77 K and 1 bar. The pore size distribution analysis from N_2 sorption data by applying the NL-DFT method suggests the pore widths for Ref. MOF is 15.85Å (Figure 7) with

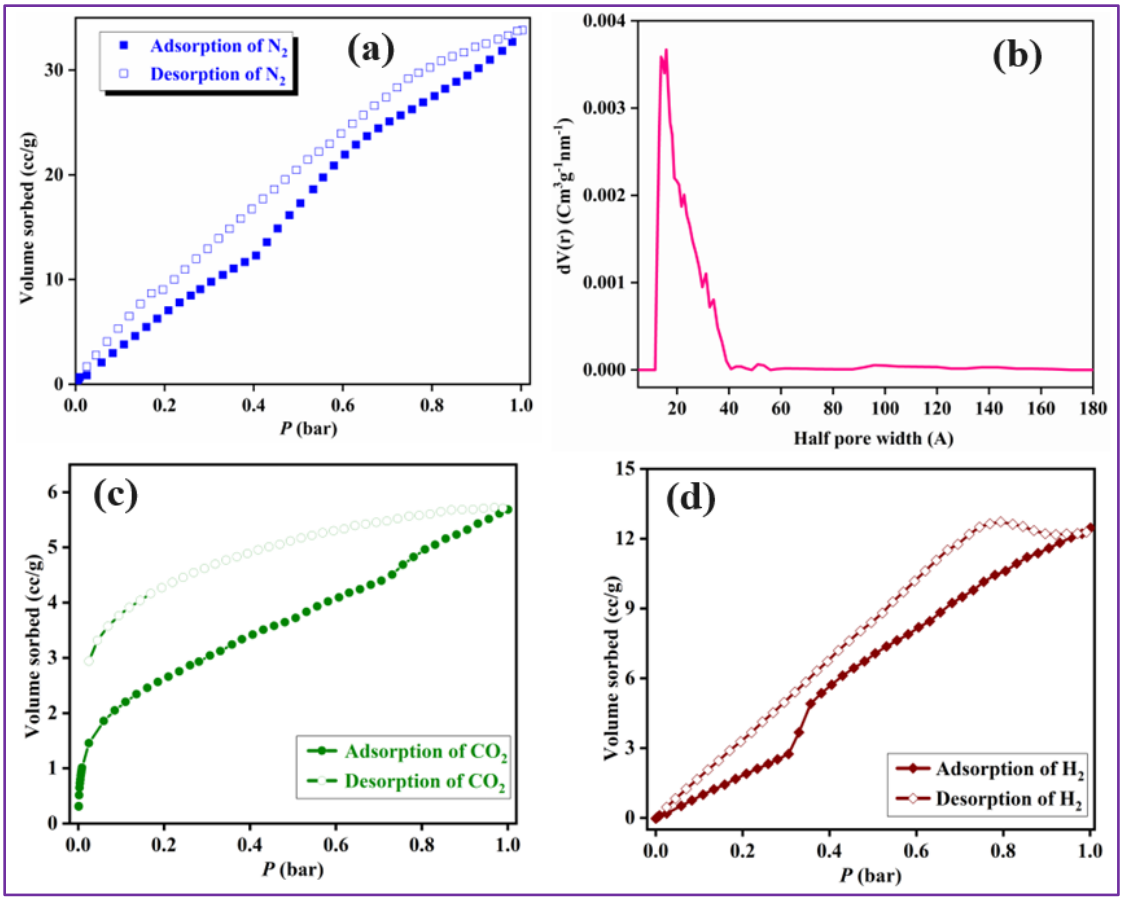

Figure 7. (a) N_2 sorption curve of Ref. MOF. (b) NL-DFT pore size distribution curve of Ref. MOF. (c) CO_2 sorption curve of Ref. MOF. (d) H_2 sorption curve of Ref. MOF.

surface area 22.76 m^2/g for maximum N_2 uptake of 36 cc/g (Figure 7). Although, the compound has competence in carbon dioxide uptake in term of open metal site and pore centric polar nitro (-NO_2) group, yet its maximum capacity is remarkably negligible, capped only 5 cc/g carbon dioxide under pressures up to 1 bar (Figure 7). The limited absorption of carbon dioxide can be clarified by the pore-blocking effect resulting from polycatenation in both *a* and *b* directions, as depicted in Figure 2. Additionally, in the *c* direction the repulsion between quadrupolar carbon dioxide and the bulky nitro group oriented towards the 1D channel also contributes to this lower carbon dioxide uptake phenomenon. In the context of H_2 sorption, the negligible absorption of 12 cc/g is likely attributed to a comparable pore-blocking influence of polycatenation. Conversely, the higher uptakes in comparison to CO_2 could be ascribed to the tiny size of hydrogen (with a kinetic diameter of 2.9 Å), allowing it to readily enter the 1D channel along the c-axis, as illustrated in Figure 7, as opposed to CO_2 with a larger kinetic diameter of 3.3 Å.

6.3.6. PAAs Detection and Selectivity

Considering the advantage of polycatenated structure with micro porosity, the Ref. MOF is subjected to study its change in luminescence property in presence of several primary aromatic amines (PAA) to explore the sensing behavior. PL spectra were recorded on specified concentration mentioned before (0.024 mmol of Ref. MOF in DMF: H_2O, 20:1) and it found that the compound emits strongly at 352 nm upon excitation at 280 nm (Figure 4). The recognition study has primarily focused on two categories of amines compounds, namely, compounds containing electron rich aromatic ring such as PAAs in group A and electron deficient compounds including electron deficient rings and aliphatic amines as well in the group B segment of study (Table 4). It has been observed that all PAAs (AN, OPD, MPD, PPD, 1,5-DAN) act as fluorescence enhancer for ref. MOF (Figure 8,9). Among them, the most effective enhancing analyte is 1,5-DAN whereas the least effective one is OPD. The percentage of enhancement goes up in the order as OPD, 56.1%; MPD, 78.2%; AN, 83.4%; PPD, 127% and 1,5-DAN 130% with respect to the intensity of Ref. MOF (Figure 10). The order of enhancing effectiveness for the selected PAAs is 1,5-DAN>PPD>Aniline>MPD>OPD.

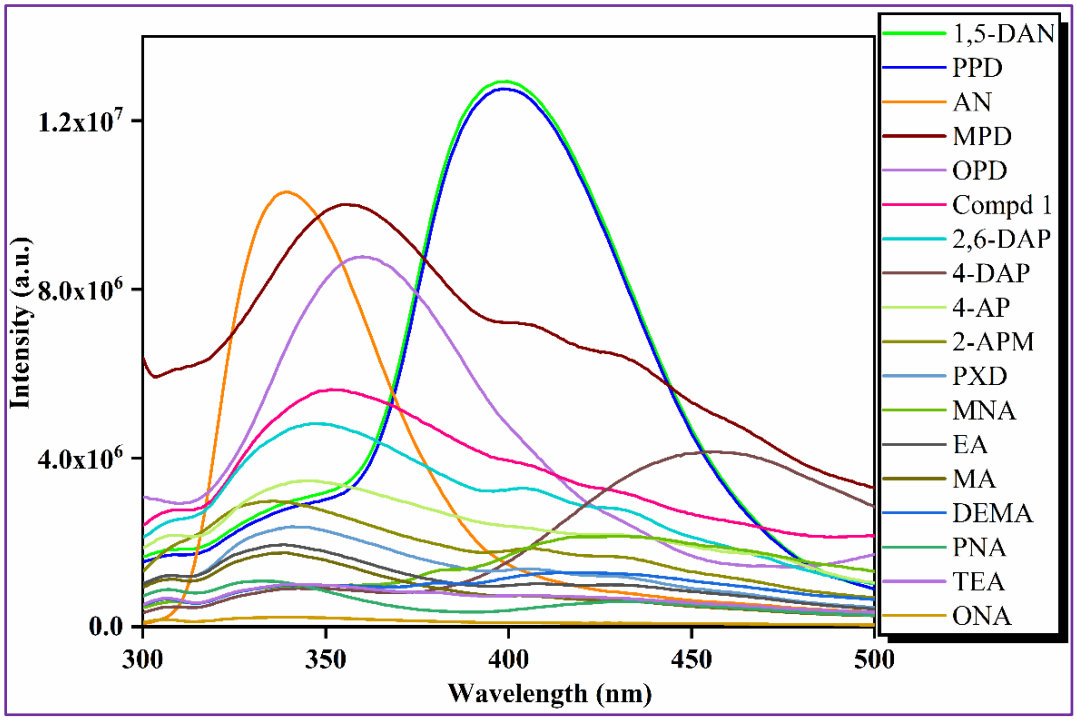

Figure 8. Fluorescence spectra of Ref. MOF in presence of different amines in DMF: H_2O (20:1) solvent. Where concentration of Ref. MOF and amines are fixed 0.024 mmol in every respective spectrum except the standard one, where only Ref. MOF present in 0.024 mmol concentration.

Table 4. List of Different Types of Amines used as Analyte

Analyte amine	Abbreviation used	Analyte amine	Abbreviation used
1,5-Diaminonaphthalene	1,5-DAN	p-Phenylenediamine	PPD
Phenylamine	AN	m-Phenylenediamine	MPD
2,6-Diamino pyridine	2,6-DAP	o-Phenylenediamine	OPD
4-Dimethyl amino pyridine	4-DAP	4-Amino pyridine	4-AP
2-Amino pyrimidine	2-APM	p-Xylene diamine	PXD
m-Nitroaniline	MNA	p-Nitroaniline	PNA
o-Nitroaniline	ONA	Ethylenediamine	EA
Methylamine	MA	Dimethylamine	DMA
Triethylamine	TEA		

Surprisingly, this order is not fully in agreement with the trend of electron-rich rings, but here the solubility of amines and steric hindrance of the amines group in diamine PAAs is also acts as a directing factor. With accounting the enhancement of intensity, the shifting of emission maxima for mono amine and diamine PAAs show different trends, blue and red shift with respect to the emission maxima of Ref. MOF respectively (Figure 9), which is pretty interesting in terms of fine differentiation in sensing ability. A behavior has been observed in case of the electron deficient aromatic amines mentioned in the group B of Table 2. The Ref. MOF shows fluorescence quenching effect for electron deficient aromatic rings such as 2,6-DAP, 4-DAP, 4-AP, 2-APM, PXD, MNA, PNA, ONA (Figure 4, 5).

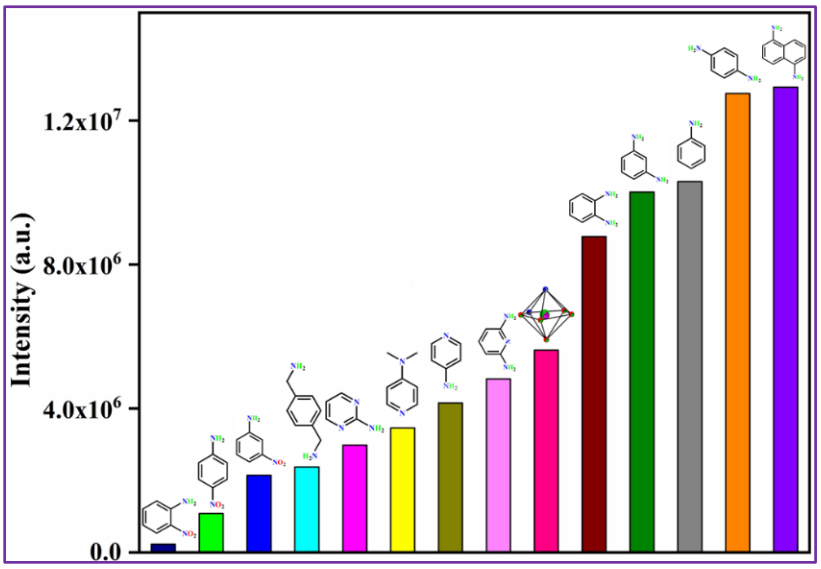

Figure 9. Comparison of fluorescence intensity of different types of aromatic amines with respect to Ref. MOF.

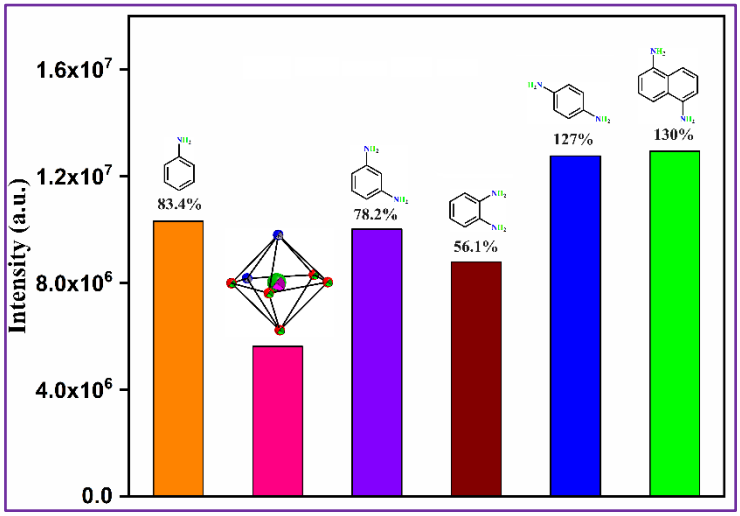

Figure 10. Enhancement of intensity with respect to the Ref. MOF, including blue and red shifts of emission maxima of mono and di $–NH_2$ group containing aromatic amines respectively.

The percentage of quenching follows the order as 2,6-DAP, -14.2%; 4-DAP, -26%; 4-AP, -38.5%; 2-APM, -47%; PXD, -58%; MNA, -62%; PNA, -81%; ONA, -96% (Figure 9). This behaviour is commensurate with the arrangement/density of π electrons in the aromatic rings of the respective amines. The fluoresce spectra of Ref. MOF also studied in presence of aliphatic amines as well where all of them show quenching behavior, due to their sigma electron density and direct interaction with the $–NO_2$ groups of Ref. MOF.

6.3.7. Mechanism of Enhancement and Quenching Phenomenon

The examined fluorescence enhancement and attenuation can be interpreted by the donor-acceptor electron-transfer mechanism. The basic nature of electron distribution of electron rich aromatic analytes, the lowest unoccupied MO (LUMO) has higher energy π*-type orbital stabilized by the NH_2 group through +R type conjugation (Figure 8), and its energy is above the conduction band (CB) of Ref. MOF. Whereas, for the electron deficient aromatic amines, the lowest unoccupied MO (LUMO) is a low-lying π*-type, which stabilize by the hetero atom present in rings and $-NO_2$ group for nitro derivative analytes through conjugation (Figure 11), which has lower energy than the conduction band (CB) of Ref. MOF. Even though all MOFs have spread conjugated net structures, they often characterized by contracted energy bands, because of highly centric electronic states, in particularly those containing d^{10} metals. In those cases, they may be considered as “massive molecules”, and their valence band (VB) and CB energy levels can be described in a way similar to that for MOFs. From the UV-Vis absorbance data tauc plot (Figure 12) has been

drawn, which shows three band gaps as 3.27 eV, 3.33 eV and 3.6 eV. These three band gaps represent the n→π*, π→π* and n→σ* transition energy differences. Upon excitation, electrons in VB are promoted to the CB of Ref. MOF to the LUMO, a high-lying π*−antibonding state of the electron rich PPAs analyte, guiding to an enhancement effect (Figure 11). This mechanism has been well demonstrated for conjugated polymers[38-43] and this experimental result proved here for Ref. MOF (Figure 8-10). For an aromatic electron deficient amines analyte, the excited electrons from its LUMO, a low-lying π*−antibonding state with its energy below the CB of the Ref. MOF, are transferred to the CB of Ref. MOF, thereby guiding to fluorescence quenching (Figure 8). Secondly, the transfer of electron between the photoexcited states (VB, CB) of Ref. MOF and the HOMO-LUMO of analytes may be measured by their reduction potentials. Consequently, Ref. MOF behaves as an electron acceptor in the case of PAAs analytes and an electron donor for electron deficient aromatic amines analytes (Figure 11).

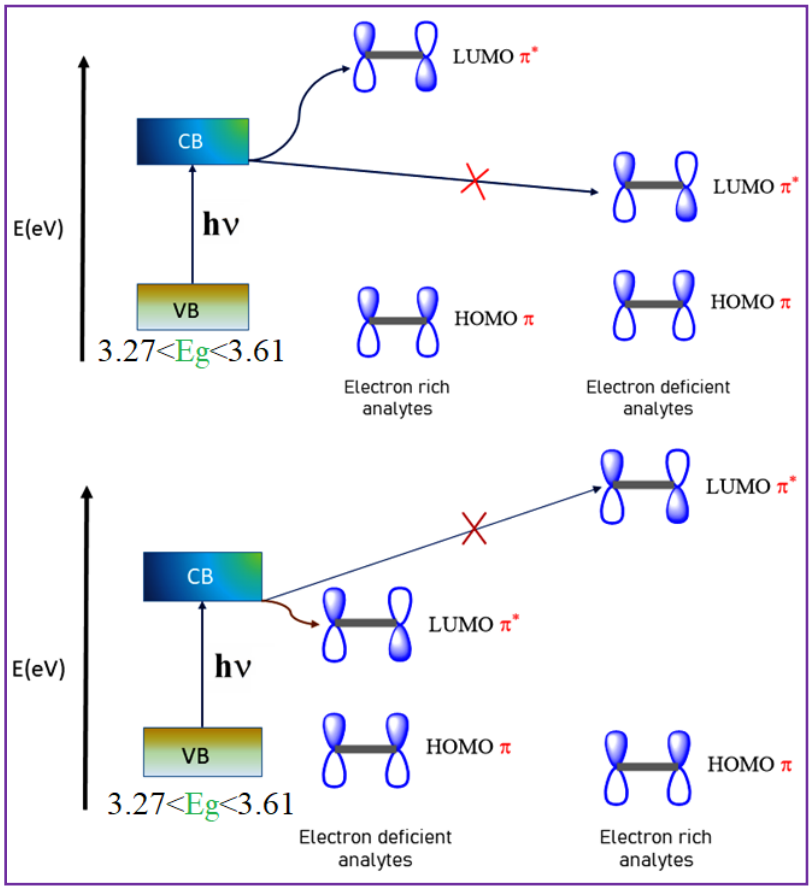

Figure 11. Schematic representation of band gap of Ref. MOF with demonstrating the electro transfer routes between CB of Ref. MOF with electron rich (above) and deficient amines (below).

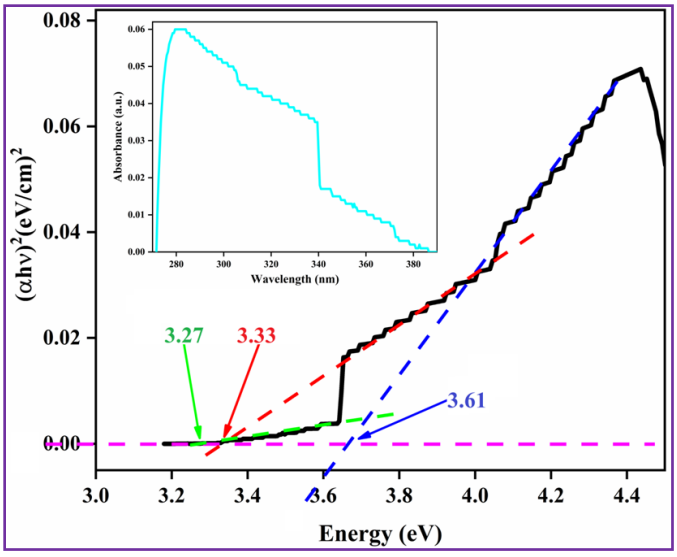

Figure 12. Tauc Plot of ref. MOF. UV-Vis plot inserted in cyan colour.

The fluorescence behavior of aliphatic compounds shows quenching due to non-planar geometry and bulky shape, which influences to direct interacts with the Ref. MOF. In the light of molecular orbital theory, the aliphatic amines have σ-type LUMO, dissimilar to the π-type conductance band of Ref. MOF. The π-type LUMO of aromatic rings (PAAs) have greater overlap probability than σ-type LUMO of aliphatic amines with the π-type CB of Ref. MOF.

6.4. CONCLUSIONS

Here the highly luminescent 2D+2D →3D inclined catenated nitro functionalized microporous MOF after the removal of guest molecules demonstrates exceptional detection and sensing of PAAs. Here the detection of PAAs through the fluorescence enhancement with different wavelength maxima for different amines by polycatenated MOF. The ref. MOF reported here have a well-organized space between the two 2D layers with ample flexibility, which can offer a commensurate space for different analyte PAAs with different sizes. This interesting feature could have achieved by the inherent flexibility of a polycatenated structure. Therefore, this work is not only representing a practicable method for the sensing of PAAs using a single compound, which is a polycatenated MOF. Perhaps, this is the most unexplored area so far in the library of properties of flexible MOF. The above findings are also supported by time resolved fluorescence spectroscopy as well. An established mechanism has also drowned in support of our understanding, considering the interaction between the CB of MOF and LUMO of amines. In summary, this work

represents the detection of various PAAs by a single polycatenated flexible MOF by the enhancement of fluorescence intensities.

REFERENCES

1. Hu, R.; Leung, N. L. C.; Tang, B. Z. *Chem. Soc. Rev.* **2014**, *43*, 4494–4562.
2. Asha, K. S.; Bhattacharjee, R.; Mandal, S. *Angew. Chem. Int. Ed.* **2016**, *55*, 11528–11532.
3. Shi, L.; He, C.; Zhu, D.; He, Q.; Li, Y.; Chen, Y.; Sun, Y.; Fu, Y.; Wen, D.; Cao, H.; Cheng, J. *J. Mater. Chem.* **2012**, *22*, 11629–11635.
4. Liu, L.; Lei, L.; Zeng, K.; Wu, K.; Yang, N. *Adv. Funct. Mater.* **2023**, *33*, 2211335.
5. Ghomi, E. R.; Niazi, M.; Ramakrishna, S. *Polym. Adv. Technol.* **2023**, *34*, 520–530.
6. Huang, Y. -C.; Hung, W. -C.; Kang, W.-Y.; Chen, W. -T.; Chai, C. -Y. *Toxicol. Lett.* **2007**, *170*, 116−123.
7. Gao, L. –F.; Lin, X.; Hai, X.; Chen, X. –W.; Wang, J. −H. *ACS Appl. Mater. Interfaces* **2018**, *10*, 43049–43056.
8. Li, G.; Zhang, B.; Yan, J.; Wang, Z. *J. Mater. Chem. A* **2014**, *2*, 18881–18888.
9. Zhao, Y. −J.; Miao, K.; Zhu, Z.; Fan, L. −J. *ACS Sens.* **2017**, *2*, 842–847.
10. Lustig, W. P.; Mukherjee, S.; Rudd, N. D.; Desai, A. V.; Li, J.; Ghosh, S. K. *Chem. Soc. Rev.* **2017**, *46*, 3242–3285.
11. Mallick, A.; El-Zohry, A. M.; Shekhah, O.; Yin, J.; Jia, J.; Aggarwal, H.; Emwas, A. −H.; Mohammed, O. F.; Eddaoudi, M. *J. Am. Chem. Soc.* **2019**, *141*, 7245–7249.
12. Jiao, Z.; Zhang, Y.; Xu, W.; Zhang, X.; Jiang, H.; Wu, P.; Fu, Y.; He, Q.; Cao, H.; Cheng, J. *ACS Sens.* **2017**, *2*, 687–694.
13. Bjorkqvist, B. *J. Chromatogr. A* **1981**, *204*, 109−114.
14. Wang, P. G.; Krynitsky, A. J. *J. Chromatogr. B* **2011**, *879*, 1795−1801.
15. Hudari, F. F.; de Almeida, L. C.; da Silva, B. F.; Zanoni, M. V. B. *Microchem. J.* **2014**, *116*, 261−268.
16. Sun, Y.; Liang, L.; Zhao, X.; Yu, L.; Zhang, J.; Shi, G.; Zhou, T. *Water Res.* **2009**, *43*, 41−46.
17. Verma, K. K.; Stewart, K. K. *Anal. Chim. Acta* **1988**, *214*, 207−216.
18. Fan, L. −J.; Zhang, Y.; Murphy, C. B.; Angell, S. E.; Parker, M. F. L.; Flynn, B. R.; Jones Jr., W. E. *Coord. Chem. Rev.* **2009**, *253*, 410−422.
19. Haldar, A.; Bhattacharya, B.; Haque, F.; Dinda, S.; Ghoshal, D. *Chem. Eur. J.* **2019**, *25*, 12196−12205.
20. Haldar, A.; Maiti, A.; Dinda, S.; Bhattacharya, B.; Ghoshal, D. *Cryst. Growth Des.* **2021**, *21*, 6110−6118.
21. Bhattacharya, B.; Haldar, A.; Paul, L.; Chakrabarti, S.; Ghoshal, D. *Chem. Eur. J.* **2016**, *22*, 14998−15005.
22. Tang, Y.; Huang, H.; Peng, B.; Chang, Y.; Li, Y.; Zhong, C. *J. Mater. Chem. A* **2020**, *8*, 16542−16550.
23. Gole, B.; Bar, A. K.; Mukherjee, P. S. *Chem. Commun.* 2011, *47*, 12137–12139.

24. Srivastava, S.; Gupta, B. K.; Gupta, R. *Cryst. Growth Des.* **2017**, *17*, 3907–3916.
25. Maity, D. K.; Halder, A.; Pahari, G.; Haque, F.; Ghoshal, D. *Inorg. Chem.* **2017**, *56*, 713–716.
26. Dinda, S.; Pahari, G.; Maiti, A.; Ghoshal, D. *CrystEngComm* **2023**, *25*, 1116–1125.
27. Tripuramallu, B. K.; Manna, P.; Das, S. K. *CrystEngComm* **2014**, *16*, 4816-4833.
28. Ghosh, S.; Das, M.; Dinda, S.; Pahari, G.; Ray, P. P.; Ghoshal, D. *Cryst. Growth Des.* **2021**, *21*, 4892−4903.
29. Blatov, V. A.; Shevchenko, A. P.; Serezhkin, V. N. *J. Appl. Crystallogr.* **2000**, *33*, 1193.
30. SMART (V 5.628), SAINT (V 6.45a), XPREP, SHELXTL; Bruker AXS Inc.: Madison, WI, **2004**.
31. Sheldrick, G. M. SADABS, Version 2.03; University of Göttingen: Germany, **2002**.
32. Sheldrick, G. M. SHELX 2016/6: University of Göttingen, Göttingen, Germany, **2014**.
33. Spek, A. L. *Acta Crystallogr. Sect. D.* **2009**, *65*, 148–155.
34. Farrugia, L. J. *J. Appl. Crystallogr.* **1999**, *32*, 837–838.
35. Macrae, C. F.; Edgington, P. R.; McCabe, P.; Pidcock, E.; Shields, G. P.; Taylor, R.; Towler, M.; Streek, J. V. D. *J. Appl. Cryst.* **2006**, *39*, 453–457.
36. Blatov, V. A.; Shevchenko, A. P.; Serezhkin, V. N. *J. Appl. Crystallogr.* **2000**, *33*, 1193.
37. Blatov, V. A.; Carlucci, L.; Ciani, G.; Proserpio, D. M. *CrystEngComm* **2004**, *6*, 377–395.
38. Toal, S. J.; Trogler, W. C. *J. Mater. Chem.* **2006**, *16*, 2871-2883.
39. Thomas, S. W.; Joly, G. D.; Swager, T. M. *Chem. Rev.* **2007**, *107*, 1339−1386.
40. Yang, J.-S.; Swager, T. M. *J. Am. Chem. Soc.* **1998**, *120*, 11864–11873.
41. Toal, S. J.; Sanchez, J. C.; Dugan, R. E.; Trogler, W. C. *J. Forensic Sci.* **2007**, *52*, 79-83.
42. Sohn, H.; Sailor, M. J.; Magde, D.; Trogler, W. C. *J. Am. Chem. Soc.* **2003**, *125*, 3821-3830.
43. Pramanik, S.; Zheng, C.; Zhang, X.; Emge, T. J.; Li, J. *J. Am. Chem. Soc.* **2011**, *133*, 4153–4155.

CHAPTER-7

Redox Insights and OER Activity in 3D-MOFs: The role of Alkali Metal Ions

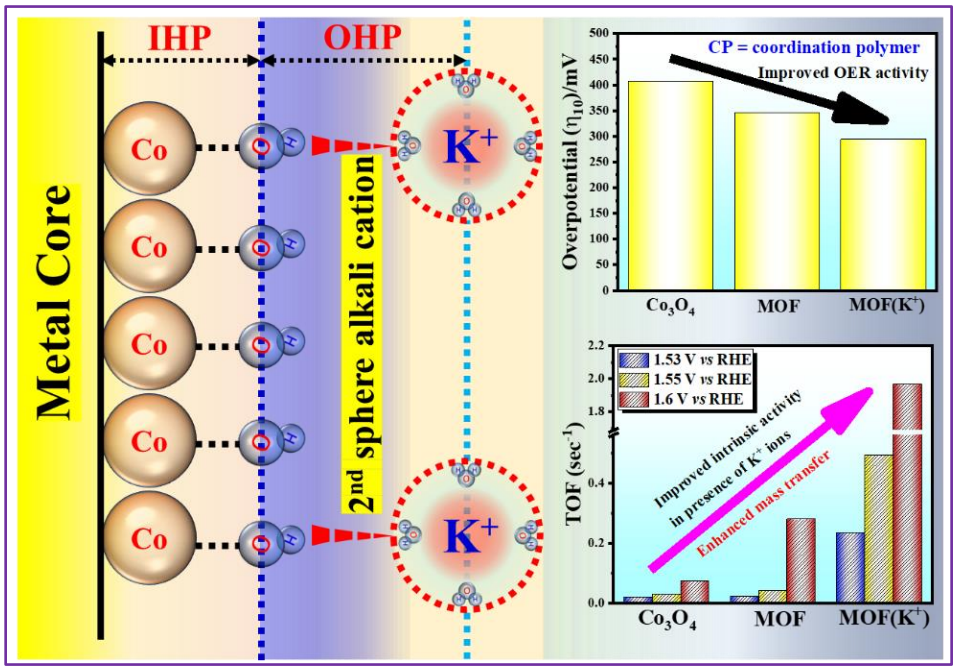

CHAPTER-7

Redox Insights and OER Activity in 3D-MOFs: The Role of Alkali Metal Ions

7.1. INTRODUCTION

Electrocatalytic oxygen evolution reaction (OER) has come out as the most prominent and promising tool for the water splitting reaction to produce hydrogen electrochemically[1,2]. As the splitting of water is associated with the celebrated bottleneck of four-electron-four proton- transfer process, therefore suitable electrocatalyst to minimize the kinetic barrier with lower energy input is very much essential to conduct the process[3,4]. In context of this the searching of suitable electrocatalyst that are cheap, efficient and environment friendly; has become the most impactful area of hydrogen evolution research in the perspective of towards alternative green energy. Oxides of Ru and Ir are generally considered as the state-of-art catalyst for doing this reaction, but high cost and scarcity of such noble metal-based oxides have greatly confined their large-scale application[5,6]. Hence, a huge attention has put forward to design nonprecious metal-based electrocatalyst such oxide, hydroxide, chalcogenide, metal organic frameworks (MOFs), coordination polymer (CP) etc., based on the 3d transition metals[7-13]. Among above all, MOFs[14-16] have fascinated significant attention because of their versatility in structure and composition, high specific surface area and capability to introduce several different types of active sites such as metals, organic functions and organic metal complexes.[17] However, the additional second metal site in MOFs i.e., bimetallic MOFs promise an effective number of adjustable electrochemically active metals sites and favor the benefit of being able to combine both homogeneous and heterogeneous catalysts[18] in a single system which can play a significant role in OER. Also, the synergistic effect between different metals, bimetallic MOFs possess good catalytic activity. There are some 2D bimetallic MOFs that have been explored greatly in the field of electrocatalysis[19,20], but the 3D bimetallic MOFs materials are more productive as an electrocatalyst[17,21-22] due to high surface area, high porosity, high density active site, framework stability and full growth of framework in all three directions. It is well known that; rate of an electrochemical reaction can be tuned by modifying the composition of the electrolyte which has been investigated widely in the previous reports[23-26]. In the year 2015 Michel et al., demonstrated the activity trend towards OER in different cationic electrolyte solution varies as $Cs^+ > K^+ > Na^+$ in iron free hydroxide solution[27].

Gracia et al., also studied the effect of mono-valent metal ions from electrolyte solution on OER by NiOOH catalyst[28]. Therefore, it is evident that the presence of certain cation could effectively enhance the electrocatalytic activity of an electrocatalyst but this improvisation is limited to a confined scale. This is possibly due lack of opportunity for the foreign cation to be attached strongly and selectively for long range effect over the improvisation of the electrocatalytic activity. So, it is the need of hour to design an effective catalyst where these foreign cations would present with an effective structural integrity so that the improved electrocatalyst could become a long-range one. Kim et *al.*, reported mesoporous K-doped $NiCo_2O_4$ materials for OER, where in-situ (i) presence of redox inactive foreign enhance the OER activity with improved charge transfer at the interface[29]. Inspired from the advantage of having K^+ ions into the interior structure of an electrocatalyst that have high surface to volume ratio, here two Co(II)-based MOF materials have been synthesized having an ionic K^+ ion layer (Set-**2** and Set-**3**) from a previously reported CP **1**[30] (Set-**1**), to perform electrolytic OER in 0.5 M KOH solution.

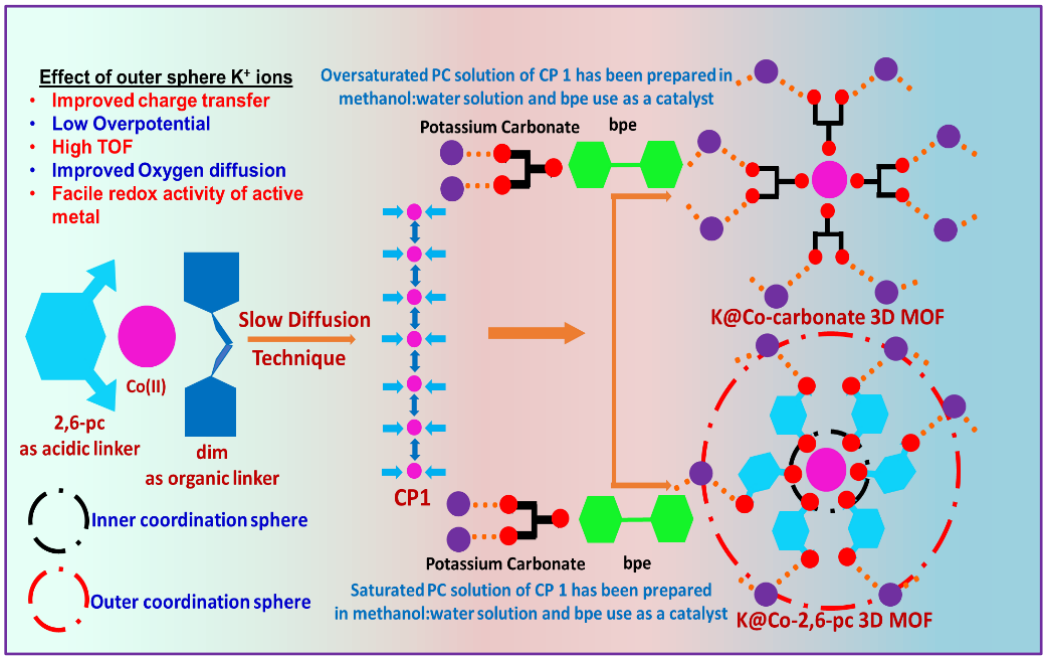

Scheme 1. Synthetic representation of CP-**1** (Set-**1**), K@Co-carbonate MOF (Set **2**) and K@Co-2,6-pc MOF (Set **3**).

The electrocatalytic activity of K^+ ion containing MOFs (Set-**2** and Set-**3**) shows an improved OER activity as compared to pristine Co(II) based CP-**1** (Set-**1**) (without having any K^+ ions). The K@Co-2,6-pc MOF (Set-**3**) demands just 294 mV of overpotential value at 10 mA/cm^2 current density whereas the CP-**1** (Set-**1**) needs 345 mV overpotential value. Here the presence of K^+ ions

successfully improvised the inner and outer Helmotz plane capacitance value and thereby facilitate the charge transfer kinetics at the interface which in turn successfully regulate the O_2 diffusion form the electrode surface as well. Moreover, improved OH^- adsorption and O_2 diffusion ability of K@Co-2,6-pc MOF (Set-**3**) material increased turnover frequency (TOF) value by 28 times as compared to CP-**1** (Set-**1**). Most importantly, structural design of Set-**2** and Set-**3** reveals that presence of all the K^+ ions in the outer coordination sphere that resembles the double layer structure of OER kinetic model, which is a unique example of quantitative structure-property relationship in case of functional MOFs.

7.2. Experimental Section

7.2.1. Materials

Immensely fresh $Co(NO_3)_2 \cdot 6H_2O$, imidazole, dichloromethane, tetrabutylammonium chloride and 2,6-pyridine carboxylic acid have been acquired from the Sigma-Aldrich Chemical Co. All other reagents and solvents have been bought from commercial sources and used except further clarification. di(1H-imidazol-1-yl)methane[31] have been synthesized by a reaction between dichloromethane and imidazole in presence potassium hydroxide and tetrabutyl alumium bromide(TBAB) at 40^0C in inert atmosphere condition. Na_2-2,6-pyridine dicarboxylate (2,6-pc) had been synthesized by the sluggish collation of solid NaOH to the analogous acids (H_2-2,6-pc) in water in a 2:1 ratio and allowed to evaporate until dryness.

7.2.2. Physical Measurements

FT-IR spectra have been obtained on a Perkin Elmer spectrometer (Spectrum II) with the samples. PerkinElmer STA8000 thermal analyzer has been used for thermogravimetric analysis (TGA) with a ramp rate of 5 °C/min from room temperature to 600 °C under nitrogen flow. Powder X-ray diffraction (PXRD) data were collected on a Bruker D8 Discover instrument with Cu-Kα radiation (λ = 1.5406 Å), operating at 40 kV and 40 mA. The synthesized MOFs were examined using Talos F-200-S with HAADF elemental mapping and HR-TEM (TecnaiTM G2 TF20) operating at a 200 kV accelerating voltage. The investigation was conducted using Theta Probe AR-XPS (Thermo Fisher Scientific, UK) X-ray photoelectron spectroscopy.

7.2.3. Synthesis

CP 1 (Set-1)

The slightly modified method has been used as reported[30] earlier, here aqueous solution of Na_2-2,6-pyridine dicarboxylate (2,6-pc) (1 mmol, 213 mg) was slowly mixed with a methanolic

solution (20 mL) of di(1H-imidazol-1-yl)methane (1 mmol, 148 mg) and stirred for 20 min to mix well. Slowly and carefully, 3ml aqueous solution of Co(II) from 20 mL aqueous solution of $Co(NO_3)_2 \cdot 6H_2O$ (1 mmol, 0.291 g) was layered with 6 mL of the aforesaid mixed-ligand solution by using 5 mL of buffer (1:1 water/ MeOH mixture) allowed to reacts through slow diffusion method. At the juncture of the solution pink block-shaped single crystals has been appeared in the layer tube after 15 days. Yield: 90%.

MOF (Set-2)

The layer tube of compound **1** has been over saturated by solid potassium carbonate (K_2CO_3) then 3 ml methanolic solution of trans-1,2-bis(4-pyridyl)ethylene ligand (bpe) (out of 20 ml solution of 1 mmol, 0.182 g) has been added, shacked for 5 minutes. The resulting solution stay for 7 days, magenta color crystals have been appeared throughout the tube that one for X-ray diffraction analysis.

MOF (Set-3)

The synthesis process is exactly same except instead of over saturation of reaction solution by K_2CO_3 of compound **1** unsaturation (below saturation) of reaction solution by K_2CO_3 has been used, black color crystals have been appeared at the bottom of the tube, collected and performed X-ray diffraction analysis.

7.2.4. Crystallographic data collection and refinement

The X-ray single-crystal data for compounds Set-**2** and **3** have been collected at room temperature in a Bruker made APEX III diffractometer. At first, single crystals of both the compounds have been isolated and then mounted on the glass fiber tip using commercial super glue. Mo−Kα radiation (λ = 0.71073 Å) from a sealed tube X-ray source has been used. The raw data have been integrated using the SAINT[32] program and by utilizing SADABS,[33] the absorption corrections were performed. The structures have been solved by SHELXL-2016/6,[34] and full-matrix least-squares refinements on F^2 for all non-hydrogen atoms were performed by SHELXL-2016/6,[34] with anisotropic displacement parameters. All the calculations and molecular graphics were done by SHELXL-2016/6,[34] PLATON v1.15,[35] WinGX system Ver-1.80,[36] Diamond v3.2, Mercury.[37]

7.2.5. Electrochemical Characterization.

AURT-M204 connected with three cell configurations has been exploited for all electrochemical characterizations. The Hg/HgO reference electrode was purchased from the CH instrument. The Pt-coil was purchased from Metroohm and was used as the counter electrode. The entire potential

data was collected by using Hg/HgO as the reference electrode, which was converted into a Reversal hydrogen electrode (E_{RHE}) scale by the Nernst equation

$$E_{RHE} = E_{ref} + 0.059\times14 + 0.098$$

Over potential (η) value of pristine CoFe- LDH and different loading of Ru@Cofe-LDH (1%, 3%, and 5%) at benchmarking current density of 10 mA/cm^2 is calculated by the following equation:

$$\eta = E_{RHE} - 1.23\ V\ (for\ OER)$$

$$\eta = 0 - E_{RHE}\ (for\ HER)$$

Tafel slope was calculated from 100 % iR-drop free LSV polarization data followed by fitting η vs log (current density) using the Tafel equation

$$\eta = \beta\cdot\log(j/j_0)$$

where β signify the Tafel slope value, j signifies the current density, and j_0 is the exchange current density. To prepare various CP and Co_3O_4 modified electrode, ink is made by mixing 3mg of catalyst powder with 200µl isopropanol + 50µl Nafion + 750µl DI water. The ink is sonicated for 30 min until fully dispersed. The as-prepared ink (34.5 µL) is drop-casted over Carbon Cloth (CC) and is dried in an oven at 60 ^oC for overnight.

7.3. RESULTS AND DISCUSSION

7.3.1. Structural Description

{[Co(2,6-pc)(dim)(H_2O)]}$_n$ (Set-1)

The single crystal X-ray diffraction analysis on CP **1**, disclosed that the asymmetric unit constructs one Co(II) ion, one deprotonated 2,6- pyridine dicarboxylate (2,6-pc) and one di(1H-imidazol-1-yl)methane (dim) ligands along with one water molecule. The hexacoordinated central metal ion Co(II) surrounds by six atoms forming CoN_3O_3 environment, two nitrogen atoms coming from two different dim ligands, one nitrogen atom coming from 2,6-pc ligand, two oxygen atoms coming from one 2,6-pc ligand and other oxygen atom coming from water molecule (Figure 1a). Here each Co(II) centre connects with one 2,6-pc and two dim ligands, dim ligand effectively connects Co(II) atoms in *c* direction situated in crystallographic *bc* plane, forms 1D chain (Figure 1b).

{K_2[Co(H_2O)$_4$(CO_3)$_2$]}$_n$ (Set-2)

The single crystal X-ray diffraction study of Set-**2** crystal, represents that the asymmetric unit of it builds with one Co(II) ion, two water molecule and two carbonate ion (Figure 2a). Additionally, two K^+ ions bind through ionic interaction (b) with the anionic oxygens of carbonate ligands and

neutral oxygen atoms of water molecules to form a 2D sheet in crystallographic *ca* plane (Figure 2b). The K^+ ions also neutralize the negative charged secondary environment of the complex (Table 1). The 1D chain of potassium ions has been shown in 2D sheet in *ca* plane (Figure 2c). The 2D sheets are connected by each other through the ionic bonds between potassium ions and oxygen atoms form 3D framework (Figure 2d).

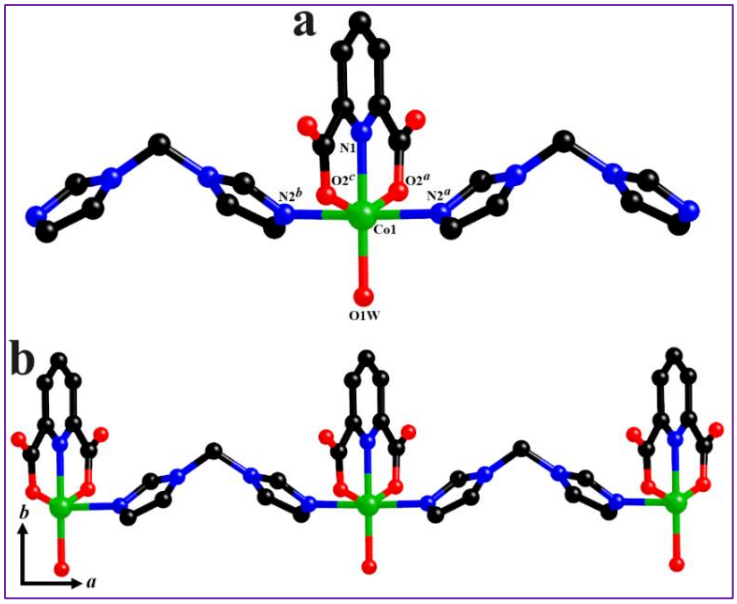

Figure 1. Structural description of CP **1**. (a) Coordination environment of CP **1**, Co green, N blue, O red and C black. (b) 1D arrangement of CP **1** in *ba* plane.

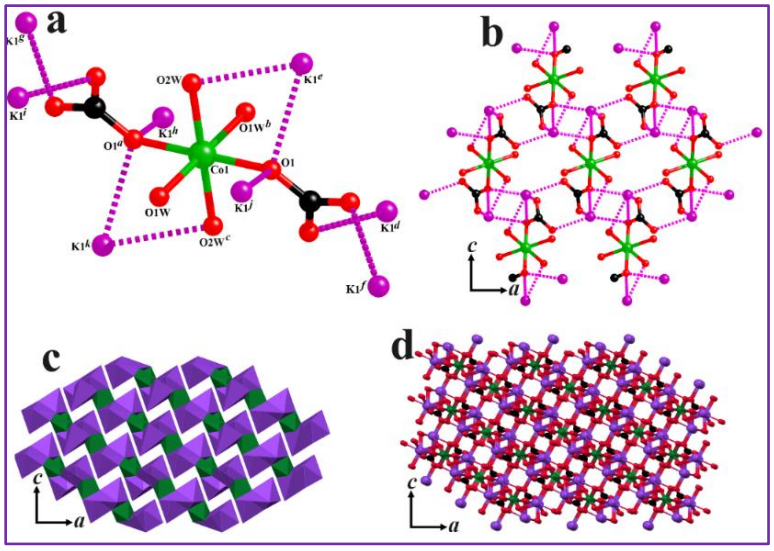

Figure 2. (a) Coordination environment of Set-**2**, Co green, K violet, N blue, O red and C black. (b) Through ionic interaction with potassium ions form 2D arrangement in *ca* plane. (c) Polyhedral style arrangement of Co and K ions in *ca* plane represents the 1D chain of potassium ions. (d) 3D framework of Set-**2** in *ca* plane.

Table 1. Selected Bond Lengths (Å) of Set-**2** MOF.

Co1-O1	2.0693(18)	Co1-O1W	2.129(2)
Co1-O2W^{a}	2.1352(19)	Co1-O2W	2.1352(19)
Co1-O1^{a}	2.0693(18)	Co1-O1W^{a}	2.129(2)
K1-O2	2.704(2)	K1-O2W	2.804(2)
K1-O3	2.740(2)	K1-O1	2.810(2)
K1-O1W	3.019(2)		

a =1-x,2-y,1-z

{K_2[Co(2,6-pc)$_2$](H_2O)$_7$}$_n$ (Set-3)

The single crystal X-ray diffraction study of Set-**3** compound represents that two potassium ions present outside the coordination sphere of Co(II), which is connected through the oxygen atoms of 2,6-pc ligands along with the seven lattice water molecules. The potassium ions neutralize two negatively charged secondary sphere of the complex. The coordination environment around Co(II) is CoO_4N_2, with two pair of oxygen and one pair of nitrogen atoms coming from two different 2,6-pc ligands. The two potassium ions are bridged by oxygen atoms of water molecule (Figure 3a). The ionic potassium bridged (Table 2) coordinated sphere of Co(II) arrange in an order to create a chain of potassium ions along c direction(Figure 3b). The connection of potassium chain and Co(II) chains form an overall 2D arrangement in *ab* plane (Figure 3c).

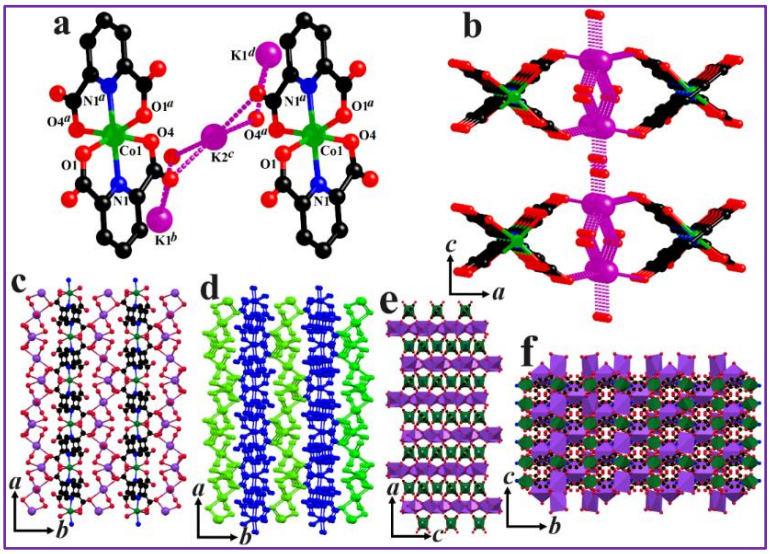

Figure 3. (a) Coordination environment of Set-**3** Co green, K violet, N blue, O red and C black. (b) Through ionic interaction with potassium ions form a chain of potassium ions in *ca* plane. (c) 2D framework in *ab* plane (d) 3D framework in *ab* plane (e) and (f) are Polyhedral style arrangement in *b* and *a* direction.

Finally, a 3D network has been formed by the ionic interactions of potassium ions between the 2D layers in *ab* plane (Figure 3d). It is important to note that the mutual disposition of the Co(II) and

K(I) polyhedral chains are orientation specific. Along crystallographic *b* axis, both the Co(II) and K(I) polyhedrons are parallelly arranged (Figure 3e) whereas along *a* the same polyhedrons are diagonally disposed (Figure 3f).

Table 2. Selected Bond Lengths (Å) of Set-**3** MOF.

Co1-O1	2.161(3)	Co1-N1	2.035(4)
Co1-O1^{b}	2.161(3)	Co1-O4^{b}	2.160(3)
Co1-N1^{b}	2.035(4)	Co1-O4	2.160(3)
K1-O2W	2.646(8)	K1-O3	2.749(4)
K1-O3^{a}	2.749(4)	K1-O4W^{b}	2.811(4)
K1-O4W^{c}	2.811(4)	K1-O1W^{h}	2.970(4)
K1-O1W^{j}	2.970(4)	K2-O1W	2.813(4)
K2-O1W^{b}	2.813(4)	K2-O3^{g}	2.883(4)
K2-O3W^{g}	2.986(6)	K2-O3^{k}	2.883(4)

a =1/2-x,1-y,z, *b* =x,3/2-y,1/2-z, *c* =1/2-x,-1/2+y,1/2-z, *g* =1/2+x,y,1-z, *h* =1-x,-1/2+y,1/2+z, *k* =1/2+x,3/2-y,-1/2+z.

7.3.2. Stability and Purity

PXRD studies of all the Set **1**, **2** and **3** compounds have been done at two forms i.e., as-synthesized form and in 1(M) KOH solution (Figure 4). The PXRD patterns of simulated form of all the compounds have similar pattens in two different forms. The resembles of simulated patterns with as-synthesized patterns indicate the bulk purity of all the compounds. Persist of all the peaks of all the compounds in 1(M) KOH solution fulfilling the desire structural/framework stability.

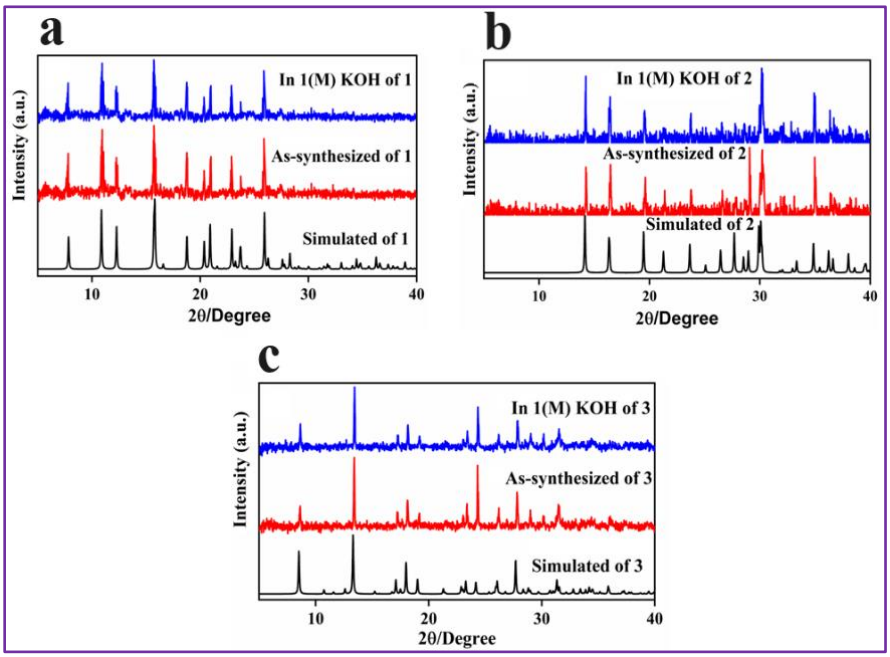

Figure 4. (a), (b) and (c) are the PXRD patterns of Set **1**, **2** and **3** compounds respectively.

Thermogravimetric analysis has been done from 30 ºC to 600 ºC at the rate of 5 ºC/min Thermogravimetric analysis has been done from 30 ºC to 600 ºC at the rate of 5 ºC/min to evaluate the framework stability with the raised of temperature.

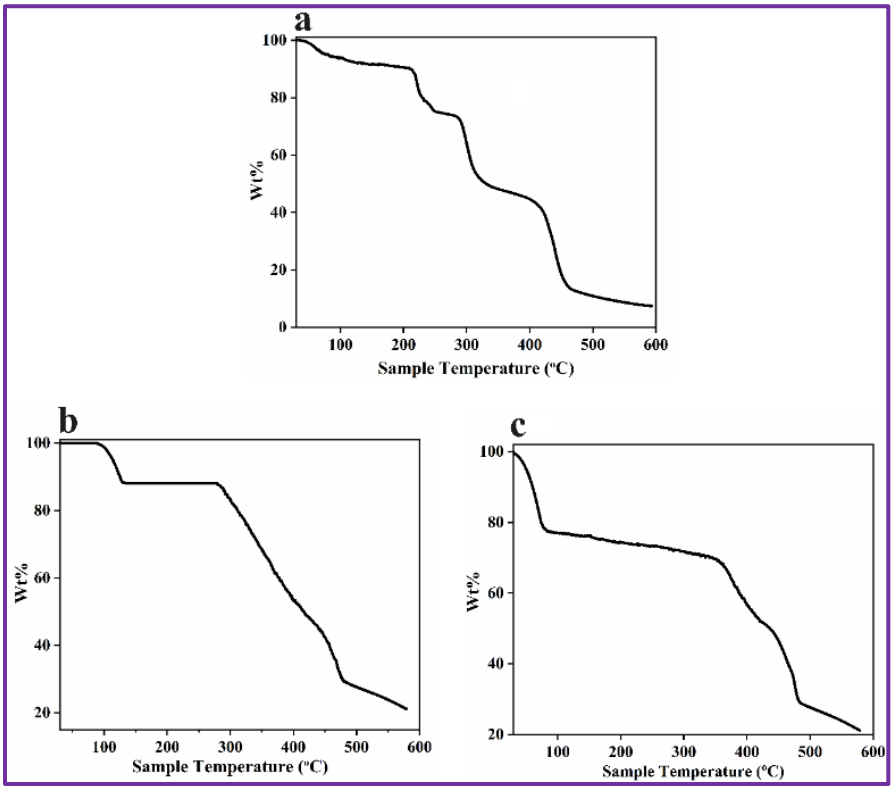

Figure 5. Thermogravimetric analysis of Set 1 **(a)** Set 2 **(b)** Set 3 **(c)**.

The curve (Figure 5a) of Set-**1** compound indicates the wight loss around 5% at close to 100 ºC due to loss of coordination water molecule after that at 200 ºC to 280 ºC the weight loss of 40% may be due to loss of flexible organic linker (dim). Finally, the complete decomposition occurred at 400 ºC. In case of Set-**2** compound the 11.5% weight loss has been occurred due to loss of two coordinated water molecules at around 110 ºC (Figure 5b). Complete decomposition started at 280 ºC. For Set-**3** compound around 22% weight loosed due to elimination of seven water molecules from the lattice at the below of 100 ºC temperature. The complete decomposition started at around 350 ºC.

IR Study.

IR spectra of Set-**1.** IR spectra (KBr pellet, 4000−400 cm^{-1}): ν(O−H), 3431 (stretch); ν(C−H), 3097 (stretch); ν(C−H, alkane), 3012 (stretch) and 1431 (bending); ν(C−C) 1573 (stretch); ν(C−O, carboxylate), 1605 (stretch) and ν(C−N), 1373 (stretch) (Figure 6a).

IR spectra of Set-**2.** IR spectra (KBr pellet, 4000−400 cm^{-1}): ν(O−H), 3238 (stretch); ν(C−O, carbonate), 1613 (stretch) (Figure 6b).

IR spectra of Set-**3.** IR spectra (KBr pellet, 4000−400 cm^{-1}): ν(O−H), 3393 (stretch) ν(C−H), 3050 (stretch) ν(C−O), 1611 (stretch) and ν(C−N), 1372 (stretch) (Figure 6c).

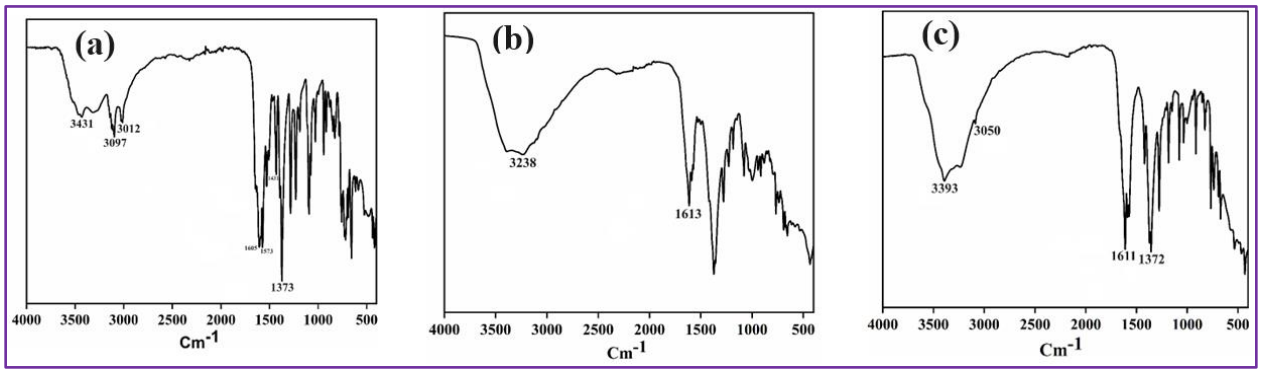

Figure 6. IR spectra of Set-**1**, Set-**2** and Set-**3**

7.3.3. XPS and HR-TEM

Chemical state and functional group analysis in Set-**3** catalyst has been scrutinized by X-ray photoelectron spectroscopy (XPS). XPS survey spectrum has been supplemented in Figure 7a which reveals the presence of C, N, O, K, and Co as constituents of a given metal-organic framework (MOF) without having any other external impurities.

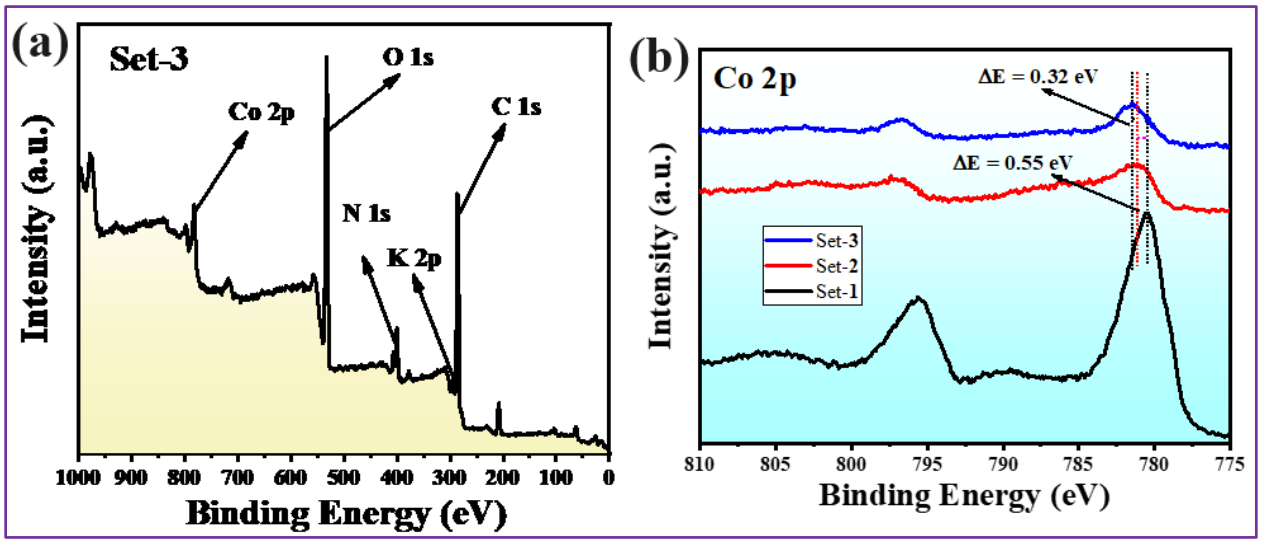

Figure 7. (a) XPS survey spectrum of Set-**3** MOF. (b) XPS spectra of Set-**1**, **2** and **3**.

The deconvoluted XPS spectrum of Co 2p orbital is portrayed in Figure 8a, which possesses two spin-orbit coupling maxima at 781.45 and 796.81 eV corresponding to respective Co $2p_{3/2}$ and Co $2p_{1/2}$ orbitals in +2 oxidation states. The effect of potassium ions over the active Co ions was

further justified from chemical structure analysis using an XPS study. The comparison of Co 2p XPS spectrum of Set-**1**, Set-**2**, and Set-**3** have been displayed in Figure 7b. From the given XPS spectrum it is evident that an increase in K^+ ion led to the shift of XPS maxima towards higher binding energy reflecting the increase in surface charge density over Co ions. This indicates a clear synergistic electronic interaction between Co^{2+} and K^+ ions in the framework structure.

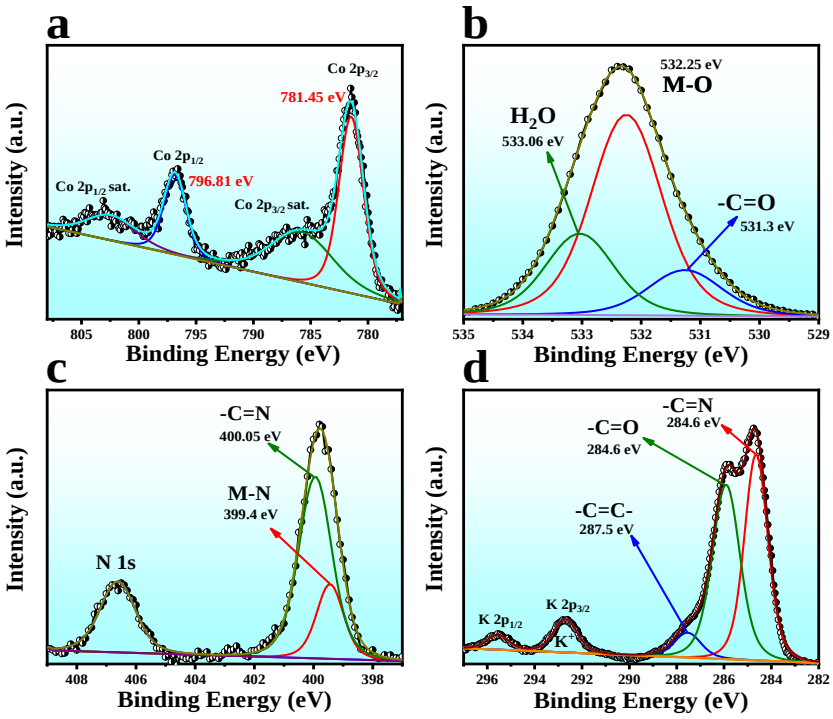

Figure 8. (a) High resolution XPS spectrum for Co 2p orbital in Set-**3** catalyst; (b-d) deconvoluted XPS spectrum of O 1s, N 1s and C 1s orbitals for the Set-**3** material respectively.

The deconvoluted XPS spectrum of O 1s orbitals depicts three spin-orbit coupling peaks at 531.3, 532.25, and 533.06 eV corresponding to the -C=O, M(Co, K)-O and H_2O functionalities respectively (Figure 8b). N 1s spectrum reveals (Figure 8c) two maxima at 399.4 and 400.05 eV binding energy values related to M(Co)-N and -C=N functional groups respectively. Figure 8d shows combined XPS outcomes of C 1s orbital and K 2p orbital in Set-**3** material. C 1s XP spectrum consists of two spin orbits coupling at 284.6 and 287.5 eV which follows -C=N and -C=C- functionalities in the ligand moiety.

Further, morphological characterization were done via high-resolution transmission electron microscopy (HR-TEM) analysis, and corresponding results are supplemented in Figure 9. Figure 9a depicts the square box-like microstructure of Set-**3** material and crystalline nature of the same

has been identified from the selected area electron diffraction (SAED) pattern given in Figure 9b. Elemental analysis was carried out via high angle annular dark field (HAADF) color mapping analysis. Figure 9c shows the HAADF area selected for color mapping analysis. The resulting elemental mapping of Mix, Co, K, C, O, and N K shell is shown in Figure 9d-i, which portrays a uniform distribution all the expected elements over the surface of the catalyst.

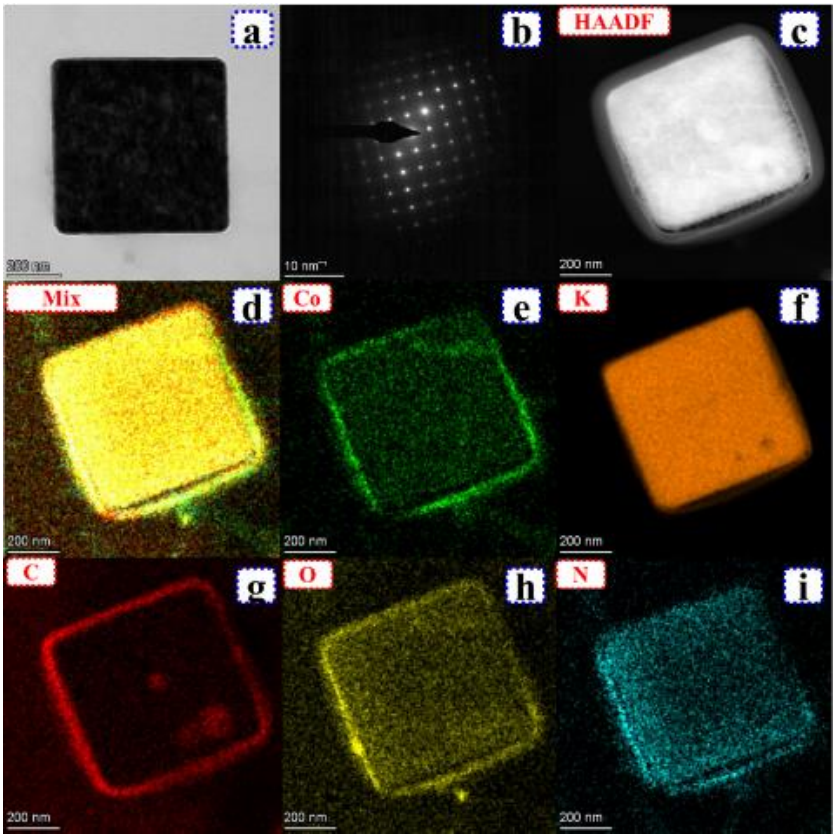

Figure 9. (a) TEM image of Set-**3** MOF; (b) corresponding SAED pattern; (c) HAADF area selected for colour mapping analysis and (d-i) colour mapping results of mix, Co, K, C, O and N K shell respectively.

7.3.4. Electrocatalytic Performance Towards OER in 1 M KOH Solution

The electrocatalytic OER studies have been executed in 0.5 M KOH solution by using a conventional three-electrode system. The modified carbon cloth (CC) substrate with different catalysts has been employed as the working electrode. First, electrocatalytic performance was monitored by linear sweep voltammetry (LSV) with a lower scan rate value of 5 mV/sec to exclude the polarization interference[38,39]. While sweeping the potential, no notable change in current density value has been observed beyond 1.48 V vs RHE due to the predomination of not faradaic process. As the applied potential raised beyond 1.48 V vs RHE, a sharp increase in current density

has been noticed suggesting the starting of faradaic process i.e., OER. All the catalyst Set-**1**, Set-**2** and Set-**3** possess substantial OER activity. The catalyst Set-**3** delivers highest OER activity with a lower overpotential value of 294 mV while driving 10 mA/cm^2 current density value (Figure 10a).

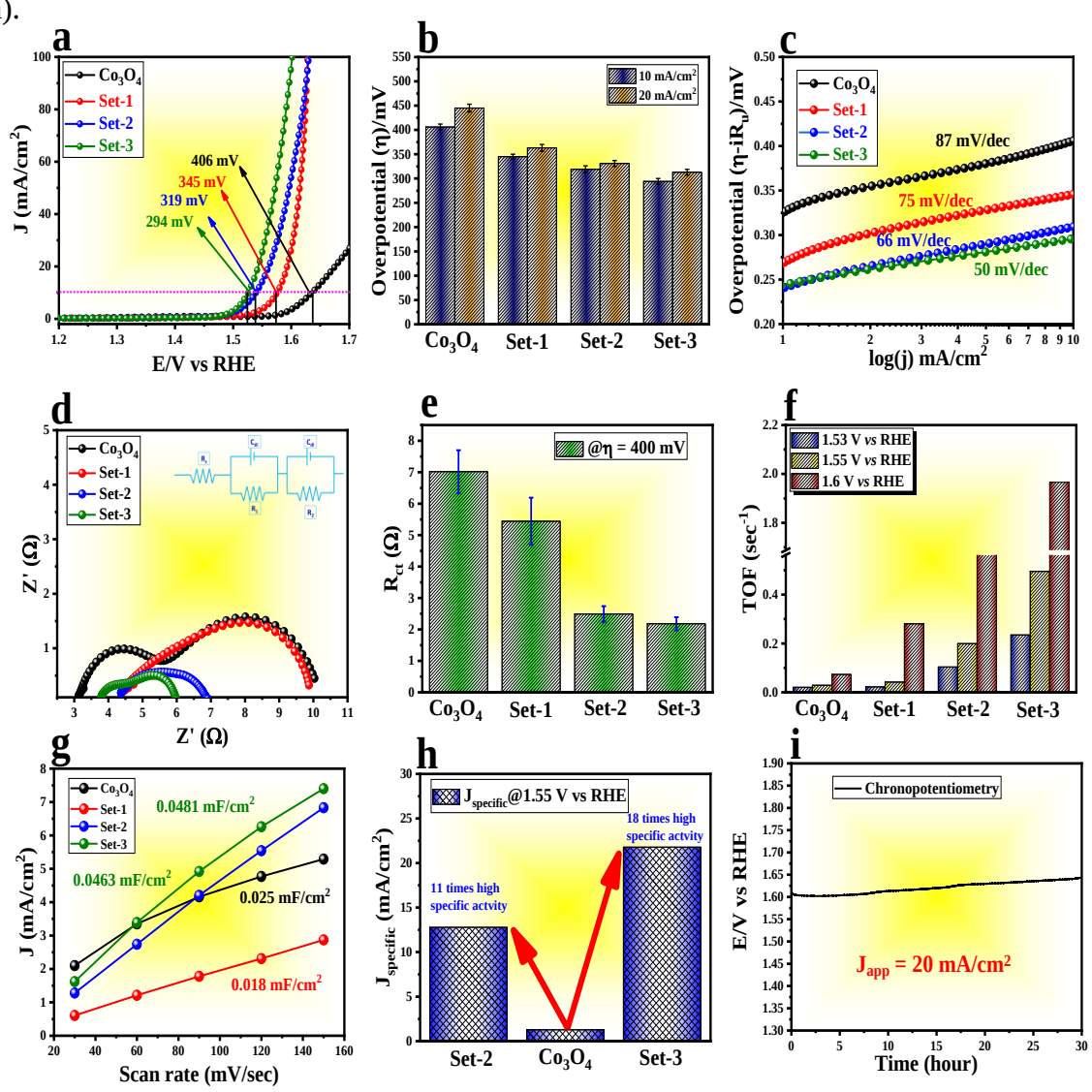

Figure 10. (a) LSV polarization curve acquired with a scan rate value of 5 mV/sec in 0.5 M KOH solution; (b) overpotential information at 10 and 20 mA/cm^2 current density value; (c) Tafel plot extracted from iR-drop free LSV polarization information; (d) electrochemical impedance spectroscopy; (e) corresponding charge transfer resistance (R_{ct}) values for all the catalysts; (f) Calculated TOF values of all the catalyst as a function of different applied potential; (g) ΔJ vs scan rate plot to determine the C_{dl} values; (h) ECSA normalized current density information for Co_3O_4 also the Set-**2** and Set-**3** MOFs and (i) chrono potentiometric outcomes of Set-**3** for 30 hours in 0.5 M KOH solution.

On the other hand, Set-**1**, Set-**2** and commercial Co_3O_4 deliver higher overpotential value of 345, 319 and 406 mV to drive same current density value.[40] Required overpotential with respect to different current densities has been analyzed and given as a bar diagram (Figure 10b). Charge transfer kinetic at the electrode-electrolyte interface has been observed via Tafel slope analysis from the *iR*-drop free LSV polarization information and given as Figure 10c. Set-**3** deliver a lower Tafel slope value of 50 mV/dec as compared to Set-**2** (60 mV/dec), Set-**1** (Set-75) and CO_3O_4 (87 mV/dec), inferring high charge transfer kinetic at the interface. Charge transfer resistance (R_{ct}) of all the catalysts is executed from impedance analysis with an applied overpotential value of 400 mV and all the impedance outcomes are shown in Figure 10d. The best active Set-**3** one delivers the lowest R_{ct} value of 2.18 Ω whereas respective R_{ct} values for Set-**1**, Set-**2** and Co_3O_4 are 5.44, 2.49 and 7.02 Ω. The lowest internal resistance of Set-**3**, allows a faster charge transfer kinetics for OER as compared to other catalysts (Figure 10e). Apart from, this total activity information, the intrinsic activity of catalysts was investigated by determining the specific activity and turnover frequency (TOF) values (Table 3). The TOF values have been calculated from redox area information (Figure S10a-d). The TOF values were evaluated at 1.53, 1.55, and 1.6 V *vs* RHE for all the catalysts. Set-**1**, Set-**2**, Set-**3**, and Co_3O_4 deliver a TOF value of 0.28, 0.77, 1.96, and 0.07 sec^{-1} respectively (Figure 10f).[41-43]

Further investigation on the enhance reactivity of Set-**3** over other, has done by studying the exposed active surface information via famous double-layer capacitance (C_{dl}) method. Cyclic voltammetry study was executed with a various scan rate value for all the catalysts. Difference in anodic and cathodic current (ΔJ) has been plotted against scan rate value in Figure 10g. The C_{dl} values are calculated from the slope of the curve. The calculated C_{dl} values are 0.018, 0.046, 0.0481 and 0.025 mF/cm^2 for Set-**1**, Set-**2**, Set-**3** and Co_3O_4 materials. From the given C_{dl} information, electrochemical active surface area (ECSA) values are calculated by employing the following relation:

$$ECSA = \frac{C_{dl}}{C_s}$$

C_s represent the capacitance value for flat electrode surface which is equal to 0.04 mF/cm^2. The calculated ECSA values are 0.45, 1.15, 1.20 and 0.625 for Set-**1**, Set-**2**, Set-**3** and Co_3O_4 respectively[44]. Therefore, high reactivity of Set-**3** material over other can be attributed to the highly exposed electrochemical active site of the same and thereby could facilitate high OH* adsorption

for OER. The specific activity of the Set-**2** and Set-**3** along with commercial Co_3O_4 was measured by employing the following relation:

$$Specific\ activity\ (J_{specific}) = \frac{J_{geo}}{ECSA}$$

Where J_{geo} represents geometrical current density value at a fixed potential (here it is 1.55 V vs RHE) obtained from Figure 10a. Comparative $J_{specific}$ value given in Figure 10h portrays that Set-**2** and Set-**3** deliver 11 and 18 times higher specific activity as compared to commercial Co_3O_4[45]. This high specific activity of Set-**2** and Set-**3** catalysts might have originated due to faster charge transfer kinetics at the interfaces as a result of the presence of K^+ ions. Apart from the specific and geometrical activity of the Set-**3** catalyst, the durability of the same was executed from chrono potentiometric (CP) analysis. The same has been done by applying a constant current density value of 20 mA/cm^2 and a change in potential has been investigated. Overall MOF studies for 30 hours (Figure 10i) show an excellent stability of the material. Overall, the electrocatalytic outcomes of Set-**3** were compared with other Co-based materials in terms of overpotential and intrinsic TOF value.

Table 3. Comparative electrochemical outcomes of pristine Co_3O_4 and various Set-**1**, Set-**2** and Set-**3** compounds.

Sl. No.	Compound	Potential (V)	Reduction surface area (VA)	Charge over the electrode surface (C)	Number of active Co sites	TOF (sec^{-1})
1	**Co_3O_4**	1.53	0.0000634	0.01268	7.91×10^{16}	0.02031
		1.55				0.02879
		1.6				0.07315
2	**Set-1**	1.53	0.000122	0.0244	1.52×10^{17}	0.02203
		1.55				0.0418
		1.6				0.28024
3	**Set-2**	1.53	0.0000892	0.01784	1.11×10^{17}	0.1037
		1.55				0.19928
		1.6				0.777
4	**Set-3**	1.53	0.0000634	0.00791	7.91×10^{16}	0.23483
		1.55				0.49489
		1.6				1.96576

7.3.5. Improved redox activity of active Co ions in the presence of K^+ ion

Improved reactivity of Co-based coordination polymer as compared to commercial Co_3O_4 was investigated via CV analysis. Here the evolution of the adsorbing binding ability of the intermediates based on the CV outcomes (Figure 11a) and d-band theory (Figure 11b). In general, Co_3O_4 has weak binding strength towards the OH^- ions and thereby possess a weak OER ability. But in the case of Co-based MOFs high binding ability can be investigated from the position of $E_{Co^{2+}/Co^{3+}}$. The MOF materials possess lower $E_{Co^{2+}/Co^{3+}}$ value as compared to Co_3O_4. This difference in redox peak position can be attributed to the upshift in the antibonding state as compared fermi level (E_f).[46] The robustness of the chemical structure of Set-**3** catalysts after the long-term stability study was performed via XRD and HR-TEM analysis.

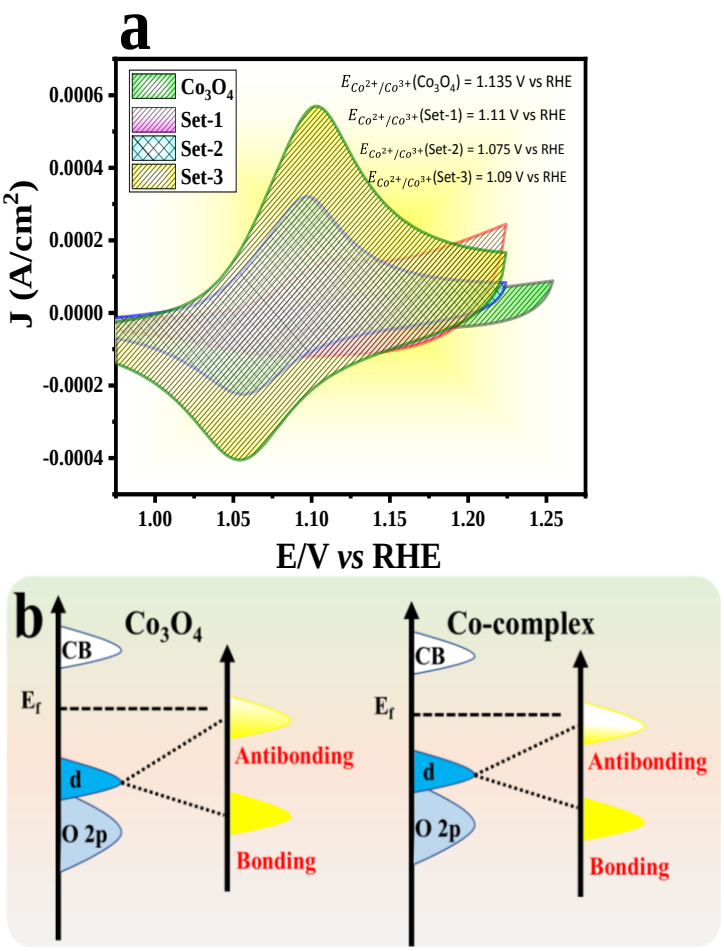

Figure 11. (a) Cyclic voltametric outcomes Set-**1** CP, Set-**2** and Set-**3** MOFs and Co_3O_4 with a scan rate value of 20 mV/sec in 0.5 M KOH solution; (b) comparison of band position of Co_3O_4 and Co-based MOFs.

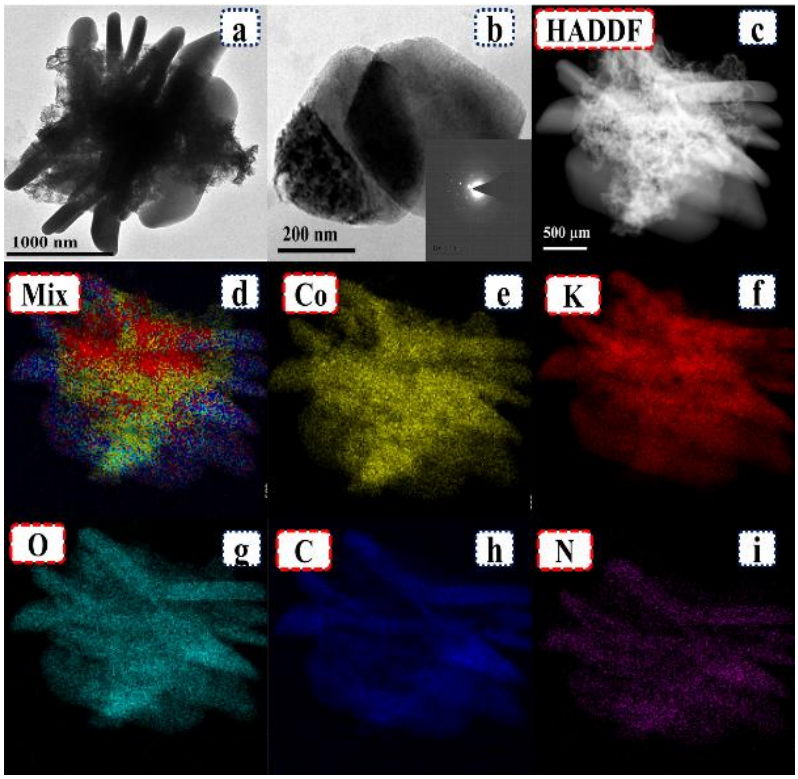

Figure 12. (a-b) Morphological outcomes of Set-**3** catalyst after long-term stability study; inset of Figure b portrays the SAED pattern; (c) represented the HADDF area selected for color mapping analysis; (d-i) shows the color mapping results of mix, Co, K, O, C, and N K shell respectively.

The given XRD pattern displays an identical diffraction pattern as before the stability study. A considerable decrease in diffraction peak intensity might be attributed to the formation of surface oxide under the applied oxidation potential. The morphological robustness of the Set-**3** catalyst was verified from the TEM analysis as portrayed in Figure 12. The morphological outcomes given in Figure 12a-b reveal a distorted 3D cubic-like structure. HADDF analysis and corresponding color mapping results (Figure 12c-i) reveal the compositional stability of Set-**3** materials under a long-term stability study.

7.3.6. Improved Charge Transfer Kinetics at the Electrode Electrolyte Interface

Further, enhanced reactivity of Set-**2** and Set-**3** as compared Set-**1**, was investigated from i-impedance analysis. Corresponding Bode plots for all three sets of coordination polymers are shown in Figure 13a-c. The Bode plot is differentiated in two different regions *i.e.,* electro-activation, or redox region (both in high-frequency site) and OER or the region of concerned faradaic process (low-frequency site).

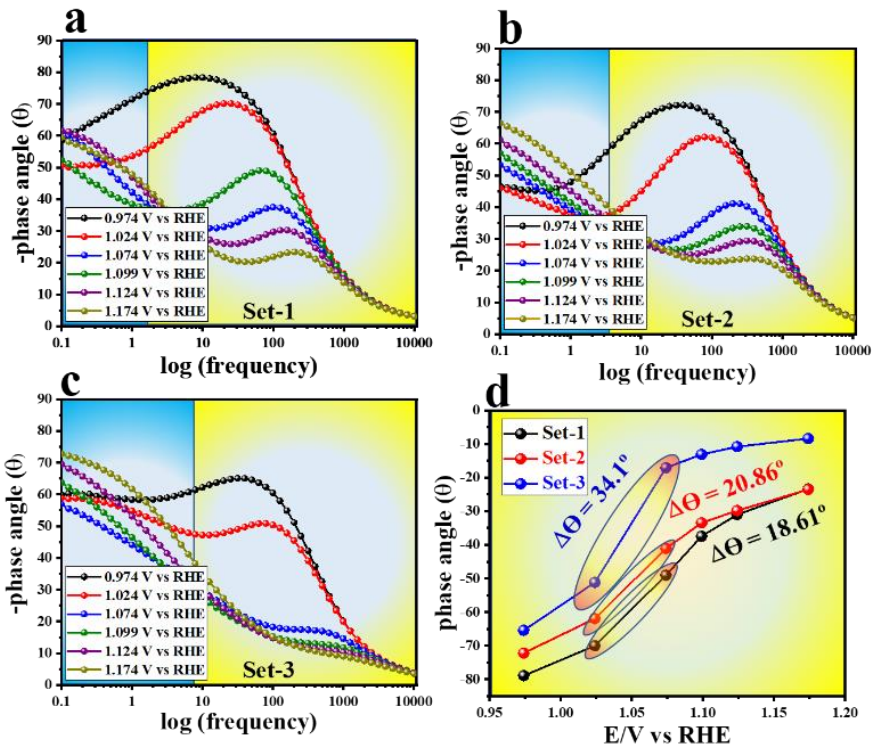

Figure 13. (a-c) Bode plot for Set-**1**, Set-**2** and Set-**3** compounds at different applied potential value and (d) Corresponding phase angle information with respect to different applied potential.

It is worth recalling that, the high electrochemical activity of an electrocatalyst can be investigated by chasing the phase angle difference with respect to the applied potential value. While comparing the Bode features it is interesting to see the as potential has been swept from 1.024 to 1.074 V *vs* RHE, the maxima corresponding to phase decreased sharply which suggests a sudden redox change as a result of oxidation of Co^{2+} ions to Co^{3+} ions. While comparing this change in phase angle concerning the applied potential for three sets of coordination polymer, Set-**3** shows the highest fall in phase angle value as compared to other materials and thereby delivers high redox activity for improved OER performance (Figure 13d).

7.3.7. Role of Second Sphere Potassium Ions in Electrocatalytic Activity

It is important to note here that in all three sets of coordination polymer, the redox-active and coordination environment around the metal ion is same. However, the difference in reactivity is originated due to the high adsorption ability of OH ions in Set-**2** and Set-**3** materials as compared to Set-**1**. The presence of K^+ ions in the second coordination sphere have a strong influence on the increased adsorption ability of metal ions present in first coordination sphere.

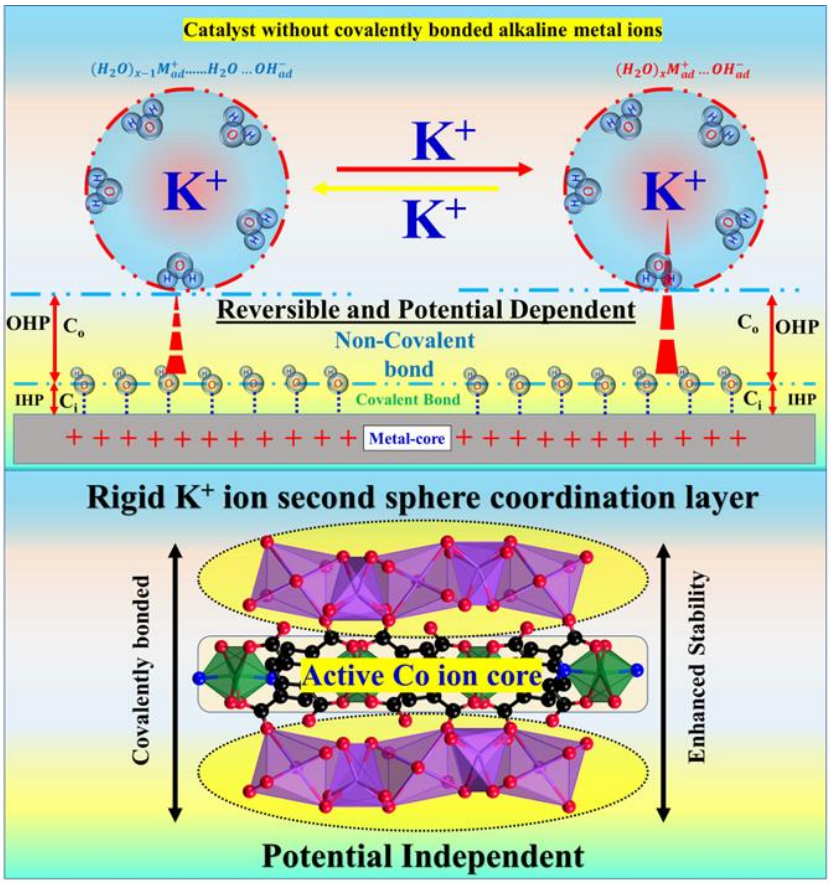

Figure 14. Schematic diagram for interaction between the active metal core and solvated K^+ ions in electrocatalytic condition.

To visualize, a schematic model has been portrayed in Figure 14. The given metal core represents the active Co site where negatively polarized OH^- ions is attached to build an inner Helmholtz plane (IHP). To balance the charge neutrality a hydrated metallic layer would form with few nanometres distance from the IHP layer which is called the outer Helmholtz plane (OHP). Both of this IHP and OHP would results in two capacitance properties of the system viz capacitance for IHP (C_i) and capacitance for OHP (C_o). The adsorption ability of OH^- ions over metal core is highly correlated with the C_o value which in turn largely influence by the C_i value. This is because enhanced C_i value would result in better OH^- adsorption as a result of improved stability by counter cation[47,48].

A systematic analysis of C_i and C_o values in all three sets of MOFs has been performed by following the given relation: First, the total capacitance can be calculated by using the following equation:

$$C = \frac{\int_{E1}^{E2} |i| dE}{2v(E_2 - E_1)}$$

Where E_1 and E_2 are the potential limits in CV measurement, i is the current density value and ν represents the scan rate value[49].

Information about the total interfacial capacitance (C_t) is executed from a scan rate-dependent CV experiment followed by using the following relation:

$$\frac{1}{C} = \frac{1}{C_t} + K_1 v^{1/2}$$

The OHP capacitance (C_o) by using a similar method for calculating C_t.

$$C = C_o + K_2 v^{-1/2}$$

The capacitance corresponding to the IHP is executed by utilizing the following relation:

$$C_i = C - C_o$$

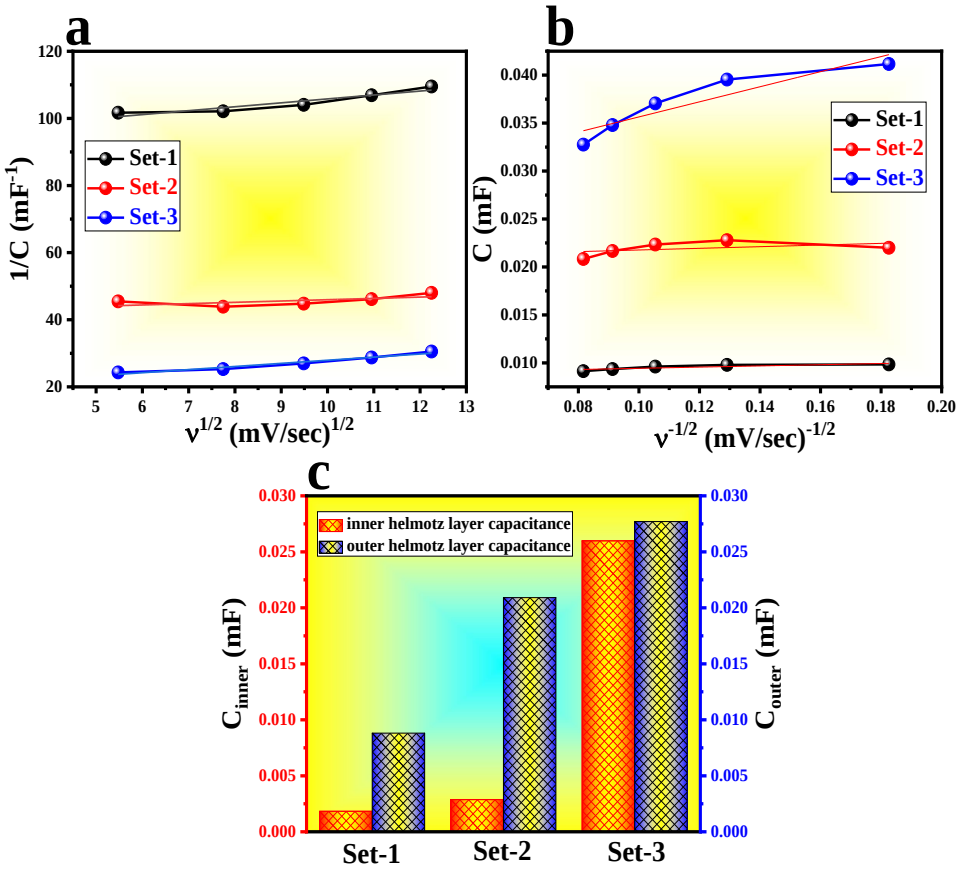

Figure 15. (a-c) Capacitance information of various MOFs along with inner and outer Helmholtz layer capacitance information.

Corresponding capacitance result of all the three materials have been portrayed in Figure 15a-c. The calculated Co values are 0.0088, 0.02091 and 0.0277 mF/cm^2 for Set-**1**, Set-**2** and Set-**3** respectively. Whereas corresponding C_i value are 0.00182, 0.00287 and 0.02598 mF/cm^2. So, materials with high K^+ ions (i.e., Set-**2** and Set-**3**) content deliver an improved C_i value which suggest high specific adsorption of OH^- ions and thereby delivers improved charge transfer kinetics at the interface. These improved C_i values of K^+ ions content materials can be attributed to improved C_o in the second coordination sphere. It is worthy to mention that the capacitive properties of the K^+ ions in the electrolyte solution are not ignorable and it is common for all catalysts. However, such an effect is highly potentially dependent and reversible. But in Set-**2** and Set-**3** catalysts presence of distinct K^+ ions layer with structural rigidity makes these two-catalyst special as compared to Set-**1** and commercial Co_3O_4.

Regarding the transferability of the given model a generalized thought can be presented as: Therefore, the electrolyte's composition would surely have an impact on a MOF, whether it contained any alkali metal ions or not. However, what distinguishes Set-**3** from others is its flawless 1D arrangement and distinct structural knowledge. Since the nature of an ionic OHP layer is highly dependent on K^+ ions and their sweep direction, the various intermediates can be stabilized more than those by relatively loosely bound K^+ ions as a function of applied potential. The Set-**3** catalyst exhibits superior electrochemical performance compared to the Set-**2** catalyst, presumably due to the latter's lack of an ordered K^+ ion layer. Therefore, MOF with redox inactive alkali metal cations and a highly organized 1D layer have an even greater advantage in terms of electrocatalytic properties. Moreover, for other catalysts except MOF, having such a highly organized shell arrangement with OER active metal core would allow the OER kinetics to a greater extent. Therefore, this work paved a new possibility of designing effective OER catalyst with high intrinsic activity.

7.4. CONCLUSION

The presence of alkali metal ions in the second coordination sphere of the 3D-metal organic framework has significantly influenced the charge transfer kinetics at the interface. The 3D-MOF with higher K^+ ion content possesses an excellent OER activity in 0.5 M KOH solution. The 3D-MOF with high K^+ ion content i.e., Set-**3** requires 294 mV of overpotential value to drive 10 mA/cm^2 current density value, which is 51 and 112 mV lesser than that of pristine CP and commercial Co_3O_4 respectively. Interestingly, 28 times increase in TOF value has been noticed

when comparing with commercial Co_3O_4, which is the highest value that has been achieved as compared to previously reported MOFs. Improved charge transfer at the interface was further evaluated from in-situ EIS analysis. The Bode plot analysis enables to find out the exact cause of the increase in OER activity of Set-**3** as compared to Set-**1** to Set-**2**. Certainly, the observed decrease in phase angle during the potential sweep from 1.024 to 1.074 V vs RHE, which suggests a redox change involving the oxidation of Co^{2+} ions to Co^{3+} ions, is an interesting finding. The Set-**1**, Set-**2,** and Set-**3** possess identical redox and OER active Co^{2+} ions sites in their first coordination sphere. However, differences in reactivity arise from Set-**2** and Set-**3**'s higher OH^* adsorption ability compared to Set-**1**, attributed to K^+ ions in the second coordination sphere. A schematic model depicts an inner Helmholtz plane (IHP) and outer Helmholtz plane (OHP) around the metal core, influencing capacitance properties (C_i and C_o) and ultimately enhancing OH- ion adsorption and charge transfer kinetics, particularly in K^+-containing materials. This structural co-relation of MOF-based materials with existing the existing kinetic model will pave a new way to creating the effective catalyst for minimizing the kinetic barrier for OER to design effective electrocatalyst for future application.

REFERENCES

1. Niu, S.; Jiang, W. -J.; Wei, Z.; Tang, T.; Ma, J.; Hu, J. -S.; Wan, L. -J. *J. Am. Chem. Soc.* **2019**, *141*, 7005–7013.
2. Karak, S.; Koner, K.; Karmakar, A.; Mohata, S.; Nishiyama, Y.; Duong, N. T.; Thomas, N.; Ajithkumar, T. G.; Hossain, M. S.; Bandyopadhyay, S.; Kundu, S.; Banerjee. R. *Adv. Mater.* **2023**, 2209919.
3. Maulana, A. L.; Chen, P. -C.; Shi, Z.; Yang, Y.; -Pueyo, C. L.; Seeler, F.; Abruña, H. D.; Muller, D.; -Arndt, K. S.; Yang, P. *Nano Lett.* **2023**, *23*, 6637–6644.
4. Chen, P. -C.; Li, M.; Jin, J.; Yu, S.; Chen, S.; Chen, C.; Salmeron, M.; Yang, P. *ACS Materials Lett.* **2021**, *3*, 1440−1447.
5. Reier, T.; Pawolek, Z.; Cherevko, S.; Bruns, M.; Jones, T.; Teschner, D.; Selve, S.; Bergmann**,** A.; Nong, H. N.; Schlögl, R.; Mayrhofer, K. J. J.; Strasser, P. *J. Am. Chem. Soc.* **2015**, *137*, 13031–13040.
6. Willinger, E.; Massué, C.; Schlögl, R.; Willinger, M. G. *J. Am. Chem. Soc.* **2017**, *139*, 12093−12101.
7. Jiang, W. -J.; Tang, T.; Zhang, Y.; Hu, J. -S. *Acc. Chem. Res.* **2020**, *53*, 1111–1123.
8. Jiang, W. -J.; Niu, S.; Tang, T.; Zhang, Q. -H.; Liu, X. -Z.; Zhang, Y.; Chen, Y. -Y.; Li, J. -H.; Gu, L.; Wan, L. -J.; Hu, J. -S. *Angew. Chem. Int. Ed.* **2017**, *56*, 6572–6577.
9. Tang, T. ; Jiang, W. -J.; Niu, S.; Liu, N.; Luo, H.; Chen, Y. -Y.; Jin, S. -F.; Gao, F.; Wan, L. -J.; Hu, J. -S. *J. Am. Chem. Soc.* **2017**, *139*, 8320−8328.
10. Wang, X.; Cai, Z. -F.; Wang, D.; Wan, L. -J. *J. Am. Chem. Soc.* **2019**, *141*, 7665−7669.
11. Farahani, F. S.; Rahmanifar, M. S.; Noori, A.; -Kady, M. F. E.; Hassani, N.; -Amal, M. N.; Kaner, R. B.; Mousavi, M. F. *J. Am. Chem. Soc.* **2022**, *144*, 3411−3428.

12. Biradha, K.; Goswami, A.; Moi, R. *Chem. Commun.* **2020**, *56*, 10824−10842.
13. Sanati, S.; Morsali, A.; Garcı´a, H. *Energy Environ. Sci.* **2022**, *15*, 3119–3151.
14. Pahari, G.; Bhattacharya, B.; Reddy, C. M.; Ghoshal, D. *Chem. Commun.* **2019**, *55*, 12515-12518.
15. Halder, A.; Bhattacharya, B.; Haque, F.; Dinda, S.; Ghoshal, D. *Chem. Eur. J.* **2019**, *25*, 12196–12205.
16. Maiti, A.; Maity, D.K.; Halder, A.; Ghoshal, D. *Inorg. Chem.* **2023**, *62*, 12403−12412.
17. Liu, J.; Zhao, Y.; Dang, L. L.; Yang, G.; Ma, L. F.; Li, D. S.; Wang, Y. *Chem. Commun.* **2020**, *62*, 8758-8761.
18. Jiao, L.; Wang, Y.; Jiang, H. L.; Xu, Q. *Adv. Mater.* **2018**, *30*, 1703663.
19. Zou, Z.; Wang, T.; Zhao, X.; Jiang, W. -J.; Pan, H.; Gao, D.; Xu, C. *ACS Catal.* **2019**, *9*, 7356–7364.
20. Ye, W.; Yang, Y.; Fang, X.; Arif, M.; Chen, X.; Yan, D. *ACS Sustainable Chem. Eng.* **2019**, *7*, 18085–18092.
21. Dong, H.; Zhang, X.; Yan, X. -C.; Wang, Y. -X.; Sun, X.; Zhang, G.; Feng, Y.; Zhang, F. -M. *ACS Appl. Mater. Interfaces* **2019**, *11*, 45080–45086.
22. Li, W.; Li, F.; Yang, H.; Wu, X.; Zhang, P.; Shan, Y.; Sun, L. *Nat Commun* **2019**, *10*, 5074-5084.
23. Guo, Y.; Tang**,** J.; Henzie**,** J.; Jiang, B.; Xia, W.; Chen, T.; Bando, Y.; Kang, Y. -M.; Hossain, M. S. A.; Sugahara, Y.; Yamauchi, Y. *ACS Nano* **2020**, *14*, 4141–4152.
24. Tang, T.; Jiang, W. -J.; Niu, S.; Liu, N.; Luo, H.; Chen, Y. -Y.; Jin, S. -F.; Gao, F.; Wan, L. -J.; Hu, J. -S. *J. Am. Chem. Soc.* **2017**, *139*, 8320–8328.
25. Li, D.; Zong, Z.; Tang, Z.; Liu, Z.; Chen, S.; Tian, Y.; Wang, X. *ACS Sustainable Chem. Eng.* **2018**, *6*, 5105–5114.
26. Xu, H.; Shan, C.; Wu, X.; Sun, M.; Huang, B.; Tang, Y.; Yan, C. -H. *Energy Environ. Sci.* **2020**, *13*, 2949–2956.
27. Ding, C.; Zhou, X.; Shi, J.; Yan, P.; Wang, Z.; Liu, G.; Li, C. *J. Phys. Chem. B* **2015**, *119*, 3560−3566.
28. Garcia, A. C.; Touzalin, T.; Nieuwl, C.; Perini, N.; Koper, M. T. M. *Angew. Chem. Int. Ed.* **2019**, *58*, 12999–13003.
29. Kim, N. W.; Yu, H.; Oh, J. *RSC Adv.* **2022**, **12**, 12371-12376.
30. Nathan, L. C.; Mai, T. D. *J. Chem. Crystallogr.* **2000**, *30*, 509–518.
31. Diez-barra, E.; De la hoz, A.; Sanchez-migallon, A.; Tejeda, J. *Heterocyles(sendai).* **1992**, *34*, 1365-1373.
32. SMART (V 5.628), SAINT (V 6.45a), XPREP, SHELXTL; Bruker AXS Inc.: Madison, WI, **2004**.
33. Sheldrick, G. M. SADABS, Version 2.03; University of Göttingen: Germany, **2002**.
34. Sheldrick, G. M. *Acta Cryst.* **2015**, A71, 3-8.
35. Spek, A. L. *Acta Crystallogr. Sect. D.* **2009**, *65*, 148–155.
36. Farrugia, L. J. *J. Appl. Crystallogr.* **1999**, *32*, 837–838.
37. Macrae, C. F.; Edgington, P. R.; McCabe, P.; Pidcock, E.; Shields, G. P.; Taylor, R.; Towler, M.; Streek, J. V. D. *J. Appl. Cryst.* **2006**, *39*, 453–457.
38. Karmakar, A.; Karthick, K.; Sankar, S. S.; Kumaravel, S.; Madhu, R.; Kundu, S. *J. Mater. Chem. A* **2021**, *9*, 1314-1352.
39. Anantharaj, S.; Ede, S. R.; Karthick, K.; Sankar, S. S.; Sangeetha, K.; Karthik, P. E.; Kundu, S. *Energy Environ. Sci.* **2018**, *11*, 744-771.

40. Singh, M.; Karmakar, A.; Seal, N.; Mondal, P. P.; Kundu, S.; Neogi, S. *ACS Appl. Mater. Interfaces* **2023**, *15*, 24504–24516.
41. Madhu, R.; Karmakar, A.; Arunachalam, P.; Muthukumar, J.; Gudlurd, P.; Kundu, S. *J. Mater. Chem. A* **2023**, *11*, 21767-21779.
42. Karmakar, A.; Nagappan, S.; Das, A.; Kalloorkal, A.; Kundu, S. *J. Mater. Chem. A* **2023**, *11*, 15635-15642.
43. Karmakar, A.; Krishnan, A. V.; Jayan, R.; Madhu, R.; Islam, M. M.; Kundu, S. *J. Mater. Chem. A* **2023**, *11*, 10684-10698.
44. McCrory, C. C. L.; Jung, S.; Ferrer, I. M.; Chatman, S. M.; Peters, J. C.; Jaramillo, T. F. *J. Am. Chem. Soc.* **2015**, **137**, 4347–4357.
45. Karmakar, A.; Mahendiran, D.; Madhu, R.; Murugan, P.; Kundu, S. *J. Mater. Chem. A* **2023**, *11*, 16349-16362.
46. Zhou, D.; Cai, Z.; Jia, Y.; Xiong, X.; Xie, Q.; Wang, S.; Zhang, Y.; Liu, W.; Duan, H.; Sun, X. *Nanoscale Horiz.* **2018**, *3*, 532-537.
47. Rosario, J. A. D.; Li, G.; Labata, M. F. M.; Ocon, J. D.; Chuang, P. -Y. A. *Applied Catalysis B: Environmental* **2021**, *288*, 119981-119990.
48. Li, G. -F.; Divinagracia, M.; Labata, M. F.; Ocon, J. D.; Chuang, P. -Y. A. *ACS Appl. Mater. Interfaces* **2019**, *11*, 33748−33758.
49. Li, G.; Anderson, L.; Chen, Y.; Pan, M.; Chuang, P. -Y. A. *Sustainable Energy Fuels*, **2018**, *2*, 237-251.

List of Publication

1. Polarity-Induced Excited-State Intramolecular Proton Transfer (ESIPT) in a Pair of Supramolecular Isomeric Multifunctional Dynamic Metal–Organic Frameworks.
Arijit Halder, Biswajit Bhattacharya, Fazle Haque, **Susanta Dinda**, Debajyoti Ghoshal
***Chem. Eur. J.* 2019, 25, 12196–12205**

2. Multifunctional Porous Coordination Polymers Synthesized by the Variation of Chain Length and Flexibility of Dicarboxylates and Size of the Metal Ions.
Saheli Ghosh, Mrinmay Das, **Susanta Dinda**, Goutam Pahari, Partha Pratim Ray, Debajyoti Ghoshal
***Cryst. Growth Des.* 2021, 21, 4892–4903**

3.* Unraveling the Role of Structural Dynamism in Metal Organic Frameworks (MOF) for Excited-State Intramolecular Proton Transfer (ESIPT) Driven Water Sensing.
Arijit Halder, Anupam Maiti, **Susanta Dinda**, Biswajit Bhattacharya, Debajyoti Ghoshal
***Cryst. Growth Des.* 2021, 21, 6110–6118.**

4. Designing of Three Mixed Ligand MOFs in Searching of Length Induced Flexibility in Ligand for the Creation of Interpenetration.
Saheli Ghosh, Goutam Pahari, Anupam Maiti, **Susanta Dinda**, Debajyoti Ghoshal
***Polyhedron* 2022, 218, 115763.**

5. Construction of Four New d^{10} Metal Ion Coordination Polymers: Synthesis, Characterization and Structural Diversity.
Anupam Maiti, Arijit Halder, **Susanta Dinda**, Goutam Pahari, Debajyoti Ghoshal
***Polyhedron* 2022, 227, 116144**

6. Polar Acylamide Functionalized Porous Cu-MOFs for Sustainable and Selective Carbon Dioxide Sorption and Separation at Ambient and High Pressure,
Anupam Maiti, **Susanta Dinda**, Arijit Halder, Pintu Das, Debajyoti Ghoshal
***Cryst. Growth Des.* 2023, 23, 1860−1867**

7.* Solvent induced reversible single-crystal-to-single-crystal structural transformation in dynamic metal organic frameworks: a case of enhanced hydrogen sorption in polycatenated framework,

Susanta Dinda, Goutam Pahari, Anupam Maiti, Debajyoti Ghoshal

***CrystEngComm*, 2023, 25, 1116-1125**

8.* Concentration Mediated Structural Modulation in a Family of Mixed-Ligand Coordination Polymers: Structure, Sorption and Luminescence Study

Susanta Dinda, Arijit Halder, Anupam Maiti, Debajyoti Ghoshal

***Polyhedron* 2023, 246, 116667**

9.* Solid-State Solvent-Independent Excited-State Intramolecular Proton Transfer in a Coordination Polymer and Its Temperature Dependence.

Arijit Halder, **Susanta Dinda**, Sourav Deb, Sujoy Baitalik, Debajyoti Ghoshal

***Inorg. Chem.* 2023, 62, 18732–18739.**

10.* Redox Insights and OER Activity in 3D-MOFs: The Role of Alkali Metal Ions

Susanta Dinda, Arun Karmakar, Debajyoti Ghoshal, Subrata Kundu

[*Communicated*]

11.* Selective Detection of Primary Aromatic Amines Through Enhanced Luminescence of a 2D+2D Inclined Polycatenated Microporous Nitro Functionalized Cd(II) MOF

Susanta Dinda, Bidyadhar Mahato, Anupam Maiti, Debajyoti Ghoshal

[*Communicated*]

* **These works are included in this thesis.**